ABSTRACT

HUANG, KE. Heart Repair with Stem Cell Derivatives. (Under the direction of Dr. Ke Cheng and Dr. Scott Laster).

Coronary heart disease (CHD) is still one of the leading causes of death in the United States. The pathological processes that lead to CHD after an acute myocardial infarction (MI) can be divided into four different phases. The first phase occurs one hour after MI and is characterized by apoptosis and necrosis of the cardiomyocytes. Then, an acute inflammatory phase takes place 1 h to 4 days after MI. In this phase, inflammatory cells infiltrate into the infarcted area, dead cardiomyocytes are removed, and extracellular matrix is degraded. From 4 days to 2 weeks, granulation tissue is formed, and the infarcted heart begins to form new blood vessels and ECM proteins. From 2 weeks to 2 months after MI, the scar tissue is formed and the myofibroblasts undergo apoptosis. Currently, the clinical reperfusion strategies used after MI mainly depend on the amount of time the heart tissue was ischemic. In most cases, patients get percutaneous coronary intervention in addition to postoperative drug combinations. Although these treatment strategies help patients dramatically, the heart reconstruction that takes place after MI frequently leads to recurrent heart failure and even death due to the poor regenerative abilities of the adult heart.

Scientists have generated a large array of preclinical and clinical research using cells derived from multiple organs (cardiosphere-derived cells, mesenchymal stem cells, endothelial progenitor cells, skeletal myoblasts, and embryonic stem cells) or cells that have been reprogrammed (cardiomyocytes, induced pluripotent stem cells, and fibroblasts) for cardiac regenerative treatment. Mounting evidence suggests that most cells impart their therapeutic benefits primarily through paracrine factors, which alter the microenvironment of the cardiac extracellular matrix and regulate the remodeling process after MI injury.

Although cell therapies have the potential to significantly enhance the field of cardiac regenerative medicine, there are many challenges hampering the utility of cell therapy in clinical applications. Firstly, stem cells are very fragile and have to be carefully preserved to keep them alive and functional until the time of transplantation. Consequently, live stem cells are not an instantly available product for clinical application. Also, the modes of action for cell therapy products remain elusive, making it difficult to standardize product-release criteria. Additionally, the undifferentiated cells, such as stem cells, can increase the risk of cancerous formations, due to their potential for unlimited proliferation. To increase host immunologic tolerance, the transplantation of autologous stem cells may be a good choice, but the generation of these stem cells would be too expensive and time consuming for patients. Moreover, the extremely low cell retention/engraftment rate, regardless of the delivery route, is still a major hurdle hampering the efficacy of the therapy.

Therefore, new therapeutics have been developed as a result of interdisciplinary cooperation. Scientists have been focused on non-live, synthetic cells, homing nanoparticles, and artificial cardiac patches for MI treatment. Exciting results have been produced in both rodent and relevant large animal models in many studies. Here, we integrated biomaterials with cell derivatives to diminish cell therapy limitations and promote therapeutic availability and efficacy. In the meantime, we also designed bispecific antibodies for endogenous stem cell recruitment in the injured heart for cardiac repair.

Heart Repair with Stem Cell Derivatives

by
Ke Huang

A dissertation submitted to the Graduate Faculty of
North Carolina State University
in partial fulfillment of the
requirements for the degree of
Doctor of Philosophy

Comparative Biomedical Sciences

Raleigh, North Carolina

2019

APPROVED BY:

_____   _____
Dr. Ke Cheng   Dr. Scott Laster
Committee Co-Chair   Committee Co-Chair

_____   _____
Dr. Ashley Brown   Dr. Donald Freytes

BIOGRAPHY

The author was born on January 28th, 1983 in Changzhi, Shanxi, China, to Jinbao Huang and Pu Zhao. He grew up in China and earned his Medical Degree from Shanxi Medical University in 2008. During his undergraduate years, he was a research assistant in Department of Physiology at Shanxi Medical University for one year. After graduation, he did his residency in the Department of Cardiology and Cardiac Care Unit at the Central Hospital of Taiyuan City for 2 years.

He came to the United States in 2010 and got his master's degree in 2013 at University of Akron in Exercise Physiology & Adult Fitness. Ke joined Cleveland Clinic Foundation as a research intern for one semester during his master's. Then, he worked as a medical assistant/scribe in Wake Spine & Pain Clinic From 2014 to 2016.

In 2016, Ke began his PhD studies in Comparative Biomedical Sciences at the NCSU College of Veterinary Medicine, under the guidance of Dr. Ke Cheng. His PhD studies focused on engineering of therapeutics from cells for myocardial regenerative therapy.

TABLE OF CONTENTS

LIST OF TABLES

Appendix B: Chapter 3 Supplemental Data

Appendix C: Chapter 4 Supplemental Data

LIST OF ABBREVIATIONS

Abbreviations	Descriptions
4-Oct	octamer-binding transcription factor 4
AD	adamantane
AFM	atomic force microscopy
AHA	American Heart Association
ALT	alanine aminotransferase
ANG II	angiotensin II
artCP	artificial cardiac patch
AST	aspartate aminotransferase
BCA	bicinchoninic acid
bFGF	basic fibroblast growth factor
BMSCs	bone marrow-derived stem cells
BsAb	bispecific antibody
BUN	blood urea nitrogen
CD	cyclodextrin
CDCs	cardiacsphere-derived cells
CHD	coronary heart disease
CMHC	cardiac myosin heavy chain
CMMP	cell-mimicking microparticle
CPCs	cardiac progenitor cells
Cr	creatinine
CS	cardiac stromal cell secretome
CSCs	cardiac stromal cells
cTnI	cardiac troponin I
DCM	dichloromethane
dECM	decellularized cardiac extracellular matrix
DLS	dynamic light scattering analysis
DOPE-NHS	dioleoylphosphatidylethanolamine N-hydroxysuccinimide

ECM	extracellular matrix
ELISA	enzyme-linked immunosorbent assay
ENO	enolase
EPCs	endothelial progenitor cells
EPs	PGE_2 receptors
ESCs	embryonic stem cells
fMLP	N-formyl-methionyl-leucyl-phenylalanine
FRET	fluorescence resonance energy transfer microscopy
FSN	fibrin-specific nanogel
GAPDH	glyceraldehyde 3-phosphate dehydrogenase
G-CSF	granulocyte colony stimulating factor
H3K27	histone 3 lysine 27
HF	heart failure
HGF	hepatocyte growth factor
HNS	half non-specific
HSCs	hematopoietic stem cells
HUVECs	human umbilical vein endothelial cells
I/R	ischemia/reperfusion
IACUC	Institutional Animal Care and Use Committee
iCMs	iPSC-derived cardiomyocytes
IGF-1	insulin-like growth factor 1
IgG	immunoglobulin G
IL	interleukin
IM	intramuscular injection
iPSCs	induced pluripotent stem cells
LAD	left anterior descending artery
LVEDD	left ventricular end diastolic diameter
LVEDV	left ventricular end-diastolic volume
LVEF	left ventricular ejection fraction

LVESD	left ventricular end systolic diameter
LVESV	left ventricular end-systolic volume
LVFS	left ventricular fraction shortening
MCP-1	monocyte chemoattractant protein -1
MI	myocardial infarction
miR	microRNA
MMPs	matrix metalloproteinases
MPs	microparticles
MRI	magnetic resonance imaging
MSCs	mesenchymal stem cells
myoECM	decellularized pig heart myocardium extracellular matrix
NAD(P)H	reduced nicotinamide adenine dinucleotide phosphate
NC	nanocell
NF-κB	nuclear factor kappa-light-chain-enhancer of activated B cells
NHT	native heart tissue
NIH	National Institutes of Health
Nox-4	NAD(P)H oxidase-4
NRCM	neonatal rat cardiomyocytes
NS	non-specific
PAI1	plasminogen activator inhibitor 1
PDGF	platelet-derived growth factor
PDI	polydispersity index
PEG	polyethylene glycol
PGE2	prostaglandin E_2
PGK	phosphoglycerate kinase
PGM	phosphoglucomutase
pH3	Phosphorylated histone H3
PINC	platelet-inspired nanocell
PKm2	pyruvate kinase m2

Pl3K	phosphatidylinositol 3-kinase
PLGA	polymer- poly lactic-co-glycolic acid
PNV-CSCs	platelet decorated nanovesicles that fused with cardiac stem cells
RFP	red fluorescent protein
SCRD BsAbs	stem cell re-directing bispecific antibodies
SD rat	sprague dawley rat
SDF-1	stromal cell-derived factor 1
SOX-2	sex determining region Y-box 2
SulfoSMCC	sulfosuccinimidyl 4-(N-maleimidomethyl) cyclohexane-1-carboxylate
synCSCs	synthetic cardiac stromal cells
TEM	transmission electron microscopy
TGF-β	transforming growth factor beta 1
TIMP1	tissue inhibitor of metalloproteinase-1
TKX cocktail	Telazol-ketamine-xylazine cocktail
TLR	toll-like receptor
TNF-α	tumor necrosis factor -α
tPA	tissue plasminogen activator
TTC	triphenyltetrazolium chloride
Tβ4	thymosin-β4
UTX	ubiquitously transcribed tetratricopeptide repeat, X chromosome
VCAM1	vascular cell adhesion molecule 1
VEGF	vascular endothelial growth factor
vWF	von Willebrand factor
w/o/w	water/oil/water
α-SA	sarcomeric alpha actinin

CHAPTER 1: Background of Cardiac Cell Therapy: Opportunities and Challenges

1. Abstract

Myocardial infarction (MI) caused by coronary heart disease (CHD) remains one of the most common causes of death in the United States. Over the last few decades, scientists have invested time and effort on the study and development of stem cell therapies for myocardial regeneration after MI. Mounting evidence supports the position that paracrine mechanisms are the main contributors to the regenerative effects attributed to these cell therapies. However, due to a number of limitations, they are not yet readily available for clinical applications. The next generation of cell-based MI therapies seek to identify and isolate stem cell products and derivatives, in combination with biocompatible materials and technologies, for the regeneration of damaged myocardial tissue. In this review, we will discuss the progress made thus far in pursuit of this new generation of stem cell therapies. We will address their fundamental regenerative mechanisms, their potential to combine with other therapeutic products, and their role in shaping new clinical approaches in heart tissue engineering.

2. Introduction

Coronary heart disease (CHD) is one of the leading causes of death in the United States[1]. It is characterized by stenosis, or obstruction of the coronary artery, and leads to myocardial infarction (MI). Each year, ~735,000 Americans suffer from a heart attack. Two thirds of those

experience an infarction for the first time[1]. Although the age-adjusted rates of recurrent CHD have declined in the past decade, the recurrence and mortality rate within 5 years after a first myocardial infarction (MI) are still high, due to the tendency for ensuing heart failure (HF)[2]. Cardiac function is carried out through the rhythmic contractions of the myocardium, which is composed of cardiomyocytes, extracellular matrix (ECM), and the capillary microcirculation[3]. The incidence of MI results in myocardial ischemic necrosis, which enervates cardiac function and induces the remodeling of both the infarcted and non-infarcted zones of the myocardium. During this remodeling process, the infarcted myocardium begins to scar over and expands with time. The maturing scar restricts proper contraction biomechanics, leading to myocardium hypertrophy and left ventricular dilation, heart failure, and death[4]. The key to preserving heart function after MI lies in saving more of the viable myocardium while dialing back the disruptive role the myocardial scar plays in the dilation of the ventricle.

The regeneration of tissues is a complex and well-choreographed biological phenomenon that restores tissue architecture, morphology, and function through the replacement of unhealthy/damaged components *via* cell proliferation and differentiation. The heart myocardium, unlike naturally regenerative organs, was once considered a terminally differentiated tissue without regenerative abilities after injury[5,6]. However, this common assertion has been challenged by a number of studies. The heart of zebrafish, for example, was found to regenerate after serious injury[7,8] due to the specificity of the myocardium environment and proliferative cardiomyocytes[9]. Additionally, neonatal mice cardiomyocytes were found to regenerate mainly through pre-existing cardiomyocytes[4]. Scientists now believe that the human heart is capable of some level of regeneration with varying degrees of myocardium renewal[10,11]. Recently, researchers promoted the regeneration of adult cardiomyocytes from mice and humans by regulating their cell cycle[12].

Researchers generated induced-pluripotent stem cells (iPSCs) from fibroblasts or bone marrow cells for heart repair using various reprogramming techniques[13,14]. Also, embryonic stem cell (ESC)-derived cardiomyocytes demonstrated their potential for cardiac tissue engineering in preclinical animal models[15]. As an important heart regenerative therapy method, adult stem cell therapy has become one of the most eye-catching research topics, generating a large array of preclinical and clinical researches. In a clinical trial using cardiosphere-derived autologous stem cells for the reversal of ventricular dysfunction (CADUCEUS), the MI patients who were intracoronarily infused with cardiosphere-derived stem cells (CDCs), experienced reduced infarct-scar mass, increased viable heart mass, a thickened reginal systolic wall, and increased reginal contractility[16,17]. Additionally, the bone marrow derived mesenchymal stem cells[18,19] and adipose tissue-derived stem cells[20] have been demonstrated to improve cardiac function for MI injured heart. There is mounting evidence demonstrating that most adult stem cells impart their therapeutic benefits primarily through paracrine factors, which alter the microenvironment of the cardiac extracellular matrix and regulate the remodeling process after MI injury[21-26]. Although cell therapies have the potential to significantly enhance the field of cardiac regenerative medicine, there are many challenges hampering the utility of cell therapy in clinical applications. Our review will address the opportunities and challenges involved with cardiac cell therapy, as well as the things we can borrow from biomaterials and bioengineering approaches to drive cell therapies to the next generation. Our review will also summarize both cellular and non-cellular approaches (or the combination of the two) for cardiac regenerative medicine purposes.

3. Paracrine mechanisms

3.1 Paracrine mechanisms of CDCs

Cardiosphere-derived cells (CDCs) are derived from myocardium tissue samples and represent a natural mixture of intrinsic cardiac stromal cells. They consistently express CD105, partially express CD90, and are negative for hematopoietic markers such as CD45, CD31, and CD34. The fraction of ckit-positive cells in CDCs is negligible and they do not contribute to the overall therapeutic benefits of CDCs. Studies have reported the ability of CDCs to protect the heart by secreting vascular endothelial growth factor (VEGF), hepatocyte growth factor (HGF), stromal cell-derived factor 1 (SDF-1), insulin-like growth factor 1 (IGF-1), and basic fibroblast growth factor (bFGF) (Fig. 1)[27-29]. VEGF is a signal protein that binds to the surface of endothelial cells, extracellular matrix proteins, and other molecules. It induces angiogenesis in the injured heart by encouraging the differentiation of vascular endothelial cells through the calcium signaling pathway and PI3K-Akt signaling pathway[30]. Other angiogenic factors, such as bFGF, which binds to heparan sulfates in the ECM, help mediate endothelial cell migration, proliferation, and tube structure formation[31]. HGF, which is found in elevated levels in the heart, helps to prevent oxidative stress after MI and promotes self-repair through the HGF/Met signaling pathway. Studies have shown that transplanted CDCs release HGF, which enhances the HGF/Met system, improving angiogenesis, repressing immunomodulation, and reducing fibrosis[32,33]. By stimulating the SDF-1/CXCR4 axis, SDF-1 preserved viable cardiomyocytes and increased vascular density in a mouse model of acute MI[34]. In addition, as a strong chemokine, SDF-1 is an effective recruiter of endothelial progenitor cells (EPCs) from bone marrow[35]. IGF-1 stimulates the Akt/Foxo pathway and plays an essential role in preventing ANG II-induced cardiac inflammation and fibrosis[36,37].

3.2 Paracrine mechanisms of MSCs

Mesenchymal stem cells (MSCs) in animal MI models have been shown to attenuate the expression of collagen types I and III in the cardiac extracellular matrix via paracrine signaling[21]. They have also been reported to decrease tissue inhibitors of metalloproteinase-1 (TIMP1) and increase matrix metalloproteinases (MMPs), which have a distinct spatial and temporal role in cardiac remodeling[38]. After MI injury, MMPs expressed by infiltrated macrophages and fibroblasts, especially MMP-2 and MMP-9, trigger regenerative signals through the MMP/TIMP axis, and mediate ECM protein degradation, cell proliferation, and migration[38,39]. Furthermore, adrenomedullin overexpression in MSCs significantly improved heart function and decreased the heart fibrosis area[40]. Thymosin-β4 (Tβ4), which is also secreted by MSCs, restores cardiac function and contributes to cardiac repair after MI injury[41,42]. Tβ4 proteins suppress the epigenetic repressor methyl-CpG-binding protein 2. In doing so, they reverse the expression of peroxisome proliferator-activated receptor-γ and downregulate fibrogenic genes, platelet-derived growth factor-β receptor, α-smooth muscle actin, collagen 1, and fibronectin, resulting in reduced fibrosis[43]. Thus, these paracrine signals, released by MSCs to communicate with surrounding cardiac cells, stimulate the production of regenerative factors that have the potential to heal damaged tissues (Fig. 1).

3.3 Paracrine mechanisms of cardiomyocytes derived from iPSCs

The successful reprogramming of somatic cells, such as fibroblasts, into induced pluripotent stem cells (iPSCs), is a cornerstone for cardiac cell therapy. iPSCs from a cardiac patient could be reprogrammed into cardiomyocytes and endothelial cells *in vitro,* and transplanted back into the patient as a way of reducing the risks of immune rejection. One of the mechanisms that iPSCs use to exert their cardiac protection is paracrine signaling[44]. For example, after the intramyocardial injection of iPSC-derived cardiomyocytes (iCMs) in the hearts of MI mouse models, researchers revealed that the cardiac phenotype of iCMs protected the injured myocardium more effectively than undifferentiated stem cells because of their upregulated production of
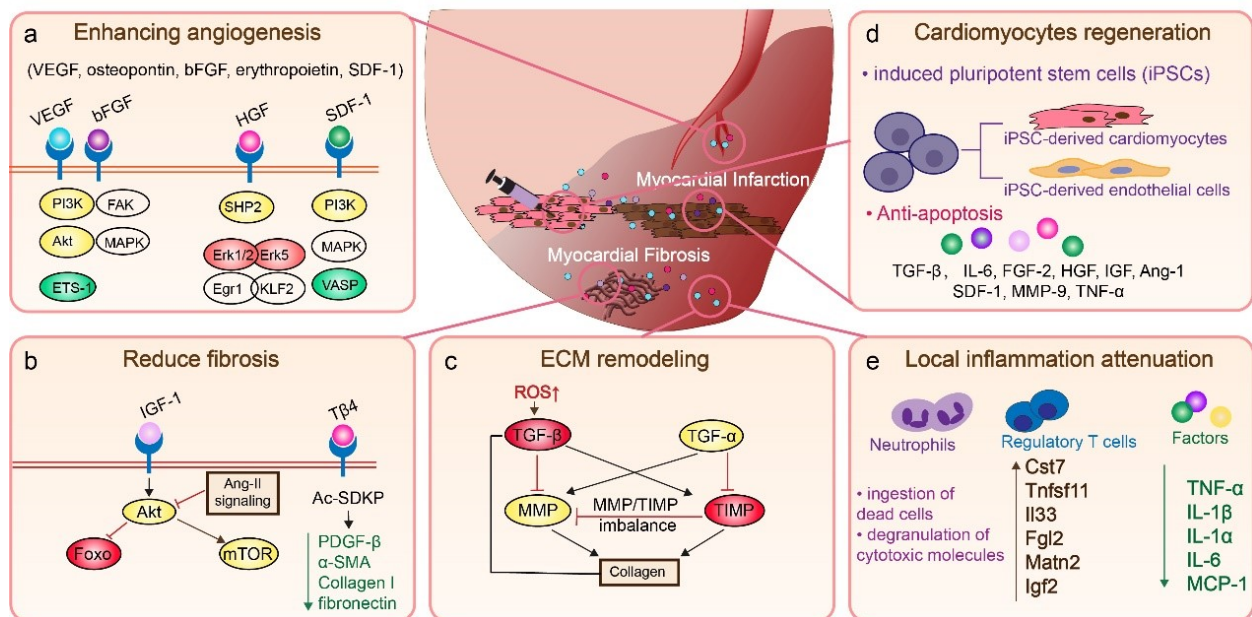
Fig 1. Regenerative factors from transplanted cells mediate communication with the surrounding cardiac tissue and change the extracellular microenvironment to attenuate local inflammation. a) Stem cell secreted factors enhance angiogenesis by mediating endothelial cell migration and proliferation; b) Factors also prevent cardiac inflammation and fibrosis after infarction; c) Factors play an important role in Post-MI extracellular matrix remodeling, such as balancing the expression of MMP and TIMP; d) Factors contribute to cardiomyocytes regeneration by promoting the recruitment and differentiation of stem cells, and direct cardiomyocyte preservation and regulation; e) Factors attenuate local inflammation through microenvironment alteration.

paracrine cytokines TNF-α, interleukin-8 (IL-8), granulocyte colony stimulating factor (G-CSF), and VEGF. In addition, the iCMs also promote cell migration by releasing the paracrine signaling molecules plasminogen activator inhibitor 1 (PAI1) and vascular cell adhesion molecule 1 (VCAM1). These factors not only enhance cell engraftment and promote angiogenesis, but also increase cell proliferation and inhibit apoptosis, leading to the repair of the MI injured myocardium (Fig. 1)[45]. Moreover, the extracellular vesicles secreted from iPSC-derived cardiomyocytes reduced arrhythmic burden and promoted cardiac function recovery[46].

3.4 Modulation of local cardiac inflammation by paracrine factors

Local inflammation after MI plays an important role in cardiac remodeling. The infarct triggers the increased expression of inflammatory cytokines through the upregulation of NF-κB expression[47]. The inflammatory cytokines include tumor necrosis factor -α (TNF-α), interleukin (IL) 1β, IL-1α, IL-6, and free radicals[48,49]. Neutrophils, prompted by IL-8, C5a, N-formyl-methionyl-leucyl-phenylalanine (fMLP), and the leukotriene B4 inflammatory cascade, migrate to the infarcted myocardium, where they ingest dead cells and degranulate cytotoxic molecules[50]. Additionally, IL-1 promotes resident and infiltrated macrophages to synthesize proteases and chemokines and consume about 40% of the apoptotic cardiac cells[50]. Post-MI remodeling also activates MMPs that degrade cardiac extracellular matrix rapidly. This degradation releases matrix fragments that drive inflammation[51]. Transplanted MSCs have attenuated local inflammation by secreting paracrine signaling molecules into the microenvironment, leading to the decreased expression of TNF-α, IL-1α, IL-6, and monocyte chemoattractant protein -1 (MCP-1)[21]. Furthermore, the administration of IL-10 enriched MSCs reduced apoptosis of cardiac cells via upregulated phosphatidylinositol 3-kinase (PI3K)/AKT pathways[52]. The over expressed IL-10 also stimulated CD11b+Ly6G- macrophage polarization

toward osteopontin-producing macrophages (galectin-3^{hi} CD206^{+}) for cardiac tissue repair and heart failure prevention after MI[53]. This macrophage polarization process was caused by an enhanced IL-10-STAT3-galactin-3 axis[53]. The overexpression of six factors (Cst7, Tnfsf11, Il33, Fgl2, Matn2, and Igf2) secreted by regulatory T cells promotes cardiomyocyte proliferation *via* paracrine signaling (Fig. 1)[54].

4. Opportunities and Challenges for clinical application

Stem cell therapies targeting the heart myocardium are clinically applicable. However, the efficacy of cardiac cell therapy is hampered by a number of limitations[55]. Their ability to differentiate and replicate with ease, makes stem cells attractive therapeutic agents, but also increases the risk of aberrant, uncontrolled replication, which can induce tumorigenicity[56]. This risk should always be taken into consideration in clinical practice[55]. In addition, the heterogenic or allogenic transplantation of stem cells may result in immunological issues[55]. Furthermore, the manufacture, storage and transportation of stem cells is complex, expensive, and time-consuming, making it difficult to meet batch quality specifications and pharmaceutical regulations. Moreover, the clinical application of stem cell transplantations is still restrained by low cell retention/engraftment rates and poor survival rates, which minimizes their long-term treatment efficacy[55,57]. The intramyocardial injection of stem cells usually requires open-chest or thoracoscopic surgery, increasing the changes of aggravating MI patients with secondary injuries and of introducing infections. Furthermore, cell therapy increased proarrhythmic risk through three major mechanisms including reentry, automaticity, and triggered activity[58,59]. Thus, cardiac stem cell therapies need to be improved before they can be successfully applied in a clinical setting.

5. Harnessing paracrine mechanisms to improve stem cell therapy

The role of stem cell paracrine signaling on myocardial regeneration has been studied for decades and has advanced our understanding of stem cell regenerative therapeutics[22]. However, the identification of paracrine factors and their functions remains a challenge due to the overwhelming range of multifunctional molecules and the cross-interactive signaling pathways involved. In addition, the diversity in the temporal and spatial expression patterns of the molecular factors and signaling pathways make the process even more complicated. Moreover, paracrine signaling not only impacts cardiac regenerative therapy, but also cardiac excitation-contraction coupling, the orchestrated process of initial myocyte electrical excitation[60]. Thus, paracrine factors contribute to the stem cells' regenerative efficacy as an orchestrated system. Relevant future studies will strengthen our knowledge of the complex processes, possibly providing us with methods and directions that will help optimize stem cell therapy for myocardial infarction and take it to the next level.

6. A new era for cardiac cell therapy intergrading biomaterials and nanomedicine

Biomaterials, such as polymers and native tissue derivatives, are high-tech materials that can be used for diagnosing, treating, repairing, or replacing diseased tissues and organs. Unlike medications, the function of biomaterials is structure-related and hardly affected by pharmacological or immunological activities. Usually, biomaterials are integrated with different drugs to promote therapeutic availability and efficiency. The study of synthetic stem cells, cardiac patches, and nanomedicine, ushered stem cell therapy into a new era.

To solve the aforementioned limitations and exploit the paracrine effects of live cell therapy, scientists have been focused on the interdisciplinary development of non-live, synthetic stem cells[61,62], nano-robots[63-65], and artificial cardiac patches[66] for MI treatment (Fig. 2). So far,

many of these studies have produced exciting results in both rodent and relevant large animal models. In the following sections, we will summarize the fundamental mechanisms used by these new cell-derived products, as well the progress made in their development to date.

6.1 Synthetic stem cells: Opportunities

The primary goal of engineering a synthetic stem cell is to selectively preserve their beneficial therapeutic functions and remove their drawbacks according to treatment needs. This is a practice that seeks to "druglize" (a.k.a pharmacoengineer) stem cell therapies using drug delivery principles. Previously, nanoparticles coated with cancer cell membranes were created for cancer immunotherapy[67]. Recently, synthetic stem cells were fabricated by encapsulating stem cell secretome with the biodegradable and biocompatible polymer poly lactic-co-glycolic acid (PLGA). The encapsulation was achieved with cell-mimicking microparticle (CMMP) technology or water/oil/water (w/o/w) emulsion technique[61]. The PLGA capsule was then coated with stem cell membranes using well-established methods[65-69]. These synthetic stem cells are similar in size to their natural homologues, and encapsulate regenerative factors normally secreted by live cells. In addition, PLGA provides a safe, non-toxic, biodegradable polymer that has been used in various control-release systems[70]. These synthetic stem cells mimic the paracrine processes of stem cells[61] and effectively obviate the danger of aberrant stem cell differentiation that may cause tumorigenicity (Fig. 3)[55]. For example, the intramyocardial administration of synthetic stem cells made from human cardiac stromal cells (CSCs)[61] and human bone marrow-derived MSCs[62] was shown to preserve cardiac function in a mouse model of MI via paracrine mechanisms.
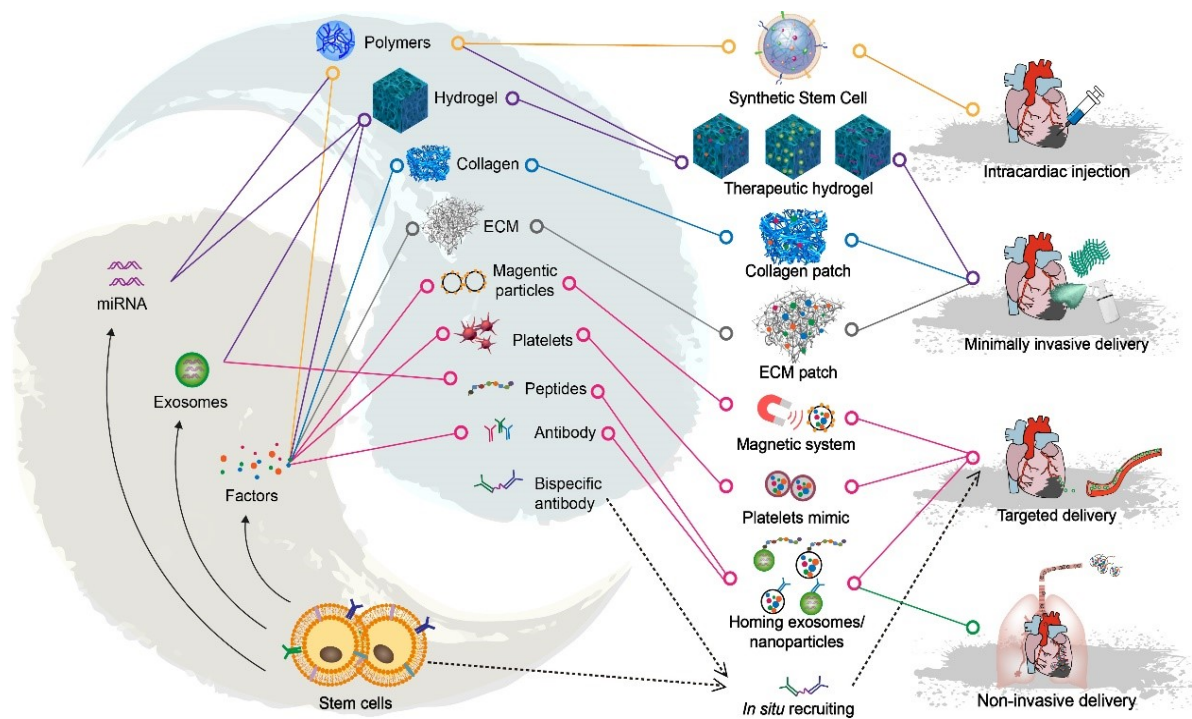
Fig 2. Toolbox elements for a new era of cardiac regenerative medicine. Stem cell produced regenerative therapeutics will usually be fused with artificial/natural materials for the fabrication of new regenerative medicine products, including synthetic stem cells, acellular cardiac patches, and targeting nanoparticles. The drug delivery method has evolved from open-chest surgical procedures to minimally-invasive procedures, non-invasive inhalation, and the intravenous delivery of drugs with specific targeting abilities.

6.2 Synthetic stem cells: Challenges

These studies not only proved the synthetic stem cell concept successfully but also demonstrated its potential for clinical application. However, there are still significant challenges keeping synthetic stem cells from transitioning to clinical practice. The first involves their optimization. The protein composition of the encapsulated regenerative secretome needs to be better defined[71]. Additionally, the treatment efficacy of each batch is hard to determine before administration, as there are no established standards. In addition, the use of different cell lines confers batch variability to the synthetic stem cells because each line may produce secretomes with

slightly different protein signatures[72]. To ensure consistency, it will be important to optimize/characterize the secretome stock and reduce variables during the manufacture process. Although the secretome profile may be changed by controlling the in vitro conditions[73,74], changing the secretome profile in vivo is not currently possible with synthetic stem cells. Furthermore, it will be essential to find a delivery method or to modify the synthetic cells in such a way that the problem of post administration retention is minimized. Currently, <10% of injected synthetic stem cells remain in the heart myocardium 7 days after injections61. Moreover, to make the clinical procedure safer, the synthetic stem cell administration paradigm should avoid innate injury from invasive surgical procedures.
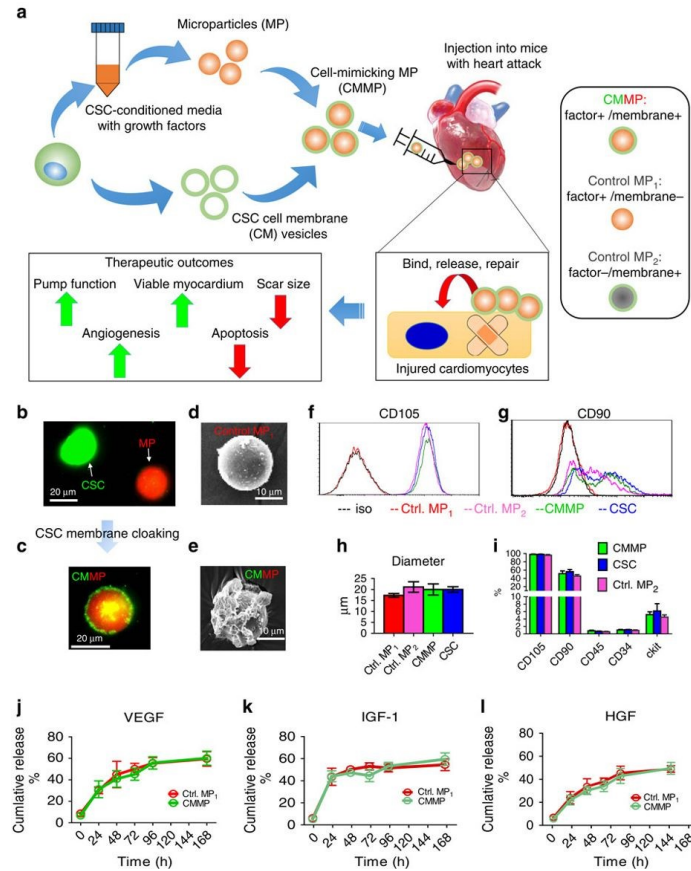
Fig 3. Fabrication of synthetic stem cells (or cell-mimicking microparticle, CMMP). a) Overall biochemical design and study model of CMMPs. MPs (that is, Control MP$_1$) were fabricated from PLGA and conditioned media of human CSCs, then MPs were cloaked with membrane fragments of CSCs to form CMMPs. Control MP$_2$ was fabricated by cloaking empty PLGA particles with CSC membranes. The therapeutic potential of CMMPs was tested in a mouse model of myocardial infarction. b-c) Texas red succinimidyl ester-labelled MPs (b, red) were cloaked with the membrane fragments of green fluorescent DiO-labelled CSCs (b, green) to form CMMP (c, red particle with green coat). Scale bar, 20 μm. d-e) SEM revealed the CSC membrane fragments on CMMPs (e) but not on Control MP$_1$ (non-cloaked MP) (d). Scale bar, 10 μm. f-g) Major human CSC markers CD105 (f) and CD90 (g) were positive on CMMPs and Control MP$_2$ but not on non-cloaked Control MP$_1$, indicating the successful membrane cloaking on CMMPs. h) CMMPs, Control MP$_1$, and Control MP$_2$ have similar sizes to those of CSCs. $n=3$ for each group. (i) CMMPs and Control MP$_2$ carried similar surface antigens as CSCs did. $n=3$ for each group. j–l) Similar release profile of CSC factors (namely vascular endothelial growth factor (VEGF), insulin-like growth factor (IGF)-1, and hepatocyte growth factor (HGF)) was observed in CMMPs and Control MP$_1$, indicating membrane cloaking did not affect the release of CSC factors from CMMPs and Control MP$_1$. $n=3$ for each time point. All data are mean ± s.d. Comparisons between any two groups were performed using two-tailed unpaired Student's t-test. Comparisons among more than two groups were performed using one-way ANOVA followed by *post hoc* Bonferroni test. This work is licensed under a Creative Commons Attribution 4.0 International License. Reproduced with permission[55]. Copyright 2018, Springer Nature Limited.

6.3 Exosomes and microRNAs: Opportunities

Exosomes are secreted by various cell types through the fusion of multivesicular bodies with the plasma membrane[75,76]. Once secreted, they are imbibed by recipient cells through receptor-ligand interactions, direct membrane fusion, and endocytosis/phagocytosis[77]. Therefore, exosomes may potentially play a role as intercellular communicators[78]. Also, as bi-lipid membrane vesicles with diameters between 30–150 nm[79,80], exosomes usually carry membrane-bound or encapsulated proteins and miRNAs with the potential to trigger many complex and diverse cellular processes and pathways[81]. In fact, studies show that stem cell-derived exosomes exert their cardiac therapeutic benefits mainly through the gene products and miRNAs they carry, which stimulate angiogenesis[82], decrease cell apoptosis[83], and reverse injury caused by inflammation[84]. Studies by Arslan et al. and Ibrahim et al., for example, showed that stem cell-derived exosomes can treat post-MI heart disfunctions[76].

To further study the therapeutic effects of exosomes, scientists have been isolating them from various types of stem cells (i.e., MSCs, CPCs, ESCs, iPSCs, and CD34+ EPCs) [80,85,82] through different isolation techniques, including ultracentrifugation, size isolation, and immunoaffinity capture. The following is a recapitulation of some identified mechanisms, listed as examples of how stem cell-derived exosomes provide regenerative or protective therapy for MI heart.

MSC-derived exosomes contain glyceraldehyde 3-phosphate dehydrogenase (GAPDH), enolase (ENO), pyruvate kinase m2 (PKm2), phosphoglycerate kinase (PGK), and phosphoglucomutase (PGM). These are important enzymes that increase ATP production by upregulating phosphofructose kinase levels[76]. The MSC-derived exosomes also contain peroxiredoxins and glutathione S-transferases that can reduce oxidative stress. Furthermore, the

MSC-derived exosomes activate adenosine receptors and phosphorylate the PI3K/Akt signaling pathway[86,76]. Additionally, the intramyocardial injection of CSC-derived exosomes has been shown to decrease infarct size and preserve left ventricular ejection fraction (LVEF) in MI injury[87,88]. When the release of exosomes in CSCs was suppressed by GW4869, a reversible inhibitor of neutral sphingomyelinase, the therapeutic efficacy of CSCs decreased[89]. It is important to note that the cells that receive and imbibe the released exosomes also play an important role. Fibroblasts uptake CSC-derived exosomes and modify their own secreted exosomes. These modified exosomes can increase collagen degradation by MMPs and decrease collagen production through TGF-β inhibition, helping to minimize the size of the infarct scar[90]. Moreover, exosomes derived from embryonic stem cells (ESCs) have been shown to enhance a number of cells in ways that induce cardiac repair. Namely, they enhance the pluripotent markers OCT-4, SOX-2, and Nanog in embryonic fibroblasts, reduce caspase-3 cleavage in H_2O_2-stressed H9c2 myoblasts and increase tube formation in human umbilical vein endothelial cells (HUVECs) in MI heart, *in vivo*[91]. Also, ESC-derived exosomes play a key role in promoting endogenous repair by regulating endogenous stem cell functions [91].

The therapeutic efficacy of exosomes is also mediated by the miRNAs inside of the exosomes. These non-coding miRNAs can regulate many important cellular pathways involved in cardiac regeneration. For example, miR-146a from CDC-derived exosomes is known to suppress MI injury *via* the targeting of *Irak-1* and *Traf6* and plays a major role in inflammation attenuation by dampening the toll-like receptor (TLR) signaling pathway[92]. In addition, miR-146a reduces oxidative stress from ischemic injury by suppressing the NAD(P)H oxidase (Nox-4), a molecule involved in producing oxygen radicals in cardiovascular pathophysiology[93]. Exosomal miR-21-5p from MSCs increases cardiac contractile force and calcium handling by regulating PI3K

signaling[94]. The importance of miRNA content in the therapeutic profile of exosome has motivated

some scientists to us a miRNA-mimicking approach to promote cardiomyocyte proliferation and

cardiac regeneration[95]. Table 1 provides a detailed summary of miRNAs related to cell therapy for

MI treatment.

Table 1. The object and function of miRNAs in cardiac therapy

miRNA	object		function	Ref
miR-1	inhibition	myoD	reprogram fibroblasts into cardiomyocytes muscle growth and differentiation	[96]
miR-1-2	inhibition	Irx4, Hrt2, Hand1, Gata6	regulation of cardiac growth and differentiation, electrical conduction, and cell-cycle control	[97]
miR-126	inhibition	Spred1, PIK3R2/p85-β	directly repressing negative regulators of the VEGF pathway; regulates angiogenic signaling and vascular integrity Stem/progenitor cells differentiation	[98]
miR-132	inhibition	RasGAP-p120	enhancing tube formation in endothelial cells.	[99]
miR-133a	inhibition	SRF, cyclin D2,	regulation of cardiac growth and differentiation, electrical conduction, and cell-cycle control	[100]
miR-146	inhibition	IRAK and TRAF6	preventing NF-κB activation, inflammatory cell infiltration	[101]
miR-15a, miR-195	inhibition	Chek1	Cardiac regeneration; associated with an increased number of mitotic cardiomyocytes	[102]
miR-17-92	inhibition	STAT3, PTEN	Cardiac development and regeneration; cardiomyocyte proliferation in postnatal and adult hearts.	[103]
miR-19a	inhibition	PTEN; SPRY2	anti-apoptotic; Stem/progenitor cells differentiation; the activation of the Akt and ERK signaling pathways	[104]
miR-204	inhibition	Jarid2	the proliferation and differentiation of human cardiomyocyte progenitor cells (hCMPCs) into cardiomyocytes	[105]
miR-21	inhibition	PTEN PI3K	induced angiogenesis; AKT and ERK activation	[106]
miR-210	inhibition	ephrin A3 and PTP1b	inhibiting apoptosis in cardiomyocytic cells	[107]
miR-22	inhibition	Mecp2	reduced cardiac fibrosis; reduced apoptosis in ischemic cardiomyocytes, ameliorated fibrosis and improved cardiac function post-myocardial infarction	[108]
miR-221	inhibition	BIM/BCL2L11; p53	vascular remodeling; increasing efficiency of cardiac cell transplantation and heart regeneration	[109]
miR-208	inhibition	β-MHC	enhance the reprogramming of fibroblasts into cardiomyocytes	[110]
miR-294	promotion	*c-myc; Klf4*	plays a central role in regulating CPC cell cycle in association with promoting proliferation, survival	[91]
miR-302	inhibition	Hippo pathway	Cardiac regeneration persistent de-differentiation in cardiomyocytes	[95]
miR-451	inhibition	GATA4	Inhibiting caspase 3/7 activation and cardiomyocyte apoptosis	[111]
miR-499	inhibition	Sox6, Rod1	enhance the reprogramming of fibroblasts into cardiomyocytes	[112]

6.4 Exosomes and miRNAs: Challenges

There is emerging evidence suggesting that exosomes released from various stem cells exert their therapeutic potential *via* the mediation of intercellular communications, the regulation of signaling pathways, and cell reprograming. However, the complexities of the massive and multifunctional exosomal proteins and miRNAs[113,114] have, thus far, prevented us from understanding the therapeutic mechanisms in detail. Thus, we still have many questions left to explore, such as where the signaling initiation begins, what the long-term therapeutic side effects are, how we distinguish between exosome-induced cardiac regeneration, repair, or preservation, what the mechanism of exosome-mediated reprograming is, how to standardize the efficiencies and dosages for MI hearts, and the biogenesis of massive miRNAs, among others. From a quantitative, systems biology perspective, future research needs to better define the role of exosomes derived from different cells, the content of exosomes, and exosome targeting[115]. It is also important to understand the stimulation dynamics/protocols that lead to miRNA signature differences in exosomes within and between cell lines[115]. For example, rather than the exosomes from regular MSCs, the exosomes from SuxiaoJiuxin-treated MSCs can specifically upregulated the protein expression of a key epigenetic chromatin marker- histone 3 lysine 27 (H3K27) in HL-1 cells (cardiomyocytes line) *via* the repressing its ubiquitously transcribed tetratricopeptide repeat, X chromosome[116]. Additional challenges that must be overcome before exosomes can be transplantable drugs include their targeting to sites of injury, retention problems, the lack of long-term efficacy data, and the need for long term cytotoxicity studies. Nonetheless, despite these challenges, exosomes and miRNAs have the potential to be the next generation of therapeutics, moving us away from the stem cell approach and into the molecular level, using their byproducts.

6.5 Cardiac patch: Opportunities

In the past two decades, tissue engineered cardiac patches have been designed to improve cardiac function after MI, with positive results seen in both small and large animal models.[117][118] To improve this therapeutic approach, scientists have sought optimal cell and material combinations as part of their efforts to refine patch creation and delivery[119,120]. Single layer cell patches were created previously. These earlier iterations suffered from cell death due to lack of blood supply after transplantation[121]. To solve this issue, researchers began to add other cell types into the patch, including ESCs, iPSCs, endothelial cells, and so forth[122,123]. These additions led to multiple cell layered cardiac patches with micro-vessels composed of self-assembled human vesicular endothelial cells that successfully integrated with the host 4 weeks after implantation[124]. More recent iterations offer a larger array of scaffolding material. For example, some scaffolds are made by suspending cells in a matrix of biomaterials. This scaffolding technique is better at achieving vascular integration than using cell sheets. Thus, these patches are more suitable for surgical applications[119]. Among the materials typically used to create cardiac patch scaffolds, the most common are collagen, fibrin, and an array of polymers. These are typically infused with synthetic agents or cellularized with therapeutic cells. Some patches, derived from animal products, can be decellularized and then recellularized with therapeutic cells, or infused with other beneficial agents[125]. Since tissue-specific ECM has a tissue-specific protein composition, researchers enhanced the bioactivity of decellularized amniotic membranes for future cardiac applications by intergrading cardiac ECM hydrogel[126]. Recently, an ECM patch, 3D-printed with bioinks composed of cardiac ECM, human cardiac progenitor cell (hCPCs), and gelatin methacrylate (GelMA), has been developed for heart repair, establishing the possibility of using bioprinting as a cardiac patch fabrication method[127]. Also, poly(N-isopropylacrylamine-co-acrylic acid) or

P(NIPAM-AA) nanogel was used to encapsulate cells for MI treatment[128]. Moreover, a new biomimetic micro-vessels (BMV)-integrated cardiac patch was created by leveraging microfluidic hydrodynamic focusing to construct biomimetic micro-vessels. The BMV lumens are lined with human umbilical vein endothelial cells (HUVECs) and encapsulated in a fibrin gel spiked with human CSCs[129]. This endothelialized BMV patch mimicked the natural vascular structure of the hearth, helping it integrate with the host myocardium after implantation[129]. Also, a human cardiac muscle patch was generated by suspending iPSCs, including cardiomyocytes, smooth muscle cells, and endothelial cells, in a fibrin scaffold. This muscle patch can beat synchronously *in vitro* during 7 days of culture and significantly reduced infarct size and left ventricular wall stress after transplantation in swine MI models[130]. Unfortunately, cardiac patches have had a slow path to clinical applications due to aforementioned live-cell therapy limitations[131]. Thus, we will introduce cardiac patches without live cells (but with acellular substances such as proteins, RNAs, or ECM alone) for MI treatment.

6.5.1 A microparticle-incorporated collagen cardiac patch

Collagen is one of the most prevalent extracellular components of the myocardium and can be molded into a variety of shapes[119]. Recently, researchers developed collagen-alginate cross-linked scaffolds with IGF-1- or HGF-loaded alginate microparticles using a spray-drying technique[125]. *In vitro* testing of the patch on CSCs substrates suggested that it was capable of releasing both proteins for 15 days. The sustained release of IFG-1 and HGF increased CSC mitogenic and proliferative effects[125]. Although this cardiac patch has not been used *in vivo* yet, it provided a successful *in vitro* model that can be used to compare the regenerative potentials of different protein factors that can be utilized to optimize the control release properties of patches.

6.5.2 A spray painted platelet-fibrin cardiac patch

To solve the problem of open-chest surgery for cardiac patch placement, researchers created a spray-paintable, polymerizable biomaterial that can be applied to the heart myocardium using a minimally invasive procedure (Fig. 4)[132]. Based on the concept that platelet-fibrin gel has an ability to rapidly aid clot formation, it was used as a new biomaterial for cardiac repair in animal studies[133]. To increase the regenerative character of platelet-fibrin gel, researchers integrated several regenerative stem cell factors, including VEGF, IGF-1, HGF, TGF-β and PDGF, into the gel during the fabrication process. Then, the plasma and calcium-containing media solution and platelet rich plasma was placed separately in each syringe lumen of a double-lumen syringe, the equipment which was connected to a CO_2 air compression tube for spraying this product directly onto the injured heart. Under scanning electron microscopy, the cardiac patch spray formed a fibrous structure quickly after implantation. This study showed that this cardiac patch can release the regenerative growth factors efficiently in the first 2 weeks after being sprayed. The spray patch increased the viability of cultured neonatal rat cardiomyocytes *in vitro*, and effectively preserved cardiac function and reduced scar fibrosis *in vivo*. This spray patch not only provides us with a concept for using stem cell factor cocktails for cardiac regenerative therapy, but also demonstrates a new drug delivery approach for potential minimally invasive patch transplantation.
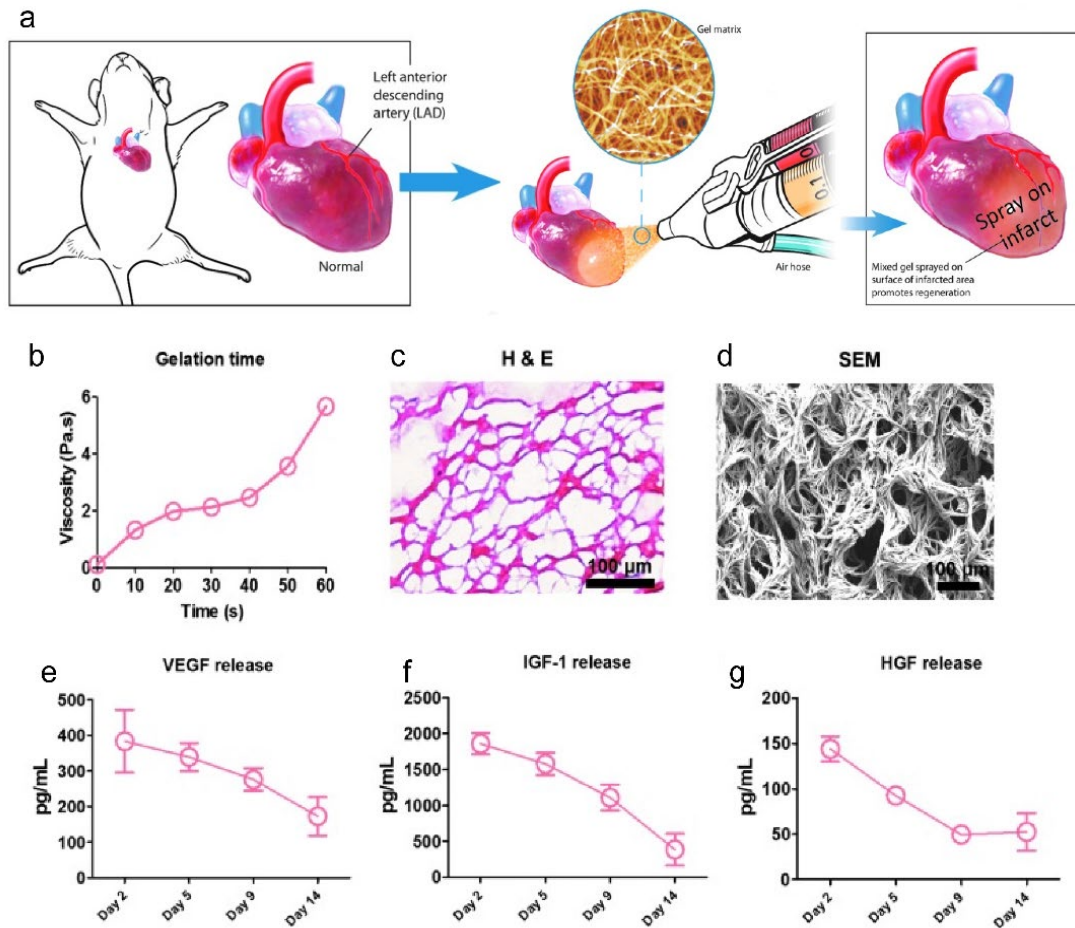
Fig 4. Spray painting of gel matrix on myocardial infarcted area. a) Schematic showing the spray painting of *in situ* polymerizable biomaterials on the heart after myocardial infarction with a minimally invasive procedure. **b)** Mixing platelet-rich plasma with calcium-containing media solution using compressed air resulted in a stable gel formation in less than 1 min; **c)** Hematoxylin–eosin staining revealed the fibrous structure of the sprayed platelet fibrin gel; **d)** Representative scanning electron microscopy images of the sprayed platelet fibrin gel; **e-i)** Enzyme-linked immunosorbent assay (ELISA) of the concentrations of vascular endothelial growth factor (VEGF), insulin-like growth factor (IGF)-1, and hepatocyte growth factor (HGF), from the sprayed platelet fibrin gel conditioned media at different time points ($n = 3$ per time points). Scale bar = 100 μm. H & E, hematoxylin and eosin. Reproduced with permission[132]. Copyright 2017, Mary Ann Liebert, Inc.
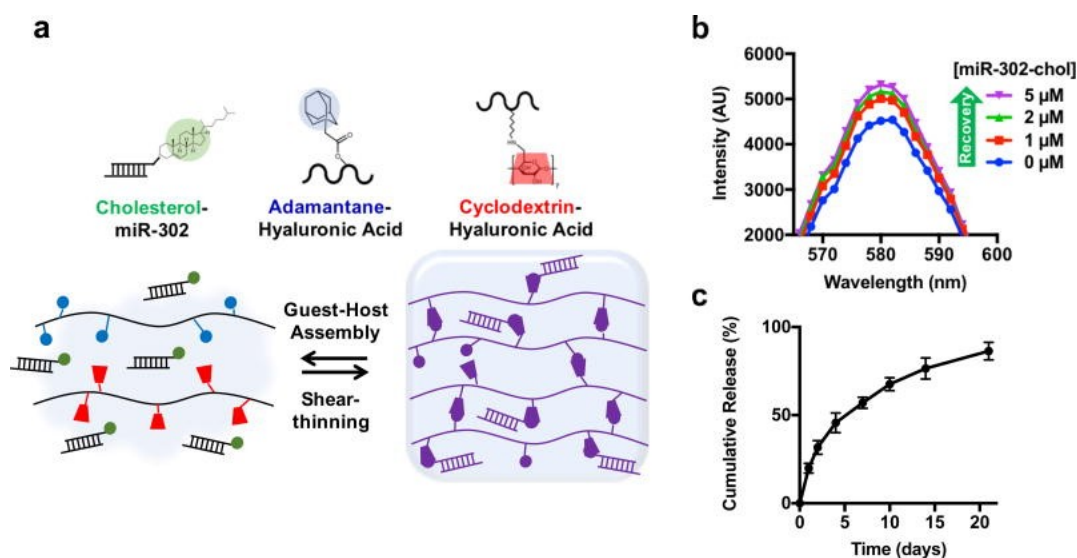
Fig 5. miR-302 control-releasing gel. a) Schematic showing gel assembly and miR-302 interactions. HA was modified with adamantane (AD) or cyclodextrin (CD) to create shear-thinning and self-healing gels, respectively. Likewise, cholesterol on miR-302-chol interacts with CD to induce the sustained release of the gel. b) Rhodamine/CD-HA interactions lead to the quenching of rhodamine fluorescence, but the fluorescence is recovered by the titration of cholesterol-modified miR-302 into the system and displacement of rhodamine complexes, indicating the integration between cholesterol and CD. c) Release of cholesterol-modified miR-302b and miR-302c (210 µM of each) from gels (5 wt%) in 1.5 mL microcentrifuge tubes over three weeks, quantified by RiboGreen, a commercially available RNA quantification kit (mean ± SD, n=3). Reproduced with permission[134]. Copyright 2017, Macmillan Publisher Limited, part of Springer Nature.

6.5.3 A miRNA-assembled hydrogel cardiac patch

In order to reap the benefits of miRNA treatment, researchers created a miRNA-assembled hydrogel cardiac patch to diminish the potential miRNA off-target rate. Since the miR-302 have a proliferative effect on neonatal mouse cardiomyocytes through the inhibition of Hippo signaling[95], researchers modified miR-302 with cholesterol and modified hydrogel β -cyclodextrin, then assembled those modified materials together and formed a complex miR-302-enriched hydrogel. This product can release miR-302 persistently for about 3 weeks (Fig. 5)[134]. The study demonstrated the regeneration of neonatal mouse cardiomyocytes, *in vitro,* and the preservation of

cardiac function, *in vivo*[134], using the patch. This study innovatively used a biochemical method to assemble therapeutic miRNAs into hydrogel patches with the capacity for sustainable release.

6.5.4 Decellularized cardiac-extracellular-matrix cardiac patch

Extracellular matrix is composed of interstitial matrix and basement membrane materials. Decellularized pig heart tissue can be used as a bioactive extracellular matrix cardiac patch with the capacity to stimulate a complex regenerative response without the addition of cells or growth factors. This decellularized cardiac extracellular matrix (dECM) patch induces *de novo* immature striated-like muscle patterns (MLC^+, $TrpI^+$, connexin43$^+$) *via* macrophage polarization towards constructive remodeling and cardiomyocyte progenitor cell recruitment[135]. Also, the dECM protein, agrin, was shown to promote heart regeneration after MI in mice[136] through Dag1, ERK, and Yap signaling pathways. Recently, dECM was mixed with hydrogel to increase its versatility[137]. Altogether, the bioactive dECM patch model provides us with a new candidate for the acellular regenerative treatment of MI hearts.

6.6 Cardiac patch: Challenges

As a promising approach for cardiac repair and regeneration after MI, the cardiac patch strategy continues to be improved and engineered to better deliver its therapeutic benefits. However, there are still many challenges left to address before it can be implemented clinically. Although a shape-memory scaffold, capable of supporting multiple stretch cycles without deformation or impeding cardiac contractions, was successfully transplanted onto the heart in a minimal-invasive procedure[138], most cardiac patches designed for epicardial delivery[131] require an open-chest surgery. Such invasive procedures cause innate surgical damage, increase the patient's risk of death during surgery, induce inflammation after surgery, and subject the patient to a long recovery period. In addition, the possibility of pericardial adhesions during cardiothoracic function

is an underlying weakness of the surgical cardiac patch transplantation which may cause disfunction of the heart or even increase morbidity and mortality[139]. Thus, the value of the cardiac patch strategy and it is worth to the patient are debatable. In order to improve on the status quo, the paradigm has shifted to emphasize minimally invasive implantation procedures, the pursuit of which has emerged as one of the most important goals in surgical transplantation[132,138]. In addition, in cardiac patch transplantation, sutures are often used to prevent patch shedding[140], which is a heavy burden for an already injured heart. Many methods, however, have been proposed and validated as effective alternatives to sutures, including the use of gold nanorods[141], biocompatible glues[142], and techniques which may require patch modifications but may not be applicable for all patches. Moreover, arrhythmia caused by large heart engraftments is still a serious, possibly fatal problem[143] that will require further study to fully understand and avoid. Although cardiac patch materials are biocompatible and biodegradable, long-term safety studies are still required to test for chronic immune rejection. Indeed, all patches are external foreign substances which may cause relevant immune rejection, either by virtue of the materials used or their metabolic derivatives[144]. Moreover, it is important to further optimize the cardiac patches' therapeutic potential, manufacture consistency, and cryo-stability before they can be fully developed clinical products.

6.7 Cardiac injury targeting: Opportunities

Due to low therapeutic retention and to avoid the risk of losing therapeutic efficacy as a result of off-target delivery, heart stem cell therapies are usually administered intramyocardially. Due to its aforementioned invasiveness, this method is clinically unappealing. Thus, research in recent years has led us toward therapeutic strategies that target MI injured hearts using molecular signals, such as stem cell secreted regenerative factors, coupled with minimally invasive avenues for cell delivery. The concept of targeted drug delivery was originally developed in the field of

cancer medicine. There, intravenously injected chemotherapy drugs are guided to the tumor tissues through a variety of methodologies. The cardiac targeting concept allows the drugs (therapeutic cells in our case) to deliberately interact with the heart's infarcted area and impart their therapeutic benefits.

6.7.1 Peptide Targeting

After screening out the three peptide sequences (CSTSMLKAC, CKPGTSSYC, and CPDRSVNNC) with the highest occurrence rates from ischemic heart tissue, researchers tested their homing ability in vivo by using conjugated synthetic peptides with fluorescein. Of these, the CSTSMLKAC peptide demonstrated the strongest affinity for the ischemic heart myocardium, as suggested by its strong fluorescein signature[145]. This cardiac homing peptide was conjugated with CSC-derived exosomes through a DOPE-NHS (dioleoylphosphatidylethanolamine N-hydroxysuccinimide) linker for cardiac regenerative therapy (Fig. 6)[64]. This technique dramatically increased the retention of therapeutic exosomes, even though the homing exosomes were delivered intravenously. From in vitro studies, the exosomes conjugated with homing peptides improved the viability and exosome-uptake of cultured neonatal rat cardiomyocytes, while reducing cell apoptosis. An in vivo study on a rat model of MI suggested that cardiac functions were effectively preserved due to the pro-angiogenic, pro-myogenic, anti-apoptotic, and anti-inflammatory roles of exosomes[64]. This research provides us with a new technique to modify membrane-based nanoparticles to target MI.

Post-MI induced myocardial disfunction and myocardium injury may require chronic treatment for years. Recently, researchers tried to deliver regenerative therapeutics in a non-invasive way to minimize the discomfort and avoid circulating drug depletion. Thus, it is necessary to maintain an effective local blood concentration and prolonged drug retention period. For this

purpose, researchers engineered therapeutic peptide-loaded calcium phosphate nanoparticles that can achieve cardiac targeting through inhalation. Inhaled nanoparticle can rapidly diffuse into the alveoli, cross the alveolar capillary membrane, and be transported to the heart through the pulmonary veins. This targeting method was proved effective by tracking the nanoparticle uptake efficiency by cardiomyocytes in vivo[146].

6.7.2 Magnetic targeting

Magnetic stem cell targeting relies on the application of a magnetic field gradient to guide bioactive molecules to the site of injury[128,147]. Superparamagnetic nanoparticles composed of a magnetite (Fe_3O_4) or maghemite (γ-Fe_2O_3) core[128] have many attractive features, such as a large, constant magnetic moment, giant-paramagnetic-atom-like behavior, fast magnetic field response, and low aggregation at room temperature148. Due to these features, several FDA-approved superparamagnetic nanoparticles have been applied in the biomedical field for a number of purposes, including drug delivery and magnetic resonance imaging (MRI)[128,149]. Intravenously administered magnetic nanoparticles coated with PEG and anti-CD34 successfully guided mononuclear cells (CD34+) to the targeted area[150]. In addition, Ferumoxytol, an FDA approved magnetic nanoparticle, has been used successfully to label human and rat CSCs, enhancing stem cell retention/engraftment in the injured area, and multiplying the therapeutic benefit[151]. It has been widely reported that the magnetic targeting strategy is non-toxic and can be applied universally to many cell types[151].
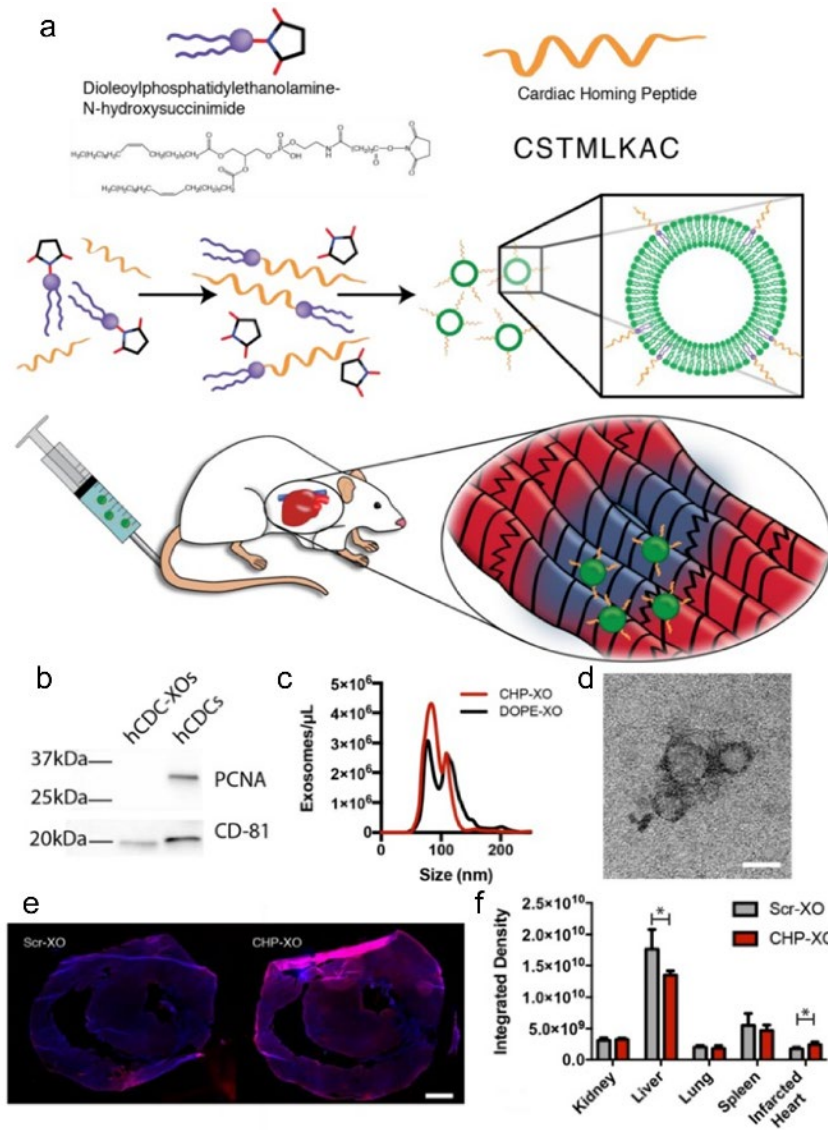
Fig 6. Cardiac homing exosomes. This is an open access article distributed under the terms of the Creative Commons Attribution (CC BY-NC) license. a) Myocardium-targeting exosomes were produced by reacting DOPE-NHS to Cardiac Homing Peptide (CHP). The lipophilic tails of the DOPE-CHP then spontaneously insert into the exosomal membrane, coating the exosome in CHP peptide. The exosomes were then intravenously injected into rats following I/R injury. b) Western blot for PCNA verifies absence of cell particulates in purified exosomes and CD-81 shows presence of exosomes. c) Nanoparticle tracking analysis shows that tagging the exosomes with CHP resulted in no significant changes in exosome size, with a modal exosome size of ~95 nm. d) Transmission electron microscopy confirms the exosome structure. e, f) *ex vivo* labelling of infarcted rat heart sections showed increased retention of both CHP-tagged exosomes compared to Scr-tagged exosomes (DAPI in blue and DiI-labeled exosomes in red). Scale bars: d = 50 nm, e = 1 mm. This is an open access article distributed under the terms of the Creative Commons Attribution (CC BY-NC) license (https://creativecommons.org/licenses/by-nc/4.0/). Reproduced with permission[64]. Copyright 2018, Ivyspring International Publisher.

6.7.3 Antibody targeting

Another important development in the past decade is the use of heart injury biomarker-specific antibodies to target therapeutic cells to the infarcted heart[152]. MI events usually occur when coronary arteries become occluded as a result of fibrin-rich thrombi that form inside the lumen[153]. During MI, extracellular matrix will be deposited with plethoric fibrin due to an imbalanced thrombin/thrombomodulin ratio[154]. Nanogels are nano-sized colloidal hydrogels with loading and releasing kinetics that are related to particle size, cross-linking density, and network homogeneity. They are well-known for their capabilities as delivery vehicles of small molecules and proteins (Fig. 7)[155]. Poly (N-isopropylacrylamide) nanogels were engineered as part of a dual-delivery system to reopen the clotted blood vessels and inhibit fibrosis during post-MI heart remodeling by targeting the deposited fibrin[63]. In the study, tissue plasminogen activator (tPA) and a small-molecule cell contractility inhibitor (Y-27632) were encapsulated inside the nanogels. An anti-fibrin antibody was conjugated to the outside of the nanogel by the EDC/Sulfo-NHS coupling of the AAc functional handles in the nanogel shell[63]. Through the conjugated anti-fibrin antibody on the surface, the intracoronary injected nanoparticles specifically recognized and bound the fibrin-enriched area, allowing for accurate drug releasing and improved cardiac function following MI, in vivo[63]. These antibody-conjugated nanogels can also be used to encapsulate various proteins or molecules. The conjugation of different antibodies can be used to specifically target different markers.
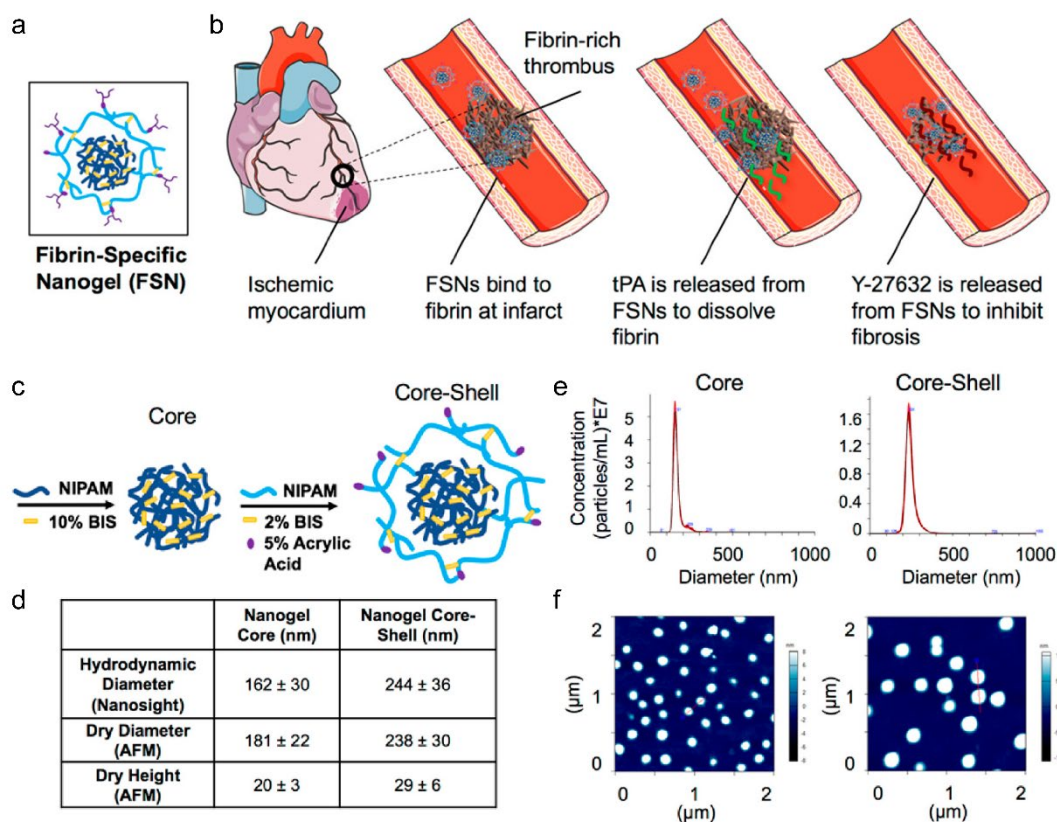
Fig 7. Fibrin-specific nanogel. a) the design of fibrin-specific nanogel; b) when drug-loaded nanoparticles combat MI, which occurs due to a fibrin-rich thrombus blocking blood flow and creating ischemic myocardium, and subsequent cardiac fibrosis upon reperfusion. Drug-loaded FSNs will bind to fibrin at the infarct site, release a fibrinolytic drug, and release a small-molecule cell contractility inhibitor to mitigate cardiac fibrosis due to reperfusion injury; c) core and C/S nanogel design; d), size characterization (n = ≥30/group); d) nano-sight particle tracking for hydrodynamic diameter measurements; e) dry AFM images on a glass surface. Reproduced with permission[63]. Copyright 2018, American Chemical Society.

6.7.4 Bispecific antibody targeting

Bispecific antibodies (BsAb) are artificial proteins usually composed of fragments from two different monoclonal antibodies that, consequently, recognize two different antigens present on different cells[156]. They have been engineered and applied for cancer immunotherapy for decades. For example, A BsAb molecule can simultaneously bind a cytotoxic T cell and a targeted tumor cell with the two Fab regions. The T cell on one Fab site releases the cytotoxins

perforin, granzymes, and granulysin to trigger a series of apoptotic events through the action of perforin. Granzymes then enter the cytoplasm of the tumor cell on the other Fab site. Additionally, the Fc region can bind to Fc receptors from macrophages, natural killer cells, or dendritic cells, facilitating antibody-dependent cell-mediated cytotoxicity and killing the attached tumor cell[157]. Nowadays, the rising knowledge in effector cell biology and the implementation of antibody engineering technologies has improved bispecific antibody strategies for immunotherapy of cardiac MI injury[158]. The binding of BsAbs with stem cells has been applied to enhance stem cell targeting and tissue regeneration[159]. BsAbs can also be conjugated with magnetic nanoparticles to help exogenous bone marrow-derived stem cells (expressing CD45) or endogenous CD34+ cells target injured neonatal rat cardiomyocytes[160]. A decade ago, researchers began to design BsAbs to target human CD34+ cells to the specific antigens expressed by ischemic myocardium[152]. They linked 2 whole antibodies (anti-CD45 and anti-MLC) on Fcs by SulfoSMCC [sulfosuccinimidyl 4-(N-maleimidomethyl) cyclohexane-1-carboxylate], the success of which was verified through flow cytometry. This study provides an example of how BsAb can be used to target hematopoietic stem cells (HSC) to injured myocardium, specifically[152].

6.7.5 Platelet-inspired MI targeting

Before ischemic heart injuries, the major blood vessels usually suffer from vascular damage and clot formation. During this process, the damaged subendothelial matrix will be exposed, including collagen, fibronectin, and von Willebrand factor (vWF). The exposed ECM helps stimulate the aggregation of platelets via many receptor-ligand interactions, including GPlb/V/IX-vWF, αIIbβ3-fibronectin, and αIIbβ3-fibrinogen. Then, ischemic heart injuries cause membrane tethers, which play an important role in platelet-matrix and platelet-platelet adhesive interactions[161]. Many platelet surface proteins, such as (GP)VI, GPIV, GPIb, GPIX, GPV, and

GPIIb/IIIa are involved in this platelet aggregation process[162,163]. Importantly, platelets have an innate ability to flow in the vascular wall until binding to the targeted injury sites[65]. Thus, researchers are developing platelet membrane coatings that effectively target the ischemic heart. In one of the studies[65], platelet membrane-decorated CSCs were formed by coating CSCs with platelet membranes using a fusion method[65,164]. Rodent and porcine ischemia/reperfusion models were used to prove the targeting proficiency and therapeutic efficacy of these bioengineered cells[65]. To further improve this strategy, a dually targeting platelet-inspired nanocell (PINC) was fabricated for ischemic heart tissue targeting. PINC achieves the targeted delivery of therapeutics due to platelet inspiration and the prostaglandin E_2 (PGE_2) that is modified on platelet membranes (Fig. 8A). In addition, the PINC particles showed better cryo-storage stability and have an innate ability to flow inside the vasculature until binding to the targeted injury sites (Figs. 8B-I)[165].
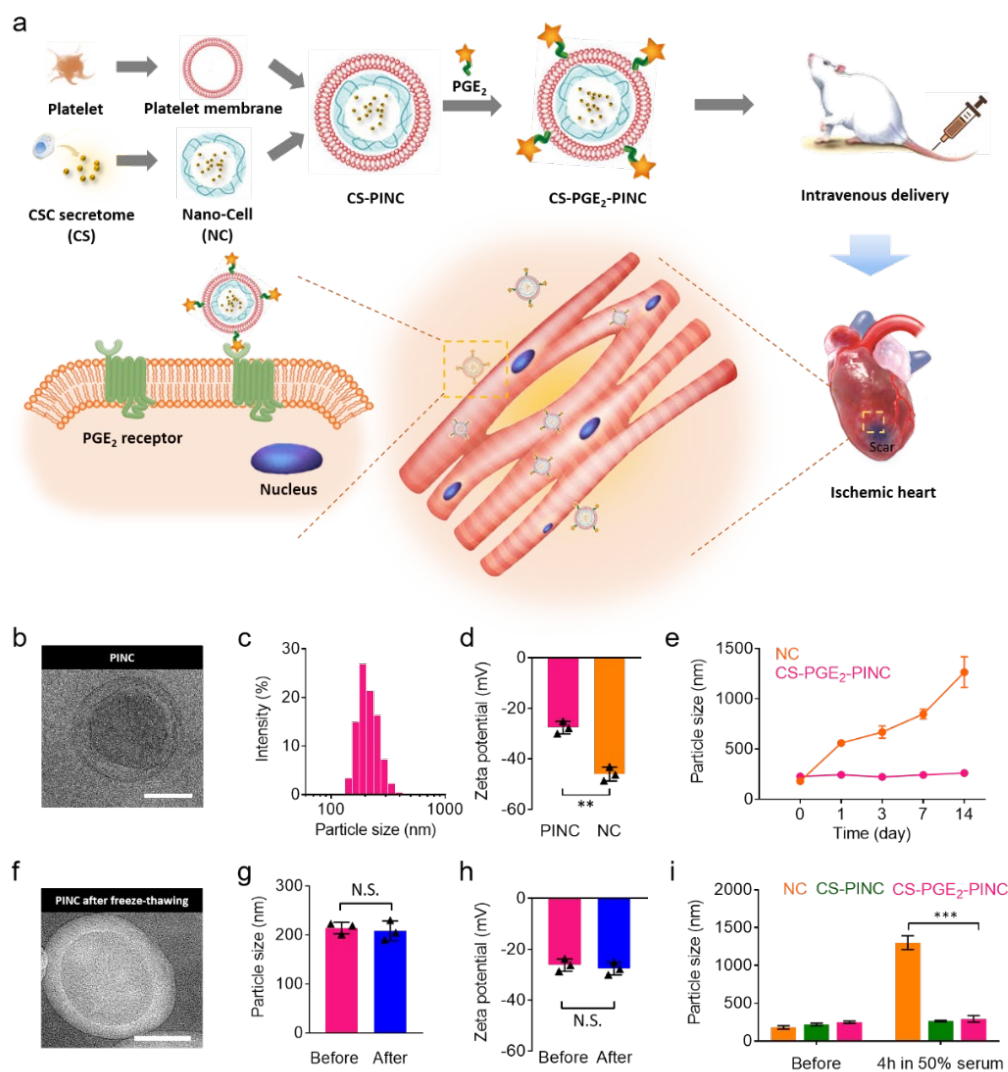
Fig 8. Fabrication and characterization of PINCs. a) Schematic illustration of the fabrication process of PINCs. The therapeutic effects of PINC injection were tested in mice with myocardial I/R injury. b) TEM image showing the ultrastructure of CS-PGE$_2$-PINC. c) Size distribution of CS-PGE$_2$-PINC measured by DLS. d) Zeta potentials of CS-PGE$_2$-PINC and NC. e) Particle sizes of bare NC and CS-PGE$_2$-PINC over 2 weeks in PBS. f) TEM image showing the ultrastructure of CS-PGE$_2$-PINC after freeze-thawing. g) The comparison of particle size and h) zeta potential of CS-PGE$_2$-PINC before and after freeze-thawing. i) In vitro stability of NC, CS-PINC, and CS-PGE$_2$-PINC before and after incubation in 50% fetal bovine serum. Scale bars, 100 nm. All data are mean ± s.d. * indicates $p < 0.05$, ** indicates $p < 0.01$, *** indicates $p < 0.001$; N.S., no statistical significance. Comparisons between any two groups were performed using two-tailed unpaired Student's t-test. Comparisons among more than two groups were performed using one-way ANOVA followed by post hoc Bonferroni test. Reproduced with permission[148]. Copyright © 2018, WILEY-VCH Verlag GmbH & Co. KGaA, Weinheim.

6.8 Cardiac injury targeting: Challenges

Although the emergence of these targeting methods has pushed myocardial regenerative therapies to brand-new heights, there are many deficiencies that need to be worked on. First, it is necessary to establish a well-accepted standard in the field for evaluating the cardiac targeting efficiency. Second, in both antibody targeting and bispecific antibody targeting cases, the antibody added may induce immune reactions due to the intact Fc region, which can bind to Fc receptors on macrophages, natural killer cells, or dendritic cells. Binding by any of these cells to the Fc site would activate an antibody-dependent cell-mediated cytotoxic response and harm the attached stem cells[157]. Furthermore, nanoparticles conjugated with antibodies may be phagocytosed and, consequently, have their therapeutic effects diminished[166]. Thus, antibodies used for therapeutic purposes should be better designed to avoid undesired immune reactions. Additionally, some targeting methods still require local (intracoronary) injections for effective delivery[65]. However, the intravenous injection of the cardiac targeting drugs, which is more attractive and less invasive, may cause increased off-targeting drug delivery due to the long circulation route from the vein to the infarcted myocardium. For example, the cell-sized carriers may be mechanically retained in the capillary networks of the lungs after intravenous injection[167]. Moreover, the magnetic cardiac targeting strategy has to be thoroughly investigated, including particle size, surface chemistry, magnetic properties, as well as a tangible and precise external magnetic field to guide the injected stem cells to the heart.

7. Conclusion

This review began with a summary of the pathological repair process that occurs after MI. The paracrine mechanisms and the molecular pathways involved in stem cell therapies are discussed and summarized in detail. Based on the current literature, we classified and analyzed

stem cell derivatives and byproducts that make up the new generation of stem cell therapeutics. These were divided into four categories: synthetic stem cells, exosomes, cardiac patches, and cardiac targeting modalities. The goals of these new concepts are to: 1) bypass the limitations of living-cell therapies by using non-live cell products; 2) optimize the therapeutic efficacy by using molecular-level therapeutics; 3) diminish the invasiveness of current drug delivery routes by developing minimally invasive procedures or targeting concepts; and 4) get closer to clinical application. However, there are still many unsolved issues for future research, including the need for the improved understanding of molecular mechanisms, the application of new materials, the update of drug administration routes, pharmacokinetics, drug stability, side effects, and toxicity. If we can address these issues, the future of stem cell products will be bright, and both the quality and longevity of life for MI patients will improve.

8. References

1. Benjamin, E. J. *et al. Heart Disease and Stroke Statistics'2017 Update: A Report from the American Heart Association. Circulation* **135,** (2017).

2. Jhund, P. S. & McMurray, J. J. V. Heart failure after acute myocardial infarction a lost battle in the war on heart failure? *Circulation* **118,** 2019–2021 (2008).

3. G. St. John Sutton, M. & Sharpe, N. *Left Ventricular Remodeling After Myocardial Infarction : Pathophysiology and Therapy. Circulation* **101,** (2000).

4. Porrello, E. R. & Olson, E. N. A neonatal blueprint for cardiac regeneration. *Stem Cell Res.* **13,** 556–570 (2014).

5. Steinhauser, M. L. & Lee, R. T. Regeneration of the heart. *EMBO Mol. Med.* **3,** 701–712 (2011).

6. Uygur, A. & Lee, R. T. Mechanisms of Cardiac Regeneration. *Dev. Cell* **36,** 362–374 (2016).

7. Gamba, L., Harrison, M. & Lien, C.-L. Cardiac Regeneration in Model Organisms. *Curr. Treat. Options Cardiovasc. Med.* **16,** 288 (2014).

8. Ito, K. *et al.* Differential reparative phenotypes between zebrafish and medaka after cardiac injury. *Dev. Dyn.* **243,** 1106–1115 (2014).

9. Ma, D. *et al.* Dynamics of Zebrafish Heart Regeneration Using an HPLC–ESI–MS/MS Approach. *J. Proteome Res.* **17,** 1300–1308 (2018).

10. Bergmann, O. *et al.* Evidence for Cardiomyocyte Renewal in Humans. *Science (80-.).* **324,** 98 LP-102 (2009).

11. Beltrami, A. P. *et al.* Evidence That Human Cardiac Myocytes Divide after Myocardial Infarction. *N. Engl. J. Med.* **344,** 1750–1757 (2001).

12. Mohamed, T. M. A. *et al.* Regulation of Cell Cycle to Stimulate Adult Cardiomyocyte Proliferation and Cardiac Regeneration. *Cell* **173,** 104–116.e12 (2018).

13. Song, G. *et al.* Transplantation of iPSc Restores Cardiac Function by Promoting Angiogenesis and Ameliorating Cardiac Remodeling in a Post-infarcted Swine Model. *Cell Biochem. Biophys.* **71,** 1463–1473 (2015).

14. Shadrin, I. Y. *et al.* Cardiopatch platform enables maturation and scale-up of human pluripotent stem cell-derived engineered heart tissues. *Nat. Commun.* **8,** (2017).

15. Moccia, F., Diofano, F., Rebuzzini, P. & Zuccolo, E. Embryonic Stem Cells for Cardiac Regeneration BT - Stem Cells and Cardiac Regeneration. in (ed. Madonna, R.) 9–29 (Springer International Publishing, 2016). doi:10.1007/978-3-319-25427-2_2

16. Makkar, R. R. *et al.* Intracoronary cardiosphere-derived cells for heart regeneration after myocardial infarction (CADUCEUS): A prospective, randomised phase 1 trial. *Lancet* **379,** 895–904 (2012).

17. Konstantinos Malliaras, MD*, Raj R. Makkar, MD*, Rachel R. Smith, PhD*, Ke Cheng, PhD*, Edwin Wu, MD†, Robert O. Bonow, MD†, Linda Marbán, PhD*, Adam Mendizabal, MS‡, Eugenio Cingolani, MD*, Peter V. Johnston, MD§, Gary Gerstenblith, MD§, Karl H. Schuleri, P. Intracoronary Cardiosphere-Derived Cells After Myocardial Infarction: Evidence of Therapeutic Regeneration in the Final 1-Year Results of the CADUCEUS Trial Konstantinos. *J Am Coll Cardiol.* **63,** 110–122 (2014).

18. Elmadbouh, I. & Ashraf, M. Tadalafil, a long acting phosphodiesterase inhibitor, promotes bone marrow stem cell survival and their homing into ischemic myocardium for cardiac repair. *Physiol. Rep.* **5,** e13480 (2017).

19. Amado, L. C. *et al.* Cardiac repair with intramyocardial injection of allogeneic

mesenchymal stem cells after myocardial infarction. *Proc. Natl. Acad. Sci. U. S. A.* **102,** 11474–11479 (2005).

20.   Miana, V. V. & González, E. A. P. Adipose tissue stem cells in regenerative medicine. *Ecancermedicalscience* **12,** 822 (2018).

21.   Mirotsou, M., Jayawardena, T. M., Schmeckpeper, J., Gnecchi, M. & Dzau, V. J. Paracrine mechanisms of stem cell reparative and regenerative actions in the heart. *J. Mol. Cell. Cardiol.* **50,** 280–289 (2011).

22.   Gnecchi, M., Zhang, Z., Ni, A. & Dzau, V. J. Paracrine mechanisms in adult stem cell signaling and therapy. *Circ. Res.* **103,** 1204–1219 (2008).

23.   Burchfield, J. S. & Dimmeler, S. Role of paracrine factors in stem and progenitor cell mediated cardiac repair and tissue fibrosis. *Fibrogenesis Tissue Repair* **1,** 4 (2008).

24.   Gnecchi, M. *et al.* Paracrine action accounts for marked protection of ischemic heart by Akt-modified mesenchymal stem cells. *Nat. Med.* **11,** 367 (2005).

25.   Crisostomo, P. R. *et al.* Embryonic stem cells attenuate myocardial dysfunction and inflammation after surgical global ischemia via paracrine actions. *Am. J. Physiol. - Hear. Circ. Physiol.* **295,** H1726–H1735 (2008).

26.   Hensley, M. T. *et al.* Cardiac regenerative potential of cardiosphere-derived cells from adult dog hearts. *J. Cell. Mol. Med.* **19,** 1805–1813 (2015).

27.   Ke Cheng, Konstantinos Malliaras, Rachel Ruckdeschel Smith, Deliang Shen, Baiming Sun, Agnieszka Blusztajn, Yucai Xie, Ahmed Ibrahim, Mohammad Amin Aminzadeh, Weixin Liu, Tao Sheng Li, Michele A. De Robertis, Linda Marban, Lawrence S. C. Czer, Alfredo Tre, E. M. Human Cardiosphere-Derived Cells From Advanced Heart Failure Patients Exhibit Augmented Functional Potency in Myocardial Repair. *JACC Hear. Fail.*

2, 49–61 (2014).

28.   D. Shen, J. Tang, M. T. Hensley, T. Li, T. G. Caranasos, T. Zhang, K. C. Effects of Matrix Metalloproteinases on the Performance of Platelet Fibrin Gel Spiked With Cardiac Stem Cells in Heart Repair. *Stem Cells Transl. Med.* **5,** 793–803 (2016).

29.   Hodgkinson, C. P., Bareja, A., Gomez, J. A. & Dzau, V. J. Emerging Concepts in Paracrine Mechanisms in Regenerative Cardiovascular Medicine and Biology. *Circ. Res.* **118,** 95–107 (2016).

30.   Koch, S. & Claesson-Welsh, L. Signal Transduction by Vascular Endothelial Growth Factor Receptors. *Cold Spring Harb. Perspect. Med.* **2,** a006502 (2012).

31.   Talwar, T. & Srivastava, M. V. P. Role of vascular endothelial growth factor and other growth factors in post-stroke recovery. *Ann. Indian Acad. Neurol.* **17,** 1–6 (2014).

32.   Gallo, S., Sala, V., Gatti, S. & Crepaldi, T. HGF/Met Axis in Heart Function and Cardioprotection. *Biomedicines* **2,** 247–262 (2014).

33.   Sala, V. & Crepaldi, T. Novel therapy for myocardial infarction: can HGF/Met be beneficial? *Cell. Mol. Life Sci.* **68,** 1703–1717 (2011).

34.   Mayorga, M. E. *et al.* Role of SDF-1:CXCR4 in Impaired Post-Myocardial Infarction Cardiac Repair in Diabetes. *Stem Cells Transl. Med.* **7,** 115–124 (2017).

35.   De Falco, E. *et al.* SDF-1 involvement in endothelial phenotype and ischemia-induced recruitment of bone marrow progenitor cells. *Blood* **104,** 3472 LP-3482 (2004).

36.   Yoshida, T., Semprun-Prieto, L., Sukhanov, S. & Delafontaine, P. IGF-1 prevents ANG II-induced skeletal muscle atrophy via Akt- and Foxo-dependent inhibition of the ubiquitin ligase atrogin-1 expression. *Am. J. Physiol. Circ. Physiol.* **298,** H1565–H1570 (2010).

37.   Gan, W. *et al.* The SGK1 inhibitor EMD638683, prevents Angiotensin II–induced cardiac

inflammation and fibrosis by blocking NLRP3 inflammasome activation. *Biochim. Biophys. Acta - Mol. Basis Dis.* **1864,** 1–10 (2018).

38.   Mishra, P. K., Givvimani, S., Chavali, V. & Tyagi, S. C. Cardiac matrix: a clue for future therapy. *Biochim. Biophys. Acta* **1832,** 2271–2276 (2013).

39.   Sandoval-Guzmán, T. & Currie, J. D. The journey of cells through regeneration. *Curr. Opin. Cell Biol.* **55,** 36–41 (2018).

40.   Li, L. L. *et al.* Mesenchymal stem cells overexpressing adrenomedullin improve heart function through antifibrotic action in rats experiencing heart failure. *Mol. Med. Rep.* **17,** 1437–1444 (2018).

41.   Philp, D. & Kleinman, H. K. Animal studies with thymosin β4, a multifunctional tissue repair and regeneration peptide. *Ann. N. Y. Acad. Sci.* **1194,** 81–86 (2010).

42.   Smart, N. *et al.* De novo cardiomyocytes from within the activated adult heart after injury. *Nature* **474,** 640–644 (2011).

43.   Shah, R. *et al.* Thymosin β4 Prevents Oxidative Stress, Inflammation, and Fibrosis in Ethanol- and LPS-Induced Liver Injury in Mice. *Oxid. Med. Cell. Longev.* **2018,** (2018).

44.   Lalit, P. A., Hei, D. J., Raval, A. N. & Kamp, T. J. Induced pluripotent stem cells for post-myocardial infarction repair: remarkable opportunities and challenges. *Circ. Res.* **114,** 1328–1345 (2014).

45.   Tachibana, A. *et al.* Paracrine Effects of the Pluripotent Stem Cell-Derived Cardiac Myocytes Salvage the Injured Myocardium. *Circ. Res.* **121,** e22–e36 (2017).

46.   Liu, B. *et al.* Cardiac recovery via extended cell-free delivery of extracellular vesicles secreted by cardiomyocytes derived from induced pluripotent stem cells. *Nat. Biomed. Eng.* **2,** 293–303 (2018).

47. Frangogiannis, N. G., Smith, C. W. & Entman, M. L. The inflammatory response in myocardial infarction. *Cardiovasc. Res.* **53,** 31–47 (2002).

48. Ye, Y. *et al.* Synergistic Transcutaneous Immunotherapy Enhances Antitumor Immune Responses through Delivery of Checkpoint Inhibitors. *ACS Nano* **10,** 8956–8963 (2016).

49. Guo, J., Lin, G., Bao, C., Hu, Z. & Hu, M. Anti-Inflammation Role for Mesenchymal Stem Cells Transplantation in Myocardial Infarction. *Inflammation* **30,** 97–104 (2007).

50. Frangogiannis, N. G. Cell biological mechanisms in regulation of the post-infarction inflammatory response. *Curr. Opin. Physiol.* **1,** 7–13 (2018).

51. Dobaczewski, M., Gonzalez-Quesada, C. & Frangogiannis, N. G. The extracellular matrix as a modulator of the inflammatory and reparative response following myocardial infarction. *J. Mol. Cell. Cardiol.* **48,** 504–511 (2010).

52. Nakajima, M. *et al.* Mesenchymal Stem Cells Overexpressing Interleukin-10 Promote Neuroprotection in Experimental Acute Ischemic Stroke. *Mol. Ther. Methods Clin. Dev.* **6,** 102–111 (2017).

53. Shirakawa, K. *et al. IL-10-STAT3-Galectin-3 Axis is Essential for Osteopontin-Producing Reparative Macrophage Polarization After Myocardial Infarction. Circulation* (2018). doi:10.1161/CIRCULATIONAHA.118.035047

54. Zacchigna, S. *et al.* Paracrine effect of regulatory T cells promotes cardiomyocyte proliferation during pregnancy and after myocardial infarction. *Nat. Commun.* **9,** 2432 (2018).

55. Tang, J.-N. *et al.* Concise Review: Is Cardiac Cell Therapy Dead? Embarrassing Trial Outcomes and New Directions for the Future. *Stem Cells Transl. Med.* 354–359 (2018). doi:10.1002/sctm.17-0196

56. Heslop, J. A. *et al.* Concise Review: Workshop Review: Understanding and Assessing the Risks of Stem Cell-Based Therapies. *Stem Cells Transl. Med.* **4,** 389–400 (2015).

57. Duelen, R. & Sampaolesi, M. Stem Cell Technology in Cardiac Regeneration: A Pluripotent Stem Cell Promise. *EBioMedicine* **16,** 30–40 (2017).

58. Philippe, M. Stem Cell Therapy for Heart Failure. *Circulation* **119,** 2735–2740 (2009).

59. Fisher, S. A., Doree, C., Mathur, A., Taggart, D. P. & Martin-Rendon, E. Cochrane Corner: stem cell therapy for chronic ischaemic heart disease and congestive heart failure. *Heart* **104,** 8 LP-10 (2018).

60. Joshua, M. *et al.* Physiologic, Pathologic, and Therapeutic Paracrine Modulation of Cardiac Excitation-Contraction Coupling. *Circ. Res.* **122,** 167–183 (2018).

61. Tang, J. *et al.* Therapeutic microparticles functionalized with biomimetic cardiac stem cell membranes and secretome. *Nat. Commun.* **8,** 1–9 (2017).

62. Luo, L. *et al.* Fabrication of Synthetic Mesenchymal Stem Cells for the Treatment of Acute Myocardial Infarction in Mice. *Circ. Res.* **120,** 1768–1775 (2017).

63. Mihalko, E., Huang, K., Sproul, E., Cheng, K. & Brown, A. C. Targeted Treatment of Ischemic and Fibrotic Complications of Myocardial Infarction Using a Dual-Delivery Microgel Therapeutic. *ACS Nano* (2018). doi:10.1021/acsnano.8b01977

64. Vandergriff, A. *et al.* Targeting regenerative exosomes to myocardial infarction using cardiac homing peptide. *Theranostics* **8,** 1869–1878 (2018).

65. Tang, J. *et al.* Targeted repair of heart injury by stem cells fused with platelet nanovesicles. *Nat. Biomed. Eng.* **2,** 17–26 (2018).

66. Sarig, U. *et al.* Natural myocardial ECM patch drives cardiac progenitor based restoration even after scarring. *Acta Biomater.* **44,** 209–220 (2016).

67. Fang, R. H. *et al.* Cancer Cell Membrane-Coated Nanoparticles for Anticancer Vaccination and Drug Delivery. *Nano Lett.* **14,** 2181–2188 (2014).

68. Liang, H. *et al.* Mesenchymal Stem Cell/Red Blood Cell-Inspired Nanoparticle Therapy in Mice with Carbon Tetrachloride-Induced Acute Liver Failure. *ACS Nano* **12,** 6536–6544 (2018).

69. Pei, Q. *et al.* Light-Activatable Red Blood Cell Membrane-Camouflaged Dimeric Prodrug Nanoparticles for Synergistic Photodynamic/Chemotherapy. *ACS Nano* **12,** 1630–1641 (2018).

70. Hu, C.-M. J., Fang, R. H., Luk, B. T. & Zhang, L. Polymeric nanotherapeutics: clinical development and advances in stealth functionalization strategies. *Nanoscale* **6,** 65–75 (2014).

71. Tran, C. & Damaser, M. S. Stem cells as drug delivery methods: application of stem cell secretome for regeneration. *Adv. Drug Deliv. Rev.* **82–83,** 1–11 (2015).

72. Liu, P. *et al.* Quantitative secretomic analysis of pancreatic cancer cells in serum-containing conditioned medium. *Sci. Rep.* **6,** 37606 (2016).

73. Teixeira, F. G. *et al.* Do hypoxia/normoxia culturing conditions change the neuroregulatory profile of Wharton Jelly mesenchymal stem cell secretome? *Stem Cell Res. Ther.* **6,** 133 (2015).

74. Ahn, C.-S., Kim, J.-G., Shin, M. H., Lee, Y. A. & Kong, Y. Comparison of Secretome Profile of Pathogenic and Non-Pathogenic Entamoeba histolytica. *Proteomics* **18,** 1700341 (2018).

75. Kowal, J., Tkach, M. & Théry, C. Biogenesis and secretion of exosomes. *Curr. Opin. Cell Biol.* **29,** 116–125 (2014).

76. Arslan, F. *et al.* Mesenchymal stem cell-derived exosomes increase ATP levels, decrease oxidative stress and activate PI3K/Akt pathway to enhance myocardial viability and prevent adverse remodeling after myocardial ischemia/reperfusion injury. *Stem Cell Res.* **10,** 301–312 (2013).

77. He, C., Zheng, S., Luo, Y. & Wang, B. Exosome Theranostics: Biology and Translational Medicine. *Theranostics* **8,** 237–255 (2018).

78. Sahoo, S. & Losordo, D. W. Exosomes and cardiac repair after myocardial infarction. *Circ. Res.* **114,** 333–344 (2014).

79. Borges, F. T., Reis, L. A. & Schor, N. Extracellular vesicles: structure, function, and potential clinical uses in renal diseases. *Brazilian J. Med. Biol. Res.* **46,** 824–830 (2013).

80. Li, P., Kaslan, M., Lee, S. H., Yao, J. & Gao, Z. Progress in Exosome Isolation Techniques. *Theranostics* **7,** 789–804 (2017).

81. Yan, S. *et al.* Exosome-encapsulated microRNAs as circulating biomarkers for colorectal cancer. *Oncotarget* **8,** 60149–60158 (2017).

82. Sahoo, S. *et al.* Exosomes from Human CD34(+) Stem Cells Mediate their Pro-angiogenic Paracrine Activity. *Circ. Res.* **109,** 724–728 (2011).

83. Lee, C. *et al.* Exosomes Mediate the Cytoprotective Action of Mesenchymal Stromal Cells on Hypoxia-Induced Pulmonary Hypertension. *Circulation* **126,** 2601–2611 (2012).

84. Kishore, R. & Khan, M. More than Tiny Sacks: Stem Cell Exosomes as Cell-free Modality for Cardiac Repair. *Circ. Res.* **118,** 330–343 (2016).

85. Ong, S.-G., Lee, W. H., Zhou, Y. & Wu, J. C. Mining Exosomal MicroRNAs from Human-Induced Pluripotent Stem Cells-Derived Cardiomyocytes for Cardiac Regeneration BT - MicroRNA Protocols. in (ed. Ying, S.-Y.) 127–136 (Springer New York, 2018).

doi:10.1007/978-1-4939-7601-0_10

86.   Li, X. *et al.* Metabolic Adaptation to a Disruption in Oxygen Supply during Myocardial Ischemia and Reperfusion Is Underpinned by Temporal and Quantitative Changes in the Cardiac Proteome. *J. Proteome Res.* **11,** 2331–2346 (2012).

87.   Barile, L., Milano, G. & Vassalli, G. Beneficial effects of exosomes secreted by cardiac-derived progenitor cells and other cell types in myocardial ischemia. *Stem Cell Investig.* **4,** 93 (2017).

88.   Ibrahim, A. G.-E., Cheng, K. & Marbán, E. Exosomes as Critical Agents of Cardiac Regeneration Triggered by Cell Therapy. *Stem Cell Reports* **2,** 606–619 (2014).

89.   Essandoh, K. *et al.* Blockade of Exosome Generation with GW4869 Dampens the Sepsis-Induced Inflammation and Cardiac Dysfunction. *Biochim. Biophys. Acta* **1852,** 2362–2371 (2015).

90.   Gallet, R. *et al.* Exosomes secreted by cardiosphere-derived cells reduce scarring, attenuate adverse remodelling, and improve function in acute and chronic porcine myocardial infarction. *Eur. Heart J.* **38,** 201–211 (2017).

91.   Khan, M. *et al.* Embryonic Stem Cell-Derived Exosomes Promote Endogenous Repair Mechanisms and Enhance Cardiac Function Following Myocardial Infarction. *Circ. Res.* **117,** 52–64 (2015).

92.   Cheng, K. *et al.* Relative Roles of CD90 and c-Kit to the Regenerative Efficacy of Cardiosphere-Derived Cells in Humans and in a Mouse Model of Myocardial Infarction. *J. Am. Heart Assoc.* **3,** e001260–e001260 (2014).

93.   Vasa-Nicotera, M. *et al.* miR-146a is modulated in human endothelial cell with aging. *Atherosclerosis* **217,** 326–330 (2011).

94.   Mayourian, J. *et al.* Exosomal microRNA-21-5p Mediates Mesenchymal Stem Cell Paracrine Effects on Human Cardiac Tissue Contractility. *Circ. Res.* CIRCRESAHA.118.312420 (2018). doi:10.1161/CIRCRESAHA.118.312420

95.   Tian, Y. *et al.* A microRNA-Hippo pathway that promotes cardiomyocyte proliferation and cardiac regeneration in mice. *Sci. Transl. Med.* **7,** 279ra38 LP-279ra38 (2015).

96.   Liu, N. *et al.* An intragenic MEF2-dependent enhancer directs muscle-specific expression of microRNAs 1 and 133. *Proc. Natl. Acad. Sci.* **104,** 20844 LP-20849 (2007).

97.   Zhao, Y. *et al.* Dysregulation of Cardiogenesis, Cardiac Conduction, and Cell Cycle in Mice Lacking miRNA-1-2. *Cell* **129,** 303–317 (2007).

98.   Fish, J. E. *et al.* miR-126 Regulates Angiogenic Signaling and Vascular Integrity. *Dev. Cell* **15,** 272–284 (2008).

99.   Barile, L. *et al.* Extracellular vesicles from human cardiac progenitor cells inhibit cardiomyocyte apoptosis and improve cardiac function after myocardial infarction. *Cardiovasc. Res.* **103,** 530–541 (2014).

100.   Liu, N. & Bezprozvannaya, S. microRNA-133a regulates cardiomyocyte proliferation and suppresses smooth muscle gene expression in the heart. *Genes ...* 3242–3254 (2008). doi:10.1101/gad.1738708.al.

101.   Wang, X. *et al.* Increased expression of microRNA-146a decreases myocardial ischaemia/reperfusion injury. *Cardiovasc. Res.* **97,** 432–442 (2013).

102.   Porrello, E. R. *et al.* miR-15 Family Regulates Postnatal Mitotic Arrest of Cardiomyocytes. 670–679 (2011). doi:10.1161/CIRCRESAHA.111.248880

103.   Gu, H., Liu, Z. & Zhou, L. Roles of miR-17-92 Cluster in Cardiovascular Development and Common Diseases. **2017,** (2017).

104. Yu, B. *et al.* Exosomes Secreted from GATA-4 Overexpressing Mesenchymal Stem Cells Serve as a Reservoir of Anti-Apoptotic microRNAs for Cardioprotection. *Int. J. Cardiol.* **182,** 349–360 (2015).

105. Liang, D. *et al.* miRNA-204 drives cardiomyocyte proliferation via targeting Jarid2. *Int. J. Cardiol.* **201,** 38–48 (2015).

106. Wang, K. *et al.* Enhanced Cardioprotection by Human Endometrium Mesenchymal Stem Cells Driven by Exosomal MicroRNA-21. *Stem Cells Transl. Med.* **6,** 209–222 (2016).

107. Wang, N. *et al.* Mesenchymal stem cells-derived extracellular vesicles, via miR-210, improve infarcted cardiac function by promotion of angiogenesis. *Biochim. Biophys. Acta - Mol. Basis Dis.* **1863,** 2085–2092 (2017).

108. Feng, Y., Huang, W., Wani, M., Yu, X. & Ashraf, M. Ischemic Preconditioning Potentiates the Protective Effect of Stem Cells through Secretion of Exosomes by Targeting Mecp2 via miR-22. *PLoS One* **9,** e88685 (2014).

109. Chistiakov, D. A., Sobenin, I. A., Orekhov, A. N. & Bobryshev, Y. V. Human miR-221 / 222 in Physiological and Atherosclerotic Vascular Remodeling. **2015,** (2015).

110. Callis, T. E. *et al.* MicroRNA-208a is a regulator of cardiac hypertrophy and conduction in mice. *J. Clin. Invest.* **119,** 2772–2786 (2009).

111. Chen, L. *et al.* Cardiac progenitor-derived exosomes protect ischemic myocardium from acute ischemia/reperfusion injury. *Biochem. Biophys. Res. Commun.* **431,** 566–571 (2013).

112. Hosoda, T. *et al.* Human Cardiac Stem Cell Differentiation Is Regulated by a Mircrine Mechanism. *Circulation* **123,** 1287–1296 (2011).

113. Lai, R. C. *et al.* Proteolytic Potential of the MSC Exosome Proteome: Implications for an Exosome-Mediated Delivery of Therapeutic Proteasome. *Int. J. Proteomics* **2012,** 971907

(2012).

114. Chen, T. S. *et al.* Mesenchymal stem cell secretes microparticles enriched in pre-microRNAs. *Nucleic Acids Res.* **38,** 215–224 (2010).

115. Davis, M. E. Exosomes: What do we love so much about them? *Circ. Res.* **119,** 1280–1282 (2016).

116. Ruan, X. *et al.* Exosomes from Suxiao Jiuxin pill-treated cardiac mesenchymal stem cells decrease H3K27 demethylase UTX expression in mouse cardiomyocytes in vitro. *Acta Pharmacol. Sin.* **39,** 579 (2018).

117. Zimmermann, W.-H. *et al.* Engineered heart tissue grafts improve systolic and diastolic function in infarcted rat hearts. *Nat. Med.* **12,** 452 (2006).

118. Kawamura, M. *et al.* Feasibility, safety, and therapeutic efficacy of human induced pluripotent stem cell-derived cardiomyocyte sheets in a porcine ischemic cardiomyopathy model. *Circulation* **126,** 29–37 (2012).

119. Zhang, J. Engineered Tissue Patch for Cardiac Cell Therapy. *Curr. Treat. Options Cardiovasc. Med.* **17,** 399 (2015).

120. Zhang, J., Zhu, W., Radisic, M. & Vunjak-Novakovic, G. Can We Engineer a Human Cardiac Patch for Therapy? *Circ. Res.* **123,** 244–265 (2018).

121. Suzuki, R. *et al.* Omentopexy enhances graft function in myocardial cell sheet transplantation. *Biochem. Biophys. Res. Commun.* **387,** 353–359 (2009).

122. Stevens, K. R. *et al.* Physiological function and transplantation of scaffold-free and vascularized human cardiac muscle tissue. *Proc. Natl. Acad. Sci. U. S. A.* **106,** 16568–16573 (2009).

123. Kreutziger, K. L. *et al.* Developing Vasculature and Stroma in Engineered Human

Myocardium. *Tissue Eng. Part A* **17,** 1219–1228 (2011).

124. A., Schaefer, J., A., Guzman, P., B., Riemenschneider, S., J., Kamp, T. & T., Tranquillo, R. A cardiac patch from aligned microvessel and cardiomyocyte patches. *J. Tissue Eng. Regen. Med.* **12,** 546–556 (2017).

125. S., O. H. *et al.* A collagen cardiac patch incorporating alginate microparticles permits the controlled release of hepatocyte growth factor and insulin-like growth factor-1 to enhance cardiac stem cell migration and proliferation. *J. Tissue Eng. Regen. Med.* **12,** e384–e394 (2016).

126. Becker, M. *et al.* Towards a Novel Patch Material for Cardiac Applications: Tissue-Specific Extracellular Matrix Introduces Essential Key Features to Decellularized Amniotic Membrane. *International Journal of Molecular Sciences* **19,** (2018).

127. Bejleri, D. *et al.* A Bioprinted Cardiac Patch Composed of Cardiac-Specific Extracellular Matrix and Progenitor Cells for Heart Repair. *Adv. Healthc. Mater.* **0,** 1800672 (2018).

128. Cores, J., Caranasos, G. T. & Cheng, K. Magnetically Targeted Stem Cell Delivery for Regenerative Medicine. *Journal of Functional Biomaterials* **6,** (2015).

129. Su, T. *et al.* Cardiac Stem Cell Patch Integrated with Microengineered Blood Vessels Promotes Cardiomyocyte Proliferation and Neovascularization after Acute Myocardial Infarction. *ACS Appl. Mater. Interfaces* **10,** 33088–33096 (2018).

130. Ling, G. *et al.* Large Cardiac Muscle Patches Engineered From Human Induced-Pluripotent Stem Cell–Derived Cardiac Cells Improve Recovery From Myocardial Infarction in Swine. *Circulation* **137,** 1712–1730 (2018).

131. Ogle, B. M. *et al.* Distilling complexity to advance cardiac tissue engineering. *Sci. Transl. Med.* **8,** 342ps13 LP-342ps13 (2016).

132. Tang, J. *et al.* A Regenerative Cardiac Patch Formed by Spray Painting of Biomaterials onto the Heart. *Tissue Eng. Part C Methods* **23,** 146–155 (2017).

133. Shen, D. *et al.* Effects of Matrix Metalloproteinases on the Performance of Platelet Fibrin Gel Spiked With Cardiac Stem Cells in Heart Repair. *Stem Cells Transl. Med.* **5,** 793–803 (2016).

134. Wang, L. L. *et al.* Sustained miRNA delivery from an injectable hydrogel promotes cardiomyocyte proliferation and functional regeneration after ischaemic injury. *Nat. Biomed. Eng.* **1,** 983–992 (2017).

135. Sarig, U. *et al.* Natural myocardial ECM patch drives cardiac progenitor based restoration even after scarring. *Acta Biomater.* **44,** 209–220 (2016).

136. Bassat, E. *et al.* The extracellular matrix protein agrin promotes heart regeneration in mice. *Nature* **547,** 179–184 (2017).

137. Spang, M. T. & Christman, K. L. Extracellular matrix hydrogel therapies: In vivo applications and development. *Acta Biomater.* **68,** 1–14 (2018).

138. Montgomery, M. *et al.* Flexible shape-memory scaffold for minimally invasive delivery of functional tissues. *Nat. Mater.* **16,** 1038–1046 (2017).

139. Cannata, A. *et al.* Postsurgical Intrapericardial Adhesions: Mechanisms of Formation and Prevention. *Ann. Thorac. Surg.* **95,** 1818–1826 (2013).

140. Sugiura, T., Hibino, N., Breuer, C. K. & Shinoka, T. Tissue-engineered cardiac patch seeded with human induced pluripotent stem cell derived cardiomyocytes promoted the regeneration of host cardiomyocytes in a rat model. *J. Cardiothorac. Surg.* **11,** 163 (2016).

141. Malki, M., Fleischer, S., Shapira, A. & Dvir, T. Gold Nanorod-Based Engineered Cardiac Patch for Suture-Free Engraftment by Near IR. *Nano Lett.* **18,** 4069–4073 (2018).

142. Fujimatsu, T. *et al.* Patch-and-glue repair in combination with or without direct suture for cardiac rupture after myocardial infarction. *Gen. Thorac. Cardiovasc. Surg.* **55,** 345–350 (2007).

143. Chong, J. J. H. *et al.* Human embryonic-stem-cell-derived cardiomyocytes regenerate non-human primate hearts. *Nature* **510,** 273 (2014).

144. Morais, J. M., Papadimitrakopoulos, F. & Burgess, D. J. Biomaterials/tissue interactions: possible solutions to overcome foreign body response. *AAPS J.* **12,** 188–196 (2010).

145. Kanki, S. *et al.* Identification of Targeting Peptides for Ischemic Myocardium by In Vivo Phage Display. *J. Mol. Cell. Cardiol.* **50,** 841–848 (2011).

146. Miragoli, M. *et al.* Inhalation of peptide-loaded nanoparticles improves heart failure. *Sci. Transl. Med.* **10,** (2018).

147. Sensenig, R., Sapir, Y., MacDonald, C., Cohen, S. & Polyak, B. Magnetic nanoparticle-based approaches to locally target therapy and enhance tissue regeneration in vivo. *Nanomedicine (Lond).* **7,** 1425–1442 (2012).

148. Lu, A.-H., Salabas, E. L. & Schüth, F. Magnetic Nanoparticles: Synthesis, Protection, Functionalization, and Application. *Angew. Chemie Int. Ed.* **46,** 1222–1244 (2007).

149. Arbab, A. S. *et al.* Intracytoplasmic tagging of cells with ferumoxides and transfection agent for cellular magnetic resonance imaging after cell transplantation: Methods and techniques. *Transplantation* **76,** 1123–1130 (2003).

150. Chen, J. *et al.* Guidance of Stem Cells to a Target Destination in Vivo by Magnetic Nanoparticles in a Magnetic Field. *ACS Appl. Mater. Interfaces* **5,** 5976–5985 (2013).

151. Vandergriff, A. C. *et al.* Magnetic targeting of cardiosphere-derived stem cells with ferumoxytol nanoparticles for treating rats with myocardial infarction. *Biomaterials* **35,**

8528–8539 (2014).

152. Lee, R. J. *et al.* Antibody Targeting of Stem Cells to Infarcted Myocardium. *Stem Cells* **25,** 712–717 (2009).

153. Srikanth, S. & Ambrose, J. A. Pathophysiology of Coronary Thrombus Formation and Adverse Consequences of Thrombus During PCI. *Curr. Cardiol. Rev.* **8,** 168–176 (2012).

154. Nesheim, M. Myocardial infarction and the balance between fibrin deposition and removal. *Ital Hear. J* **2,** 641–645 (2001).

155. Malmsten, M. *Microgels in Drug Delivery*. (2011).

156. Byrne, H., Conroy, P. J., Whisstock, J. C. & O'Kennedy, R. J. A tale of two specificities: bispecific antibodies for therapeutic and diagnostic applications. *Trends Biotechnol.* **31,** 621–632 (2013).

157. Mellman, I., Coukos, G. & Dranoff, G. Cancer immunotherapy comes of age. *Nature* **480,** 480 (2011).

158. Tang, J., Shen, D., Zhang, J., Ligler, F. S. & Cheng, K. Bispecific antibodies, nanoparticles and cells: bringing the right cells to get the job done. *Expert Opin. Biol. Ther.* **15,** 1251–1255 (2015).

159. Lum, L. G. *et al.* Targeting of Lin−Sca+ hematopoietic stem cells with bispecific antibodies to injured myocardium. *Blood Cells, Mol. Dis.* **32,** 82–87 (2004).

160. Cheng, K. *et al.* Magnetic antibody-linked nanomatchmakers for therapeutic cell targeting. *Nat. Commun.* **5,** (2015).

161. Jackson, S. P. The growing complexity of platelet aggregation. *Blood* **109,** 5087 LP-5095 (2007).

162. Lippi, G., Franchini, M. & Targher, G. Arterial thrombus formation in cardiovascular

disease. *Nat. Rev. Cardiol.* **8,** 502 (2011).

163. Modery-Pawlowski, C. L., Kuo, H.-H., Baldwin, W. M. & Gupta, A. Sen. A platelet-inspired paradigm for nanomedicine targeted to multiple diseases. *Nanomedicine* **8,** 1709–1727 (2013).

164. Hu, C.-M. J. *et al.* Nanoparticle biointerfacing by platelet membrane cloaking. *Nature* **526,** 118 (2015).

165. Su, T. *et al.* Platelet-Inspired Nanocells for Targeted Heart Repair After Ischemia/Reperfusion Injury. *Adv. Funct. Mater.* **0,** 1803567 (2018).

166. Overdijk, M. B. *et al.* Antibody-mediated phagocytosis contributes to the anti-tumor activity of the therapeutic antibody daratumumab in lymphoma and multiple myeloma. *MAbs* **7,** 311–320 (2015).

167. Muzykantov, V. & Muro, S. Targeting delivery of drugs in the vascular system. *Int. J. Transp. Phenom.* **12,** 41–49 (2011).

CHAPTER 2: Therapeutic Potential of an Artificial Cardiac Patch in Rats and Pigs with Myocardial Infarction

Unpublished data as of dissertation submission date; under revision at *Science Translational Medicine.*
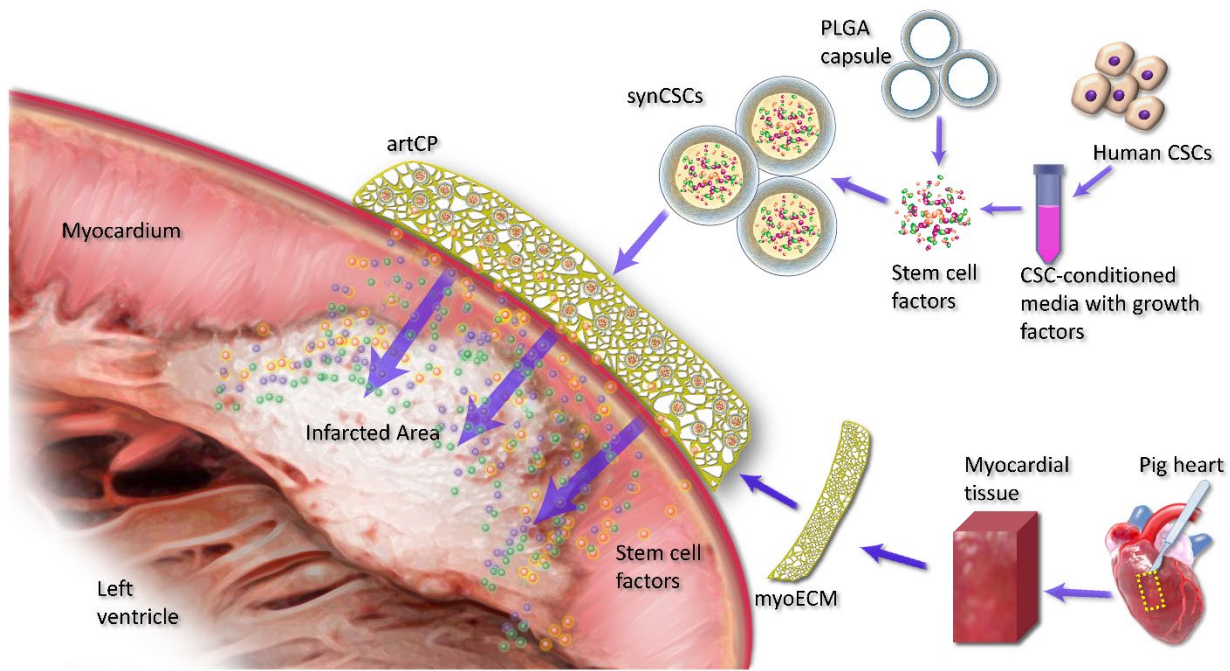
Fig Scheme. Schematic showing the concept of fabricating an off-the-shelf therapeutic cardiac patch for cardiac repair after myocardial infarction.

1. Abstract

Cell therapy has been a promising strategy for therapeutic heart regeneration. To overcome the limitation of low cell retention/engraftment, the cardiac patch strategy involves seeding a scaffolding material with cells before transplantation onto the surface of the heart. These patches need to be freshly made and long-term storage is not feasible. We developed an off-the-shelf therapeutic cardiac patch, composed of a decellularized porcine myocardial extracellular matrix

from pig myocardium, and synthetic cardiac stromal cells (synCSC) from the secreted factors of human cardiac stromal cells (Fig. Scheme). This fully acellular artificial cardiac patch (artCP) maintained its potency after long-term cryopreservation. In a rat model of acute myocardial infarction (MI), transplantation of artCP supports cardiac recovery by reducing scarring, promoting angiomyogenesis, and boosts cardiac function. The safety and therapeutic efficacy of artCP is further confirmed in a porcine MI model. Compare to current cardiac patch strategies, artCP offers clinically feasible, easy-to-store, and cell-free advantages.

2. Introduction

Coronary heart disease has been a leading cause of death in the United States, killing over 360,000 people a year[1]. Present myocardial infarction (MI) treatment approaches, including limiting the initial injury and blocking secondary maladaptive pathways, greatly reduce cardiovascular morbidity and mortality. However, the remodeling process after acute MI still frequently leads to arrhythmias and heart failure (HF) and contribute to cardiovascular morbidity and mortality[2]. Cell therapy focus on using cells derived from different sources to promote myocardial regeneration by altering the cardiac remodeling process and reducing MI scar size [3-5]. Heart-derived cardiac stromal cells (CSCs) offer regenerative therapeutic benefits through paracrine regenerative factors[6-8] and direct interaction with the injured cardiomyocytes[9]. Beneficial effects from CSC therapy have been confirmed in clinical trials for mild-moderate MI[10-13].

The clinical applications of cell therapy for heart repair have several limitations[14-16]. First, cells are very fragile and have to be carefully preserved to keep them alive and functional[17] prior to transplantation. Consequently, live cells are not an off-the-shelf product for clinical application and result in huge costs in manpower and material expense. The modes of action for cell therapy products also remain elusive, making it difficult to standardize product-release criteria. These

issues are further complicated by the fact that some undifferentiated cells can become tumor-forming due to the potential of unlimited proliferation[14,18]. To increase host immunologic tolerance, transplantation of autologous cells may be a good choice[19], but generation of these cells is expensive and time consuming[14]. Furthermore, the extremely low cell retention/engraftment regardless of the delivery route is a major hurdle that hampers the efficacy of the therapy[20,21]. Such rapid cell loss is not mainly due to cell death[22], but rather the "washing away" of the cells caused by poor adherence to the injured heart[23-25].

In recent years, cardiac patches have been engineered to serve as the scaffolding materials for myocardial regeneration. Different cardiac patches include three-dimensional (3D) scaffolds embedded with stem cells[26-30], microvessel layer integrated bilayer patches[31], and microneedle cardiac patches[32]. However, the aforementioned limitations associated with natural cells remain unsolved for cellular cardiac patches. In order to overcome these challenges, we designed and fabricated an artificial cardiac patch (artCP) by embedding synthetic cardiac stromal cells (synCSC) within decellularized myocardial extracellular matrix (myoECM). myoECM which was derived from decellularized porcine myocardium offers an optimal scaffolding material by providing native ultrastructural and material properties. myoECM also provides bioactivity that has been shown to promote constructive remodeling and vascularization after transplantation[33]. synCSCs were fabricated by encapsulating human CSC-secreted factors into biodegradable PLGA microparticles[34,35]. These two components synergistic properties: the 3D reticulate structure of myoECM offers mechanical support[36] to the native myocardium while the embedded synCSCs secrete regenerative factors. Both components are acellular, overcoming the shortages of using live cells and providing an off-the-shelf product with an extended shelf life. In the present study, we tested the mechanical/biological properties and cryo-stability of artCP *in vitro* and determined

its therapeutic benefits in rodent and porcine models of MI, artCP represents a novel cardiac tissue engineering product which packages cell and ECM biology in a clinically feasible and off-the-shelf fashion.

3. Materials & Methods

3.1 Preparation of Conditioned Media

Conditioned media from human CSCs was prepared as previously described[34,37]. Briefly, 2×10^6 human CSCs from 9 cell lines were cultured in T-75 flasks and incubated with 1 ml FBS-free media for 14 days in 5% CO_2 at 37°C. Then, the media was collected and centrifuge at 1000g for 10 min to remove the cells and large fragments. To diminish the variable batch quality, conditioned media from 9 cell lines were mixed before lyophilization and storage.

3.2 Preparation of myoECM

Porcine hearts were decellularized as previously described[36]. Briefly, whole hearts of market weight porcine were obtained from Nahunta Pork Center (Raleigh, NC). The tissues were cleaned of excess tissue and washed thoroughly with tap water. The tissues were then patted dry and placed at -80°C for at least 48 hours. The heart was sliced into 1 mm thin pieces and agitated in a series of washes. The tissues were first rinsed with dH 2 0 and 2x PBS washes then washed for 2 hours in 0.05% Trypsin (Thermo Fisher Scientific, Waltham, MA), 2 hours in 2% Tween-20 (Sigma-Aldrich, St. Louis, MO) and 2 hours with 4% sodium deoxycholate solution (Sigma-Aldrich) with 5 min dH 2 0 and 15 min 2xPBS washes in between. The heart slices were then sterilized with a 0.1% peracetic acid solution (Sigma-Aldrich) and washed three times with sterile 1x PBS. Decellularized myoECM was then placed flat in aluminum foil and lyophilized for at least 24 hours. Lyophilized myoECM scaffolds were then sterilized using ethylene oxide.

3.3 DNA quantification of myoECM

Samples of ~10 mg were taken before and after decellularization and were digested at 60°C overnight with 0.2 mg/mL of papain (Sigma-Aldrich). The samples were then accessed for DNA content using the Quant-IT Picogreen dsDNA Assay (Thermo Fisher Scientific, Waltham, MA) according to the manufacturer's instructions. 100 µL samples were read at 538 nm with an excitation at 485 nm using a fluorescence spectrometer. Before decellularization, samples contained 418.8 ± 27.33 ng DNA/mg of tissue, n=8 and after decellularization, samples contained 17.66 ± 3.869 ng DNA/mg of tissue, n=8.

3.4 Characterization of myoECM

Biopsy punches (7mm) were taken of the heart tissue before and after decellularization, fixed with 4% paraformaldehyde (Sigma-Aldrich) overnight and stored in 70% EtOH. Cross sections were cut at 5 µm and stained for Van Gieson's, Gömöri's Trichrome and Alcian Blue. Slides were imaged using an AZ100 multi-purpose zoom microscope system. Mechanical testing was done on an Instron 5944 with a 50 N load cell. Samples of myocardium were randomly cut into rectangular pieces, hydrated in 1X PBS until testing and then secured at opposite ends onto customized clamps. Samples of native heart tissue (NHT) were 12.62 ± 0.60 mm in width and 1.79 ± 0.13 mm in thickness. Processed myoECM samples were 10.05 ± 0.59 mm in width (9.47 ± 0.60 mm for n=8) and 1.54 ± 0.13 mm (or 1.23 ± 0.13 mm for n=8) in thickness. Samples were pre-conditioned by using 5 cycles at a rate of 1 %strain/sec with a preload of 0.06N. This was followed by a uniaxial stretch of until failure at a rate of 1% strain/sec. Data was collected using Bluehill3 Testing Software and processed.

3.5 Fabrication and characterization of artCPs

myoECM (diameter = 3.5 cm) was hydrolyzed with sterilized PBS for 24 hours and then was placed on the filtration area of the 50ml vacuum filtration system (Steriflip® Filter Units). synCSC suspended in sterilized PBS ($7 \wedge 10^6$ /ml) was added evenly on top of the myoECM so that the vacuum extraction force drove the synCSCs into the reticulate structure of myoECM during vacuum filtration and formed artCP. The artCP was cut into round pieces (diameter = 5 mm) with a size 10 scalpel for both *in vitro* study and *in vivo* rat study. Whereas, the artCP for *in vivo* porcine study was a round piece with diameter of 3.5 cm. The morphology of artCP was studied by SEM (Philips XL30 scanning microscope, Philips, The Netherlands). Freeze-dried samples were mounted on aluminium stubs with double-sided tape and coated with a thin layer of gold. The coated samples were then scanned and photographed under the microscope at an acceleration voltage of 15 kV. To examine the embedding efficiency and retention of synCSCs *in vitro*, we pre-labeled myoECM with anti-collagen I (1:100, ab34710, Abcam) and FITC-conjugated secondary antibodies (1:200). Also, we pre-labeled synCSCs with red-fluorescent Texas red succinimidyl ester (1mg/ml) (Invitrogen, Carlsbad, California). Then, the artCP (n=6) was produced for imaging before and after sterilized PBS wash. Images were taken with an epi-fluorescent microscope (Olympus IX81). The retained synCSCs were characterized and compared from the same images using the NIH Image J software.

3.6 Cryo-stability analysis of artCPs

We created 5 batches (n=4 in each batch) of artCP every 7 days. For the first 4 batches, the artCP were washed with PBS and cryo-stored in -20°C directly after fabrication. On day 28, the first 4 batches were thawed and the 5th batch of artCP were made freshly. Then, we rinsed all batches of artCP with sterile PBS for 3 times and soaked into 1ml sterile PBS. After that, we

incubated them in a 37°C incubator for 4 days. The regenerative factors (VEGF, HGF and IGF) in the supernatant were assessed through ELISA kits (R&D Systems). Total protein contents of synCSCs that used for artCP batch creation were determined as previous studies[34]. Briefly, 10 mg freeze-dried synCSCs were dissolved in 1ml dichloromethane (DCM) for 60 min. Then, 1 ml PBS was added into solution followed by agitation for 10 min to extract protein from DCM into PBS. After centrifugation, the concentration of protein in the aqueous phase was determined by a BCA Protein Assay Kit (Thermo Fisher Scientific, Waltham, MA, USA).

3.7 *In vitro* potency of artCPs

Neonatal rat cardiomyocytes (NRCMs) were derived from SD rat as previous described[38]. We cultured NRCMs on 4-well chamber slides. Fresh-artCP, cryo-artCP, myoECM or synCSCs were placed onto NRCMs for 3 days. A solitary NRCM culture was included as control. Cell proliferation was evaluated by the percentage of α-SA$^+$(1:100, a7811, Sigma) /Ki67$^+$ (1:100, ab15580, Abcam) NRCMs. For assessment of cell apoptosis, the cells were incubated with TUNEL solution (Roche Diagnostics GmbH, Mannheim, Germany) and counter-stained with DAPI (Life Technology, NY, USA). A Live/Dead Viability/Cytotoxicity Kit (ThermoFisher) was used to determine the cell viability of NRCMs. Images were taken with a confocal fluorescent microscope (ZEISS LSM 880). Tissue morphology was characterized by images using the NIH Image J software and ZEN lite software.

3.8 Angiogenesis Assay

Human umbilical vein endothelial cells (HUVECs) were co-incubated with PBS, myoECM, cryo-artCP or fresh artCP for 24 hr, then plated on growth factor-deprived Matrigel (BD Biosciences, San Jose, CA) to evaluate angiogenesis[61]. Eight hours later, tube formation was measured with a white light microscope and analyzed with NIH Image J software.

3.9 Rat model of myocardial infarction

All animal work was compliant with the Institutional Animal Care and Use Committee at North Carolina State University. Animal care was in accordance to the Institutional Animal Care and Use Committee (IACUC) guidelines. 5-7-week-old female Sprague Dawley rats (Charles River Laboratories) were induced with a 1.5% isofluorane-oxygen mixture. Then, the rats were intraperitoneal administered with 0.8-0.9μl/g anesthetic combination (ketamine and xylazine with a proportion of 2:1). Under artificial ventilation with a rodent ventilator (SAR-1000 Small Animal Ventilator, CWE, Inc.), a MI surgical operation was performed under sterile conditions. Briefly, the heart was exposed by left thoracotomy at 4th intercostal space and acute MI was produced by permanent ligation of LAD (6-0 prolene blue 30", Esutures). Then, the rats were left *in-situ* for 20 mins covered with a sterile PBS soaked cotton gauze pad (Fisherbrand). The heart was randomized to receive one of the following 3 treatment: 1) MI group: MI induction without any treatment; 2) MI + myoECM group: empty myoECM patch was sutured (6-0 prolene blue 30", Esutures) onto the surface of discolored infarcted area ; (3) MI + artCP group: artCP was sutured onto the surface of discolored infarcted area (6-0 prolene blue 30", Esutures). After the surgery, rats were then extubated and observed for approximately 30 minutes until they were able to move. 21 days (rat 21 days equal to human 1.5 years)[62] after MI surgical operation, the animals were euthanized for further study.

3.10 Immunohistochemistry (IHC)

Heart cryo-sections were fixed with 4% paraformaldehyde solution, permeabilized and blocked with 0.01% saponin (Sigma-Aldrich, St. Louis, MO) Dako (Dako, Glostrup, Denmark) solution and then incubated with primary antibodies overnight at 4°C: mouse anti-alpha sarcomeric actin (1:100, a7811, Sigma), rabbit anti-Ki67 (1:100, ab15580, Abcam), rabbit anti- von

Willebrand factor (1:100, ab6994, Abcam), rabbit anti- pH3 (1:100, ab5176, Abcam), rabbit anti-AuroraB (1:100, ab2254, Abcam). FITC- or Texas-Red secondary antibodies (1:200) were obtained from Abcam Company and used for the conjunction with these primary antibodies for 1.5 hour at room temperature. Samples were then treated with DAPI (LifeTech, Carlsbad, CA) and mounted in Prolong Gold Mounting Media (LifeTech, Carlsbad, CA). For assessment of cell apoptosis, heart cryo-sections were incubated with TUNEL solution (Roche Diagnostics GmbH, Mannheim, Germany) and counter-stained with DAPI (Life Technology, NY, USA). Images were taken with an epi-fluorescent microscope (Olympus IX81) and confocal fluorescent microscope (ZEISS LSM 880). Tissue morphology was characterized by images using the NIH Image J software and ZEN lite software.

3.11 Immunogenicity detection after artCP transplantation

SD rats with integrity immune system were anaesthetized with ketamine and xylazine cocktail (proportion of 2:1). Under sterile conditions, the heart was infarcted by LAD ligation. ArtCP was transplanted onto the heart (6-0 prolene blue 30", Esutures). After 7 days, all rats were sacrificed, and hearts were collected for cryo-sections as previously described. Then, IHC was performed with the primary antibodies including rabbit anti-CD3 (1:100, ab16669, Abcam), mouse anti-CD8 alpha (1:100, mca48r, abd Serotec, Raleigh, NC) and mouse anti-CD68 (1:100, ab 955, Abcam). FITC- secondary antibodies (1:200) were obtained from Abcam Company and used for the conjunction with these primary antibodies. Nuclei were stained with DAPI (Life Technology, NY, USA). Images were taken by an Olympus epi-fluorescence microscopy system.

3.12 synCSC retention and distribution

To track the synCSC in vivo, we fabricated artCP with DiR labelled synCSC and transplanted in rat MI models. To prepare DiR (1,1-dioctadecyl-3,3,3,3-tetramethy-

lindotricarbocyanine iodide) (D12731, Invitrogen, Life Technologies) labelled synCSC, the filtered CSC membrane was collected as previously described[34] and was incubated with 1μM fluorescent lipophilic tracer DiR at room temperature (RT) for 20 minutes. Then, we cloaked the synCSC core with DiR labelled CSC membrane so that the DiR fluorescence could be traced. The animals administrated with intramyocardial injection of DiR labelled synCSC and transplantation of empty myoECM were used as controls (n=3 in each group). Then, Animals were euthanized, and the organs were harvested 24 hours after treatment. We placed hearts and other organs in Xenogen IVIS imaging system (Caliper Life Sciences, Mountain View, CA) to detect RFP fluorescence for biodistribution analysis.

3.13 artCP transplantation in a porcine MI model

Yorkshire porcine (Palmetto, 60-70lbs) were used for surgical (open-chest) MI models. While porcine were in their quarters, they were sedated with TKX cocktail (1 mL/13-30 kg IM). Then, the animals were intubated, and anesthesia were maintained with a mixture of isoflurane (0-5% in 100% oxygen) at the constant-rate infusion of 5-10 ug/kg/hr. While under anesthesia, the porcine were monitored per veterinary hospital guidelines. A partial midline stemotomy was performed under sterile conditions and the pericardium was sectioned. Then, the MI was created by permanent ligation (Silkam 2/0, B/ Braun Suture) at the distal (left) LAD after the second diagonal branch. Heparin (5000 IU IV) was administered just before LAD occlusion. 10 mins later, the artCP was transplanted by suturing (2/0 suture, Esutures, MokenIL) on the heart surface downstream of the LAD, where there was a sign of ischemia. During surgery, positive pressure ventilation was maintained at a rate of 10-12 breaths per minute, and normal saline (10 mL/kg hourly) was infused through the venous cannula in the auricular vein to maintain preload stability. After the study, arterial oxygen tension, locomotor activity, respiratory changes, body temperature,

and food and water intake was closely monitored by veterinary services staff. Porcine were carried out until 7 days after MI surgery.

3.14 Statistical analysis

All results are expressed as mean ± s.d. Comparison between two groups was performed with two-tailed Student's *t*-test. Comparisons among more than two groups were performed using one-way ANOVA followed by *post hoc* Bonferroni test. Differences were considered statistically significant when the *P* value < 0.05.

4. Results

4.1 Fabrication of artCP

As the base material for artCP, myoECM was derived from decellularized porcine myocardium. To test whether the myoECM had appropriate structure and mechanical characteristics for heart transplantation, we compared myoECM with native heart tissue (NHT) *via* histology and mechanical testing (Fig. 1). The result indicated that myoECM was produced efficiently by decellularization, and the remaining fibrillar collagen provided its mechanical stability, structural support and morphology (Fig. 1A). Also, the compliance of myoECM (Figs. 1B and C) was similar to that of NHT within a similar thickness (Fig. 1D). Moreover, the decellularization effectively also removed DNA (Fig. 1E). These results confirmed that decellularized myoECM preserved its reticular structure and maintained a relatively similar elasticity as NHT making them mechanically feasible for heart transplantation.
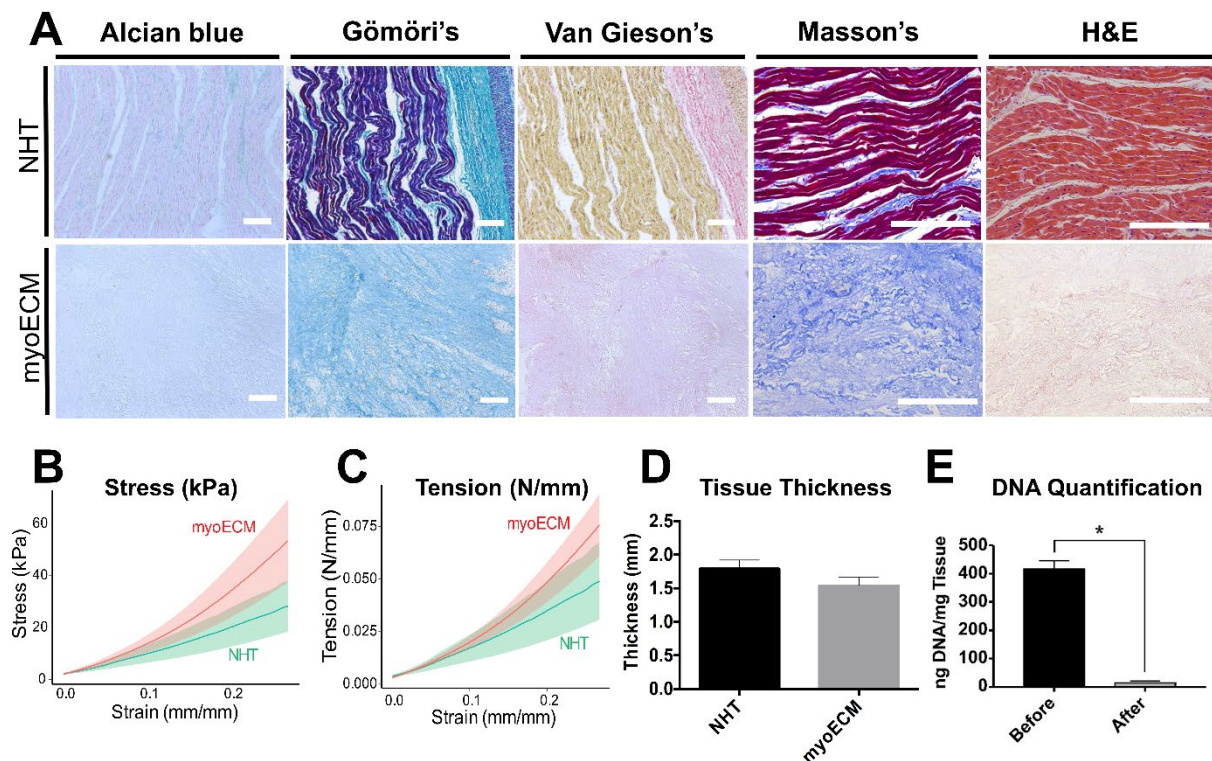
Fig 1. Histological and mechanical comparison between decellularized myoECM and native heart tissue (NHT). (A) Histology comparison between NHT (top) and decellularized myoECM (bottom) including Alcian blue, Gormori's Blue,Van Gieson's, Masson's trichrome, and H&E staining. Scale bar = 200 µm. (B-C) Uniaxial testing on native heart tissue (NHT) and processed heart ECM (myoECM) n = 5. (B) Plots of tension vs strain. (C) Plots of stress vs strain. (D) Thickness comparison of NHT and myoECM samples for uniaxial testing. (E) DNA quantification before and after myoECM decellularization. All data were means ± s.d. Comparisons between two groups were performed using two-tailed unpaired Student's *t*-test.
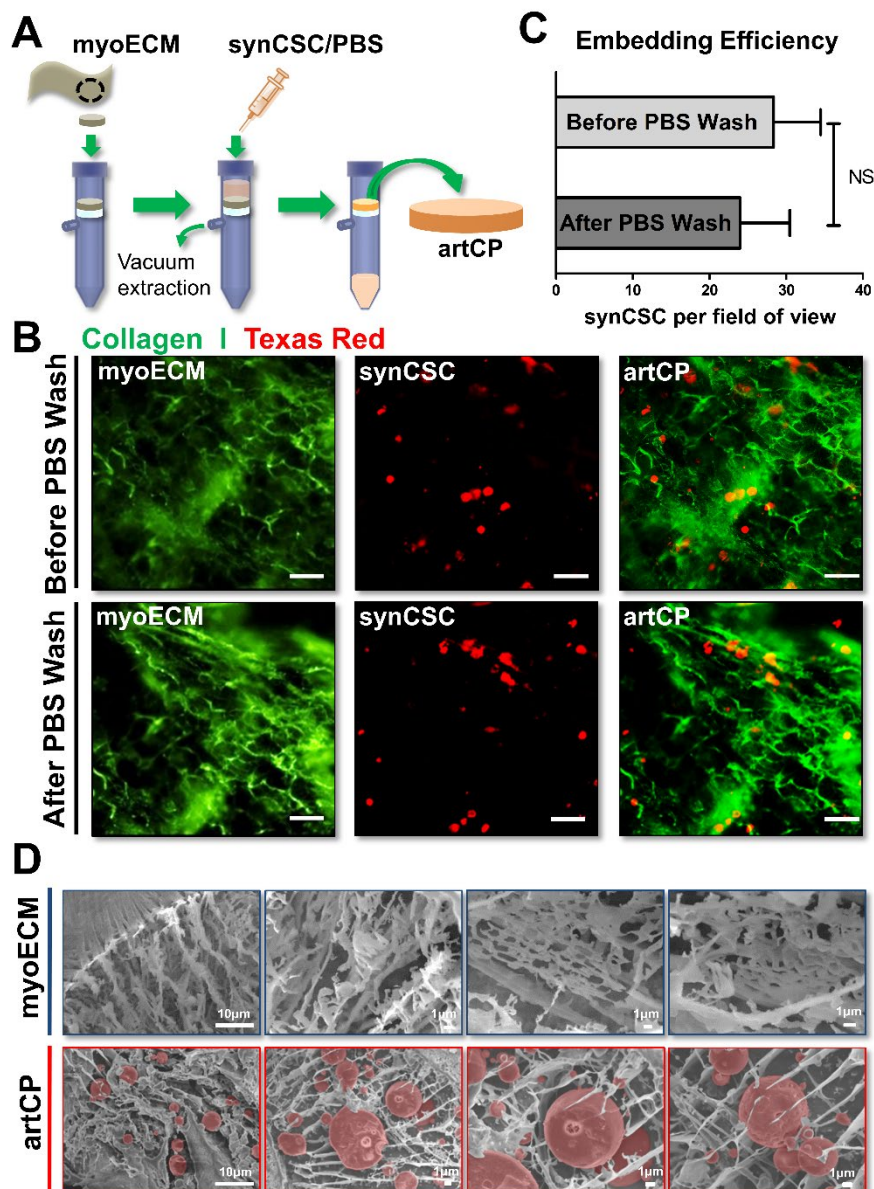
Fig 2. Generation of artCP by embedding synCSCs into myoECM via vacuum filtration.
(A) Schematic showing the vacuum filtration method. (B) Representative fluorescent images showing artCPs before and after PBS wash. synCSC (red) were prelabeled with Texas red succinimidyl ester and myoECM (green) were prelabeled with anti-collagen I and FITC-conjugated secondary antibodies. Scale bar = 25μm. (C) Quantitation of embedded synCSC numbers before and after wash (n = 6). All data were means ± s.d. Comparisons between two groups were performed using two-tailed unpaired Student's *t*-test. NS indicated *P* > 0.05. (D) Representative SEM images showing the cross-sectional view of myoECM (blue outline) and artCP (red outline).

To fabricate the final product artCP, we embedded synCSCs (Fig. S1A) into myoECM *via* a vacuum filtration method (Fig. 2A). The controllable vacuum drove the synCSC particles into the myoECM structure. To confirm synCSC embedding efficiency and retention, artCPs were washed 3 time with PBS. synCSCs remained in the artCP after wash (Figs. 2B and C). Scanning electron microscope (SEM) confirmed that synCSCs were efficiently embedded in the reticulate structure of myoECM with limited structural change in both myoECM and synCSCs (Fig. 2D). Confocal imaging confirmed that synCSC were successfully embedded into myoECM and evenly distributed (Fig. S1B). Taking together, vacuum filtration was able to embed synCSCs in myoECM to form artCP without harming to the structural integrity of both myoECM and synCSCs.

4.2 Characterization of artCP

One major advantage of an artCP over a live cardiac patch is its foreseeable cryo-stability. CSCs rely on their secretion to exert their regenerative potency[13], we assessed the concentrations of various regenerative factors released by artCPs that had been cryo-stored for various time periods (Fig. 3A). After various periods of cryo-storage, artCPs were rinsed 3 times with sterile PBS and soaked in 1 ml of sterile PBS for a 4-day incubation at 37°C (Fig. 3A). The results indicate that the secretion ability of artCP was not affected by cryo-storage (Figs. 3B-D). As a quality control, we confirmed that the initial total protein amounts in the synCSCs of different batches of artCPs were equivalent. (Fig. 3E). Additionally, we further evaluated the mechanical properties of cryo-stored and fresh artCPs. The result indicated that the 28day cryo-storage did not affect the mechanical properties of the patch (Figs. S1C-E). Moreover, the degradative capability of artCP was shown in enzyme-mediated degradation analysis *in vitro* (Fig. S1F).

4.3 Regenerative potency of artCP *in vitro*

As an *in vitro* potency assay, we co-cultured freshly prepared or cryo-stored artCPs with neonatal rat cardiomyocytes (NRCMs) for 3 days and then assessed cell viability and proliferation. Equal amounts of synCSCs, myoECM, or empty-artCP (myoECM embedded with empty PLGA particles with no CSC factors) were included as proper controls. NRCMs cultured in regular media were used as negative control. Proliferating NRCMs were identified by Ki67$^+$ expression (green) in the nuclei (blue) (Fig. 4A). Our data suggested that co-culture with synCSCs, cryo artCP or fresh artCP promoted the proliferation of NRCMs (Fig. 4B). Co-culture with synCSCs, cryo artCP or fresh artCP increased cell viability and decreased cell death, resulting in an increase in overall cell numbers (Figs. 4C and D). In addition, TUNEL staining revealed that co-culture with synCSCs, cryo artCP or fresh artCP inhibited cell apoptosis (Figs. 4E and F). Moreover, artCP promoted tube formation of endothelial cells (Figs. S2A-C). In all these measures, the potency of cyro-stored artCP was similar to that from freshly prepared artCP. Together, these data supported the notion that artCP retained the regenerative potency of synCSCs and cryo-storage did not undermine such potency.
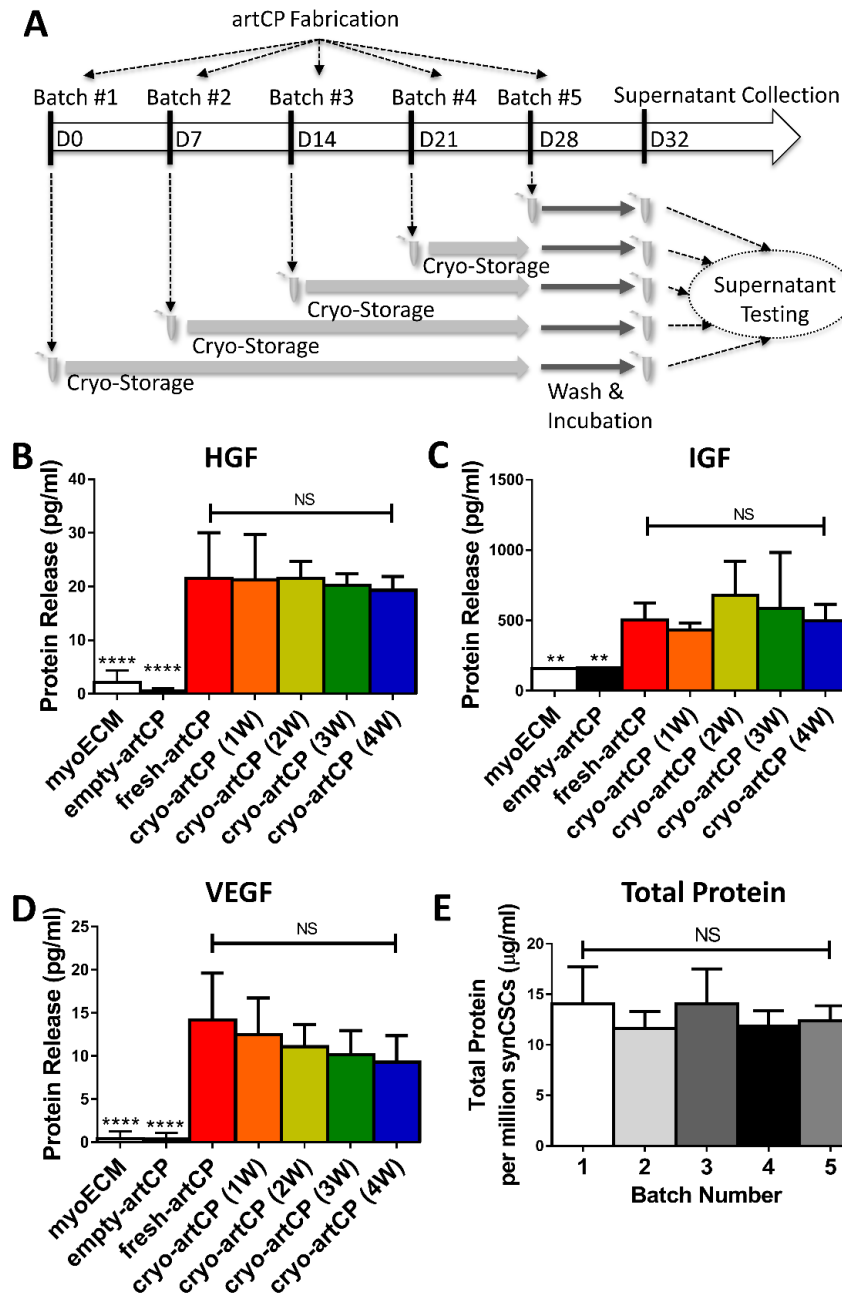
Fig 3. Cryo-stability of artCP. (A) Schematic showing the study design. Hepatocyte growth factor (HGF) (B), insulin-like growth factor (IGF) (C), and vascular endothelial growth factor (VEGF) (D) were analyzed by ELISA (n = 4). myoECM and empty-artCP (myoECM embedded with empty-synCSCs) were used as controls. (E) Total protein amounts in different synCSCs batches were measured by a BCA Protein Assay Kit (n=3 in each group). All data were means ± s.d. Comparisons among groups were performed using one-way ANOVA followed by *post hoc* Bonferroni test. NS indicated $P > 0.05$. "**" indicated $P < 0.01$, "****" indicated $P < 0.0001$.

4.4 Biodistribution of synCSCs and biocompatibility of artCPs

Sprague Dawley (SD) rats with acute MI were used for biodistribution studies. 24 hours after treatment, all groups of animals were euthanized, and major organs were collected for *ex vivo* fluorescent imaging. artCP effectively held synCSCs in the infarcted region with minimal off-target loss into other organs (Figs. S3A-C). Whereas, intramyocardial injected synCSC were "washed away" from the heart to other organs such as the lungs (Fig. S3C). These results were consistent with our previous study[34]. The off-target lung distribution was due to needle- caused vessel damage and the subsequent venous drainage[39]. To evaluate the biocompatibility of artCPs, an independent experiment was performed by transplanting artCPs onto the infarct heart of SD rats. The hearts were harvested for analysis of immune rejection on day 7 (Figs. S4A-C) and day 21(Fig. S4D) after transplantation. T cell and macrophage infiltrations were evaluated with CD3/CD8 and CD68 staining. artCP transplantation elicited negligible T-cell or macrophage infiltrations as the numbers of CD3$^+$/CD8$^+$ T cells or CD68$^+$ macrophages were detected in the heart.
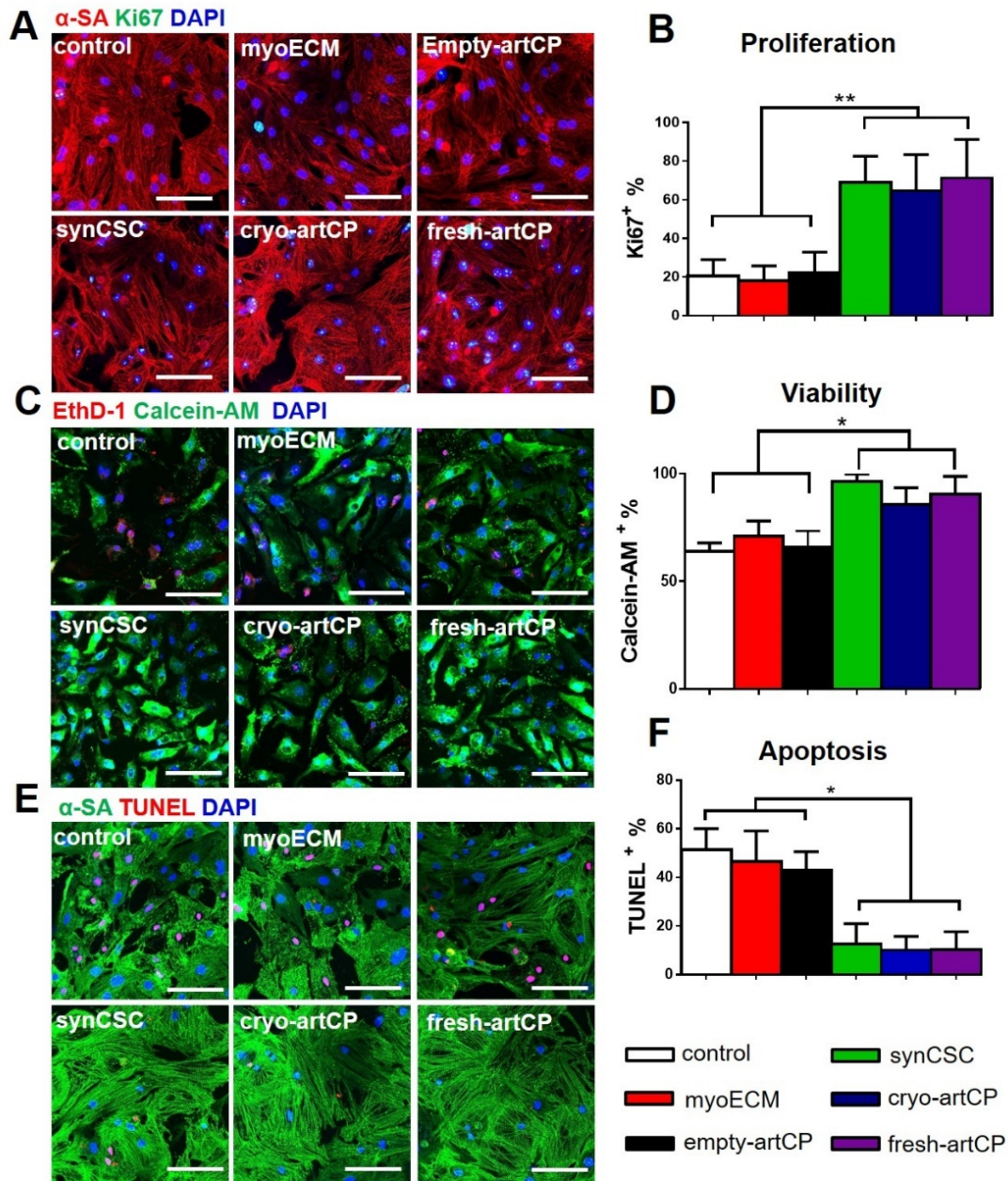
Fig 4. Effects of artCP on cardiomyocytes in vitro. (A) Representative fluorescent micrographs showing Ki67+ expression (green) in NRCMs. Scale bar = 50 μm. (B) Quantitation of Ki67+ cells. n=3 per group. (C) Live/Dead assay was used to determine the viability of NRCMs. Scale bar = 50 μm. (D) NRCM viability was measured using NIH Image J software. n=3 per group. (E) Cell apoptosis was detected based on TUNEL+ expression (red). Scale bar = 50 μm. (F) TUNEL+ NRCM percentage was determined with the NIH Image J software. n=3 per group. All data were means ± s.d. Comparisons among groups were performed using one-way ANOVA followed by *post hoc* Bonferroni test. The comparisons between samples were indicated by lines, and the statistical significance was indicated by asterisks above the lines. "*" indicated $P < 0.05$. "**" indicated $P < 0.01$.

4.5 artCP therapy in rats with acute MI

To test the therapeutic potency of artCP, we induced MI in SD rats by left anterior descending artery (LAD) ligation as previously described [41]. After LAD ligation was confirmed by color alteration of the LV, a circular piece of artCP (diameter =5 mm) containing $\sim 2\times10^6$ synCSCs was sutured onto the MI area. were myoECM control animals transplanted with a same sized empty myoECM patch without synCSCs embedded. Negative control animals did not receive any treatment after MI. All animals were sacrificed 21 days after the surgery and the hearts were harvested for histological analysis (Fig. 5A). The surgeon and the analyzer were blinded to the treatment administered. Echocardiography was performed before MI induction, 4 hours after the operation (baseline), and finally before the animals were euthanized on day 21(endpoint) (Fig. 5B). Left ventricular ejection fraction (LVEF) and fractional shortening (LVFS) before surgery and 4 hours after surgery were indistinguishable among all three groups indicating a uniform degree of background cardiac function and initial injury. 3 weeks after treatment, the hearts received artCP transplantation had the greatest LVEFs (Figs. 5C-F) and LVFSs (Figs. 5G-J) by preserving cardiac contraction capability (Fig. S5). Hematoxylin and eosin (H&E) staining revealed the structures of artCP and myoECM 3 weeks post transplantation (Fig. 6A). Cells residing in the structures were fibroblasts, smooth muscle cells and endothelial cells (Fig. S6). Masson's trichrome staining (Fig. 6B) revealed that artCP transplantation led to decrease in infarction size (Fig. 6C), increase in viable tissue in the risk area (Fig. 6D), and increase in LV wall thickness (Fig. 6E). Interestingly, we found a large size of viable cardiac tissue in the infarcted region that was covered by the artCP (Figs. 6A and B). Consistent with previous studies[33,40], empty myoECM transplantation also generated a certain degree of therapeutic effects. However, the embedding of synCSCs in the artCP further amplified the therapeutic benefits.

4.6 artCP's therapeutic effects are not affected by cryo-storage

We also performed an independent animal study to compare the therapeutic potency of cryo-stored artCPs to their freshly made counterparts. Immediately after MI induction, animals received transplantation of a fresh-artCP or a cryo-artCP (cryo-stored for 28 days). Animals received MI (but no treatment) or treatment of empty-artCP were used as controls. LVEFs and LVFSs were determined before MI, 4 hours after MI and three weeks afterwards (Figs. S7A-P). The LVEFs and LVFSs before MI and 4 hours after MI were indistinguishable among these groups, indicating a similar degree of initial injury (Figs. S7A and B). 28 days of cryo-storage did not affect the artCP's ability in protecting cardiac functions (Figs. S7A-P). In addition, infarct sizes were effectively reduced by either cryo- or fresh- artCP transplantation to a similar degree (Figs. S8A and B). Viable tissue in the risk area (Fig. S8C) and infarct wall thickness (Fig. S8D) were increased by both therapies. These results demonstrated the cryo-stability of artCP products. On day 21, the serum levels of alanine aminotransferase (ALT), aspartate aminotransferase (AST), creatinine, and blood urea nitrogen (BUN) (Fig. S9) were indistinguishable among all groups, indicating no toxicity from either cryo- or fresh- artCP transplantation.
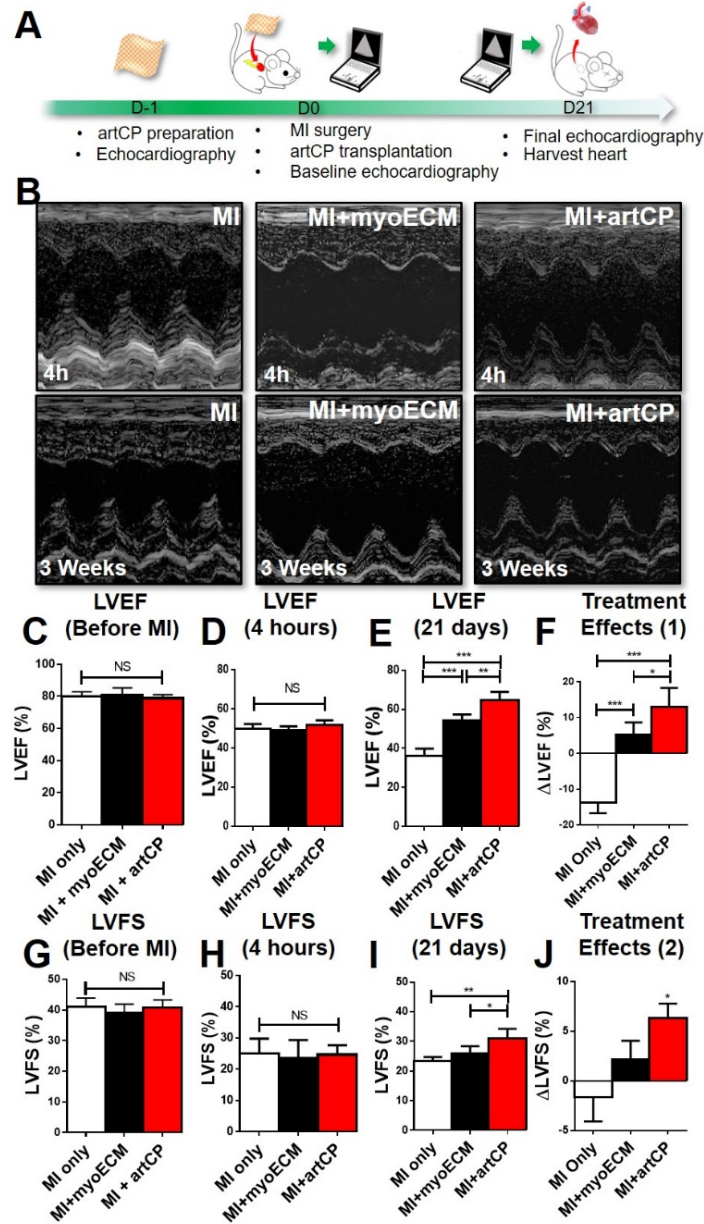
Fig 5. Transplantation of artCP in rats with MI. (A) Schematic showing the study design. Cardiac function was assessed before MI, 4 hours after MI (baseline) and 21 days after MI (endpoint). (B) Representative M-mode echocardiography images that shown at baseline and endpoint were taken from one random animal in each group. LVEF was analyzed before MI (C), 4hours after MI (D) and 21days after MI (E), and treatment effects were determined as the changes in LVEF (F). n=5 in each group. LVFS was also analyzed before MI (G), 4hours after MI (H) and 21days after MI (I), and treatment effects were calculated as well (J). n=5 in each group. All data were means ± s.d. Comparisons among groups were performed using one-way ANOVA followed by *post hoc* Bonferroni test. The comparisons between samples were indicated by lines, and the statistical significance was indicated by asterisks above the lines. NS indicated $P > 0.05$. "*" indicated $P < 0.05$. "**" indicated $P < 0.01$, "***" indicated $P < 0.001$.
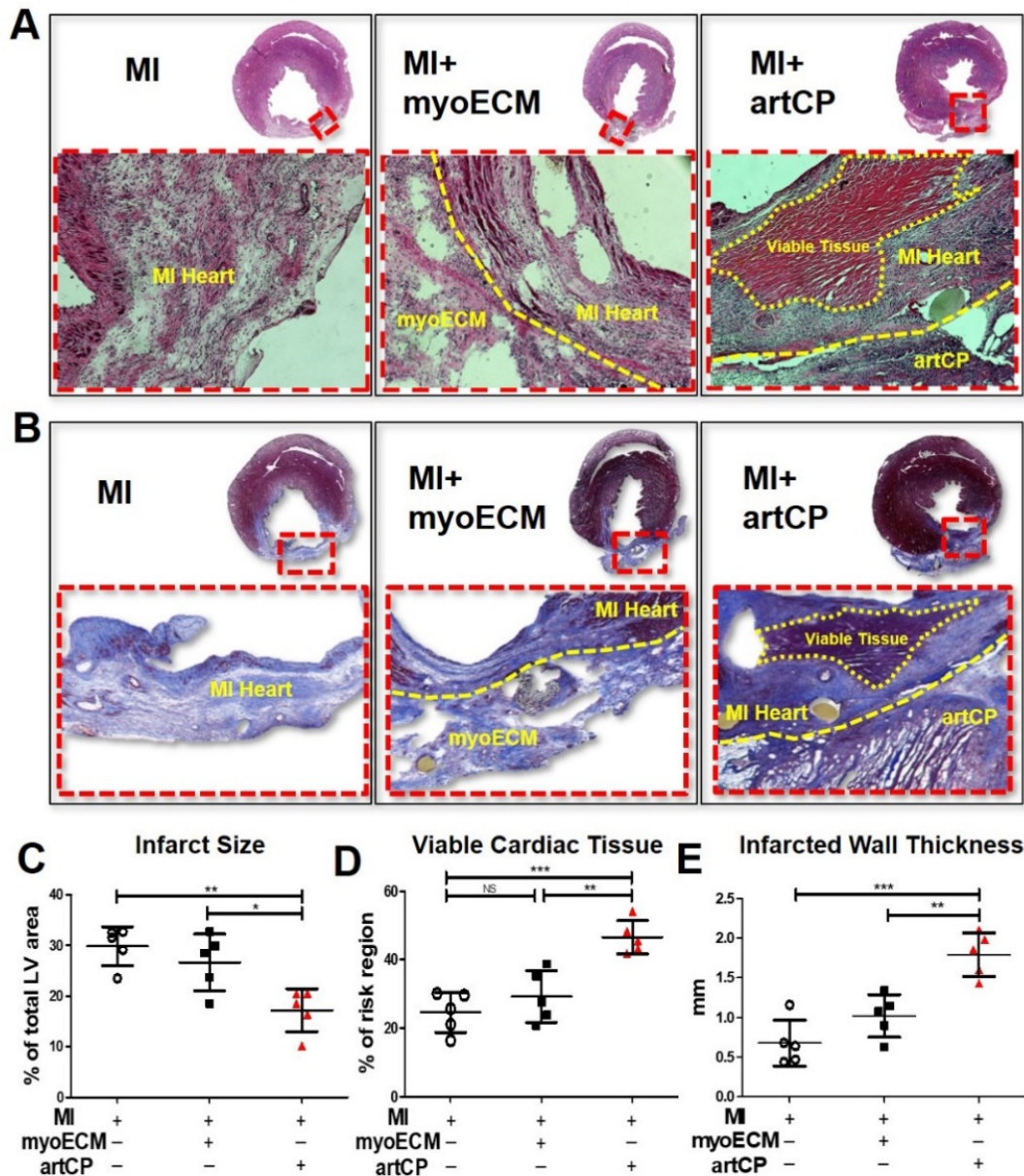
Fig 6. Heart morphometry was assessed through H&E and Masson's trichrome staining.
(A) H&E staining was performed with the thickness of 10 μm cryo-sections by using traditional methods and chemicals. (B) Masson's Trichrome staining was performed using HT15 Trichrome Staining (Masson) Kit on the thickness of 5 μm cryo-sections. Morphometric parameters including infarct size (C), the percentage of viable myocardium at risk area (D), and infarct wall thickness (E) were measured from the Masson's Trichrome stained slides *via* NIH ImageJ software. n=5 in each group. All data were means ± s.d. Comparisons among groups were performed using one-way ANOVA followed by *post hoc* Bonferroni test. The comparisons between samples were indicated by lines, and the statistical significance was indicated by asterisks above the lines. NS indicated $P > 0.05$. "*" indicated $P < 0.05$. "**" indicated $P < 0.01$, "***" indicated $P < 0.001$.

4.7 artCP therapy promotes angiomyogenesis in rats with MI

artCP transplantation increased capillary density in the infarct area (Figs. 7A and B). To further explore whether cardiac function improvement was accompanied by myocardial regeneration, three cell cycling markers were employed, including Ki67, phosphorylated histone H3 (pH3) and Aurora B kinase (Aurora B). The myocyte and non-myocyte localizations of these markers were confirmed by z-stack confocal imaging. The results indicated that Ki67$^+$ expressions in artCP-treated group were mostly overlaid with myocardium nuclei, whereas, the Ki67$^+$ expression in the other two groups were generally overlaid with non-myocyte nuclei (Figs. 7C and D). pH3$^+$ (Figs. 7E-G) and Aurora B$^+$ (Figs. S10A and B) staining confirmed the pro-proliferative effects of artCP therapy. TUNEL assay indicated that artCP transplantation significantly decreased cell apoptosis in the infarct border zone (Figs. S11A and B). The pro-regenerative and anti-apoptotic mechanisms of artCP therapy were confirmed by western blot analysis (Figs. S11C-F). Moreover, fresh or cryo-stored artCP therapy promoted angiomyogenesis (Fig. S12). Taken together, transplantation of cryo-stored or fresh artCPs strengthened angiomyogenesis but reduced cell apoptosis.

Fig 7. ArtCP treatment mechanism was explored through IHC staining. (A) Endothelial cell marker vWF (green) was detected in the heart infarcted area that interfaced with transplanted artCP or myoECM. Scale bar= 200 μm. (B) The pooled data of vWF$^+$ signal counting per high power field (HPF) was assessed by Image J software. n=5 in each group. (C) Ki67$^+$ expression (green) were detected on the infarct periphery. Scale bar = 50 μm. Scale bar zoomed snapshot =10 μm. (D) Ki67$^+$ expressed cells were counted per HPF through Image J software. n=5 in each group. (E) Phosphorylated histone H3 (pH3$^+$) expression signals (green) were also detected. Scale bar = 25 μm. Scale bar zoomed snapshot =10 μm. (F) pH3$^+$ cells and (G) pH3$^+$ cardiomyocytes were counted per HPF through Image J software. n=5 in each group. All data were means ± s.d. Comparisons among groups were performed using one-way ANOVA followed by *post hoc* Bonferroni test. The comparisons between samples were indicated by lines, and the statistical significance was indicated by asterisks above the lines. "*" indicated $P < 0.05$. "**" indicated $P < 0.01$, "***" indicated $P < 0.001$.

77

**Fig 8. Transplantation of artCP to porcine MI models.** (A) Schematic showing the study design. The representative pictures showing the porcine MI model creation *via* LAD ligation (left) and artCP transplantation (right). (B) Electrocardiography (ECG) was collected pre-MI, 24 hours and 7 days post-MI from 2 groups. MI was indicated by ST-segment elevation. (C) Serum cardiac troponin I (cTnI) was measured pre-MI, 24 hours and 7 days post-MI in each group of animals. n=3 in each group. (D) In the picture of the top left (MI control), the red circle indicated the area of infarction due to successful MI creation. Five sections (1cm in thickness) were cut from Apex to bottom. In the picture of the bottom left (artCP transplanted), the red circle indicated the artCP transplanted area. The right side of the picture showed TTC staining of 5 heart sections (from one heart) in MI only group (top right) and artCP treated group (bottom right). The white area in TTC stained heart sections indicated infarction. The position of artCP was outlined with green. (E) The infarction area percentage was measured in heart slice 2, 3 and 4 through image J software. n=3 in each group. All data were means ± s.d. Comparisons among groups were performed using one-way ANOVA followed by *post hoc* Bonferroni test. The comparisons between samples were indicated by lines, and the statistical significance was indicated by asterisks above the lines. (F) Masson's trichrome staining of the infarct periphery was performed to detect the myocardium integrity. Scale bar = 400 μm.

4.8 artCP therapy in a porcine model of MI

Despite the widespread use of rodent models for cardiovascular researches, the use of the porcine model is well-justified as the porcine heart has human-like myocardial blood flow, ventricular mechanics, and dimensions[41]. Porcine MI model was created in Yorkshire-pigs (female, 50-70 lbs) by open chest surgery and LAD ligation at distal to the 2nd diagonal branch (Fig. 8A). A piece of artCP (diameter = 3.5 cm) was transplanted onto the surface of the porcine heart to cover the MI area. Control animals did not receive any treatment. All animals were euthanized 7 days after treatment and the hearts were harvested for morphometry and histology studies. Blood samples and ECGs were collected pre-MI, 24 hours and 7 days post MI. Induction of MI was verified by the elevation of ST segment on ECG and increased cardiac troponin I (cTnI) level 24 hours post-MI (Figs. 8B and C). An interesting observation from the ECG is that control animals still had ST segment elevation at Day 7, while such abnormality disappeared in the artCP-treated animals (Fig. 8B). After the last echocardiography session, animals were sacrificed, and all hearts were collected and cryo-sectioned transversally (1 cm in thickness) from apex to bottom for triphenyltetrazolium chloride (TTC) staining. The infarcted size in each slice was quantified by Image J analysis. The macroscopic images from TTC staining suggested that the infarcted area of artCP-transplanted hearts was relatively smaller on Slice 1 and Slice 2 (Figs. 8D and E). Masson's trichrome staining revealed that artCP treatment reduced myocardial fibrosis at the microscopic level (Fig. 8F). Echocardiography data were collected at 24 hours (baseline) and 7 days post MI (endpoint) for cardinal function analysis (Figs. S13A-H). The result showed that artCP treatment significantly improved cardiac pump functions (Figs. S13A and B). Also, cardiac contractility (measured by LVFSs) was enhanced by artCP therapy (Figs. S13C and D). To assess the safety of artCP transplantation, liver and kidney functions were evaluated with blood samples from pre-MI,

24 hours post MI and 7 days post MI time points. The levels of alanine aminotransferase (ALT) and aspartate aminotransferase (AST) expressions were indistinguishable among all groups (Figs. S14A and B), indicating artCP transplantation did not alter liver functions. Furthermore, the blood creatinine and blood urea nitrogen (BUN) measurements indicate that artCP transplantation did not impact on kidney function (Figs. S14C and D). To address the immune reaction against the transplanted artCP, WBCs, PMNs, and lymphocytes were also quantified (Figs. S15A-D). No changes were detected in the artCP-treated animals. These results further proved that artCP was biocompatible in the porcine models. Interestingly, the reactive lymphocytes in artCP-treated animals were suppressed when compared to the nontreated group (Fig. S15D). Taken together, these results indicated the safety of artCP transplantation.

5. Discussion

As emerging new strategies in tissue engineering and regenerative medicine, cardiac patches [42-44] and stem cell therapy [13,45-47] have become the focus of multiple studies targeting myocardial tissue repair during the past decade. A cardiac patch normally involves spiking a scaffolding material with various types of stem cells[48-50]. In general, these patches rely on the added cells to impart functional benefits. However, as a living component, the cells also make the cardiac patch product vulnerable to ambient storage and shipping conditions [14]. One of our major questions remain: how do we make a therapeutic cardiac patch that is stable at room temperature and offer read-to-use convenience? The recent development in synthetic strategies provides some alternative solutions[34,35,51-53]. In the resent study, we embedded therapeutic synthetic cardiac stem cells (synCSCs) within decellularized myoECM to generate a fully acellular artificial cardiac patch (artCP). The artCP approach adopts a "particle in matrix" design harnessing the proven beneficial effects of synCSCs and myoECM: the synCSCs mimicks the therapeutic features of live stem cells

while overcoming their storage and survival problems; the myoECM preserves the extracellular matrix structures and bioactivity found within the native cardiac tissue.

We confirmed the unimpaired factor release capability of artCPs after 28 days of cryo-storage. The *in vitro* potency assay using cardiomyocytes confirmed that artCPs remained potent after at least 15 days of cryo-storage. The storage properties of artCP overcome an essential shortage of a conventional cardiac patches which traditionally need to be maintained under physiological conditions after preparation. If not stored and handled properly, traditional cardiac patches would suffer from the cell death within the patch rendering it noneffective or even lead to negative effects after transplantation. Additionally, the myoECM in artCP augments the cardiac retention of synCSCs further increasing their beneficial effects. In our previous work, synCSCs were directly injected into the myocardium[34] and, despite encouraging proof-of-concept results, suffered from significant loss of synCSCs to the lungs. This was confirmed by the present study. The artCP approach reinforced the retention of synCSCs on the heart and diminished their off-target biodistribution to other organs. On the other hand, the synCSCs release regenerative factors to the myopcardium, producing additional benefits on top of the myocardium-emulating structures of myoECM. Additionally, cryo-storage did not affect the therapeutic potency of artCP. In both rodent and porcine models of myocardial infarction, we demonstrated that transplantation of an artCP improved heart pump function, reduced fibrosis/infarct size, increased in viable myocardial tissue, and promoted angiomyogenesis.

Our study has several limitations. To reduce the injury associated with open-chest surgery, minimally invasive approaches of patch delivery needs to be developed in future iterations[54-56]. Also, further mechanistic studies on myocardium regenerative pathways[57-59] could help elucidate the modes of action of artCP therapies. Additionally, the length of factor releases and artCP

degradation need to be optimized to match the post-MI LV remodeling. Never the less, the present study shows the potential synergistic effects of using synCSCs with myoECM to provide an off-the-shelf cardiac patch with significant regenerative capacity.

6. References

1.   Benjamin, E. J. *et al. Heart Disease and Stroke Statistics'2017 Update: A Report from the American Heart Association. Circulation* **135,** (2017).

2.   Swynghedauw, B. Molecular mechanisms of myocardial remodeling. **79,** 215–262 (1999).

3.   Tompkins, B. A. *et al.* Preclinical Studies of Stem Cell Therapy for Heart Disease. *Circ. Res.* **122,** 1006–1020 (2018).

4.   Duelen, R. & Sampaolesi, M. Stem Cell Technology in Cardiac Regeneration: A Pluripotent Stem Cell Promise. *EBioMedicine* **16,** 30–40 (2017).

5.   Matsa, E., Burridge, P. W. & Wu, J. C. Human Stem Cells for Modeling Heart Disease and for Drug Discovery. *Sci. Transl. Med.* **6,** 239ps6 LP-239ps6 (2014).

6.   Hodgkinson, C. P., Bareja, A., Gomez, J. A. & Dzau, V. J. Emerging Concepts in Paracrine Mechanisms in Regenerative Cardiovascular Medicine and Biology. *Circ. Res.* **118,** 95–107 (2016).

7.   Walter, J., Ware, L. B. & Matthay, M. A. Mesenchymal stem cells: Mechanisms of potential therapeutic benefit in ARDS and sepsis. *Lancet Respir. Med.* **2,** 1016–1026 (2014).

8.   Giacomo Lanzoni, Tsunekazu Oikawa, Yunfang Wang, Cai-Bin Cui, Guido Carpino, Vincenzo Cardinale, David Gerber, Mara Gabriel, Juan Dominguez-Bendala, Mark E. Furth, Eugenio Gaudio, Domenico Alvaro, Luca Inverardi, Lola M. Reid. Clinical programs of stem cell therapies for liver and pancreas. *Stem Cells* **31,** 1–28 (2013).

9.   Yucai Xiea, b, Ahmed Ibrahima, Ke Chenga, Zhijun Wub, Wenbin Lianga, Konstantinos Malliarasa, Baiming Suna, Weixin Liua, Deliang Shena, c, Hee Cheol Choa, Taosheng Lia, L. & Lub, Guoping Lub, and E. M. Importance of cell-cell contact in the therapeutic benefits of cardiosphere-derived cells. **32,** 2397–2406 (2014).

10. Makkar, R. R. *et al.* Intracoronary cardiosphere-derived cells for heart regeneration after myocardial infarction (CADUCEUS): A prospective, randomised phase 1 trial. *Lancet* **379,** 895–904 (2012).

11. R. Bolli, A. R. Chugh, D. D' Amario, J. H. Loughran, M. F. Stoddard, S. Ikram, G. M. Beache, S. G. Wagner, A. Leri, T. Hosoda, J. B. Elmore, P. Goihberg, D. Cappetta, N. K. Solankhi, I. Fahsah, D. G. Rokosh, M. S. Slaughter, J. Kajstura, P. A. Effect of cardiac stem cells in patients with ischemic cardiomyopathy: initial results of the SCIPIO Trial. *Can. J. Cardiol.* **378,** 1847–1857 (2011).

12. Konstantinos Malliaras, MD*, Raj R. Makkar, MD*, Rachel R. Smith, PhD*, Ke Cheng, PhD*, Edwin Wu, MD†, Robert O. Bonow, MD†, Linda Marbán, PhD*, Adam Mendizabal, MS‡, Eugenio Cingolani, MD*, Peter V. Johnston, MD§, Gary Gerstenblith, MD§, Karl H. Schuleri, P. Intracoronary Cardiosphere-Derived Cells After Myocardial Infarction: Evidence of Therapeutic Regeneration in the Final 1-Year Results of the CADUCEUS Trial Konstantinos. *J Am Coll Cardiol.* **63,** 110–122 (2014).

13. Cheng, K. *et al.* Relative Roles of CD90 and c-Kit to the Regenerative Efficacy of Cardiosphere-Derived Cells in Humans and in a Mouse Model of Myocardial Infarction. *J. Am. Heart Assoc.* **3,** e001260–e001260 (2014).

14. Tang, J.-N. *et al.* Concise Review: Is Cardiac Cell Therapy Dead? Embarrassing Trial Outcomes and New Directions for the Future. *Stem Cells Transl. Med.* 354–359 (2018). doi:10.1002/sctm.17-0196

15. Kruse, C., Danner, S. & Rapoport, D. H. Current stem cell technology: Limitations and realistic expectations. *Eng. Life Sci.* **8,** 13–18 (2008).

16. Lim, J. M., Lee, M., Lee, E. J., Gong, S. P. & Lee, S. T. Stem cell engineering: Limitation,

alternatives, and insight. *Ann. N. Y. Acad. Sci.* **1229,** 89–98 (2011).

17.   Strobel J, Brenner L, Zimmermann R, Weiss D, Zingsem J, Eckstein R, W. V. Influence of Duration and Temperature of Transport and Storage Prior to Processing on Cell Quality of Cord Blood Units--A German. Experience. *Clin Lab.* **61,** 1453–61 (2015).

18.   Herberts, C. A., Kwa, M. S. G. & Hermsen, H. P. H. Risk factors in the development of stem cell therapy. *J. Transl. Med.* **9,** 29 (2011).

19.   Chabannon, C. *et al.* Hematopoietic stem cell transplantation in its 60s: A platform for cellular therapies. *Sci. Transl. Med.* **10,** (2018).

20.   Zeng, L. *et al.* Bioenergetic and functional consequences of bone marrow-derived multipotent progenitor cell transplantation in hearts with postinfarction left ventricular remodeling. *Circulation* **115,** 1866–1875 (2007).

21.   Hong, K. U. *et al.* A highly sensitive and accurate method to quantify absolute numbers of c-kit+ cardiac stem cells following transplantation in mice. *Basic Res. Cardiol.* **108,** 346 (2013).

22.   Cambria, E. *et al.* Translational cardiac stem cell therapy: advancing from first-generation to next-generation cell types. *npj Regen. Med.* **2,** 17 (2017).

23.   John V. Terrovitis, Rachel Ruckdeschel Smith, and E. M. Assessment and Optimization of Cell Engraftment after Transplantation into the Heart. **31,** 1713–1723 (2013).

24.   Blocklet, D. *et al.* Myocardial homing of nonmobilized peripheral-blood CD34+ cells after intracoronary injection. *Stem Cells* **24,** 333–336 (2006).

25.   Doyle, B. *et al.* Dynamic Tracking During Intracoronary Injection of 18F-FDG-Labeled Progenitor Cell Therapy for Acute Myocardial Infarction. *J. Nucl. Med.* **48,** 1708–1714 (2007).

26. Feiner, R. *et al.* Engineered hybrid cardiac patches with multifunctional electronics for online monitoring and regulation of tissue function. *Nat. Mater.* **15,** 679–685 (2016).

27. Gaetani, R. *et al.* Epicardial application of cardiac progenitor cells in a 3D-printed gelatin/hyaluronic acid patch preserves cardiac function after myocardial infarction. *Biomaterials* **61,** 339–348 (2015).

28. Wang, Q. *et al.* Functional engineered human cardiac patches prepared from nature's platform improve heart function after acute myocardial infarction. *Biomaterials* **105,** 52–65 (2016).

29. Gao, L. *et al.* Myocardial Tissue Engineering With Cells Derived from Human Induced-Pluripotent Stem Cells and a Native-Like, High-Resolution, 3-Dimensionally Printed Scaffold. *Circ. Res.* (2017).

30. Weinberger, F. *et al.* Cardiac repair in guinea pigs with human engineered heart tissue from induced pluripotent stem cells. *Sci. Transl. Med.* **8,** 363ra148 LP-363ra148 (2016).

31. Schaefer, J. A., Guzman, P. A., Riemenschneider, S. B., Kamp, T. J. & Tranquillo, R. T. A cardiac patch from aligned microvessel and cardiomyocyte patches. *J. Tissue Eng. Regen. Med.* **12,** 546–556 (2018).

32. Tang, J. *et al.* Cardiac cell–integrated microneedle patch for treating myocardial infarction. *Sci. Adv.* **4,** eaat9365 (2018).

33. Pacelli, S. *et al.* Strategies to develop endogenous stem cell-recruiting bioactive materials for tissue repair and regeneration. *Adv. Drug Deliv. Rev.* **120,** 50–70 (2017).

34. Tang, J. *et al.* Therapeutic microparticles functionalized with biomimetic cardiac stem cell membranes and secretome. *Nat. Commun.* **8,** 1–9 (2017).

35. Luo, L. *et al.* Fabrication of Synthetic Mesenchymal Stem Cells for the Treatment of Acute

Myocardial Infarction in Mice. *Circ. Res.* **120,** 1768–1775 (2017).

36. Donald O Freytes, John D O'Neill, Yi Duan-Arnold, Emily Wrona, and G. V.-N. Native Cardiac Extracellular Matrix Hydrogels for Cultivation of Human Stem Cell-Derived Cardiomyocytes. *Methods Mol Biol.* **1181,** 69–81. (2014).

37. Su, T. *et al.* Platelet-Inspired Nanocells for Targeted Heart Repair After Ischemia/Reperfusion Injury. *Adv. Funct. Mater.* **29,** 1803567 (2019).

38. Vandergriff, A. C., Hensley, M. T. & Cheng, K. Isolation and Cryopreservation of Neonatal Rat Cardiomyocytes. *J. Vis. Exp.* 1–7 (2015). doi:10.3791/52726

39. Al Kindi A, Ge Y, Shum-Tim D, C. R. Cellular cardiomyoplasty: routes of cell delivery and retention. *Front Biosci.* **1,** 2421–34 (2008).

40. Sarig, U. *et al.* Natural myocardial ECM patch drives cardiac progenitor based restoration even after scarring. *Acta Biomater.* **44,** 209–220 (2016).

41. Koudstaal, S. *et al.* Myocardial Infarction and Functional Outcome Assessment in Pigs. *J. Vis. Exp.* 1–10 (2014). doi:10.3791/51269

42. Lakshmanan, R., Kumaraswamy, P., Krishnan, U. M. & Sethuraman, S. Engineering a growth factor embedded nanofiber matrix niche to promote vascularization for functional cardiac regeneration. *Biomaterials* **97,** 176–195 (2016).

43. Tang, J. *et al.* A Regenerative Cardiac Patch Formed by Spray Painting of Biomaterials onto the Heart. *Tissue Eng. Part C Methods* **23,** 146–155 (2017).

44. Santiago, R. *et al.* Postinfarction Functional Recovery Driven by a Three-Dimensional Engineered Fibrin Patch Composed of Human Umbilical Cord Blood-Derived Mesenchymal Stem Cells. *Stem Cells Transl. Med.* **4,** 956–966 (2015).

45. Sharp, T. E. *et al.* Cortical Bone Stem Cell Therapy Preserves Cardiac Structure and

Function After Myocardial Infarction. *Circ. Res.* **121,** 1263–1278 (2017).

46.   Hensley, M. T. *et al.* Cardiac regenerative potential of cardiosphere-derived cells from adult dog hearts. *J. Cell. Mol. Med.* **19,** 1805–1813 (2015).

47.   Ma, Y. & Wang, B. Co-injection basic fibroblast growth factor for adipose derived stem cells transplantation: Improved cardiac remodelling and function of myocardial infarction. *J. Am. Coll. Cardiol.* **63,** S44 (2014).

48.   Ye, L. *et al.* Cardiac repair in a porcine model of acute myocardial infarction with human induced pluripotent stem cell-derived cardiovascular cell populations. *Cell Stem Cell* **15,** 750–761 (2014).

49.   Chen, Y. Y. & Smolke, C. D. From DNA to Targeted Therapeutics: Bringing Synthetic Biology to the Clinic. *Sci. Transl. Med.* **3,** 106ps42 LP-106ps42 (2011).

50.   Booth, M. J., Schild, V. R., Graham, A. D., Olof, S. N. & Bayley, H. Light-activated communication in synthetic tissues. *Sci. Adv.* **2,** (2016).

51.   D. Shen, J. Tang, M. T. Hensley, T. Li, T. G. Caranasos, T. Zhang, K. C. Effects of Matrix Metalloproteinases on the Performance of Platelet Fibrin Gel Spiked With Cardiac Stem Cells in Heart Repair. *Stem Cells Transl. Med.* **5,** 793–803 (2016).

52.   Shadrin, I. Y. *et al.* Cardiopatch platform enables maturation and scale-up of human pluripotent stem cell-derived engineered heart tissues. *Nat. Commun.* **8,** 1825 (2017).

53.   Yuan, X. *et al.* Stem cell delivery in tissue-specific hydrogel enabled meniscal repair in an orthotopic rat model. *Biomaterials* **132,** 59–71 (2017).

54.   Montgomery, M. *et al.* Flexible shape-memory scaffold for minimally invasive delivery of functional tissues. *Nat. Mater.* **16,** 1038 (2017).

55.   Miragoli, M. *et al.* Inhalation of peptide-loaded nanoparticles improves heart failure. *Sci.*

Transl. Med. **10,** (2018).

56. Annabi, N. *et al.* Engineering a highly elastic human protein–based sealant for surgical applications. *Sci. Transl. Med.* **9,** (2017).

57. Zhu, W., Zhao, M., Mattapally, S., Chen, S. & Zhang, J. CCND2 Overexpression Enhances the Regenerative Potency of Human Induced Pluripotent Stem Cell-Derived Cardiomyocytes: Remuscularization of Injured Ventricle. *Circ. Res.* (2017).

58. Ceholski, D. K. *et al.* CXCR4 and CXCR7 play distinct roles in cardiac lineage specification and pharmacologic β-adrenergic response. *Stem Cell Res.* **23,** 77–86 (2017).

59. Bylund, J. B. *et al.* Coordinated Proliferation and Differentiation of Human-Induced Pluripotent Stem Cell-Derived Cardiac Progenitor Cells Depend on Bone Morphogenetic Protein Signaling Regulation by GREMLIN 2. *Stem Cells Dev.* **26,** 678–693 (2017).

CHAPTER 3. Platelet-Inspired Nano-Cells for Targeted Heart Repair After Ischemia/Reperfusion Injury

1. Abstract

Cardiovascular disease is the leading cause of mortality in the world. While reperfusion therapy is vital for patient survival post-heart attack, it also causes further tissue injury, known as myocardial ischemia/reperfusion (I/R) injury in clinical practice. Exploring ways to attenuate I/R injury is of clinical interest for improving post-ischemic recovery. A platelet-inspired nano-cell (PINC) that incorporates both prostaglandin E2 (PGE_2)-modified platelet membrane and cardiac stromal cell-secreted factors to target the heart after I/R injury is introduced. By taking advantage of the natural infarct-homing ability of platelet membrane and the overexpression of PGE_2 receptors in the pathological cardiac microenvironment after I/R injury, the PINCs can achieve targeted delivery of therapeutic payload to the injured heart. Furthermore, a synergistic treatment efficacy can be achieved by PINC, which combines the paracrine mechanism of stem cell therapy with the PGE_2/EP receptor signaling that is involved in the repair and regeneration of multiple tissues. In a mouse model of myocardial I/R injury, intravenous injection of PINCs results in augmented cardiac function and mitigated heart remodeling, which is accompanied by the increase in cycling cardiomyocytes, activation of endogenous stem/progenitor cells, and promotion of

angiogenesis. This approach represents a promising therapeutic delivery platform for treating I/R injury.

2. Introduction

Cardiovascular disease is the leading cause of mortality globally, accounting for over 17.3 million deaths each year. Coronary heart disease, including myocardial infarction (commonly known as heart attack), angina (chest pain), and cardiac arrest, contributes to at least 50% of deaths[1]. Coronary artery obstruction produces myocardial ischemia, which is usually treated with reperfusion therapy. While reperfusion of ischemic tissue is vital for survival, it also initiates myocardial ischemia/reperfusion (I/R) injury comprising oxidative damage, cell death, and a profound inflammatory immune response, which currently lacks an effective clinical therapy[2].

In the past decade, the potential of using stem cells, including mesenchymal stem cells (MSCs), resident cardiac stem/ stromal cells (CSCs), and induced pluripotent stem cells (iPSCs) for cardiac regenerative therapy has generated immense interest[3]. Numerous studies indicate that adult stem cells such as MSCs and CSCs have very limited, if any, ability to differentiate into cardiomyocytes. Those cells exert their functional benefits mainly through paracrine effects, i.e., secreted factors from stem cells promote cardiac regeneration and inhibit fibrosis and inflammation. However, cell therapy suffers from several limitations, such as low cellular retention and survival in the ischemic myocardium, special precautions needed during cryopreservation, and easy entrapment in the lung during intravenous delivery due to the cell size[4,5].

Nanotechnology holds great promise to revolutionize cardiovascular therapy. In recent years, the development of nanoparticles for active targeting the heart after ischemic injury is receiving increasing attention[6-8]. The enhanced permeability and retention effect of the leaky vasculature in the infarcted heart has been commonly used for designing targeted nanoparticles,

although these nanoparticles are limited by rapid clearance within a few hours to days[7]. A recently reported matrix metalloproteinase (MMP)-responsive nanoparticle showed successful retention in the infarcted heart for up to 28 days[8]. Yet, the therapeutic efficacy of these nanoparticle systems in protecting the heart from I/R injury still remains elusive.

Recently, cell membrane-coated nanoparticles have emerged as a novel platform that can successfully combine the functionalities of various types of cells[9-14]. We previously reported that fusing platelet-derived nanovesicles onto the surface of CSCs boosts the infarct-targeting ability and functional outcomes of CSCs in rats and pigs with myocardial infarction[15]. We also fabricated therapeutic cell-mimicking microparticles by encasing CSC- or MSC-secreted factors in a biodegradable and biocompatible poly (lactic-co-glycolic acid) (PLGA) shell coated with cell membranes and tested their regenerative potential in a rodent model of heart injury[16,17]. Prostaglandin E2 (PGE$_2$) is an FDA-approved medication (known as dinoprostone) that participates in many biological pathways. PGE$_2$ exerts its physiologic effects *via* four subtypes of receptors (EPs), i.e., EP1, EP2, EP3, and EP4, among which EP2, EP3, and EP4 are overexpressed on the surface of cardiomyocytes following I/R injury[18,19]. Recent studies have identified PGE$_2$ as an important signaling molecule that activates endogenous stem/progenitor cells for cardiac repair post-ischemic injury[20].

Based on those concepts, we designed a platelet-inspired nano-cell (PINC) that has a CSC core and a platelet membrane shell. The CSC core consists of therapeutic CSC secretome encapsulated in a PLGA nanoparticle. PLGA has been widely used in drug delivery system due to its capability of protecting growth factors from degradation while allowing for sustained release of growth factors and has been approved by the U. S. Food and Drug Administration for clinical applications[16]. In addition, recent studies showed that CSC secretome exhibited therapeutic

benefits similar to CSCs for the treatment of cardiovascular disease[17,21-23]. The platelet membrane is conjugated with PGE_2 which is expected to both enhance targeting to cardiovascular cells and facilitate the endogenous repair through PGE_2/EP receptor signaling after I/R injury (Fig. 1A). As a novel biomimetic therapeutic nanoparticle, PINC offers the following advantages compared to natural stem cells: (i) Systemic administration: the nanometer size of PINC enables intravenous application; unlike stem cells, PINCs are less likely to clog the lungs; (ii) Dual targeting: the platelet membrane on PINCs enhances targeting to the injured blood vessels while the PGE_2 enhances targeting to the injured cardiomyocytes in I/R injury; (iii) Stability: unlike real stem cells, PINCs can be readily manipulated and cryopreserved since there are no living components.

In this study, we fabricated PINCs and tested their *in vitro* bioactivity, biodistribution, and functional benefits in an immunocompetent mouse model of myocardial I/R injury.

3. Experimental Section

3.1 Materials

All chemical reagents were purchased from Sigma-Aldrich or Thermo Fisher Scientific and were used as received unless specifically noted.

3.2 Preparation of CSC Secretome-loaded PLGA Nanoparticles (NCs)

Human CSCs were derived from donor human hearts according to the previously published method[17]. Heart tissues from patients 2 – 4 weeks after myocardial infarction (with LVEF of 25 – 45%) were used. All procedures were approved by the institutional review board and written informed consent was obtained from all patients. The CSCs were used at passage 2 – 4. Briefly, the CSCs were cultured in serum-free media for 3 days and then the supernatant was collected to harvest conditioned media. The collected conditioned media was filtered through a 0.22 μM filter into a sterile 50 mL conical to remove any cell debris and contaminants. Sterile conditioned media

was then lyophilized by a LABCONCO FreeZone 2.5 Liter Freeze Dry System to produce the purified CSC secretome. The CSC secretome-loaded PLGA cores were fabricated through a double emulsion method followed by membrane extrusion. In brief, concentrated CSC secretome aqueous solution was prepared as the internal aqueous phase in polyvinyl alcohol (PVA, MW: 30000 ~ 50000, 0.1% w/v), and then injected into DCM containing PLGA (MW: 7000 ~ 17000) as the oil phase. The whole content was sonicated on ice for emulsification using a Misonix XL2020 sonicator. Afterward, the emulsion was immediately transferred into water containing 0.7% (w/v) PVA. The secondary emulsion was emulsified again to produce the final water/oil/water PLGA nanoparticle emulsion. The w/o/w emulsion was continuously stirred overnight to promote solvent evaporation. The nanoparticles were then sequentially extruded 19 times through polycarbonate membranes with pore sizes of 400 and 200 nm, respectively, using an extruder (Avanti Polar Lipids, USA). To determine the secretome loading capacity and efficiency, the nanoparticles were pelleted by centrifugation at 20000 × g and then the non-encapsulated amount of secretome in the supernatant was measured using a BCA protein assay.

3.3 Isolation of Platelet Membrane

The platelet membrane was isolated from human platelet-rich plasma (PRP, ZenBio, USA) through gradient centrifugation as previously described with modification[15]. Briefly, the PRP was centrifuged at 100 × g for 20 mins. PBS (1 ×, pH 7.4) containing 1 mM of ethylenediaminetetraacetic acid and 2 μM of prostaglandin E1 was added to keep platelets inactivated. The isolated platelets were then pelleted by centrifugation at 800 × g for 20 mins at room temperature. The platelet membrane was obtained by three freeze-thaw cycles, followed by sonication. The protein content in the purified platelet membrane was determined by the BCA protein assay for further preparation of PINCs.

3.4 Preparation of PGE$_2$-Platelet Membrane Conjugate

PGE$_2$-platelet membrane conjugate was synthesized using EDC/NHS coupling chemistry. Briefly, PGE$_2$ (0.52 μg, 1.5 nmol) dissolved in anhydrous ethanol was reacted with EDC (58 μg, 0.37 μmol) and NHS (14 μg, 0.12 μmol) in 15 mL 2-(4-Morpholino) ethane sulfonic acid (MES) buffer (100 mM, pH 6.0). After 30 min of carboxylate activation, platelet membrane containing 0.36 mg protein was added. The pH of the reaction mixture was adjusted to 7.2 by the addition of 1 M sodium bicarbonate. The mixture was stirred overnight at room temperature. The resulting product was dialyzed (MWCO 1000) for 24 h against PBS. The amount of unconjugated PGE$_2$ was measured by ELISA (R&D Systems, USA) to determine the conjugation yield and the content of PGE$_2$ conjugated to the PGE$_2$-platelet membrane conjugate.

3.5 Fabrication and Characterization of PINCs

To cloak the platelet membrane or PGE$_2$-platelet membrane conjugate onto the surface of CSC secretome-loaded NCs, 0.5 mL of NCs (5×10^9 particles mL^{-1}) were incubate with 0.5 mL of platelet membrane or PGE$_2$-platelet membrane conjugate containing 0.36 mg membrane protein under ultrasonication for 5 min, and then extruded 19 times as previously described to prepare the PINCs. The CS-PGE$_2$-PINCs were prepared *via* coating the PGE$_2$-platelet membrane conjugate on the surface of NCs. The CS-PINCs were prepared *via* coating the platelet membrane on the surface of NCs while the PGE$_2$-PINCs were prepared *via* coating the PGE$_2$-platelet membrane conjugate on the surface of empty PLGA nanoparticles. A BCA-based protein assay was performed to estimate the membrane coating efficiency and the amount of membrane protein coated onto each PLGA nanoparticle. Briefly, 0.5 mL of platelet membrane solution containing 0.36 mg membrane protein was mixed with 0.5 mL of empty PLGA nanoparticles (5×10^9 particles mL^{-1}) to fabricate the membrane-coated nanoparticles. After pelleting the membrane-coated nanoparticles from the

remaining free platelet membrane by centrifugation at $20000 \times g$, the amount of membrane protein in the remaining solution was measured using a BCA protein assay. The membrane coating efficiency was determined by comparing the difference between the amount of total platelet membrane protein before the membrane coating and that of the remaining free platelet membrane. The pelleted nanoparticles were then resuspended back to their original volume, followed by examination using NanoSight NS300 to determine the total number of membrane-coated nanoparticles for calculating the amount of membrane protein coated onto each PLGA nanoparticle.

3.6 Physicochemical Characterization

Nanoparticle size and surface zeta potential were measured by dynamic light scattering (DLS) using a Malvern ZEN 3600 Zetasizer. Nanoparticle concentration was examined by NanoSight NS300. The nanoparticle structure was visualized using a JEOL JEM-2000FX transmission electron microscope after negative staining with vanadium (Abcam). To assess the stability of the different nanoformulations over time, the bare NCs, CS-PINCs, PGE_2-PINCs, and CS-PGE_2-PINCs were suspended in PBS ($1 \times$, pH 7.4) at a concentration of 10^9 particles mL^{-1}. The change of particle size was measured by DLS at pre-determined time-points over the course of 2 weeks. To evaluate the stability in serum, the different nanoformulations were incubated with 50% fetal bovine serum (Hyclone, USA). The change of particle sizes within 4 h was determined by DLS. Long-term stability was assessed by the particle size change measured by DLS before lyophilization in 10 wt% sucrose and after resuspension in PBS ($1 \times$, pH 7.4) back to the original volume. SDS-PAGE was performed to examine the protein components of the platelet membrane and the different PINCs. Western blotting was performed to assess the presence of specific platelet membrane markers using rabbit anti-human CD42b (Santa Cruz, sc-292722) and rabbit anti-

human CD36 (Santa Cruz, sc-9154) antibodies, respectively, along with a goat anti-rabbit HRP-conjugated secondary antibody.

3.7 Collagen Surface Binding Assay

GFP-tagged HUVECs (Angio-Proteomie, USA) were seeded on collagen-coated 4-well culture chamber slides and cultured for 24 h. The cells were then incubated with DiI-labeled CS-PGE$_2$-PINCs in PBS (1 ×, pH 7.4) at 4 °C for 60 s. Then the cells were washed with PBS twice. Images were taken on an Olympus IX81 fluorescent microscope and analyzed using NIH ImageJ software.

3.8 Growth Factor Release Study

Total protein and growth factor release from PINCs were determined as previously described[16][17]. In brief, freeze-dried PINCs were dissolved in DCM. After that, PBS was added to the solution. The sample was subjected to vortex for 5 min to isolate proteins from the oil phase to the water phase. After centrifugation, the protein concentration in the water phase was measured by BCA protein assay. For growth factor release studies, nanoparticles were incubated in PBS at 37°C. The supernatant was collected at various time points (day 3, 7, 11, 14) after centrifugation at 20000 × g for 30 min to pellet the nanoparticles. The concentrations of various growth factors were measured using ELISA kits (R&D Systems, USA) according to the manufacturer's instructions. The data were averaged from three independent measurements.

3.9 Cell Viability and Proliferation Assay

The H9c2 cardiomyoblasts derived from embryonic rat heart (Sigma-Aldrich) were incubated with different concentrations of PINCs. PBS (1 ×, pH 7.4) was used as a control, the cell viability and proliferation were assessed by using a Cell Counting Kit-8 (CCK-8) according to the manufacturer's instructions.

3.10 NRCM Uptake Assay

NRCMs were derived from SD rats and cultured on 4-well chamber slides for 3 days, followed by co-incubation with DiI-labeled CS-PINCs or CS-PGE$_2$-PINCs (1.5×10^9 particles mL^{-1}) in an incubator for 3 h. The beating cardiomyocytes were counted under a white-light microscope. Then, the cells were washed with PBS twice, fixed, permeabilized, and stained for α-sarcomeric actinin (α-SA, 1:200, ab9465, Abcam), followed by DAPI staining for nucleus visualization. For assessment of cell apoptosis, the cells were cocultured with CS-PINCs or CS-PGE$_2$-PINCs (1.5×10^9 particles mL^{-1}) for 48 h. Subsequently, the cells were washed with PBS twice and then exposed to serum-free medium supplemented with hydrogen peroxide (250 µM) for 3 h, followed by incubated with TUNEL solution (Roche Diagnostics GmbH, Germany) and counter-stained with DAPI. Images were taken using a Zeiss LSM 710 confocal microscope (Carl Zeiss, Germany) and analyzed using NIH ImageJ software.

3.11 Mouse Model of Myocardial I/R Injury

All animal work was compliant with the Institutional Animal Care and Use Committee (IACUC) of the University of North Carolina at Chapel Hill and North Carolina State University. Briefly, female immunocompetent CD1 mice (8–10 weeks old, Charles River Laboratories) were anesthetized with an intraperitoneal injection of ketamine (100 mg kg^{-1} mouse) plus xylazine (10 mg kg^{-1} mouse). Under sterile condition, the heart was exposed by a left thoracotomy and a 30-min ischemia was achieved by temporal ligation of the left anterior descending coronary artery. After 24 h of reperfusion, animals were randomized to receive intravenous injection of CS-PINCs (CS dose: 1.2 mg kg^{-1} mouse), PGE$_2$-PINCs (PGE$_2$ dose: 0.053 mg kg^{-1} mouse), CS-PGE$_2$-PINCs (CS dose: 1.2 mg kg^{-1} mouse, PGE$_2$ dose: 0.053 mg kg^{-1} mouse), and saline (control) every 7 days for 4 weeks, respectively. Therefore, there were total 4 injections in 4 weeks.

3.12 *In Vivo* Targeting Ability Study

Immunocompetent CD1 mice with myocardial I/R injury were randomized into 2 groups (n = 3 per group) to receive intravenous injections with DiR-labeled NCs or CS-PGE$_2$-PINCs (CS dose: 1.2 mg kg^{-1} mouse, PGE$_2$ dose: 0.053 mg kg^{-1} mouse) every 7 days for 2 weeks. After that, the mice were euthanized and the major organs (heart, lung, liver, kidney, spleen) were carefully collected. The fluorescence signals of each organ were recorded using an IVIS Spectrum imaging system (Caliper Lifesciences, USA) for quantification. For HPLC analysis, the major organs were harvested after 2 weeks from the mice treated with DiI-labeled NCs or CS-PGE$_2$-PINCs. The organs were washed with PBS, dried, and then minced into small pieces using a surgical scalpel and weighted prior to homogenization. The homogenized samples were thoroughly mixed with 500 µL of chloroform/methanol (1:1, v/v) for fluorescent dye extraction. After 10-min ultrasonication and 3 freeze-thaw cycles, the samples were centrifuged at 14000 × g for 30 min and the supernatants containing the extracted fluorescent dye were subjected to HPLC analysis. All chromatographic experiments were conducted using an Agilent 1290 Infinity system (Agilent, USA) equipped with an Agilent 1290 diode array detector set to an excitation wavelength of 210 nm and an emission wavelength of 551 nm. The retention data were recorded at 20°C using a Zorbax Eclipse XDB-C18 column at a flow rate of 0.5 mL min^{-1}. The mobile phase consisted of 90/10 acetonitrile/water (v/v) with 0.1% trifluoroacetic acid. The quantities of fluorescent dye which were in proportional to the number of nanoparticles retained in different tissue samples were quantified using a standard curve created from known concentrations of fluorescent dye diluted in the mobile phase.

3.13 *In Vivo* Pharmacokinetic Study

Six CD1 mice were randomized into two groups (n = 3 per group) and intravenously injected with CS-PGE$_2$-PINCs or NCs (CS dose: 1.2 mg kg^{-1} mouse, PGE$_2$ dose: 0.053 mg kg^{-1} mouse) 24 h after myocardial I/R injury. At pre-determined time intervals (0.5, 1, 2, 4, 12, 24, and 48 h), 20 µL of whole blood was collected and centrifuged at 800 × g for 10 min. The plasma level of human SDF-1 was analyzed using an ELISA kit (R&D Systems, USA) according to the manufacturer's instruction. The data were averaged from three independent measurements.

3.14 Cardiac Function Assessment

All animals underwent transthoracic echocardiography under anesthesia at 4 h post-I/R injury and 4 weeks after treatment using a VisualSonics Vevo 2100 Imaging System. Hearts were imaged two-dimensionally in long-axis views at the level of the greatest left ventricular diameter. Left ventricular end-diastolic volume (LVEDV) and end-systolic volume (LVESV) were measured. Left ventricular ejection fraction (LVEF) was determined by measurement from views taken from the infarcted area. All measurements were done in random order, with the surgeon and echocardiographer being blind to the treatment groups.

3.15 Heart Morphometry

Hearts were harvested and cut into 10 µm-thick tissue sections. Masson's trichrome staining was performed, and images were acquired with a PathScan Enabler IV slide scanner (Advanced Imaging Concepts, USA). Image analysis related to viable myocardium and scar size was performed using NIH ImageJ software. Three selected sections were quantified for each animal.

3.16 Immunohistochemistry assessment

Heart cryosections were fixed with 4% paraformaldehyde in PBS for 30 min, permeabilized and blocked with Protein Block Solution (DAKO) containing 0.1% saponin for 1 h at room temperature. For immunostaining, the samples were incubated overnight at 4 °C with the following primary antibodies diluted in the blocking solution: rabbit anti-mouse α-SA (1:200, ab137346, Abcam) was used to identify cardiomyocytes; rat anti-mouse Ki67 antibody (1:200, 151202, Biolegend), rabbit anti-mouse histone H3 phosphorylated at serine 10 (pH3, 1:200, ab5176, Abcam), and rabbit anti-mouse Aurora B kinase (AURKB, 1:200, ab2254, Abcam) antibodies were used to analyze cell-cycle re-entry, karyokinesis, and cytokinesis, respectively; sheep anti-mouse vWF (1:200, ab11713, Abcam) antibody was used to detect myocardial capillaries in the peri-infarct regions; goat anti-mouse Nkx2.5 (1:200, ab106923, Abcam), and rat anti-mouse CD34 (1:200, MA1-22646, Thermo Fisher Scientific) antibodies were used to examine endothelial progenitor cell recruitment; rabbit anti-mouse CD3 (1:200, ab16669, Abcam), rat anti-mouse CD8 (1:200, ab22378, Abcam), and rabbit anti-mouse CD68 (1:200, ab125212, Abcam) antibodies were used to detect immune response. After three 10-min washes with PBS, samples were stained for 1.5 h at room temperature with fluorescent secondary antibodies including goat anti-rabbit IgG-Alexa Fluor 594 conjugate (1:400, ab150080, Abcam), goat anti-rat IgG-Alexa Fluor 488 conjugate (1:400, ab150157, Abcam), donkey anti-rabbit IgG-Alexa Fluor 488 conjugate (1:400, ab150073, Abcam), donkey anti-goat IgG-Alexa Fluor 594 conjugate (1:400, ab150136, Abcam), donkey anti-sheep IgG-Alexa Fluor 488 conjugate (1:400, ab150177, Abcam), goat anti-rabbit IgG-Alexa Fluor 488 conjugate (1:400, ab150077, Abcam), and goat anti-rabbit IgG-Alexa Fluor 594 conjugate (1:400, ab150080, Abcam), and goat anti-rat IgG-Cy5 conjugate (1:400, ab6563, Abcam) based on the isotopes of the primary antibodies. This was followed by 10

min of 4, 6-diamidino-2-phenylindole dihydrochloride (DAPI) staining for nucleus visualization. Slides were mounted with ProLong Gold mountant (Thermo Fisher Scientific) and viewed under a Zeiss LSM 710 confocal microscope (Carl Zeiss). Images were analyzed using NIH ImageJ software.

3.17 Flow cytometric analysis of isolated cardiomyocytes

At 2 weeks post-treatment, the mouse hearts that received saline or CS-PGE$_2$-PINC injection were carefully excised. The cardiomyocytes were isolated using a Langendorff perfusion system according to the previously published method[24,25]. Flow cytometry was performed on a CytoFlex (Beckman Coulter, USA) and the data were analyzed using the FCS Express software (De Novo, USA). The isolated cells were labeled with rabbit anti-mouse α-SA (1:200, ab137346, Abcam) was used to identify cardiomyocytes and rat anti-mouse Ki67 antibody (1:200, 151202, Biolegend) to analyze cell-cycle re-entry.

3.18 Statistics

All experiments were performed independently at least three times, and the results were presented as mean ± s.d. Comparisons between any two groups were performed using two-tailed unpaired Student's t-test. Comparisons among more than two groups were performed using one-way ANOVA followed by post hoc Bonferroni test. Single, double, and triple asterisks represent $p < 0.05$, 0.01, and 0.001, respectively; $p < 0.05$ was considered statistically significant.

4. Results and Discussion

4.1 Synthesis and Characterization of PINCs

To substantiate our design, we combine a double-emulsion-based solvent evaporation/extraction process with cell membrane cloaking to prepare the PINCs (Fig. 1A). The CSCs were derived from adult human hearts using the previously described cardiac explant

method. Those cells consistently express CD105, partially express CD90, but do not express c-kit, CD31, CD34, or CD45, suggesting a phenotype related to cardiac stromal cells in the heart. Such cells have very limited ability to differentiate into cardiomyocytes but can secrete a variety of regenerative factors and exosomes. The conditioned medium (secretome) from CSCs was used to produce our therapeutic nanoparticles. First, the secretome derived from CSCs was incorporated into PLGA to form nano-cells (NCs) through a double emulsion method. The CSC secretome loading capacity and efficiency were 2.8 wt% and 85.3%, respectively, showing that the CSC secretome was efficiently encapsulated into the hydrophilic core of NCs. Platelet membranes were then isolated and purified from the platelet-rich plasma through gradient centrifugation[15]. In order to prepare the PINC functionalized with PGE_2, the amine groups of platelet membrane glycoproteins were further reacted with the terminal carboxyl group of PGE_2 using N-Ethyl-N'-(3-dimethylaminopropyl)carbodiimide (EDC)/N-hydroxysuccinimide (NHS) as a linker to obtain the PGE_2-platelet membrane conjugate. The content of PGE_2 conjugated to the PGE_2-platelet membrane conjugate was determined to be 0.68 mg g^{-1} dry platelet membrane by enzyme-linked immunosorbent assay (ELISA), with a high conjugation yield of over 95% (see Experimental section and Fig. S1). The conjugation of PGE_2 onto the surface of platelet membrane was validated by confocal laser scanning microscopy (CLSM). The colocalization of the fluorescence signals from the DiI-labeled platelet membrane (red) and fluorescein isothiocyanate-tagged PGE_2 (green) substantiated the successful conjugation of PGE_2 onto the platelet membrane surface (Fig. S2). The resulting PGE_2-platelet membrane conjugate was subsequently incubated with the CSC secretome-loaded NC under ultrasonication, followed by membrane extrusion to form the PGE_2-platelet-membrane-coated NC (designated CS-PGE_2-PINC). The PINC functionalized with only CSC secretome (designated CS-PINC) was prepared *via* coating the purified platelet membrane

on the surface of NC. The PINC functionalized with only PGE$_2$ (designated PGE$_2$-PINC) was prepared *via* coating the PGE$_2$-platelet membrane conjugate on the surface of empty PLGA nanoparticles. Transmission electron microscopy (TEM) studies confirmed the platelet membrane coating on the CS-PGE$_2$-PINCs that appear as a core-shell structure (Fig. 1B). Dynamic light scattering (DLS) analysis indicated that the CS-PGE$_2$-PINCs had an average diameter of about 195 nm and a narrow size distribution (polydispersity index (PDI) = 0.157) (Figs. 1B and C). Nanoparticle tracking analysis using NanoSight revealed that the majority of particles showed a particle size of about 205 nm, consistent with the results obtained from TEM and DLS measurements (Fig. S3). We employed a bicinchoninic acid (BCA)-based protein assay to determine the efficiency of membrane coating by comparing the difference between the platelet membrane protein content before membrane coating and after pelleting the platelet-membrane-coated PLGA nanoparticles from the remaining free membrane vesicles. The amount of membrane protein coated onto the PLGA core was estimated to be 0.143 picogram membrane protein per nanoparticle, with a high coating efficiency of approximately 92% (see Experimental section).

After cloaking with platelet membrane, the size of PINCs did not change significantly compared to the bare NC (Fig. S4) while the zeta potential of CS-PGE$_2$-PINC increased by about 18 mV compared with bare NC, approaching the value of -27 mV (Figs. 1D and S5). This phenomenon is consistent with the previous analyses of nanoparticles after platelet membrane coating, which can be ascribed to the veiling of the highly negative PLGA core with the less negatively charged platelet membrane[9,11,26]. To determine the stability of different nanoformulations in solution over time, NCs and CS-PGE$_2$-PINCs were stored in phosphate buffered saline (PBS, 1 ×, pH 7.4) at room temperature, respectively, and their size change was monitored by DLS. The PINCs exhibited stable size over a 2-week study period, while the NCs

showed rapidly agglomeration in PBS (Figs. 1E and S6). In addition, the cloaking of the platelet membrane endowed the PINCs with superior stability before and after incubation in 50% serum when compared with bare NC (Fig. 1I). The small size negatively charged cell-mimicking surface, and superior serum stability make the PINCs ideal for intravenous application. We further investigated the long-term storage stability of CS-PGE$_2$-PINCs. After cryopreservation for over 3 months, the thawed CS-PGE$_2$-PINCs exhibited similar morphology, size, and surface charge to those characteristics before freezing (Figs. 1F-H, and S7). Furthermore, all the PINC formulations exhibited excellent lyophilization stability, with the size and zeta potential remained nearly identical before lyophilization and after resuspension (Fig. S8).
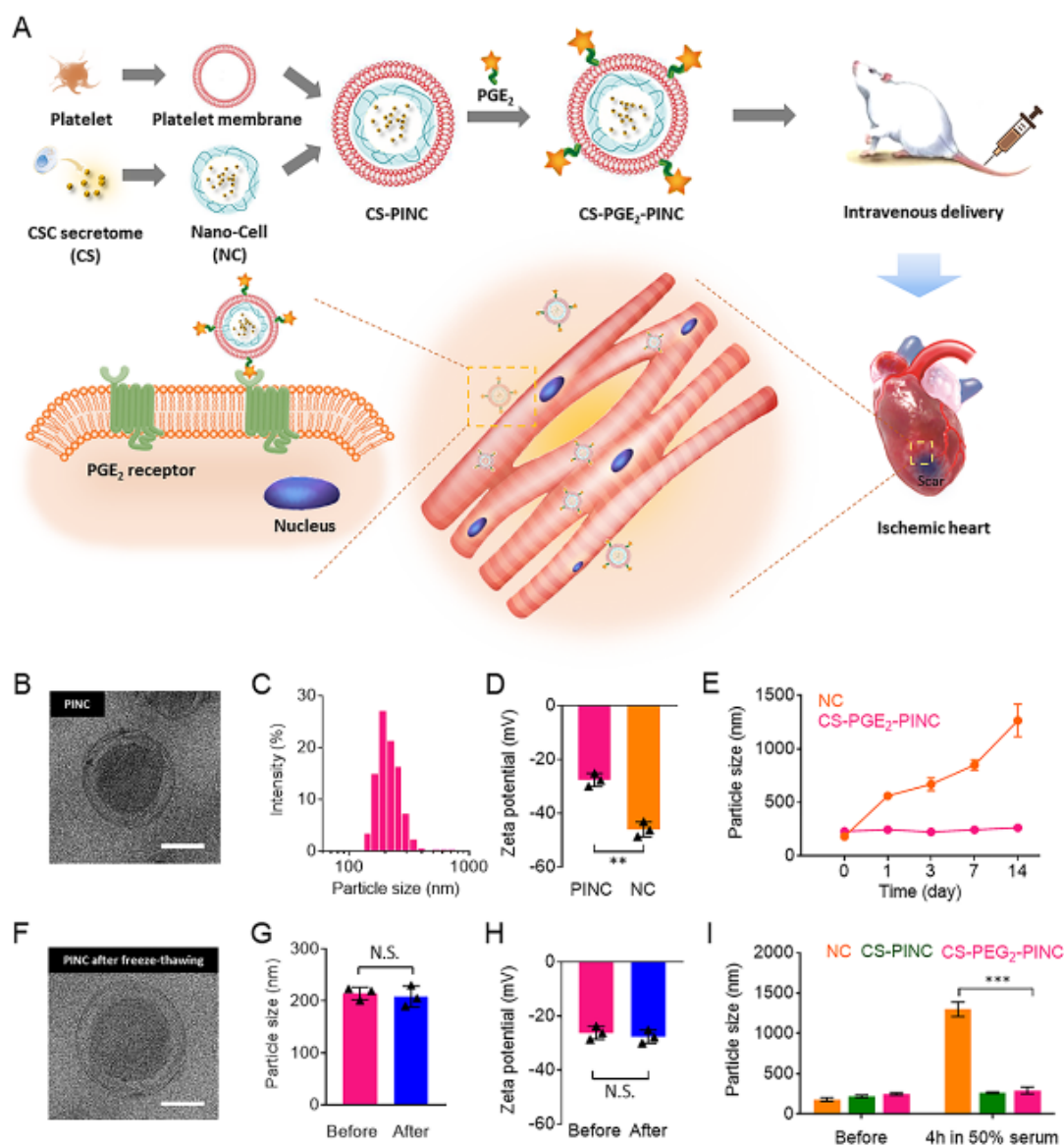
Fig 1. Fabrication and characterization of PINCs. (A) Schematic illustration of the fabrication process of PINCs. The therapeutic effects of PINC injection were tested in mice with myocardial I/R injury. (B) TEM image showing the ultrastructure of CS-PGE$_2$-PINC. (C) Size distribution of CS-PGE$_2$-PINC measured by DLS. (D) Zeta potentials of CS-PGE$_2$-PINC and NC. (E) Particle sizes of bare NC and CS-PGE$_2$-PINC over 2 weeks in PBS (F) TEM image showing the ultrastructure of CS-PGE$_2$-PINC after freeze-thawing. (G, H) The comparison of particle size (G) and zeta potential (H) of CS-PGE$_2$-PINC before and after freeze-thawing. (I) *In vitro* stability of NC, CS-PINC, and CS-PGE$_2$-PINC before and after incubation in 50% fetal bovine serum. Scale bars, 100 nm. All data are mean ± s.d. * indicates $p < 0.05$, ** indicates $p < 0.01$, *** indicates $p < 0.001$; N.S., no statistical significance. Comparisons between any two groups were performed using two-tailed unpaired Student's *t*-test. Comparisons among more than two groups were performed using one-way ANOVA followed by *post hoc* Bonferroni test.

4.2 *In Vitro* Bioactivity of PINCs

   Stem cell therapy represents a promising strategy for treating ischemic heart diseases[27]. Mounting lines of preclinical and clinical evidence indicate that stem cells, including CSCs and MSCs, exert their functional benefits through the secretion of paracrine factors, acting like "mini-drug pumps" to promote endogenous repair[28,29]. We have previously fabricated therapeutic cell-mimicking microparticles by packaging stem cell factors in a biodegradable polymeric shell and tested their regenerative potential in rodent models of heart injury[16,17]. In this study, we sought to investigate whether our PINCs could mimic CSCs by secreting regenerative growth factors. ELISA revealed that the CS-PGE$_2$-PINCs continuously released pro-myogenic and pro-angiogenic paracrine factors, such as stromal cell-derived factor-1 (SDF-1), vascular endothelial growth factor (VEGF), and hepatocyte growth factor (HGF) for at least 14 days; the platelet membrane coating did not affect the release of stem cell factors from PINCs (Figs. 2A-C). SDS-PAGE was used to run platelet membranes and all the different PINCs for protein composition analysis. As expected, all the PINCs had protein profiles that are similar to that of the platelet membrane. Western blot analysis further revealed the distinct expression of primary platelet membrane markers including CD42b (GPIba) and CD36 (GPIV) on all the PINCs, further confirming the successful platelet membrane coating onto PINCs (Figs. 2D and S9). CD42b is one of the major adhesion molecules that regulate the binding of platelets to the injured vasculature and plays an important role in homing the platelet-nanovesicle-decorated CSCs to the ischemic heart after I/R injury[15,26]. Therefore, the PINCs inherited the binding motifs of platelets. Owing to the platelet-mimicking properties, the PINCs showed robust binding to the collagen-coated surface (Fig. S10). In addition, DiI-labeled PINCs were plated onto green fluorescent protein-tagged human umbilical vein

endothelial cells (GFP-HUVECs) cultured on the collagen-coated surface, and the selective adherence of PINCs to the collagen region was confirmed (Figs. 2E and F).
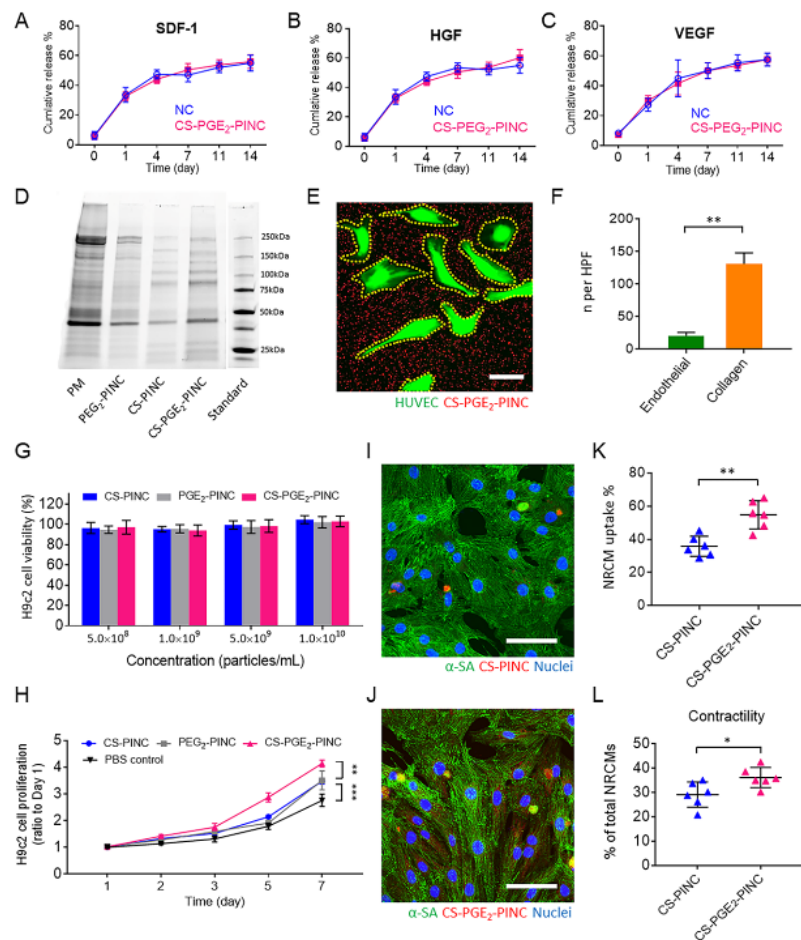

Fig 2. In vitro bioactivity of PINCs. (A-C) Quantitative analysis of the releases of SDF-1, HGF, VEGF from NC and CS-PGE$_2$-PINC over 2 weeks. (D) Protein content visualization of platelet membrane (PM), PGE$_2$-PINC, CS-PINC, and CS-PGE$_2$-PINC run on SDS-PAGE at equivalent protein concentrations. (E) Collagen-coated 4-well slides seeded with human umbilical vein endothelial cells (HUVECs) were incubated with CS-PGE$_2$-PINCs for 60 s, followed by fluorescence microscopy showing selective CS-PGE$_2$-PINC adherence to exposed collagen versus endothelial surfaces. (F) Quantification of CS-PGE$_2$-PINC in endothelial- and collagen-covered surface, respectively. (G) Cytocompatibility of PINCs at various concentrations. (H) The proliferation of H9c2 cells over time in the presence of different PINCs. (I, J) Representative confocal image showing the internalization of CS-PINC (I) and CS-PGE$_2$-PINC (J) by NRCMs. (K) Quantitative analysis of the percentage of NRCMs with different nanoparticle endocytosis. (K) Quantitative analysis of NRCM contractility when cocultured with different PINCs. Scale bars, (E) 20 μm; (I, J) 50 μm. All data are mean ± s.d. Comparisons between any two groups were performed using two-tailed unpaired Student's *t*-test. Comparisons among more than two groups were performed using one-way ANOVA followed by *post hoc* Bonferroni test. * indicates $p < 0.05$, ** indicates $p < 0.01$, *** indicates $p < 0.001$.

Next, we tested the effect of the PINCs on the H9c2 cardiomyoblasts, a widely-used cardiac cell line isolated from the embryonic rat heart tissue. The CS-PINCs, PGE$_2$-PINCs, and CS-PGE$_2$-PINCs have excellent cytocompatibility as confirmed by the cell viability assay. The cells maintain high viability upon exposure to the PINCs (> 95% viability), regardless of nanoparticle concentration (Fig. 2G). In addition, a cell proliferation assay using a cell count kit-8 (CCK-8) revealed that the CSC secretome shows similar bioactivity before and after being encapsulated into PLGA nanoparticles (Fig. S11) and that PINCs promote the growth of H9c2 cardiomyoblasts, indicating that the release of therapeutic stem cell factors from the PINCs promote cell attachment and proliferation, consistent with our previous studies[15-17,30]. The H9c2 cells treated with CS-PGE$_2$-PINCs exhibited significantly higher proliferative potential than those treated with CS-PINCs or PGE$_2$-PINCs (Fig. 2H). In contrast, the non-secretome-encapsulated PLGA nanoparticles, either with or without platelet membrane coating, were not able to promote H9c2 cardiomyoblast proliferation (Fig. S12). Furthermore, after cryopreservation for 3 months, the thawed CS-PGE$_2$-PINCs exhibited comparable potency in promoting the growth of H9c2 cells to the freshly prepared controls, indicating the excellent cryostability of CS-PGE$_2$-PINCs (Fig. S13). We further investigated the effect of PGE$_2$ decoration on the cardiomyocyte protective ability of PINCs *in vitro*. Neonatal rat cardiomyocytes (NRCMs) were cocultured with DiI-labeled CS-PINCs or CS-PGE$_2$-PINCs (red, Figs. 2I and J) with equivalent concentrations. After coculturing for 3 h, the uptake of CS-PGE$_2$-PINCs into NRCMs (stained by α-sarcomeric actinin (α-SA), green) was significantly higher than that of the nanoparticles without PGE$_2$ decoration (Fig. 2K). Furthermore, CS-PGE$_2$-PINCs significantly promoted NRCM contractility compared with CS-PINCs (Fig. 2L). Following exposure to serum-free medium supplemented with hydrogen peroxide (250 μM) for 3 h, which simulates an ischemic microenvironment, TUNEL staining

showed that the NRCMs pretreated with CS-PGE$_2$-PINCs were less apoptotic than those pretreated with CS-PINCs (Fig. S14). Together, these results suggest the enhanced heart-targeting ability and regenerative potential of CS-PGE$_2$-PINCs relative to CS-PINCs, which could be attributable to the specific interactions between CS-PGE$_2$-PINCs and the PGE$_2$ receptors expressed on cardiomyocyte or cardiomyoblast surface[20,31].

4.3 *In Vivo* Heart Targeting and Bioactivity of PINCs in Mice with Myocardial I/R Injury

Myocardial reperfusion therapy restores blood flow and is the current standard treatment for patients after a heart attack[32]. However, it paradoxically causes further lethal tissue injury, known as myocardial I/R injury in clinical practice. Exploring ways to control or attenuate I/R injury is of clinical interest for improving post-ischemic recovery; thus, we sought to test the bioactivity of PINCs in immunocompetent CD1 mice with I/R injury (Fig. 3A). Following a temporary left anterior descending coronary artery (LAD) ligation for 30 min to create ischemia injury and a subsequent 24-h reperfusion, the mice were randomly divided into four groups and treated with saline (negative control), CS-PINCs, PGE$_2$-PINCs, and CS-PGE$_2$-PINCs *via* tail vein injection, respectively.

To evaluate the heart targeting capability of PINC, the mice intravenously administrated with DiR-labeled CS-PGE$_2$-PINCs or bare NCs following myocardial I/R injury were autopsied after 14 days to collect major organs for *ex vivo* fluorescent imaging. The infarcted hearts that received CS-PGE$_2$-PINCs exhibited a stronger fluorescent signal than other organs as well as the hearts that received NCs (Fig. 3B). The quantitive region-of-interest (ROI) analysis confirmed that the CS-PGE$_2$-PINC-recipient hearts showed 14.9-fold higher radiance efficiency (i.e., a measure of photon flux from the fluorescently-labeled nanoparticle in the organ of interest, normalized by the area of emission, the exposure time, and the solid angle of the detector) than those treated with

bare NCs, as well as 3.4-fold and 8.6-fold higher than the liver and kidney, respectively, validating the notable heart targeting ability of CS-PGE$_2$-PINCs (Fig. 3C). In contrast, greater nanoparticle accumulation was observed in the livers of animals that received the bare NCs compared to other organs, suggesting significant clearance of nanoparticles by the liver macrophages as expected. These findings were further corroborated by the quantitative analysis of DiI-labeled CS-PGE$_2$-PINC or NC retention in different organs using high performance liquid chromatography (HPLC)[33,34]. The mice treated with DiI-labeled CS-PGE$_2$-PINCs showed markedly higher nanoparticle retention in the injured heart than those treated with DiI-labeled NCs at 14 days post-treatment, which is consistent with the histological analysis (Figs. S15 and S16). The pharmacokinetics of intravenously injected CS-PGE$_2$-PINCs was evaluated by quantitatively monitoring the human SDF-1 concentration in the blood plasma. The SDF-1 released from CS-PGE$_2$-PINCs has a longer blood retention than that from NCs in mice with myocardial I/R injury (Fig. S17), which was in good accordance with previous studies and the *in vitro* factor release results[13,26]. We further evaluated the biocompatibility of PINCs. Negligible T-cell and macrophage infiltration were confirmed by the presence of few CD3-/CD8-positive T cells and CD68-positive macrophages in the hearts that received different PINCs, indicating good biocompatibility of these nanoformulations (Fig. S18).
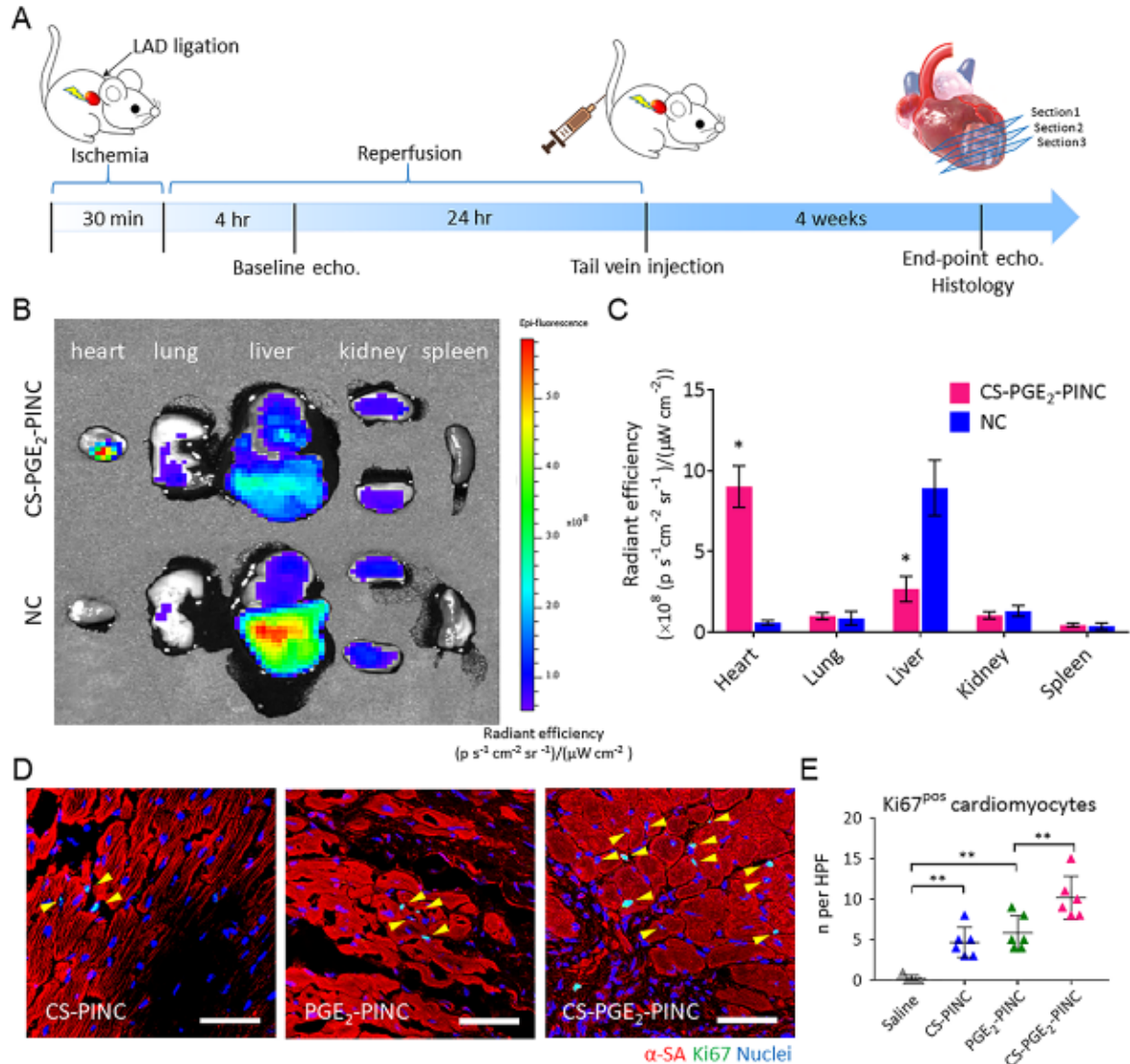
Fig 3. Biodistribution and in vivo bioactivity of PINCs. (A) Schematic showing the animal study design. (B) Biodistributions of CS-PGE$_2$-PINCs and NCs after intravenous delivery in mice with myocardial I/R injury. Representative *ex vivo* fluorescent imaging of mouse organs (heart, lung, liver, kidney, and spleen) at 14 days post-intravenous injections of CS-PGE$_2$-PINCs and NCs. (C) Quantitative analysis of fluorescent intensities (n=3 animals per group). (D) Representative images showing cycling cardiomyocytes (yellow arrowheads) as indicated by α-SA and Ki67 double-positive staining in the peri-infarct regions of the hearts treated with CS-PINCs, PGE$_2$-PINCs, and CS-PGE$_2$-PINCs at week 4. (E) Quantification of Ki67-positive cardiomyocytes at week 4 in the saline control (n = 5), CS-PINC (n = 6), PGE$_2$-PINC (n = 6), and CS-PGE$_2$-PINC (n = 6) groups. Scale bars, 50 μm. All data are mean ± s.d. Comparisons between any two groups were performed using two-tailed unpaired Student's *t*-test. Comparisons among more than two groups were performed using one-way ANOVA followed by *post hoc* Bonferroni test. * indicates $p < 0.05$, ** indicates $p < 0.01$.

It has been established that adult cardiomyocytes have extremely limited capacity to proliferate *in vivo*. To test the bioactivity of PINCs in adult mouse cardiomyocytes, we first assessed the cardiomyocyte proliferation 4 weeks after treatment by α-SA and Ki67 expressions. The number of Ki67-positive cardiomyocytes in the peri-infarct region of both the CS-PINC-recipient and the PGE$_2$-PINC-recipient hearts was significantly higher than that of the control hearts treated with a saline injection, although the difference between the two groups was indiscernible (Figs. 3D and S19). Notably, the highest number of cycling cardiomyocytes was found in the peri-infarct region of the CS-PGE$_2$-PINC-recipient hearts among all the groups (Figs. 3D-E). We further stained the hearts for a specific marker of late G2/mitosis, phosphorylated histone H3 (pH3), and a marker of cytokinesis, Aurora B kinase (AURKB). Remarkably, CS-PGE$_2$-PINCs induced robust mitotic activity of cardiomyocytes in the injured hearts after 4 weeks of treatment as evidenced by the elevated number of pH3-positive cardiomyocytes at the peri-infarct zone compared to other PINC treatment (Figs. 4A and B). Expression of AURKB suggested that the cardiomyocytes not only entered the cell cycle but also were undergoing cytokinesis (Figs. 4C and D). We further performed the Langendorff perfusion to isolate the cardiac cells from the saline-recipient or the CS-PGE$_2$-PINC-recipient hearts collected 2 weeks post-treatment. Flow cytometry analysis revealed an increase in the percentage of Ki67-positive cycling cardiomyocytes in the CS-PGE$_2$-PINC-recipient hearts relative to the saline-treated control hearts, which corroborates the previous findings of the immunohistochemical study (Fig. S20).
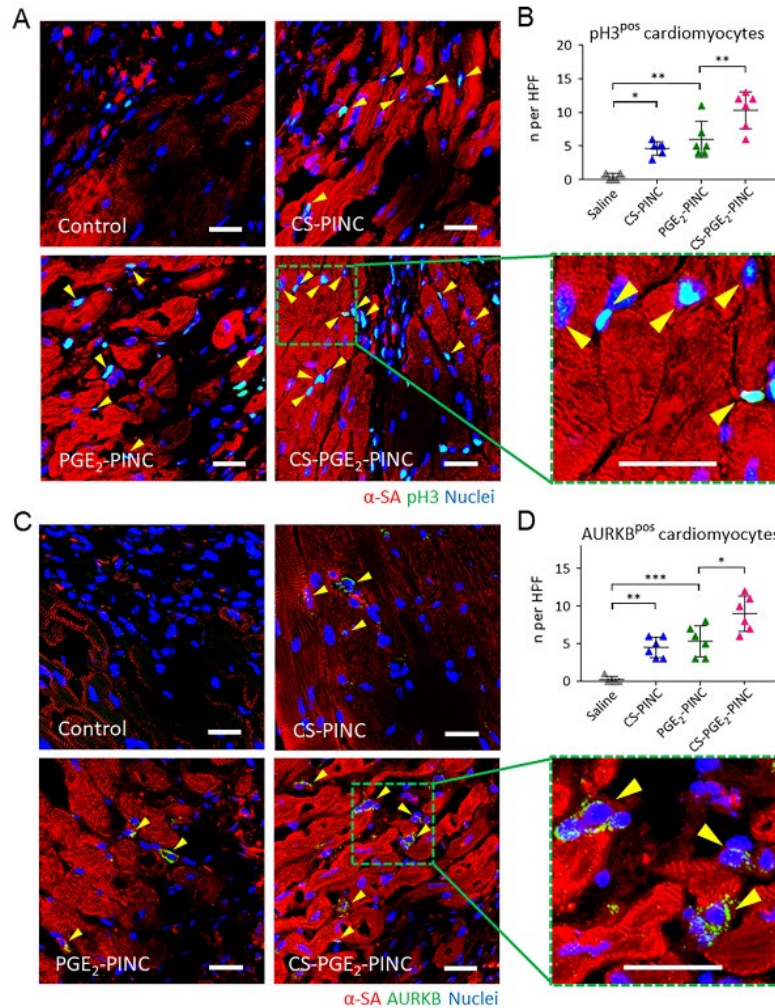
Fig 4. In vivo mitotic activities of cardiomyocytes. (A, B) Visualization of phospho-histone H3 phosphorylation in cardiomyocytes (yellow arrowheads) in the peri-infarct regions of saline control-, CS-PINC-, PGE_2-PINC-, and CS-PGE_2-PINC-treated hearts at week 4. Representative images are in (A) (blue: DAPI, staining nuclei; red: α-SA, staining cardiomyocytes; green: pH3, indicating the cells that are in late G2/mitosis phase; the green square highlights the localization of pH3 (yellow arrowheads) in the nuclei of cycling cardiomyocytes). Quantification in (B) shows pH3-positive cardiomyocytes at week 4 in the saline control (n = 5), CS-PINC (n = 6), PGE_2-PINC (n = 6), and CS-PGE_2-PINC (n = 6) groups. (C, D) Visualization of AURKB in cardiomyocytes (yellow arrowheads) in the peri-infarct regions of saline control-, CS-PINC-, PGE_2-PINC-, and CS-PGE_2-PINC-treated hearts at week 4. Representative images are in (C) (blue: DAPI, staining nuclei; red: α-SA, staining cardiomyocytes; green: AURKB, marking the cells in karyokinesis and cytokinesis; the green square highlights the localization of AURKB in midbodies (yellow arrowheads). Quantification in (D) shows AURKB-positive cardiomyocytes at week 4 in the saline control (n = 5), CS-PINC (n = 6), PGE_2-PINC (n = 6), and CS-PGE_2-PINC (n = 6) groups. Scale bars, 20 μm. All data are mean ± s.d. Comparisons among more than two groups were performed using one-way ANOVA followed by *post hoc* Bonferroni test. * indicates $p < 0.05$; ** indicates $p < 0.01$; *** indicates $p < 0.001$.

114

4.4 Functional Benefits of PINC Therapy in a Mouse Model of I/R

   To test the potency of PINCs for the treatment of heart injury after I/R, adult mice were randomized to intravenously receive CS-PINCs, PGE_2-PINCs, CS-PGE_2-PINCs or saline injection after myocardial I/R injury. After 4 weeks of treatment, heart morphometry imaged by Masson's trichrome staining revealed the protective effects of PINC injections on heart morphometry (Fig. 5A). When quantified, CS-PGE_2-PINC injection resulted in the highest amount of viable myocardium (Fig. 5B) with the smallest scar size (Fig. 5C). The reduced cardiac remodeling of CS-PGE_2-PINC-treated mice was further demonstrated by the reductions in left ventricular end diastolic volume (LVEDV) and end systolic volume (LVESV), respectively, compared with CS-PINCs, PGE_2-PINCs or saline controls (Figs. 5D-E). Left ventricular ejection fraction (LVEFs), LVEDVs, and LVESVs were similar at baseline among all the groups, indicating a similar degree of initial injury (Figs. 5F and S21). After 4 weeks, the LVEF of saline-treated animals evidently declined, while LVEF was well preserved in the CS-PINC and PGE_2-PINC treatment groups. The hearts of CS-PGE_2-PINC-treated animals showed the highest LVEF (Fig. 5F). When we calculated the treatment effects (i.e., change of LVEFs from baseline), it was clear that saline injection had negative treatment effect; CS-PINCs and PGE_2-PINC treatments preserved cardiac functions, and CS-PGE_2-PINC injection robustly boosted cardiac functions (Fig. 5G).
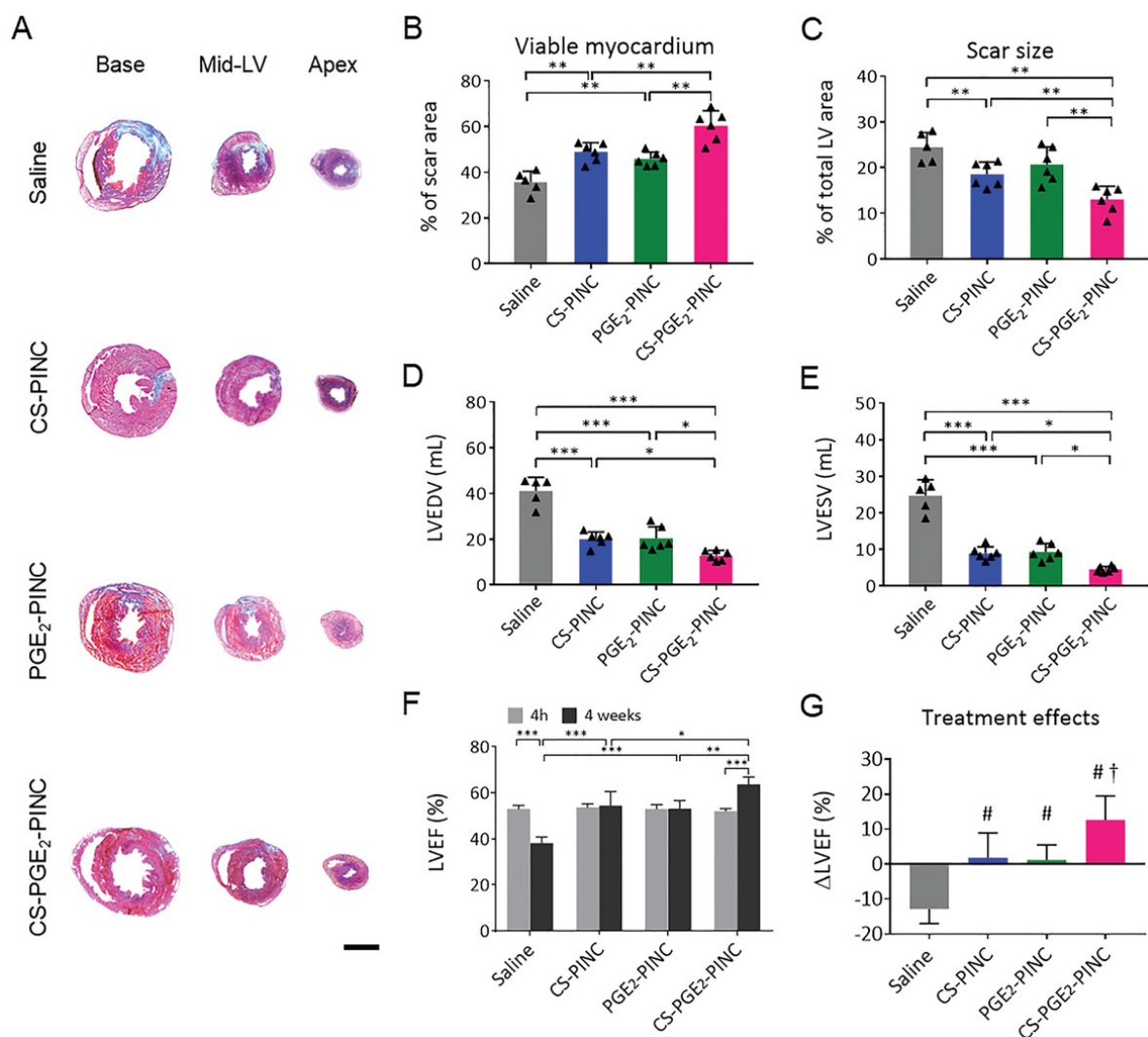
Fig 5. Functional benefits of PINC therapy in mice with myocardial I/R injury. (A) Representative Masson's trichrome sections showing scar tissue (blue) and viable myocardium (red) in the hearts 4 weeks after treatment with saline (n = 5), CS-PINCs (n = 6), PGE$_2$-PINCs (n = 6), and CS-PGE$_2$-PINCs (n = 6), respectively. (B, C) Quantitative analyses of viable myocardium (B) and scar size (C) from the Masson's trichrome images. (D, E) Left ventricular end-diastolic (D) and end-systolic (E) volumes (LVEDV and LVESV) measured by echocardiography at 4 weeks after I/R in mice treated with saline, CS-PINCs, PGE$_2$-PINCs, and CS-PGE$_2$-PINCs, respectively. (F) Left ventricular ejection fraction (LVEF) measured by echocardiography at baseline (4h post-I/R) and 4 weeks afterward in the saline, CS-PINC, PGE$_2$-PINC, and CS-PGE$_2$-PINC groups. Scale bar, 2 mm. All data are mean ± s.d. * indicates $p < 0.05$; ** indicates $p < 0.01$; *** indicates $p < 0.001$. (G) Treatment effects were assessed by the change in LVEF over the 4-week time course relative to baseline. # indicates $p < 0.05$ when compared with saline control group; † indicates $p < 0.05$ when compared with any other groups.

4.5 PINC Injection Promotes Endogenous Repair in the Infarcted Heart

To reveal the mechanisms underlying the functional effects of PINCs, we performed immunostaining analysis with Nkx2.5 (Fig. 6A), CD34 (Fig. 6B), and von Willibrand Factor (vWF, Fig. 6C) in the infarcted hearts of saline-, CS-PINC-, PGE_2-PINC-, and CS-PGE_2-PINC-treated mice. Previous studies have confirmed the important roles of Nkx2.5-positive cells in cardiomyogenesis and heart repair[35,36]. Compared with control, PINC treatments remarkably increased the recruitment of Nkx2.5-positive cardiac progenitor cells to the infarcted heart, with the highest number of cardiac progenitor cells entering the peri-infarct region of the CS-PGE_2-PINC-treated hearts (Fig. 6D). In addition, a greater number of CD34-positive cells were found in the CS-PGE_2-PINC-treated hearts compared with other treatment groups (Fig. 6E), suggesting the homing of endothelial progenitor cells may also be elicited after PINC injection. This was corroborated by the enhanced vWF-positive vessel density found in the PINC-treated hearts compared with the control. Together, these results suggest that the therapeutic effects of PINCs may be through activation of Nkx2.5-positive cells, endothelial progenitor cells, and promotion of neovascularization.
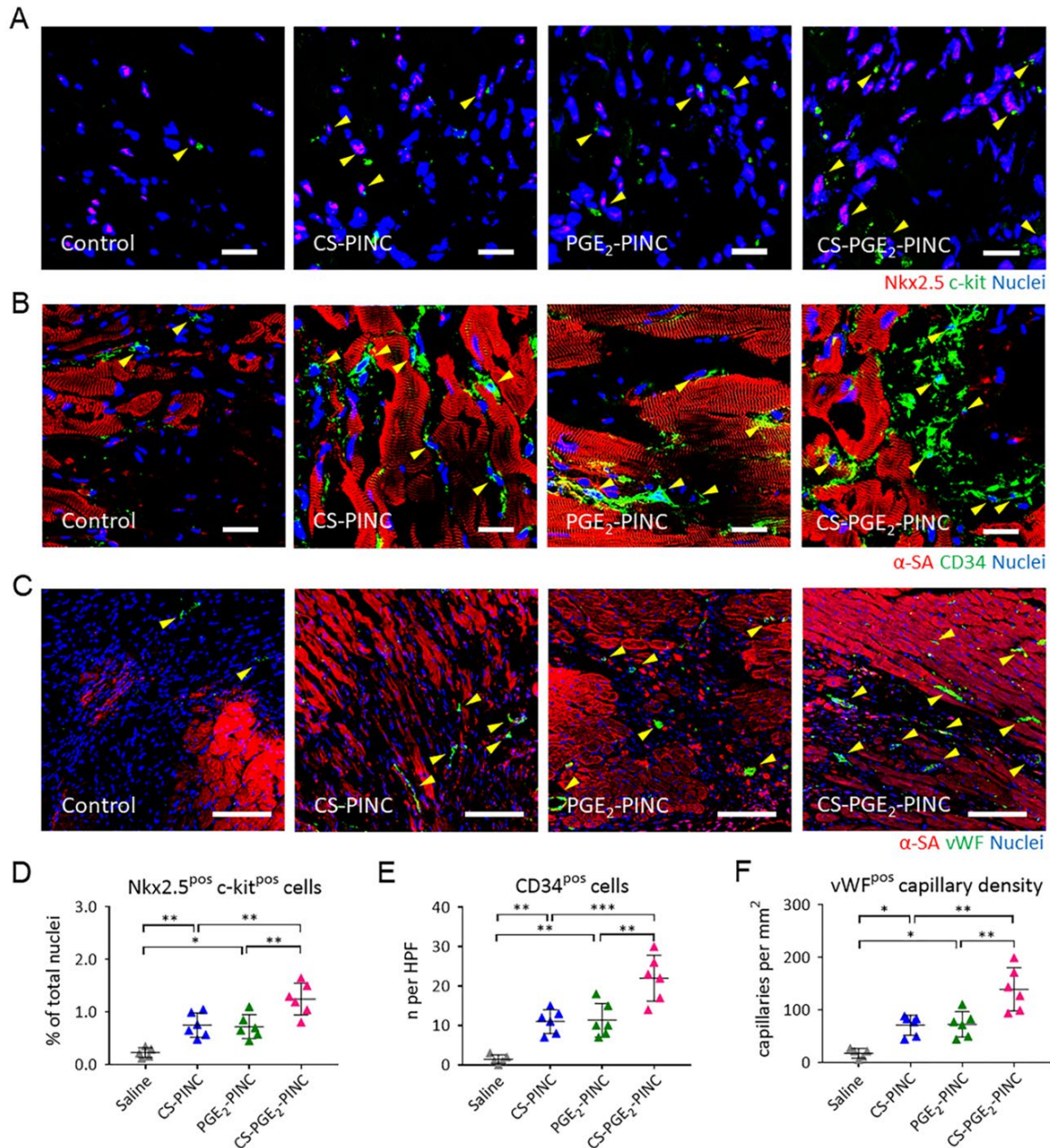
Fig 6. PINC injection promotes endogenous repair in the infarcted heart. (A-C) Representative images showing Nkx2.5 and c-kit double-positive cells, CD34-positive cells, and vWF-positive capillaries in the infarcted hearts 4 weeks after saline (n = 5), CS-PINC (n = 6), PGE$_2$-PINC (n = 6), or CS-PGE$_2$-PINC (n = 6) treatment. Yellow arrowheads indicate the positively stained cells. (D-F) Quantification of the number of Nkx2.5 and c-kit double-positive cells (D), CD34-positive cells (E), and vWF-positive capillary density (F) in the infarcted hearts 4 weeks after saline (n = 5), CS-PINC (n = 6), PGE$_2$-PINC (n = 6), or CS-PGE$_2$-PINC (n = 6) treatment. Scale bars, (A, B) 20 μm; (C) 100 μm. Comparisons among more than two groups were performed using one-way ANOVA followed by *post hoc* Bonferroni test. * indicates $p < 0.05$; ** indicates $p < 0.01$; *** indicates $p < 0.001$.

To date, most nanoformulations aiming at treating myocardial infarction employed the passive targeting mechanism (i.e., enhanced permeability and retention effect of the leaky vasculature in the acutely ischemic heart), thus were limited by the short-term retention from a few hours to days in the injured heart[7,37]. Christman, Gianneschi, and coworkers reported an enzyme-responsive nanoparticle that can form a network-like structure in response to the up-regulated MMPs following acute myocardial infarction for realizing long-term nanoparticle retention[8]. Recently, we reported that the decoration of CSCs with platelet membrane nanovesicles boosts CSC retention in the infarcted myocardium and therapeutic outcomes in rats and pigs with ischemic heart injury[15]. In addition, it has been established that the expression levels of three subtypes of EPs, EP2, EP3, and EP4, are remarkably upregulated in the heart after myocardial I/R injury[38,39]. PGE_2 not only activated the endogenous stem/progenitor cells to replenish cardiomyocytes after ischemic injury, but also enhanced the recruitment of CD34-positive hematopoietic stem cells after xenotransplantation through PGE_2/EP2/EP4 signaling[20,40]. The CS-PGE_2-PINCs reported here harness both the natural myocardial infarction-homing ability of platelet membrane and the upregulation of PGE_2 receptors in the cardiac microenvironment after I/R injury, resulting in prolonged retention in the infarcted heart after minimally-invasive intravenous delivery. Our findings showed that the released regenerative factors and PGE_2/EPs signaling could synergistically boost the therapeutic efficacy of CS-PGE_2-PINCs. As a result, the animals that received intravenous injection with CS-PGE_2-PINCs exhibited significantly augmented cardiac function and mitigated heart remodeling compared to other treatment groups. Such functional benefit was accompanied by the increase in cycling cardiomyocytes, activation of endogenous progenitor cells, and promotion of angiogenesis. Nevertheless, our study has several limitations. Firstly, we investigated the cardiac repair through immunohistochemical analysis.

Lineage tracing using transgenic mice will allow for more insightful analysis of the origin of newly formed blood vessels and cardiomyocytes. Secondly, our study did not include an empty (no secretome) nanoparticle control in the animal studies. Nonetheless, based on the *in vitro* data (Fig. S12), these control nanoparticles are not expected to improve cardiac functions in the animal model. In addition, for clinical applicability, a large animal model of I/R injury and longer study duration will be needed to fully characterize the efficacy and safety of the PINC therapy.

5. Conclusions

In summary, we reported a novel platelet-inspired nano-cell that incorporates both PGE_2-modified platelet membrane and regenerative factors to target the heart after ischemic injury. CS-PGE_2-PINC was fabricated by functionalizing a CSC factor-releasing core with a platelet membrane shell with PGE_2 decoration. By taking advantage of the natural infarct-homing ability of platelet membrane and the overexpression of EPs in the pathological cardiac microenvironment, the CS-PGE_2-PINC can realize targeted delivery of the therapeutic payload to the injured heart. Furthermore, the synergistic treatment efficacy can be achieved by CS-PGE_2-PINC, which combines the paracrine mechanism of stem cell therapy with the PGE_2/EP receptor signaling that is involved in the repair and regeneration of multiple tissues[19,40,41]. This platelet-inspired nano-cell can be applied as a promising therapeutic delivery platform for treating multiple diseases.

6. References

1.   Wickramasinghe, K. *et al.* Cardiovascular disease in Europe: epidemiological update 2016. *Eur. Heart J.* **37**, 3232–3245 (2016).

2.   Chouchani, E. T. *et al.* Ischaemic accumulation of succinate controls reperfusion injury through mitochondrial ROS. *Nature* **515**, 431–435 (2014).

3.   Bolli, R. & Ghafghazi, S. Cell therapy for cardiac repair: what is needed to move forward? *Nat. Rev. Cardiol.* **14**, 257 (2017).

4.   Lin, Z. & Pu, W. T. Strategies for Cardiac Regeneration and Repair. *Sci. Transl. Med.* **6**, 239rv1 LP-239rv1 (2014).

5.   Fischer, U. M. *et al.* Pulmonary passage is a major obstacle for intravenous stem cell delivery: the pulmonary first-pass effect. *Stem Cells Dev.* **18**, 683–692 (2009).

6.   Dvir, T. *et al.* Nanoparticles targeting the infarcted heart. *Nano Lett.* **11**, 4411–4414 (2011).

7.   Paulis, L. E. *et al.* Distribution of lipid-based nanoparticles to infarcted myocardium with potential application for MRI-monitored drug delivery. *J. Control. Release* **162**, 276–285 (2012).

8.   Nguyen, M. M. *et al.* Enzyme-Responsive Nanoparticles for Targeted Accumulation and Prolonged Retention in Heart Tissue after Myocardial Infarction. *Adv. Mater.* **27**, 5547–5552 (2015).

9.   Wang, F. *et al.* Nanoparticle-Based Antivirulence Vaccine for the Management of Methicillin-Resistant Staphylococcus aureus Skin Infection. *Adv. Funct. Mater.* **26**, 1628–1635 (2016).

10.   Anselmo, A. C. *et al.* Platelet-like nanoparticles: mimicking shape, flexibility, and surface biology of platelets to target vascular injuries. *ACS Nano* **8**, 11243–11253 (2014).

11.   Hu, Q. *et al.* Engineered Nanoplatelets for Enhanced Treatment of Multiple Myeloma and Thrombus. *Adv. Mater.* **28**, 9573–9580 (2016).

12.   Dehaini, D. *et al.* Erythrocyte-Platelet Hybrid Membrane Coating for Enhanced Nanoparticle Functionalization. *Adv. Mater.* **29**, 10.1002/adma.201606209 (2017).

13.   Hu, Q. *et al.* Anticancer Platelet-Mimicking Nanovehicles. *Adv. Mater.* **27**, 7043–7050 (2015).

14.   Hickman, D. A., Pawlowski, C. L., Sekhon, U. D. S., Marks, J. & Gupta, A. Sen. Biomaterials and Advanced Technologies for Hemostatic Management of Bleeding. *Adv. Mater.* **30**, 1700859 (2018).

15.   Tang, J. *et al.* Targeted repair of heart injury by stem cells fused with platelet nanovesicles. *Nat. Biomed. Eng.* **2**, 17–26 (2018).

16.   Luo, L. *et al.* Fabrication of Synthetic Mesenchymal Stem Cells for the Treatment of Acute Myocardial Infarction in Mice. *Circ. Res.* **120**, 1768–1775 (2017).

17.   Tang, J. *et al.* Therapeutic microparticles functionalized with biomimetic cardiac stem cell membranes and secretome. *Nat. Commun.* **8**, 13724 (2017).

18.   Kim, S. H. *et al.* Cardiomyocyte-targeted siRNA delivery by prostaglandin E(2)-Fas siRNA polyplexes formulated with reducible poly(amido amine) for preventing cardiomyocyte apoptosis. *Biomaterials* **29**, 4439–4446 (2008).

19.   Zhang, Y. *et al.* TISSUE REGENERATION. Inhibition of the prostaglandin-degrading enzyme 15-PGDH potentiates tissue regeneration. *Science* **348**, aaa2340–aaa2340 (2015).

20.   Hsueh, Y.-C., Wu, J. M. F., Yu, C.-K., Wu, K. K. & Hsieh, P. C. H. Prostaglandin E_2 promotes post-infarction cardiomyocyte replenishment by endogenous stem cells. *EMBO Mol. Med.* **6**, 496–503 (2014).

21. Srikanth Garikipati, V. N. & Kishore, R. Young Hearts Run Free: Therapeutic Potential of Neonatal Human Cardiac Progenitor Cells Secretome. *Circ. Res.* **120**, 751–752 (2017).

22. Tang, J.-N. *et al.* Concise Review: Is Cardiac Cell Therapy Dead? Embarrassing Trial Outcomes and New Directions for the Future. *Stem Cells Transl. Med.* 354–359 (2018). doi:10.1002/sctm.17-0196

23. Torán, J. L. *et al.* CXCL6 is an important paracrine factor in the pro-angiogenic human cardiac progenitor-like cell secretome. *Sci. Rep.* **7**, 12490 (2017).

24. Qian, L. *et al.* In vivo reprogramming of murine cardiac fibroblasts into induced cardiomyocytes. *Nature* **485**, 593–598 (2012).

25. Malliaras, K. *et al.* Cardiomyocyte proliferation and progenitor cell recruitment underlie therapeutic regeneration after myocardial infarction in the adult mouse heart. *EMBO Mol. Med.* **5**, 191–209 (2013).

26. Hu, C.-M. J. *et al.* Nanoparticle biointerfacing by platelet membrane cloaking. *Nature* **526**, 118 (2015).

27. Bel, A. *et al.* Human embryonic stem cell-derived cardiac progenitors for severe heart failure treatment: first clinical case report. *Eur. Heart J.* **36**, 2011–2017 (2015).

28. Li, T.-S. *et al.* Direct Comparison of Different Stem Cell Types and Subpopulations Reveals Superior Paracrine Potency and Myocardial Repair Efficacy With Cardiosphere-Derived Cells. *J. Am. Coll. Cardiol.* **59**, 942 LP – 953 (2012).

29. Barry, F. & Murphy, M. Mesenchymal stem cells in joint disease and repair. *Nat. Rev. Rheumatol.* **9**, 584 (2013).

30. Tang, J. *et al.* Heart Repair Using Nanogel-Encapsulated Human Cardiac Stem Cells in Mice and Pigs with Myocardial Infarction. *ACS Nano* **11**, 9738–9749 (2017).

31. Li, C. *et al.* Qishen granules inhibit myocardial inflammation injury through regulating arachidonic acid metabolism. *Sci. Rep.* **6**, 36949 (2016).

32. Vicencio, J. M. *et al.* Plasma Exosomes Protect the Myocardium From Ischemia-Reperfusion Injury. *J. Am. Coll. Cardiol.* **65**, 1525–1536 (2015).

33. Lundy, D. J., Chen, K.-H., Toh, E. K.-W. & Hsieh, P. C.-H. Distribution of Systemically Administered Nanoparticles Reveals a Size-Dependent Effect Immediately following Cardiac Ischaemia-Reperfusion Injury. *Sci. Rep.* **6**, 25613 (2016).

34. Chen, K.-H. *et al.* Nanoparticle distribution during systemic inflammation is size-dependent and organ-specific. *Nanoscale* **7**, 15863–15872 (2015).

35. Chen, W.-P., Liu, Y.-H., Ho, Y.-J. & Wu, S. M. Pharmacological inhibition of TGFβ receptor improves Nkx2.5 cardiomyoblast-mediated regeneration. *Cardiovasc. Res.* **105**, 44–54 (2015).

36. Ye, L. *et al.* Cardiac repair in a porcine model of acute myocardial infarction with human induced pluripotent stem cell-derived cardiovascular cell populations. *Cell Stem Cell* **15**, 750–761 (2014).

37. Chang, M.-Y. *et al.* Functionalized nanoparticles provide early cardioprotection after acute myocardial infarction. *J. Control. Release* **170**, 287–294 (2013).

38. Hishikari, K. *et al.* Pharmacological activation of the prostaglandin E2 receptor EP4 improves cardiac function after myocardial ischaemia/reperfusion injury. *Cardiovasc. Res.* **81**, 123–132 (2009).

39. Laura, C. *et al.* High-Density Lipoproteins Protect Isolated Rat Hearts From Ischemia-Reperfusion Injury by Reducing Cardiac Tumor Necrosis Factor-α Content and Enhancing Prostaglandin Release. *Circ. Res.* **92**, 330–337 (2003).

40. Goessling, W. *et al.* Prostaglandin E2 enhances human cord blood stem cell xenotransplants and shows long-term safety in preclinical nonhuman primate transplant models. *Cell Stem Cell* **8**, 445–458 (2011).

41. North, T. E. *et al.* Prostaglandin E2 regulates vertebrate haematopoietic stem cell homeostasis. *Nature* **447**, 1007–1011 (2007).

CHAPTER 4. Bispecific Antibody Therapy for Effective Cardiac Repair Through Redirection of Endogenous Stem Cells

1. Abstract

Bone marrow stem cells (BMSCs), are a promising strategy for cardiac regenerative therapy for myocardial infarction (MI). However, cell transplantation has to overcome a number of hurdles, such as cell quality control, clinical practicality, low cell retention/engraftment, and immune reactions when allogeneic cells are used. Bispecific antibodies (BsAbs) have been developed as potential agents in cancer immunotherapy but their application is sparse in cardiovascular diseases. In the present study, BsAbs are designed by chemical cycloaddition of F(ab')$_2$ fragments from monoclonal anti-CD34 and anti- cardiac myosin heavy chain (CMHC) antibodies, which specifically targets circulating CD34-positive cells and injured cardiomyocytes simultaneously. We hypothesized that intravenous administration of stem cell re-directing (SCRD) BsAbs (anti-CD34-F(ab')$_2$--anti-CMHC-F(ab')$_2$) can home endogenous BMSCs to the injured heart for cardiac repair. Our *in vivo* studies in a mouse model with heart ischemia/reperfusion (I/R) injury demonstrated the safety and therapeutic potency of SCRD BsAb, which supports cardiac recovery by reducing scarring, promoting angiomyogenesis, and boosting cardiac function.

2. Introduction

Coronary heart disease (CHD) is still having a severely high prevalence in the United States, an estimated 6.3% in US adults over 20 years of age. Based on American Heart Association (AHA) computation, one American will have a myocardial infarction (MI) every 40 seconds1. The

patients with the first MI will have a high risk of MI recurrence, stroke, and mortality within 5 years[1]. The therapeutics, particularly adult stem cell therapy[2-4] and tissue engineering[5-7], have been extensively investigated for MI treatment and has been shown promising therapeutic potential for cardiac regenerative therapy.

Bone marrow-derived stem cells (BMSCs) that have been widely studied in this field include hematopoietic stem cells (HSCs), lymphoid cells, mesenchymal stem cells (MSCs), and endothelial progenitor cells (EPCs)[8]. Administration BMSCs as therapeutics can effectively modulate inflammation and fibrogenesis which was associated with benefit in terms of reducing levels of fibrogenesis-related growth factors[9]. Additionally, BMSCs have been tested for cardiac repair in various clinical trials[10]. Nonetheless, such cells have quite limited cardiac differentiation potential. Numerous studies reported no trans-differentiation of BMSCs into cardiomyocytes[10,11]. Although BMSCs cannot differentiate into cardiomyocytes in vivo, there are mounting lines of evidence showing that they contribute to angiogenesis and myogenesis through paracrine mechanisms[12]. Subpopulations of BMSCs, such as MSCs13 and EPCs[14], have also been widely studied in clinical cardiac repair[15]. There are abundant evidence showing that MSCs and EPCs also exert their cardiac regenerative benefits mainly by secretion of regenerative factors[16,17].

Cell transplantation faces challenges. As "live drugs", cells can be tumorigenic and immunogenic[18]. Cell manufacturing is time-consuming and costly. In contrast, endogenous cell recruitment therapy is a promising approach to replace exogenous cell transplantation and solve this intrinsic problem. Via the CXCR4/CXCL12 axis[19], granulocyte colony-stimulating factor (G-CSF) mobilizes BMSCs and increases their amount in the circulation system[20]. Despite some promising preclinical results[21], meta-analyses indicated that G-CSF treatment has no overall benefit for MI patients[22,23].
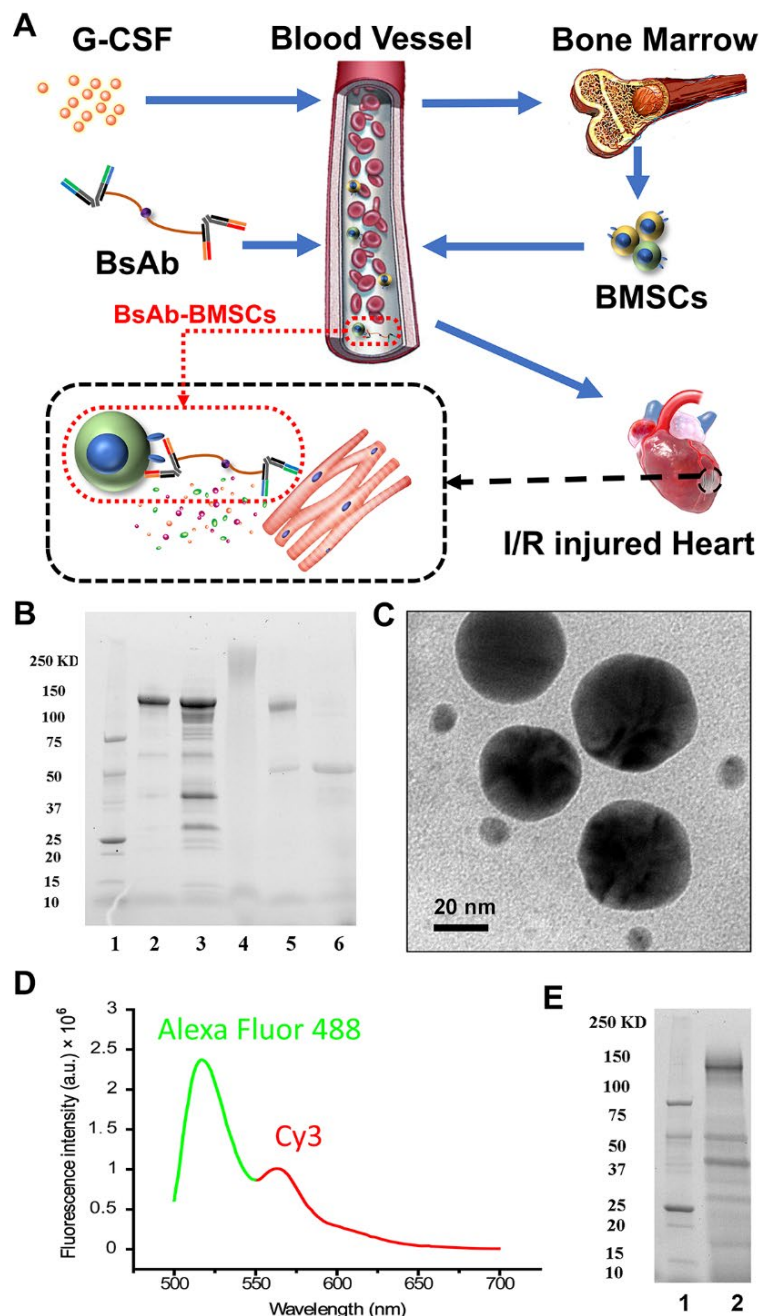
Fig 1. Fabrication and characterization of SCRD BsAbs. (A) Schematic illustration showing the redirection of endogenous stem cells *via* SCRD BsAbs. (B) SDS-PAGE showing products during the process of SCRD BsAbs fabrication. 1, marker; 2, Anti-CD34; 3, Anti-CD34-F(ab')$_2$; 4, Az-PEG-anti-CD34-F(ab')$_2$; 5, Anti-CMHC; 6, Anti-CMHC-F(ab')$_2$. (C) Transmission electron microscopy (TEM) image confirmed the successful conjugation of the two F(ab')$_2$ to form SCRD BsAb. The anti-CD34-F(ab')$_2$ and anti-CMHC-F(ab')$_2$ on the BsAbs were labelled with Gold nanoparticles with a diameter of 40 nm and 10 nm, respectively. Scale bar, 20nm. (D) FRET fluorescence intensity of Alexa Fluor 488 (donor) and Cy3 (receptor). (E) SDS-PAGE showing full product of SCRD BsAbs. 1, marker; 2, SCRD BsAbs.

Bispecific antibodies (BsAbs) have been developed as potent agents in cancer immunotherapy. They are capable of binding two different targets simultaneously by combining variable domains of desired monoclonal antibodies into an integrated structure. In the past decades, most of the BsAbs are designed to recruit cytotoxic immune cells to effectively target and against pathogenic cells[24]. Practically, BsAbs was divided into immunoglobulin G (IgG)-like molecules and non-IgG-like molecules[25]. The BsAbs IgG-like formats have better solubility, stability and could be purified easier due to their retained Fc region. Moreover, they also have longer serum half-lives due to their large size and Fc receptor-mediated recycling[26]. However, Non-IgG-like BsAbs that lack of the Fc region[25] are advantageous for tissue penetration enhancement26 though they can be eliminated rapidly through kidney during in vivo studies[27].

A growing number of alternative BsAb formats have been created through exploiting modular architecture of immunoglobulins. These formats include dual variable domain antibodies, diabodies, tandem scFv, tandem diabodies, and heterodimerization[28]. Bispecific antibodies serve as vehicles to deliver targeted radionuclides are of great interest[29,30]. In the present study, we engineered stem cell re-directing (SCRD) BsAbs via the chemical cycloaddition of F(ab')$_2$ fragments from monoclonal antibodies which specifically bind to injured myocardium or BMSCs. F(ab')$_2$ fragments were used to diminish the possible Fc-mediated effector functions including antibody-dependent cell mediated cytotoxicity, complement-dependent cytotoxicity, and antibody-dependent cellular phagocytosis[31]. Our hypothesis is that administration of SCRD BsAbs with G-CSF mobilization could enhance the homing ability of BMSCs to the infarcted heart and generate a functional benefit (Fig. 1A).

3. Materials and Methods

3.1 Fabrication of SCRD BsAbs

3.1.1 F(ab')$_2$ fragments extraction

The F(ab')$_2$ fragments were extracted respectively from anti-CD34 (CD34 Monoclonal antibody MEC14.7, Invitrogen) and anti-CMHC antibodies (anti- cardiac myosin heavy chain antibody, ab207926) via Pierce F(ab')$_2$ preparation kit.

3.1.2 The Synthesis of SCRDBsAbs

AZ-PEG-anti-CD34-F(ab')$_2$ and DBCO-PEG-anti-CMHC-F(ab')$_2$ was synthesized by reacted from AZ-PEG-NHS and DBCO-PEG-NHS with the F(ab')$_2$ fragments from anti-CD34 and anti-CMHC antibodies, respectively. Topically, NHS activated polymer was dissolved in PBS and added to the extracted F(ab')$_2$ through dropwise techniques. This reaction was kept in 4°C. 24 hours later, the esters that not linked to F(ab')$_2$ were removed by dialysis (Slide-A-Lyzer MINI Dialysis Units, 10,000 MWCO) and centrifugation (Amicon Ultra-0.5 filter, 100 kDa).

3.1.3 SCRD BsAbs Conjugation and characterization

Equimolar AZ-PEG-anti-CD34-F(ab')$_2$ and DBCO-PEG-anti-CMHC-F(ab')$_2$ was reacted in PBS by click reaction at 4°C for 48 hours. Then, transmission electron microscopy (TEM) proved the successful conjugation by labelling different F(ab')$_2$ fragments with different diameter gold nanoparticles-labelled secondary antibodies. Generally, AZ-PEG-anti-CD34-F(ab')$_2$ (rat) and DBCO-PEG-anti-CMHC-F(ab')$_2$ (mouse) derived from different species was conjugated together and then anti-rat gold nanoparticles (40 nm) and anti-mouse gold nanoparticles (10 nm) were used to pinpoint the two different F(ab')$_2$ of SCRD BsAbs.[30] Further, SCRD BsAbs and semi-products in different level was confirmed by SDS-PAGE.

3.2 The coculture of normal or injured NRCM with SCRD BsAbs

Neonatal Rat Cardiomyocytes (NRCMs) were derived from SD rat as previously described32. After cultured NRCMs on 4-well chambers for 3 days, some wells of the NRCMs were randomly permeabilized with Cytofix/Cytoperm fixation and permeabilization kit (BD) for 5 mins at 4 °C. After wash with sterile PBS, these injured NRCMs and the nonpermeabilized ones were incubated with SCRD BsAbs or NHS BsAbs (non-specific IgG-F(ab')$_2$-anti-CD34-F(ab')$_2$) for 1 h at 37 °C. After wash, Fluorescent secondary antibody (Goat Anti-rat IgG, Alexa Fluor® 647, Invitrogen) was added to those cells and incubated at 37 °C for 1 hour. The cells were then washed and fixed with 4% paraformaldehyde solution, permeabilized and blocked with 0.01% saponin (Sigma-Aldrich, St. Louis, MO) Dako (Dako, Glostrup, Denmark) solution and then incubated with primary antibodies overnight at 4°C: mouse anti-alpha sarcomeric actin (1:100, a7811, Sigma), FITC secondary antibodies (1:200, Abcam) were used for conjunction with primary antibodies. Samples were then mounted in Prolong Gold Antifade Mountant with DAPI (Thermofisher, P36935). Images were taken with a confocal fluorescent microscope (ZEISS LSM 880). Tissue morphology was characterized by images using ZEN lite software.

3.3 Evaluation of SCRD BsAbs recruiting ability

We created an *in vitro* blood environment to mimic the BMSCs recruitment. Briefly, the whole blood from the C57BL/6 mice was collected and the RBCs were lysed by RBC lysis buffers. The EPCs (1^10^6) that pre-stained with DiD were mixed into 1 mL of RBC-lysed blood. Then, 2 µg SCRD BsAbs or HNS BsAbs (non-specific IgG-F(ab')2-anti-CMHC-F(ab')$_2$) were added for 30 min. Then, we detacted the recruited EPCs with FITC secondary antibody. The samples were analyzed using flow cytometry (CytoFlex Flow Cytometer, Beckman Coulter, USA). Data analyzation was processed with the FCS Express 6 software (De Novo, USA).

3.4 Fluorescence resonance energy transfer microscopy (FRET)

Equimolar AZ-PEG-anti-CD34-F(ab')$_2$ and DBCO-PEG-anti-CMHC-F(ab')$_2$ was reacted in PBS by click reaction at 4°C for 48 hours. Then, fluorescence resonance energy transfer microscopy (FRET) proved the successful conjugation by labelling different F(ab')$_2$ fragments with different fluorescence-labelled secondary antibodies. Generally, AZ-PEG-anti-CD34-F(ab')$_2$ (rat) and DBCO-PEG-anti-CMHC-F(ab')$_2$ (mouse) derived from different species was conjugated together and then anti-rat conjugated (Alexa Fluor 488, donor) and anti-mouse conjugated (Cy3, acceptor) secondary antibodies were used to pinpoint the two different F(ab')$_2$ of SCRD BsAbs. The FRET was performed by using FLS980 Fluorescence Spectrometer.

3.5 Biodistribution of BsAbs

To confirm the homing ability of SCRD BsAbs, Sham and I/R injured animals were recruited for both NS and SCRD BsAb administration after 3 days of G-CSF stimulation. The BsAbs were prelabeled with Novus Biologicals™ Lightning-Link™ Rapid DyLight™ 633 Antibody Labeling Kit. The flurecence signals were detected via IVIS imaging system at different time interval. The data was processed via living image software version 3.0.

3.6 Mice model of ischemia/reperfusion (I/R) injury

All animal work was compliant with the Institutional Animal Care and Use Committee at North Carolina State University. Animal care was in accordance with the Institutional Animal Care and Use Committee (IACUC) guidelines. 5-7-week-old C57BL/6 mice were sedated by administration of KX cocktail (i.p. ketamine: 100 mg/kg body weight, xylazine: 10 mg/kg body weight). Artificial ventilation (SAR-1000 Small Animal Ventilator, CWE, Inc.) were used for animal life support during an I/R surgical operation. The ischemia was achieved through a 30 min temporal ligation of the left anterior descending artery (LAD) (MANI 8-0 silk suture).[33] The mice

then randomly received following treatments: 1) PBS group (treated with PBS instead of G-CSF mobilization and SCRD BsAb treatment); 2) G-CSF only group (G-CSF mobilization without following SCRD BsAb treatment); 3) SCRD BsAb only group (SCRD BsAb treatment without G-CSF pre-mobilization); and 4) G-CSF + SCRD BsAbs group (Both G-CSF mobilization and SCRD BsAb treatment were applied). G-CSF pre-mobilization was achieved by daily administration of G-CSF for 3 continuous days (i.p. 300 µg/kg body weight) [34]. SCRD BsAbs (i.v. 0.5 mg/kg body weight) were administered 6 hours after the final dose of G-CSF.

3.7 Immunogenicity detection after SCRD BsAbs administration

SCRD BsAbs were administered to normal C57BL/6 mice through tail vein injection. After 7 days, Hearts were collected for cryo-sections as previously described. Then, IHC was performed with the primary antibodies including anti-CD3 (1:200, ab16669, Abcam), anti-CD8 (1:200, ab22378, Abcam) and anti-CD68 (1:200, ab125212, Abcam). FITC- secondary antibodies (1:400, Abcam) were applied for antibody conjunction. Samples were then mounted in Prolong Gold Antifade Mountant with DAPI (Thermofisher, P36935). Images were taken with a confocal fluorescent microscope (ZEISS LSM 880). Tissue morphology was characterized by images using ZEN lite software.

4. Results

4.1 Fabrication of SCRD BsAbs

Since the purpose of SCRD BsAbs is to re-direct pre-mobilized BMSCs to the ischemic heart, the targeting proteins were chosen due to their selected specificity. CD34, a transmembrane phosphoglycoprotein, has been predominantly regarded as an important marker of HSCs[35], MSCs36, and EPCs[37,38]. Additionally, CD34 also expresses on several other cell types, including interstitial dendritic cells[39] and epithelial progenitors cells[40]. Thus, the monoclonal antibody that

targeting CD34 epitope class Ia[38] was selected for vitalizing SCRD BsAbs with the ability to recruit endogenous BMSCs from the blood stream.

Myocardial apoptosis plays an important role in MI and I/R caused cardiac dysfunction[41]. An adenosine triphosphate-driven molecular motor protein, cardiac myosin, plays an important role in this process physiologically and pathologically[42]. Since myosin subtypes have been expressed in different organs[43], we aroused SCRD BsAbs ability of homing to the injured myocardium by chose anti-cardiac myosin heavy chain (CMHC) monoclonal antibody.

Although the Fc region could improve solubility and stability and increase the serum half-life of the molecule, we digested Fc regions from those two monoclonal antibodies before SCRD BsAbs fabrication due to the aforementioned cytotoxic Fc-mediated effector functions[31] (Fig. 1B). Then, we conjugated F(ab')$_2$ from anti-CD34 antibodies with Azido-Polyethylene glycol–N-hydroxysuccinimidyl ester (Az-PEG-NHS) and obtained a polymerized anti-CD34 F(ab')$_2$ group (Az-PEG- anti-CD34-F(ab')$_2$). Additionally, we reacted F(ab')$_2$ from anti- heavy chain cardiac myosin antibodies with Dibenzocyclooctyne-Polyethylene glycol–N-hydroxysuccinimidyl ester (DBCO-PEG-NHS) to form a polymerized anti-CMHC F(ab')$_2$ group (DBCO-PEG-anti-CMHC-F(ab')$_2$). Transmission electron microscope (Fig. 1C) and fluorescence resonance energy transfer (FRET) microscopy (Fig. 1D) confirmed successful conjugation of polymer-modified F(ab')$_2$ as SCRD BsAbs (anti-CD34-F(ab')$_2$-Polymer-anti-CMHC-F(ab')$_2$) by click reaction. Also, polyacrylamide gel electrophoresis indicated the size and purity of the final BsAb products (Fig. 1E). PEG was added into our linking ester because it has an ability to reduce antigenicity and immunogenicity of PEG-linked molecules and improve the circulating half-lives in vivo due to apparent size increasing[44].

4.2 SCRD BsAbs binding ability assessment

To test the binding potency of SCRD BsAbs to the injured myocardium in vitro, we cocultured SCRD BsAbs with normal and injured new natal rat cardiomyocytes (NRCMs). The half non-specific (HNS) BsAbs (non-specific IgG-F(ab')$_2$-anti-CD34-F(ab')$_2$) were created for control purpose (Fig. 2). The result demonstrated that SCRD BsAbs had a strong binding ability with injured NRCMs rather than normal NRCMs. To test the BMSCs-recruitment potency of SCRD BsAbs in the blood stream, we created an in vitro blood environment to mimic the BMSCs recruitment (Fig. S1). The group of HNS BsAbs (non-specific IgG-F(ab')$_2$-anti-CMHC-F(ab')$_2$) was used as a control group. In contrast to the control group, the SCRD BsAbs successfully recruited 10.7% of BMSCs.
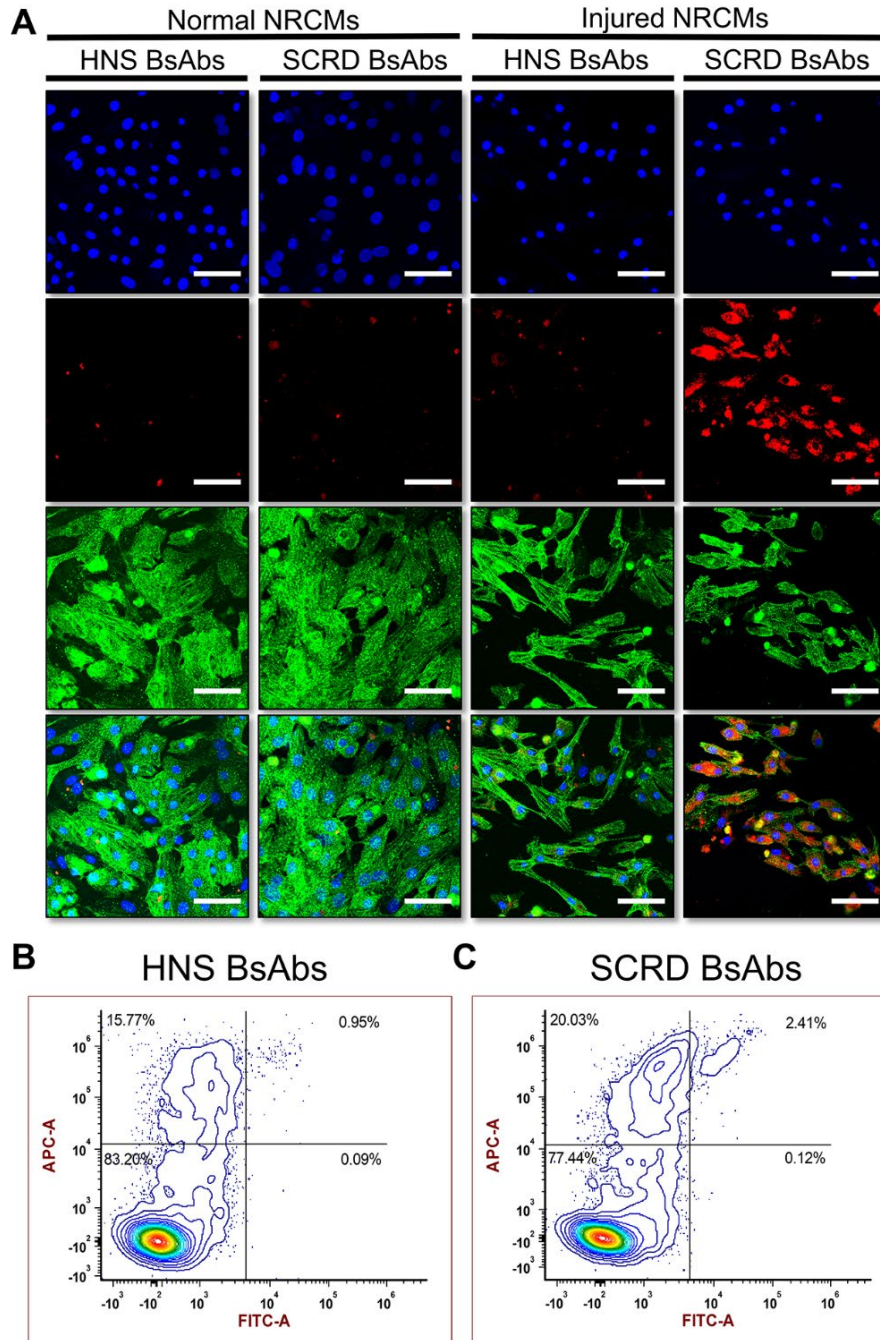
Fig 2. Binding ability of SCRD BsAbs. Representative fluorescent micrographs showing SCRD BsAbs or half non-specific (HNS) BsAbs (non-specific IgG-F(ab')$_2$-anti-CD34-F(ab')$_2$) was incubated with normal or injured NRCM for 1 h at 37 °C. Successful Cell binding was detected by antibodies (red). NRCMs were stained with anti-alpha sarcomeric actin antibodies (green). Nuclei were detected by DAPI. Scale bar, 50 μm. We created an *in vitro* blood environment to mimic the BMSCs recruitment by adding 1×10^6 DiD pre-labeled EPCs, and then mixed with HNS BsAbs (non-specific IgG-F(ab')$_2$-anti-CMHC-F(ab')$_2$) (A); or SCRD BsAbs (B). The recruited EPCs were detected with FITC secondary antibody.
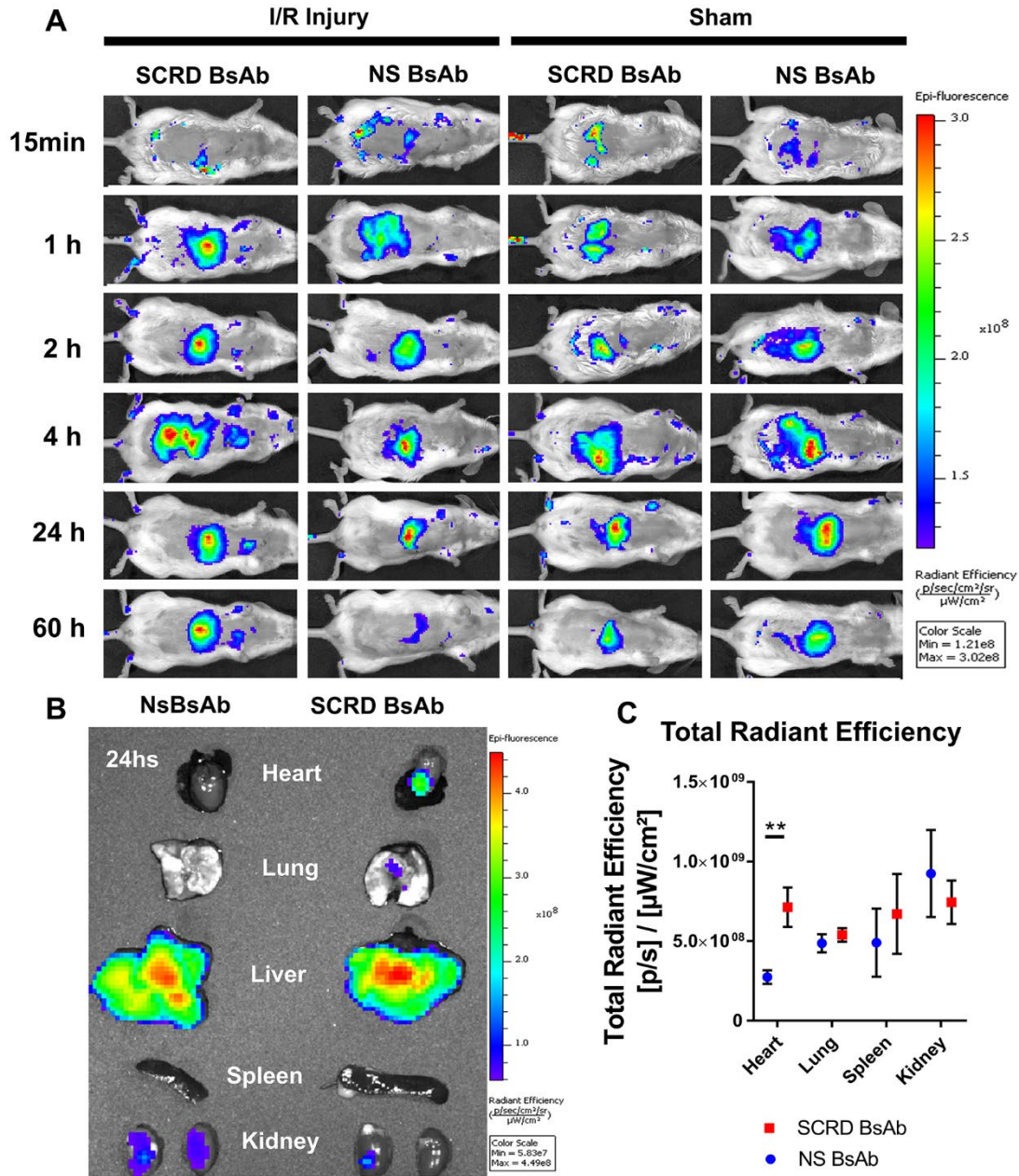
Fig 3. Biodistribution of SCRD BsAbs in G-CSF pre-mobilized mice with or without I/R heart injury. (A) SCRD and NS BsAbs that prelabeled with fluorescence tracer 633 were injected into G-CSF pretreated mice. IVIS images were taken at 15 mins, 1 h, 2 hrs, 4 hrs, 24 hrs and 60 hrs after BsAb injection. (B) 24 hrs after BsAb injection, major organs were excised and imaged. (C) The total radiant efficiencies in heart, lung, spleen and kidney were measured. n=3 in each group. All data were means ± s.d. Comparisons among groups were performed using two-way ANOVA followed by *post hoc* Bonferroni test. The comparisons between samples were indicated by lines, and the statistical significance was indicated by asterisks above the lines. "**" $P < 0.01$.

To test the homing potency of SCRD BsAbs to the injured myocardium in vivo, we intravenously injected prelabeled SCRD or non-specific (NS) BsAbs into I/R injured or sham mice. The prelabeled BsAbs were tracked with the IVIS imaging system for 60 hours (Fig. 3A). The results showed that SCRD BsAbs had a higher ability to home to injured myocardium than that of control groups and retained in the injured heart for at least 60 hours. Biodistribution of SCRD BsAbs and NS BsAbs in the I/R injured mice was assessed using IVIS at 24 hours after BsAb injection (Fig. 3B and C). The data not only confirmed the homing ability of SCRD BsAbs to I/R injured heart, but also suggested that liver and kidney were two main routes for BsAb elimination.

4.3 Redirecting of endogenous BMSCs to the injured myocardium by SCRD BsAbs

To test the therapeutic safety and efficacy of SCRD BsAbs, we induced MI in mice with an ischemic/reperfusion (I/R) procedure. This model highly mimicked the MI after myocardial reperfusion therapy such as PCI[33]. The animals were randomly separated into 5 different groups. Sham and PBS groups were used as positive and negative controls, respectively. The rest of animals with MI injury received treatments as: 1) G-CSF mobilization only (without SCRD BsAbs administration); 2) SCRD BsAbs only (without G-CSF mobilization); or 3) G-CSF with SCRD BsAbs.

The G-CSF mobilization is a well-established strategy[21]. Our previous study confirmed the relationship between G-CSF administration timeline and the elevation of $CD34^+$ cells in the blood stream[30]. After 3 days of G-CSF administration, SCRD BsAbs was administered 6 hours after the final dose of G-CSF (Fig. 3A). Echocardiography was performed 4 hours after the surgery on day 0 (baseline) and again before the animals were euthanized on day 21(endpoint) (Fig. 4A). Left ventricular ejection fraction (LVEF) (Fig. 4B) and left ventricular fractional shortening (LVFS)

(Fig. 4E) at baseline were indistinguishable among all 4 groups except sham group, which means that a uniform degree of initial myocardial infarct was created. 3 weeks after various treatment, the hearts from the group with both G-CSF mobilization and SCRD BsAbs administration had the highest LVEFs (Fig. 4C) and LVFSs (Fig. 4F). The treatment effects showed that the group with G-CSF mobilization and SCRD BsAbs administration had the largest restoration of LVEF (Fig. 4D) and LVFS (Fig. 4G). Masson's trichrome staining (Fig. 5A) revealed that SCRD BsAbs treatment after G-CSF administration led to decrease in infarction size (Fig. 5B), increase in LV wall thickness (Fig. 5C), and increase in viable tissue in the risk area (Fig. 5D). Moreover, to evaluate the biocompatibility of SCRD BsAbs, an independent experiment was performed by giving of SCRD BsAbs in normal mice and euthanized those animals 7 days after. The infiltration of T lymphcytes (CD3$^+$, CD8$^+$) and macrophages (CD68$^+$) were not found in the cardiac tissue (Fig. S1). Taken together, SCRD BsAb is a biocompatible drug which restored cardiac functions and preserved cardiac morphometry with G-CSF pre-mobolization.
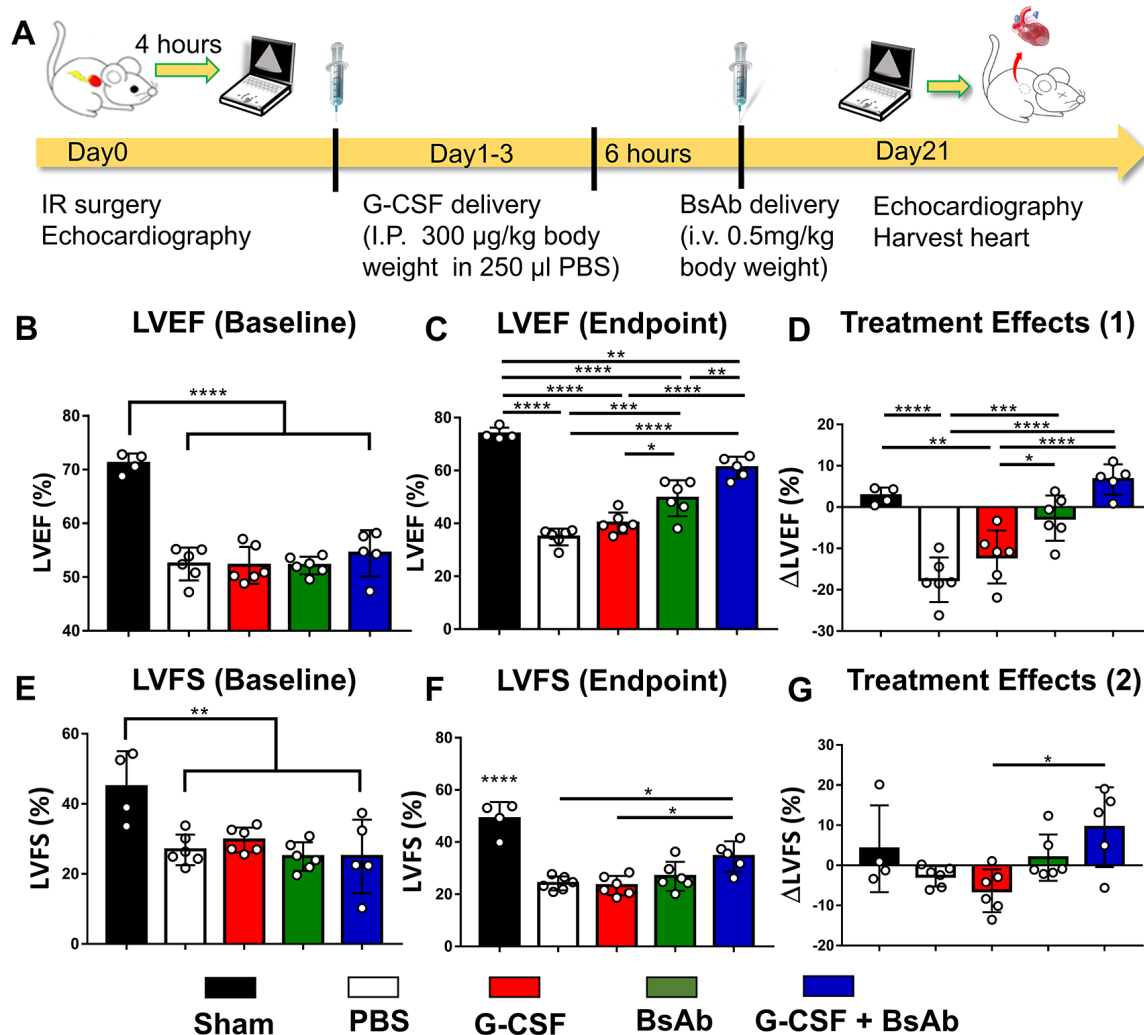
Fig 4. Cardiac functional benefits of SCRD BsAb treatment in G-CSF pre-mobilized animals. (A) Schematic showing the overall animal study design. Cardiac functions were assessed at baseline (4 h) and endpoint (3 weeks), including LVEF (B-D) and LVFS (E-G). n=4 for Sham group, n=6 for PBS, G-CSF, and BsAb group, and n=5 for G-CSF + BsAb group. All data were means ± s.d. Comparisons among groups were performed using one-way ANOVA followed by *post hoc* Bonferroni test. The comparisons between samples were indicated by lines, and the statistical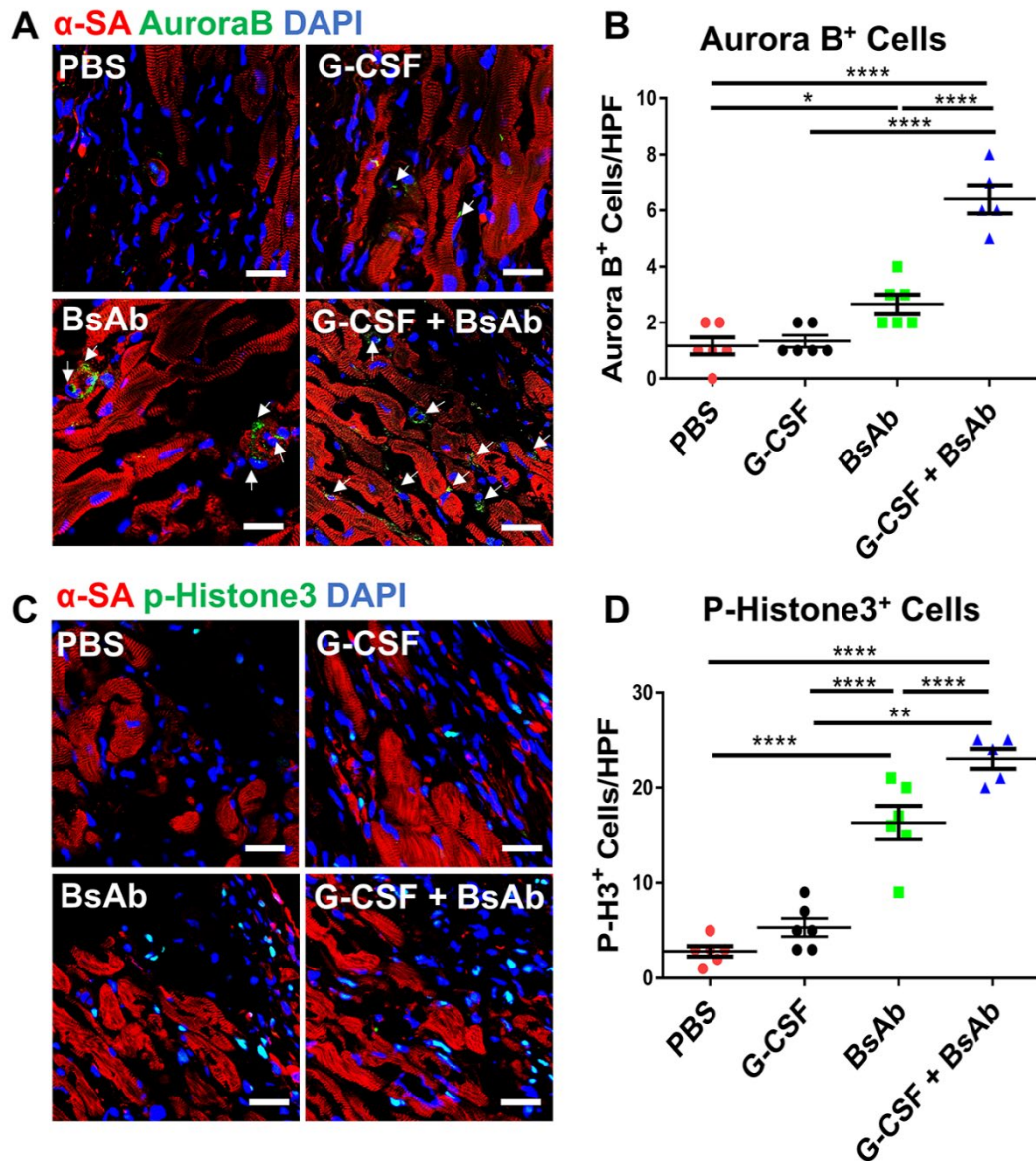 significance was indicated by asterisks above the lines. "*" indicated *P* < 0.05. "**" P <0.01. "***" P <0.001. "****" P <0.0001.
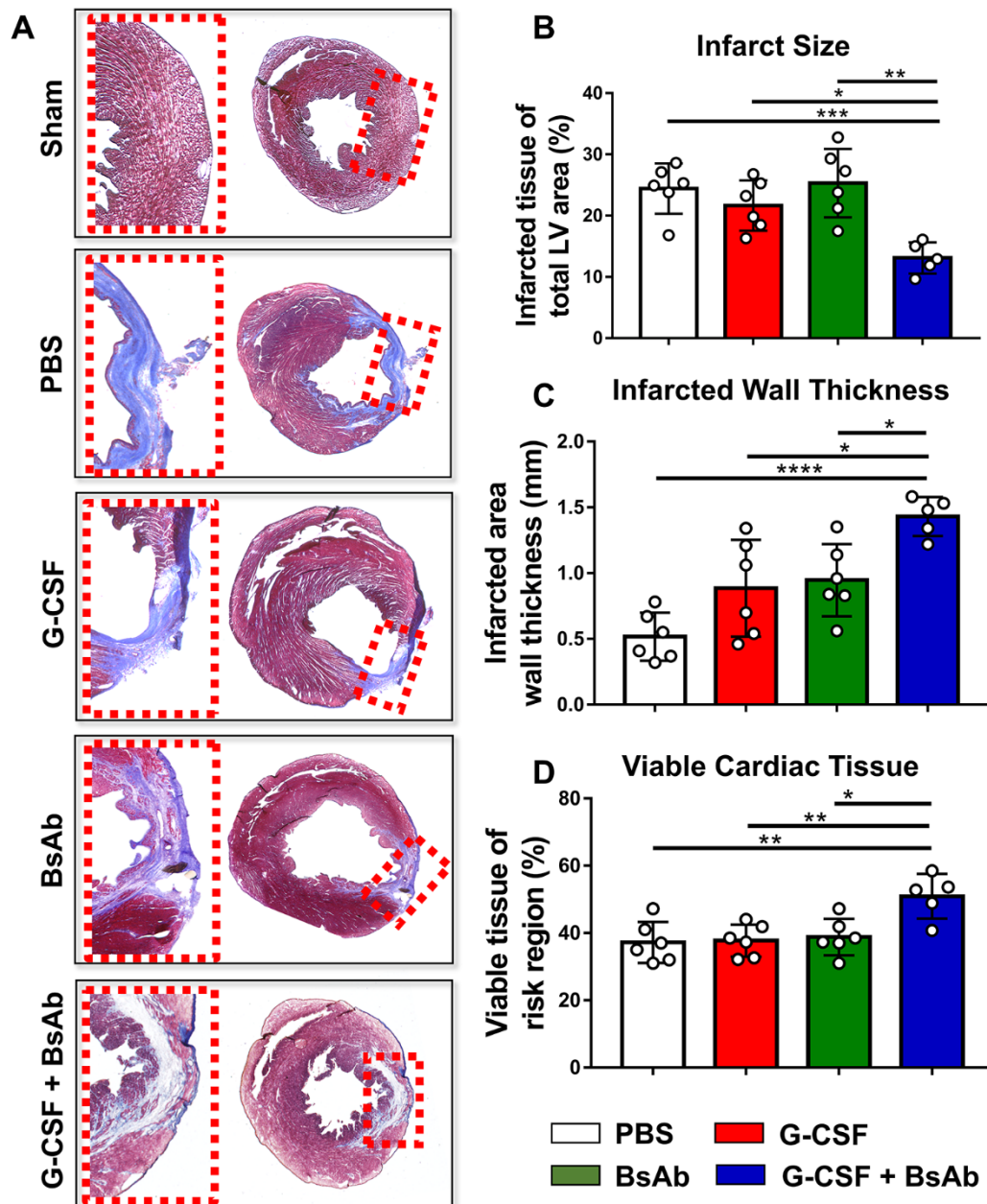
Fig 5. Cardiac structural benefit from SCRD BsAb treatment. (A) Masson's Trichrome staining was performed 10 μm-thick heart cryo-sections. Morphometric parameters including infarct size (B), infarct wall thickness (C) and the percentage of viable myocardium at risk area (D), measured from Masson's Trichrome staining images *via* NIH Image J software. n=6 for PBS, G-CSF, and BsAb group, n=5 for G-CSF + BsAb group. All data were means ± s.d. Comparisons among groups were performed using one-way ANOVA followed by *post hoc* Bonferroni test. The comparisons between samples were indicated by lines, and the statistical significance was indicated by asterisks above the lines. "*" indicated $P < 0.05$. "**" $P < 0.01$.

4.4 SCRD BsAbs promote cell cycling *via* BMSCs recruitment

SCRD BsAbs therapy after G-CSF treatment increased the vasculature density in the infarcted area (Figs. 6A and B). To explore the BMSCs recruitment potency, the BMSCs in the heart infarct zone was detected by immunohistochemistry method (Figs. 6C and S2). The result confirmed that BMSCs were efficiently recruited and homing to the infarcted myocardium. Furthermore, 3 cell cycling markers, including Aurora B (Figs. 7A and B), phospho-Histone3 (p-H3) (Figs. 7C and D) and ki67 (Fig. S3), were used to explore the mechanism of BMSCs caused cardiac repair. The result indicated that SCRD BsAbs therapy after G-CSF treatment promoted cell cycling in the infarcted region via BMSCs recruitment.

Fig 6. SCRD BsAbs treatment promotes angiogenesis and BMSC recruitment. (A) vWF-positive (green) capillary structures in the infarct area. Scale bar, 50 μm. (B) Quantitation of vWF-positive vasculatures. n=6 for PBS, G-CSF, and BsAb group, n=5 for G-CSF + BsAb group. (C) CD34+ cells in the infarcted area were detected *via* CD34 antibodies (green). Scale bar, 20 μm. (D) Quantitation of CD34-positive cells. n=6 for PBS, G-CSF, and BsAb group, n=5 for G-CSF + BsAb group. All data were means ± s.d. Comparisons among groups were performed using one-way ANOVA followed by *post hoc* Bonferroni test. The comparisons between samples were indicated by lines, and the statistical significance was indicated by asterisks above the lines. "****" P <0.0001.

143

Fig 7. SCRD BsAbs treatment promotes angiogenesis and BMSC recruitment. (A) vWF-positive (green) capillary structures in the infarct area. Scale bar, 50 μm. (B) Quantitation of vWF-positive vasculatures. n=6 for PBS, G-CSF, and BsAb group, n=5 for G-CSF + BsAb group. (C) CD34+ cells in the infarcted area were detected *via* CD34 antibodies (green). Scale bar, 20 μm. (D) Quantitation of CD34-positive cells. n=6 for PBS, G-CSF, and BsAb group, n=5 for G-CSF + BsAb group. All data were means ± s.d. Comparisons among groups were performed using one-way ANOVA followed by *post hoc* Bonferroni test. The comparisons between samples were indicated by lines, and the statistical significance was indicated by asterisks above the lines. "****" P <0.0001.

5. Discussion

Stem cell therapy, which makes use of cellular paracrine secretions, is promising for heart regenerative therapy[45-47]. In the last decade, scientists have been using biomaterial and bioengineering approaches to deliver different stem cells[48] and stem-cell products[16] to the heart for MI treatment. However, the transplantation of biomaterials or allogeneic stem cells still needs to overcome a number of hurdles, such as the quality control of cell products, clinical practicality, the toxicity of biomaterial degradation, low cell retention/engraftment, and immune reactions[18]. To minimize these limitations, our study introduces an immunotherapy approach that engineering a SCRD BsAb to redirect and lead the pre-mobilized endogenous BMSCs for cardiac repair. SCRD BsAbs exerts a binding specificity to CD34 on BMSCs and CMHC on injured myocardium. Since the design of SCRD BsAb is based on chemically connecting $F(ab')_2$ fragments from different antibodies *via* esters with PEG, SCRD BsAb may reduce antigenicity and immunogenicity and improve circulating half-lives *in vivo* due to its apparent size increasing[44]. The present study confirmed the safety and therapeutic efficacy of SCRD BsAbs in mice with I/R heart injury. Intravenous administration of SCRD BsAbs supports cardiac recovery by reducing scarring, promoting vasculature density, and boosting cardiac functions. Compare to the current stem cell therapy strategies, SCRD BsAb offers a better drug delivery route rather than intramyocardial injection[49] or surgical heart transplantation[16]. Moreover, SCRD BsAbs do not trigger "live-drug" issues because they are cell-free drugs that recruiting endogenous cells. For further clinical translation, we still need to optimize many aspects of SCRD BsAbs, such as cryo-stability, dose-response, simple/multiple dose response, half-life period and the risk of embolization in the veins. We will also need to optimize the design of BsAb to maximize BsAb affinity quantitatively *via* comparing the affinity of BsAb to Fab and $F(ab')_2$ fragments. Additionally, we need to evaluate

the impact of polymer link length and click reaction on the affinity of BsAb. However, as a proof-of-concept study using BsAbs to recruit pre-mobilized BMSCs for heart repair, the present study provides a new option on endogenous stem cell therapy.

6. References

1.   Benjamin, E. J. *et al. Heart Disease and Stroke Statistics'2017 Update: A Report from the American Heart Association. Circulation* **135**, (2017).

2.   Hensley, M. T. *et al.* Cardiac regenerative potential of cardiosphere-derived cells from adult dog hearts. *J. Cell. Mol. Med.* **19**, 1805–1813 (2015).

3.   Müller, P., Lemcke, H. & David, R. Stem Cell Therapy in Heart Diseases – Cell Types, Mechanisms and Improvement Strategies. *Cell. Physiol. Biochem.* **48**, 2607–2655 (2018).

4.   Porrello, E. R. & Olson, E. N. A neonatal blueprint for cardiac regeneration. *Stem Cell Res.* **13**, 556–570 (2014).

5.   Sarig, U. *et al.* Natural myocardial ECM patch drives cardiac progenitor based restoration even after scarring. *Acta Biomater.* **44**, 209–220 (2016).

6.   D. Shen, J. Tang, M. T. Hensley, T. Li, T. G. Caranasos, T. Zhang, K. C. Effects of Matrix Metalloproteinases on the Performance of Platelet Fibrin Gel Spiked With Cardiac Stem Cells in Heart Repair. *Stem Cells Transl. Med.* **5**, 793–803 (2016).

7.   Fleischer, S., Shapira, A., Feiner, R. & Dvir, T. Modular assembly of thick multifunctional cardiac patches. *Proc. Natl. Acad. Sci.* **114**, 1898 LP – 1903 (2017).

8.   Cuende, N., Rico, L. & Herrera, C. Concise review: bone marrow mononuclear cells for the treatment of ischemic syndromes: medicinal product or cell transplantation? *Stem Cells Transl. Med.* **1**, 403–408 (2012).

9.   Abreu, S. C. *et al.* Bone marrow-derived mononuclear cells vs. mesenchymal stromal cells in experimental allergic asthma. *Respir. Physiol. Neurobiol.* **187**, 190–198 (2013).

10.   Leong, Y. Y., Ng, W. H., Ellison-Hughes, G. M. & Tan, J. J. Cardiac Stem Cells for Myocardial Regeneration: They Are Not Alone. *Front. Cardiovasc. Med.* **4**, 47 (2017).

11. Murry, C. E. *et al.* Haematopoietic stem cells do not transdifferentiate into cardiac myocytes in myocardial infarcts. *Nature* **428**, 664 (2004).

12. Fujii, H. *et al.* A novel application of myocardial contrast echocardiography to evaluate angiogenesis by autologous bone marrow cell transplantation in chronic ischemic pig model. *J. Am. Coll. Cardiol.* **43**, 1299–1305 (2004).

13. Lai, R. C. *et al.* Proteolytic Potential of the MSC Exosome Proteome: Implications for an Exosome-Mediated Delivery of Therapeutic Proteasome. *Int. J. Proteomics* **2012**, 971907 (2012).

14. Bianconi, V. *et al.* Endothelial and cardiac progenitor cells for cardiovascular repair: A controversial paradigm in cell therapy. *Pharmacol. Ther.* **181**, 156–168 (2018).

15. Agbulut, O. *et al.* Can bone marrow-derived multipotent adult progenitor cells regenerate infarcted myocardium? *Cardiovasc. Res.* **72**, 175–183 (2006).

16. Huang, K., Hu, S. & Cheng, K. A New Era of Cardiac Cell Therapy: Opportunities and Challenges. *Adv. Healthc. Mater.* **0**, 1801011 (2018).

17. Takayuki, A. *et al.* Bone Marrow Origin of Endothelial Progenitor Cells Responsible for Postnatal Vasculogenesis in Physiological and Pathological Neovascularization. *Circ. Res.* **85**, 221–228 (1999).

18. Tang, J.-N. *et al.* Concise Review: Is Cardiac Cell Therapy Dead? Embarrassing Trial Outcomes and New Directions for the Future. *Stem Cells Transl. Med.* 354–359 (2018). doi:10.1002/sctm.17-0196

19. Greenbaum, A. M. & Link, D. C. Mechanisms of G-CSF-mediated hematopoietic stem and progenitor mobilization. *Leukemia* **25**, 211 (2010).

20. Hopman, R. K. & DiPersio, J. F. Advances in stem cell mobilization. *Blood Rev.* **28**, 31–40

(2014).

21. Orlic, D. *et al.* Mobilized bone marrow cells repair the infarcted heart, improving function and survival. *Proc. Natl. Acad. Sci.* **98**, 10344 LP – 10349 (2001).

22. England, T. J. *et al.* Granulocyte-Colony Stimulating Factor (G-CSF) for stroke: an individual patient data meta-analysis. *Sci. Rep.* **6**, 36567 (2016).

23. Choudhury, T. *et al.* An exploratory randomized control study of combination cytokine and adult autologous bone marrow progenitor cell administration in patients with ischaemic cardiomyopathy: the REGENERATE-IHD clinical trial. *Eur. J. Heart Fail.* **19**, 138–147 (2017).

24. Husain, B. & Ellerman, D. Expanding the Boundaries of Biotherapeutics with Bispecific Antibodies. *BioDrugs* **32**, 441–464 (2018).

25. Fan, G., Wang, Z., Hao, M. & Li, J. Bispecific antibodies and their applications. *J. Hematol. Oncol.* **8**, 130 (2015).

26. Kontermann, R. E. & Brinkmann, U. Bispecific antibodies. *Drug Discov. Today* **20**, 838–847 (2015).

27. Bannas, P., Hambach, J. & Koch-Nolte, F. Nanobodies and Nanobody-Based Human Heavy Chain Antibodies As Antitumor Therapeutics. *Front. Immunol.* **8**, 1603 (2017).

28. Jost, C. & Plückthun, A. Engineered proteins with desired specificity: DARPins, other alternative scaffolds and bispecific IgGs. *Curr. Opin. Struct. Biol.* **27**, 102–112 (2014).

29. Sharkey, R. M., Rossi, E. A., McBride, W. J., Chang, C.-H. & Goldenberg, D. M. Recombinant bispecific monoclonal antibodies prepared by the dock-and-lock strategy for pretargeted radioimmunotherapy. *Semin. Nucl. Med.* **40**, 190–203 (2010).

30. Li, Z. *et al.* Pretargeting and Bioorthogonal Click Chemistry-Mediated Endogenous Stem

Cell Homing for Heart Repair. *ACS Nano* **12**, 12193–12200 (2018).

31. Spiess, C., Zhai, Q. & Carter, P. J. Alternative molecular formats and therapeutic applications for bispecific antibodies. *Mol. Immunol.* **67**, 95–106 (2015).

32. Vandergriff, A. C., Hensley, M. T. & Cheng, K. Isolation and Cryopreservation of Neonatal Rat Cardiomyocytes. *J. Vis. Exp.* 1–7 (2015). doi:10.3791/52726

33. Su, T. *et al.* Platelet-Inspired Nanocells for Targeted Heart Repair After Ischemia/Reperfusion Injury. *Adv. Funct. Mater.* **0**, 1803567 (2018).

34. Petit, I. *et al.* G-CSF induces stem cell mobilization by decreasing bone marrow SDF-1 and up-regulating CXCR4. *Nat. Immunol.* **3**, 687 (2002).

35. Servida, F. *et al.* Functional and Morphological Characterization of Immunomagnetically Selected CD34+ Hematopoietic Progenitor Cells. *Stem Cells* **14**, 430–438 (1996).

36. Quirici, N. *et al.* Isolation of bone marrow mesenchymal stem cells by anti-nerve growth factor receptor antibodies. *Exp. Hematol.* **30**, 783–791 (2002).

37. Fina, L. *et al.* Expression of the CD34 gene in vascular endothelial cells. *Blood* **75**, 2417 LP – 2426 (1990).

38. Sidney, L. E., Branch, M. J., Dunphy, S. E., Dua, H. S. & Hopkinson, A. Concise review: evidence for CD34 as a common marker for diverse progenitors. *Stem Cells* **32**, 1380–1389 (2014).

39. Nakayama, H. *et al.* Differential expression of CD34 in normal colorectal tissue, peritumoral inflammatory tissue, and tumour stroma. *J. Clin. Pathol.* **53**, 626–629 (2000).

40. Blanpain, C., Lowry, W. E., Geoghegan, A., Polak, L. & Fuchs, E. Self-Renewal, Multipotency, and the Existence of Two Cell Populations within an Epithelial Stem Cell Niche. *Cell* **118**, 635–648 (2004).

41. Li, F. *et al.* Inhibition of myosin IIA–actin interaction prevents ischemia/reperfusion induced cardiomyocytes apoptosis through modulating PINK1/Parkin pathway and mitochondrial fission. *Int. J. Cardiol.* **271**, 211–218 (2018).

42. CALAMINUS, S. D. J. *et al.* MyosinIIa contractility is required for maintenance of platelet structure during spreading on collagen and contributes to thrombus stability. *J. Thromb. Haemost.* **5**, 2136–2145 (2007).

43. Hartman, M. A. & Spudich, J. A. The myosin superfamily at a glance. *J. Cell Sci.* **125**, 1627–1632 (2012).

44. Chapman, A. P. PEGylated antibodies and antibody fragments for improved therapy: a review. *Adv. Drug Deliv. Rev.* **54**, 531–545 (2002).

45. Chen, T. S. *et al.* Mesenchymal stem cell secretes microparticles enriched in pre-microRNAs. *Nucleic Acids Res.* **38**, 215–224 (2010).

46. Davis, M. E. Exosomes: What do we love so much about them? *Circ. Res.* **119**, 1280–1282 (2016).

47. Wang, K. *et al.* Enhanced Cardioprotection by Human Endometrium Mesenchymal Stem Cells Driven by Exosomal MicroRNA-21. *Stem Cells Transl. Med.* **6**, 209–222 (2016).

48. Segers, V. F. M. & Lee, R. T. Stem-cell therapy for cardiac disease. *Nature* **451**, 937–942 (2008).

49. Amado, L. C. *et al.* Cardiac repair with intramyocardial injection of allogeneic mesenchymal stem cells after myocardial infarction. *Proc. Natl. Acad. Sci. U. S. A.* **102**, 11474–11479 (2005).

CHAPTER 5. Concluding Remarks and Future Directions

At present, the safety of cardiac cell therapy in clinical treatments has been widely demonstrated, but there are many limitations in its application and effectiveness. The goal of this dissertation is to present studies that have sought to develop safe and effective ways to deliver cell derivatives to the injured myocardium for heart repair after MI. To this end, it explains 3 major methods that reduce the drawbacks of using live cells and investigates better pre-clinical treatment methods of using translatable cell derivatives or bispecific antibodies.

Chapter 1 mainly provides the background and elaborates on the design and application of cell derivatives that integrate with multiple types of biomaterials to create new treatment strategies. Paracrine mechanisms play an important role in cell therapy. Cell-secreted growth factors, chemokines, and other bioactive substances promote myocardial protection and angiogenesis, regulating local inflammatory responses, and promoting extracellular matrix remodeling. However, clinical applications of cell therapy are hampered by several limitations, including low retention/engraftment of cells, low stability, risk of immunogenicity, and tumorigenicity. Thus, interdisciplinary studies of biomaterials, nanotechnology, and biomedicine may overcome these challenges and usher in cardiac regenerative therapies into a new era. The opportunities and challenges of many new treatment strategies in recent years have been discussed and evaluated herein so as to provide a rich theoretical basis for future research on cardiac cell therapy.

Chapter 2 introduces a clinically feasible, easy-to-store, and acellular artificial cardiac patch (artCP) that can overcome aforementioned obstacles. It also provides a proof-of-concept study with the patch in rodent and porcine models of cardiac injury. In this study, synthetic cardiac stromal cells (synCSC) were developed by encapsulating protein factors derived from CSC

conditioned media in PLGA. For better retention/engraftment, we embed synCSCs in a decellularized myoECM made from porcine hearts. This ECM has a natural ECM reticulated structure and elastic properties. The final product of artCP has a sustainable paracrine factor release ability and maintains its potency after long-term cryopreservation. In both rat and pig models of MI, transplantation of artCP improves cardiac recovery by reducing scarring, promoting angiomyogenesis, and boosting cardiac function.

Our study has several limitations. To reduce the injury associated with open-chest surgery, minimally invasive approaches to deliver the patch need to be developed in future iterations. Also, further mechanistic studies on myocardial regenerative pathways could help elucidate the modes of action involved in artCP therapies. Additionally, the length of the release of factors and artCP degradation rate are properties that need to be optimized to match the post-MI LV remodeling. Nevertheless, the present study shows the potential synergistic benefits of using synCSCs together with myoECM to provide an off-the-shelf cardiac patch with significant regenerative capacity.

Chapter 3 introduces a platelet-inspired nano-cell (PINC) that incorporates both prostaglandin E2 (PGE_2)-modified platelet membranes and cardiac stromal cell-secreted factors to target the I/R injured heart. Due to the duel targeting character of PINCs, their intravenous administration intervenes in the cardiac remodeling process after MI and potentially helps the MI patients after acute revascularization therapy. In this study, we evaluated the *in vitro* bioactivity of PINCs and their biodistribution after IV administration. The functional benefits in a mouse model of myocardial I/R injury showed that PINCs augmented cardiac function and mitigated heart remodeling, which is accompanied by the increase in cycling cardiomyocytes, the activation of endogenous stem/progenitor cells, and the promotion of angiogenesis.

Nevertheless, our study has several limitations. First, we investigated the cardiac repair through immunohistochemical analysis. Lineage tracing using transgenic mice will allow for more insightful analysis of the origin of newly formed blood vessels and cardiomyocytes. Second, our animal studies did not include an empty (no secretome) nanoparticle control group. Nonetheless, based on the *in vitro* data, these control nanoparticles are not expected to improve cardiac function in the animal model. In addition, for clinical applicability, a large animal model of I/R injury and a longer study duration will be needed to fully characterize the efficacy and safety of the PINC therapy.

Chapter 4 describes the design a stem cell re-directing (SCRD) bispecific antibody (BsAb) that is created by chemically linking F(ab')$_2$ fragments from monoclonal anti-CD34 and anti-cardiac myosin heavy chain (CMHC) antibodies *via* click reaction. This BsAb specifically targets circulating CD34-positive cells and injured cardiomyocytes simultaneously, so that the intravenous administration of BsAb redirects pre-mobilized BMSCs into the injured heart for cardiac repair. This method focused on recruiting endogenous stem cells rather than providing exoteric cells or cell-derivatives. Our studies in a mouse model with I/R injury demonstrated the safety and therapeutic potency of SCRD BsAb.

However, to be a clinically feasible product, we still need to elucidate many characteristics of the SCRD BsAbs, such as their cryo-stability, dose-response properties, simple/multiple dose response dynamics, half-life period, and the risk they pose of forming clots inside of veins. We also have to optimize their design to maximize BsAb affinity quantitatively by comparing the affinity of BsAb to Fab and F(ab')$_2$ fragments. Additionally, we need to evaluate the impact of polymer link length and click reaction to the affinity of BsAb. However, as a proof of concept for using BsAbs to recruit pre-mobilized BMSCs for heart repair, the present study effectively shows

the potential benefits of using SCRD BsAbs and provides a different perspective on stem cell therapies.

The role of paracrine mechanisms in cardiac regeneration has been studied for decades, but the mechanisms that drive cardiac repair in response to each paracrine molecule are still unclear, in part because these molecules are multifunctional and involved in a wide range of signaling pathways during cardiac remodeling. In addition, the diversity of molecular signaling pathways in space and time increases the complexity of the analysis. So, further exploration of specific mechanisms may enhance the development of paracrine therapeutic effects and benefit translational studies by upgrading cellular drugs into precision-guided therapeutics.

The drug delivery routes used and the safety of each treatment paradigm are major concerns for the clinical innovation of cell therapeutics. Although cardiac patches in some studies are delivered via a minimal-invasive procedure, most cardiac patches still require an open-chest surgery, which increases surgical trauma, risk of inflammation, and even death in the case of a failed operation. Thus, the value of the cardiac patch strategy and its worth to the patient is debatable. The intravenous delivery of cell therapeutics is obviously a less invasive, more favorable route for clinical practice. However, we have to improve many deficiencies the injectable drugs/biologics, such as their heart-homing ability, half-life, toxicity, effective dose, and elimination from the body over time.

These new therapeutic strategies need optimization in order to reach industrial production standards for viable clinical translation. Among these standards is manufacturing uniformity, including drug size, therapeutic combinations, targeting ability, purity, and so on. However, these new treatment paradigms are essential bridges that may enable the transfer of lab technologies into real clinical treatments which will potentially benefits patients with MI.

APPENDICES

Appendix A: Chapter 2 Supplemental Data

Supplementary Materials and methods

Derivation of human cardiac stem cells (CSCs)

Human cardiosphere-derived CSCs were derived from human hearts *via* cardiosphere method as previously described[10]. Briefly, myocardial samples harvested from human hearts were cut into fragments of 2 mm^3, washed with phosphate-buffered saline, and partially digested with collagenase (Sigma-Aldrich). The tissue fragments were cultured as cardiac explants on a 0.5 mg/ml fibronectin (Corning, Corning, NY, USA) solution coated surface in Iscove's modified Dulbecco's medium (Invitrogen, Carlsbad, CA, USA) containing 20% fetal bovine serum (Corning). A layer of stromal-like cells emerged from the cardiac explant with phase-bright cells over them. The explant-derived cells were harvested using TryPEL Select (Gibco). Harvested cells were seeded at a density of 2×10^4 cells/ml in Ultra Low Attachment flasks (Corning, Corning, NY) for cardiosphere formation. In about one week, explant-derived cells spontaneously aggregated into cardiospheres. The cardiospheres were collected and plated onto fibronectin-coated surfaces to generate cardiosphere-derived CSCs. All cultures were incubated in 5% CO2 at 37°C. Our lab has banked >50 human cardiosphere-derived CSC lines. These cells were ready for use in the lab so there was no need for recruitment of new human subjects.

Fabrication of synCSCs

The conditioned media contains various growth factors secreted by CSCs. As a biocompatible and biodegradable polymer, poly lactic-co-glycolic acid (PLGA) has provided a safe and non-toxic building block for various control-release systems. synCSC was fabricated through previous polymer encapsulation and membrane cloaking approaches[34,59]. Briefly, we

fabricated CSC factor-loaded synCSC by a water/oil/water (w/o/w) emulsion technique. We mix human CSC conditioned media containing polyvinyal alcohol (PVA) (0.1% w/v) as the internal aqueous phase in methylene chloride (DCM) containing PLGA as the oil phase. The mixture was sonicated on ice for 30 s and immediately introduced into water with PVA (0.7% w/v) to produce a w/o/w emulsion. The secondary emulsion was emulsified for 5 min on a high-speed homogenizer. The w/o/w emulsion was continuously stirred overnight at room temperature to promote solvent evaporation. The solidified synCSC was centrifuged, washed with sterilize PBS, lyophilized and stored at -80 °C. By varying the volumetric ratio of w/o/w and the amount of PLGA in the oil phase, we can fabricate PLGA microparticles with different sizes and shell thicknesses.

Enzyme-Mediated Degradation of artCPs

A round-shaped myoECM or artCP (diameter: 5 mm, thickness: 1 mm) was placed in DI water for 24 h and then placed in HEPES-buffered saline (HBS) solution with 0.2 mg/mL sodium azide (Sigma Chemical Co., St. Louis, MO) and 2 mg/mL collagenase (Sigma Chemical Co., St. Louis, MO). As control, a round-shaped artCP (diameter: 5 mm, thickness: 1 mm) was placed in HBS solution with 0.2 mg/mL sodium azide. Samples were weighed and incubated at 37 °C for five continuous days. Three samples from each group were weighed and imaged on each day.

Cardiac function assessment of rats

In order to measure rat cardiac dimensions and function, echocardiography was performed at 4h and 21 days after MI surgical operation following induction of anesthesia with a 1.5% isofluorane-oxygen mixture. Echocardiography was performed with a Philips Cx-30 Ultrasound System with a L15-7io high frequency probe. Two-dimensional long axis images were record from the left caudal (apical) view. Two-dimensional guided M-mode images at chordae tendineae level were evaluated. M-mode measurements of left ventricle end-diastolic and end-systolic dimensions

(LVEDD and LVESD, respectively) were performed by using the leading-edge method of the American Society of Echocardiography[63]. For estimation of each parameter, the average of three measurements from three different cycles in an image was obtained. Left ventricular end-diastolic and systolic volumes (LVEDV and LVESV, respectively) were calculated by the biplane method of disks (modified Simpson's rule). Ejection fraction (EF) was determined by using (LVEDV-LVESV/LVEDV) × 100%, and fractional shortening (FS) was calculated from the M-mode echocardiography images as (LVEDD-LVESD/LVEDD) × 100%.

Heart morphometry studies

After all animals were euthanized, hearts from rats or infarct cubic piece (1×1×1 cm) of pig hearts were collected and frozen in optimum cutting temperature (OCT) compound (Tissue-Tek, Torrance, CA) after equilibrated with increasing sucrose solutions up to 30% overnight. Hearts were then snap-frozen in liquid nitrogen, and cryo-sectioned with a thickness of 5 μm from the apex to the ligation level with 100 μm intervals for Masson's Trichrome staining. Masson's trichrome staining was performed as described in previous studies[34,35,64]. Images were acquired with a PathScan Enabler IV slide scanner (Advanced Imaging Concepts, Princeton, NJ). From the Masson's trichrome images, morphometric parameters including viable myocardium and infarct thickness were measured in each section with ImageJ software[36,37]. The cryo-sectioned with a thickness of 10 μm for Haematoxylin and eosin staining (H&E). Slides were fixed in Hematoxylin (Sigma-Aldrich, MO, USA) for 5 min at room temperature, and then rinsed in running water for 2 minutes; after decolorizing in acid alcohol for 2 seconds, rinsed again in sodium bicarbonate for 5 dips; rinsed out container with Dehydrant after 95% iso for 30 seconds, and then fixed in Eosin (Sigma-Aldrich, MO, USA) for 2 minutes, and then washed in dehydrant 100% (Richard-Allan

Scientific, MI, USA) and Xylnene (VWR, PA, USA) for 3 times. The slides were photographed by AZ100 multi-purpose zoom microscope system.

Triphenyl tetrazolium chloride (TTC) assay

TTC assay was performed to differentiate the viable cardiac tissue and the infarcted cardiac tissue. Sterilized solution of 2,3,5-Triphenyl Tetrazolium Chloride (TTC) was made by dissolving TTC (2g; MP Biomedicals, LLC) into 200ml of sterilized PBS and then pre-warmed at 37°C incubator for 30mins. The heart was collected and washed with sterilized PBS and then placed in freezer until the heart became stiff. Five sections (1cm in thickness) were cut from Apex to bottom and incubate in pre-warmed TTC solution at 37 °C for 30mins. Afterwards, the sections were fixed in 10% formaldehyde solution for 2 hours.

Cardiac function assessment for pigs

In order to measure pig cardiac dimensions and function, echocardiography was performed at 24h and 7 days after MI surgical operation. Following induction of sedation with TKX cocktail (1 mL/13-30 kg IM) and anesthesia with a mixture of isoflurane (0-5% in 100% oxygen), Echocardiography was accomplished by a Philips Cx-30 Ultrasound System with an S4-2 broadband sector array transducer. Two-dimensional long axis images were recorded from the left caudal (apical) view. Two-dimensional guided M-mode images at chordae tendineae level were evaluated. M-mode measurements of left ventricle end-diastolic and end-systolic dimensions (LVEDD and LVESD, respectively) were performed by using the leading-edge method of the American Society of Echocardiography[63]. For estimation of each parameter, the average of three measurements from three different cycles in an image was obtained. Left ventricular end-diastolic and systolic volumes (LVEDV and LVESV, respectively) were calculated by the biplane method of disks (modified Simpson's rule). Ejection fraction (EF) was determined by using (LVEDV-

LVESV/LVEDV) × 100%, and fractional shortening (FS) was calculated from the M-mode echocardiography images as (LVEDD-LVESD/LVEDD) × 100%.

Supplementary Figures
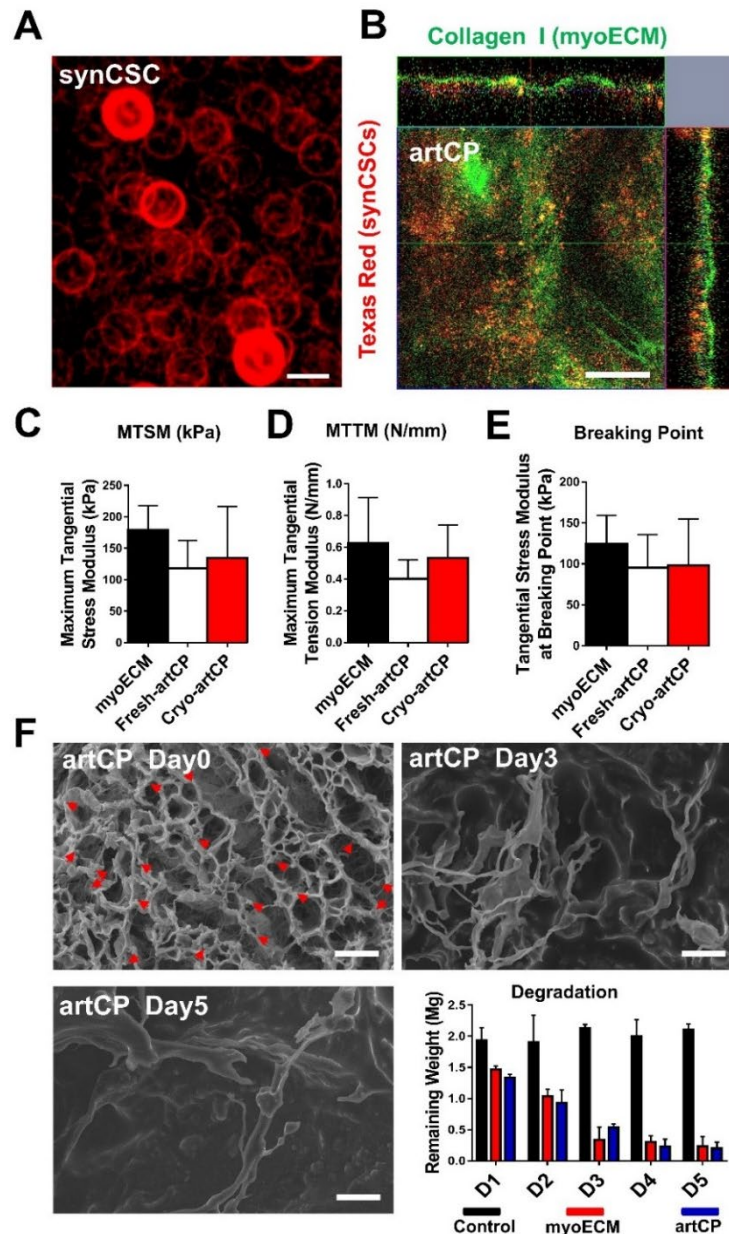
Fig. S1. Characterization of artCP. (A) Representative fluorescent micrographs showing DiD labelled synCSCs. Scale bar = 10 μm. (B) Representative 3D confocal image showing the distribution of synCSCs (red; DiD-labeled) in myoECM (green; stained with anti-collagen I antibodies). Scale bar = 25μm. Maximum tangential stress modulus (C), maximum tangential tension modulus (D), and Tangential stress modulus at breaking point (E) were measured by uniaxial mechanical testing. n = 5 in each group. (F) Enzyme-mediated degradation of myoECM and artCPs. The control group was artCP in HBS solution with 0.2 mg/mL sodium azide. n = 3 in each group. All data were means ± s.d. Comparisons among groups were performed using one-way ANOVA followed by *post hoc* Bonferroni test.

162
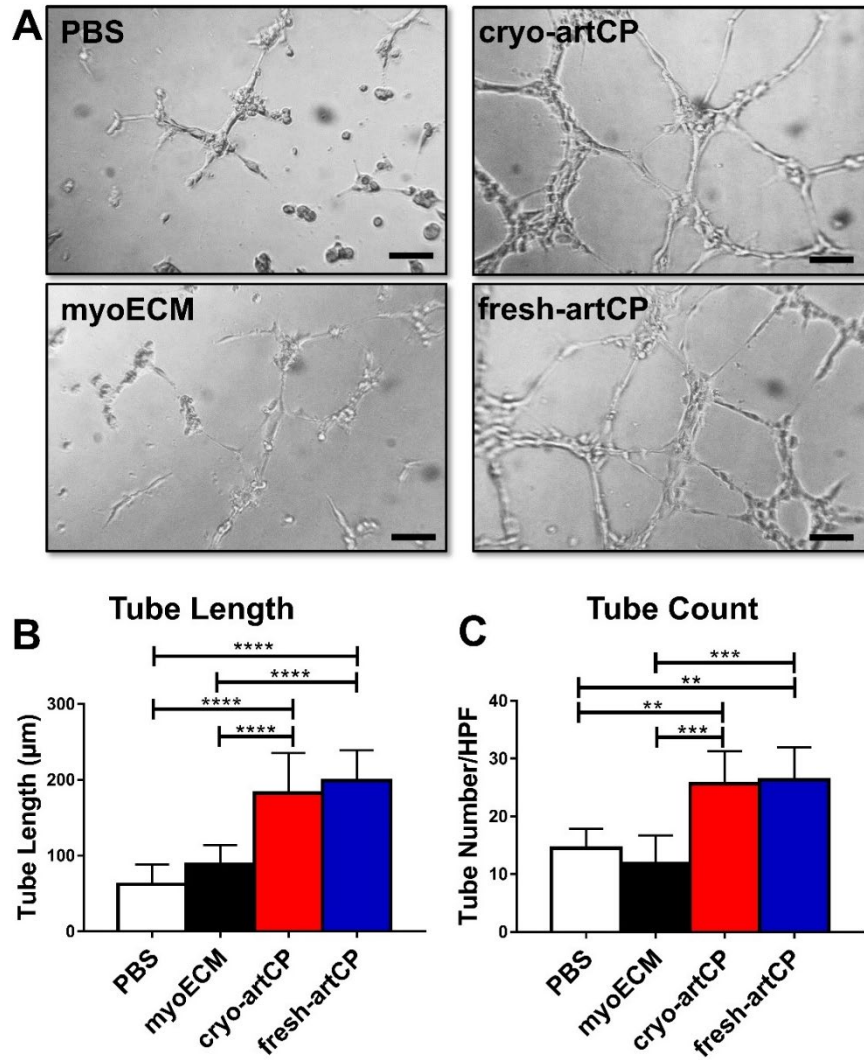
Fig. S2. Effects of artCP on endothelial cells in vitro. (A) Representative micrographs showing tube formation of endothelial cells in PBS, myoECM, cryo-artCP and fresh-artCP groups. Scale bar = 100 μm. The tube lengths (B) and tube numbers (C) were measured by Image J. n = 6 in each group. All data were means ± s.d. Comparisons among groups were performed using one-way ANOVA followed by *post hoc* Bonferroni test. The comparisons between samples were indicated by lines, and the statistical significance was indicated by asterisks above the lines. "**" indicated $P < 0.01$, "***" indicated $P < 0.001$, "****" indicated $P < 0.0001$.
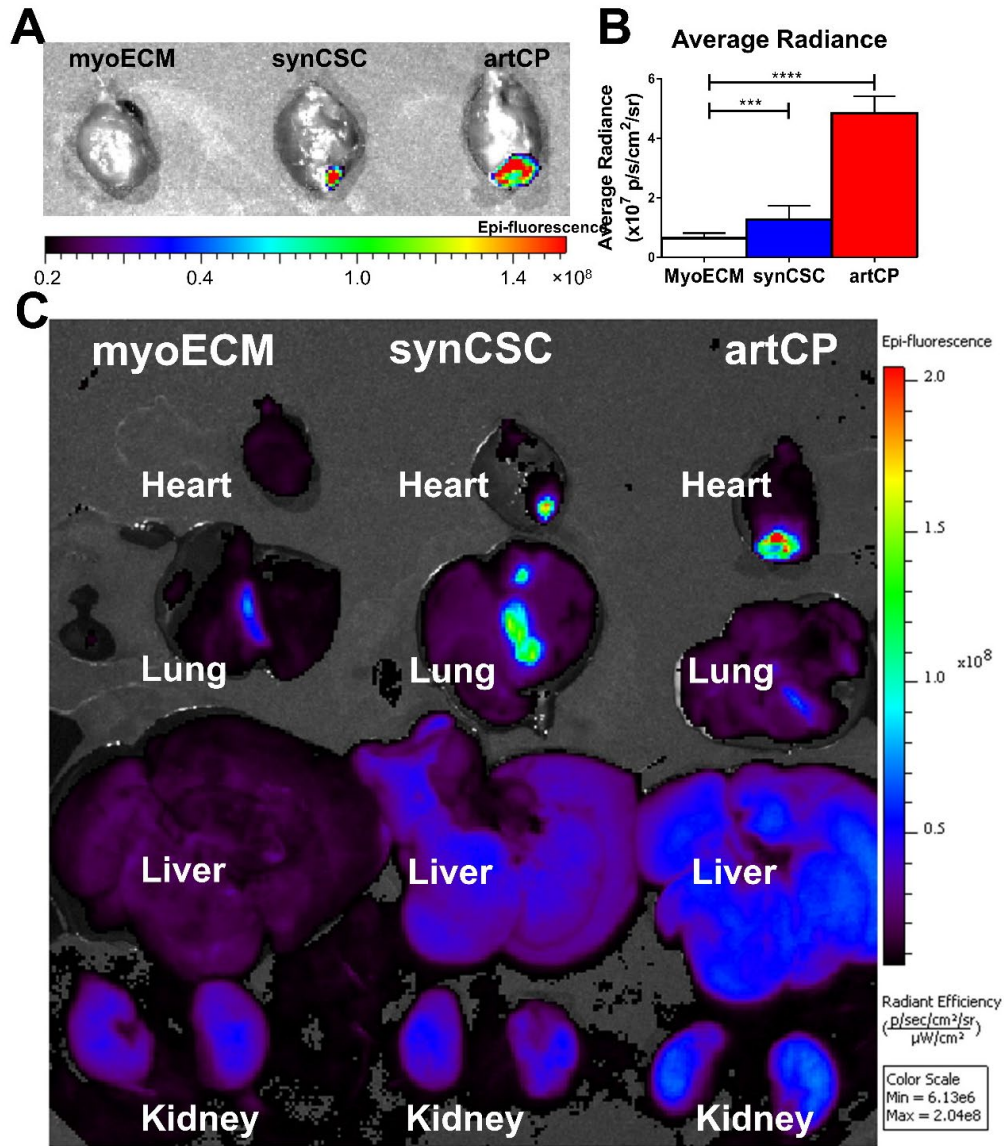
Fig. S3. SynCSC retention and distribution. To track the synCSC *in vivo*, we transplanted DiR labelled artCP to the heart of rat MI models. The rats administered with DiR labelled synCSC intramyocardial injection or empty myoECM transplantation were used as controls. (A) The hearts were collected and placed in Xenogen IVIS imaging system (Caliper Life Sciences, Mountain View, CA) to detect RFP fluorescence for retention analysis. (B) The average radiance in each group was measured by the Xenogen IVIS imaging system. n = 3 in each group. (C) All major organs were collected and placed in IVIS for biodistribution studies. All data were means ± s.d. Comparisons among groups were performed using one-way ANOVA followed by *post hoc* Bonferroni test. The comparisons between samples were indicated by lines, and the statistical significance was indicated by asterisks above the lines. "***" indicated $P < 0.001$, "****" indicated $P < 0.0001$.
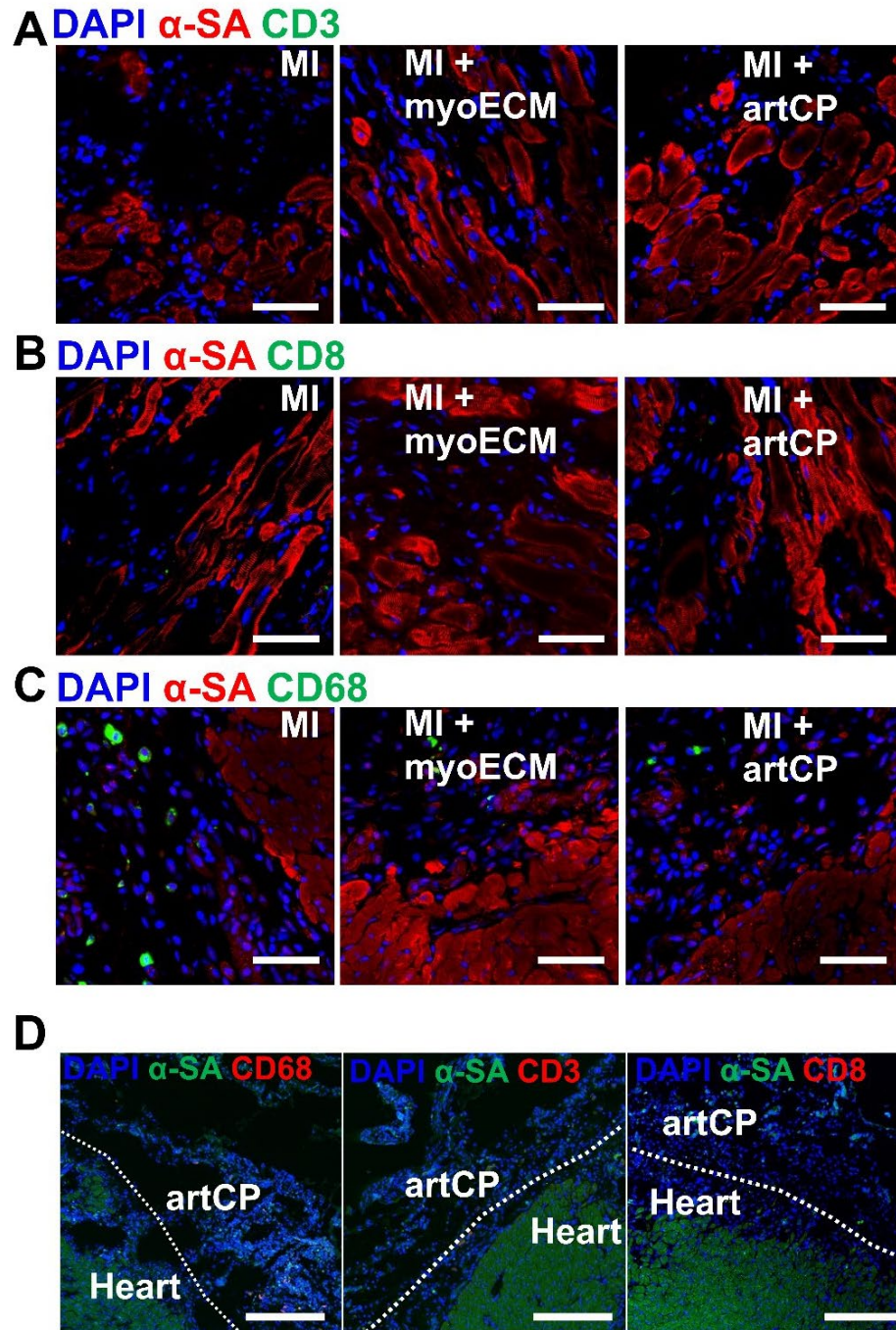
Fig. S4. Immunogenicity of artCP. 7 days after artCP or myoECM transplantation, the infiltration of T-lymphocytes, detected by anti-CD3 (A) (green) and anti-CD8 (green) (B) antibodies, were negligible. Nuclei were counterstained with DAPI (blue). Scale Bar = 50 μm. (C) Macrophages were labelled with anti-CD68 (green) antibodies. Scale Bar = 50 μm. (D) The same IHC staining was performed 21 days after transplantation. Cardiomyocytes were counterstained with anti-alpha sarcomeric actinin and FITC-conjugated secondary antibodies.
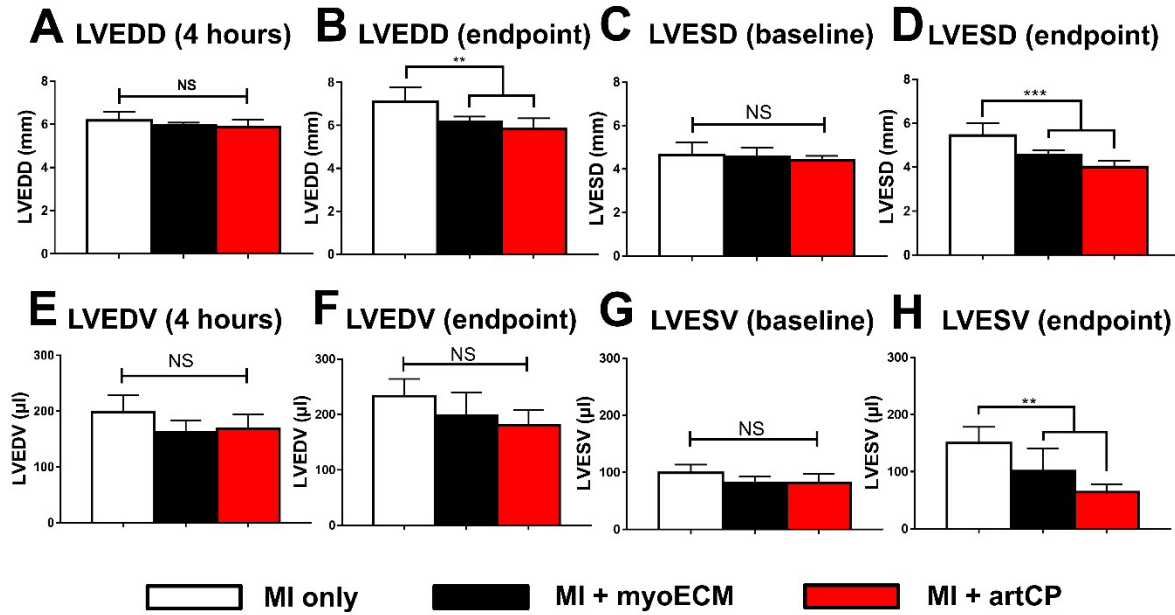
Fig. S5. Heart dimension measured by echocardiography. From the M-mode images at chordae tendineae level, left ventricle end-diastolic diameter (LVEDD) at 4 hours (baseline) (A) and 21 days (endpoint) (B) were measured. Also, the left ventricle end-systolic diameter (LVESD) at 4 hours (baseline) (C) and 21 days (endpoint) (D) were measured. From B-mode at long axis, left ventricle end-diastolic volume (LVEDV) at 4 hours (baseline) (E) and 21 days (endpoint) (F) were measured. Also, left ventricle end-systolic volume (LVESV) were also measured at 4 hours (baseline) (G) and 21 days (endpoint) (H). All data were means ± s.d. Comparisons among groups were performed using one-way ANOVA followed by *post hoc* Bonferroni test. The comparisons between samples were indicated by lines, and the statistical significance was indicated by asterisks above the lines. NS indicated $P > 0.05$, "*" indicated $P < 0.05$, "**" indicated $P < 0.01$, "***" indicated $P < 0.001$, "****" indicated $P < 0.0001$.
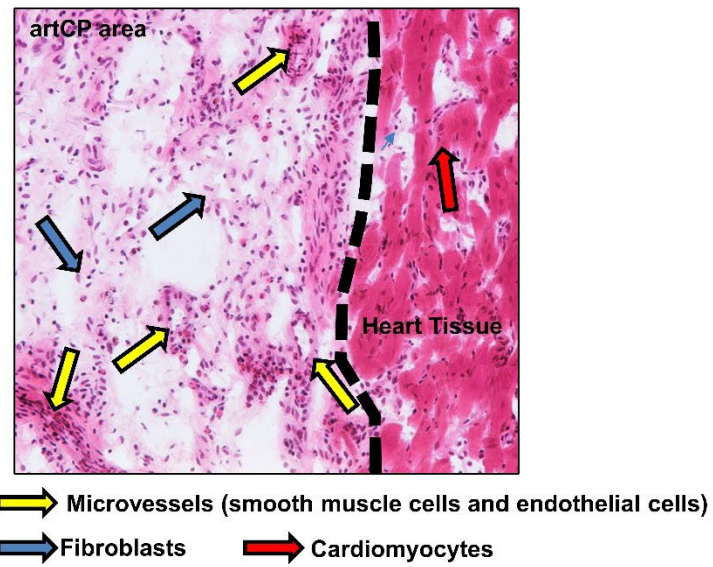
Fig. S6. H&E staining of whole artCP area on day 21. Representative H&E staining images showed that the artCP were generally replaced by fibroblasts, smooth muscle cells and endothelial cells.
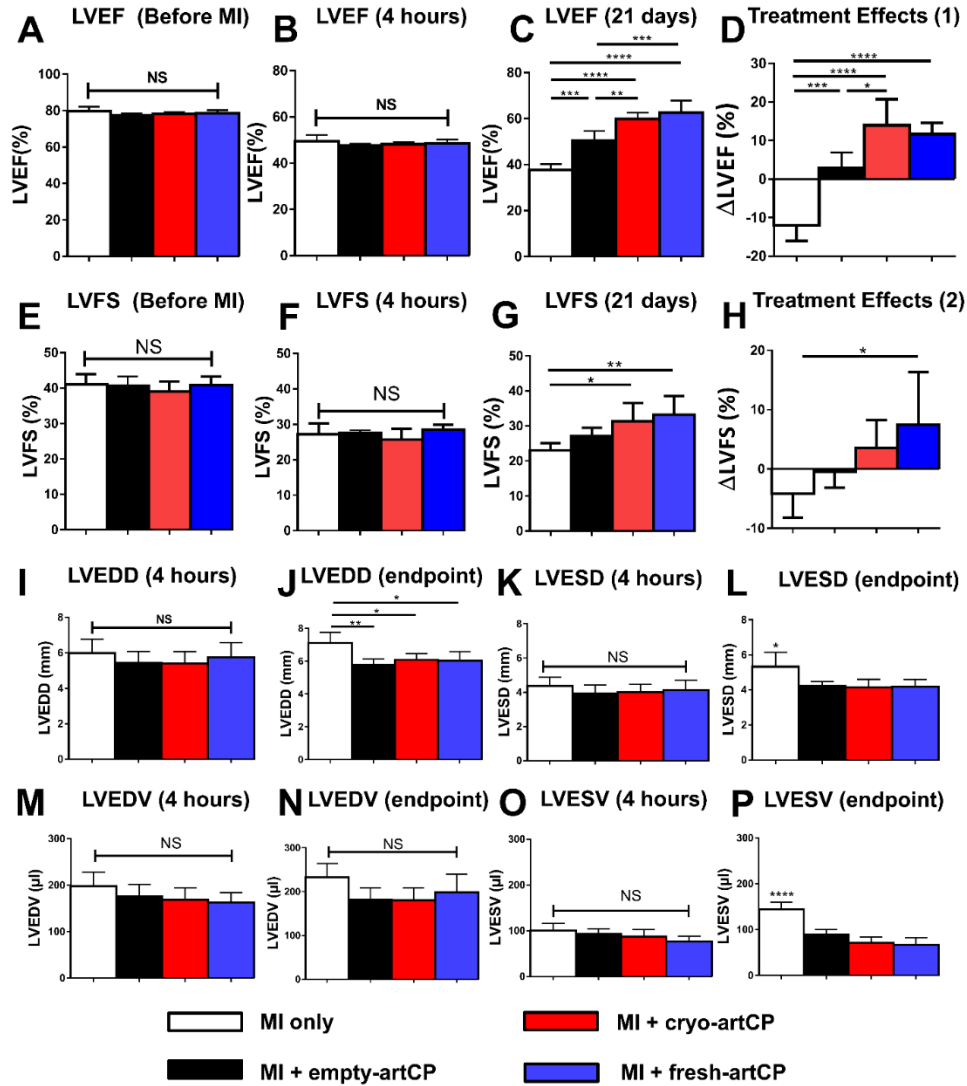
Fig. S7. Treatment effects after empty-, cryo- or fresh-artCP transplantation. The LVEF was analyzed before MI (A), 4hours after MI (B) and 21days after MI (C), and the cardiac pumping efficiency was measured by LVEF shift (D). n=5 in each group. The LVFS was also analyzed before MI (E), 4hours after MI (F) and 21days after MI (G), and the cardiac contractility was measured by LVFS variation (H). n=5 in each group. From M-mode images at chordae tendineae level, LVEDD at 4 hours (baseline) (I) and 21 days (endpoint) (J) were measured. Also, LVESD at 4 hours (baseline) (K) and 21 days (endpoint) (L) were measured. From B-mode at long axis, LVEDV at 4 hours (baseline) (M) and 21 days (endpoint) (N) were measured. Also, LVESV were also measured at 4 hours (baseline) (O) and 21 days (endpoint) (P). All data were means ± s.d. Comparisons among groups were performed using one-way ANOVA followed by *post hoc* Bonferroni test. The comparisons between samples were indicated by lines, and the statistical significance was indicated by asterisks above the lines. NS indicated $P > 0.05$, "*" indicated $P < 0.05$, "**" indicated $P < 0.01$, "***" indicated $P < 0.001$, "****" indicated $P < 0.0001$.
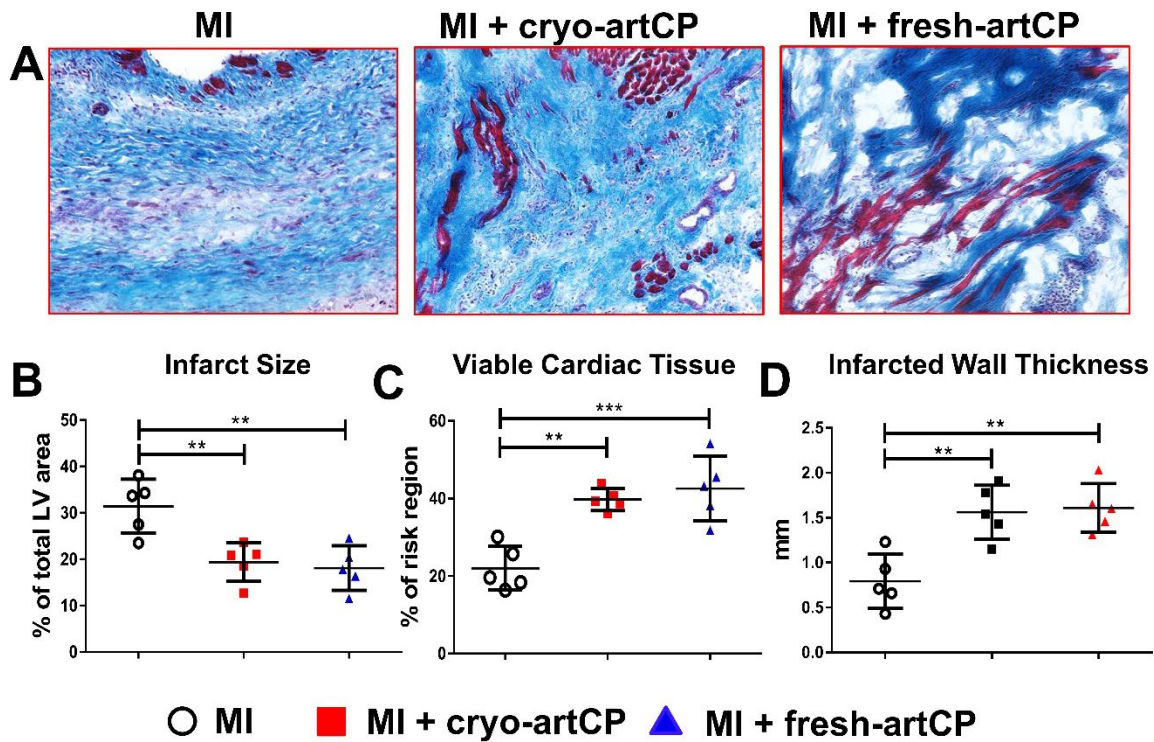
Fig. S8. Heart morphometry assessment. (A) Masson's Trichrome staining was performed using the HT15 Trichrome Staining (Masson) Kit on 5 μm cryo-sections. Morphometric parameters including infarct size (B), the percentage of viable myocardium at risk area (C), and infarct wall thickness (D) were measured from the Masson's Trichrome stained images via NIH ImageJ software. n=5 in each group. All data were means ± s.d. Comparisons among groups were performed using one-way ANOVA followed by *post hoc* Bonferroni test. The comparisons between samples were indicated by lines, and the statistical significance was indicated by asterisks above the lines. "**" indicated $P < 0.01$, "***" indicated $P < 0.001$.
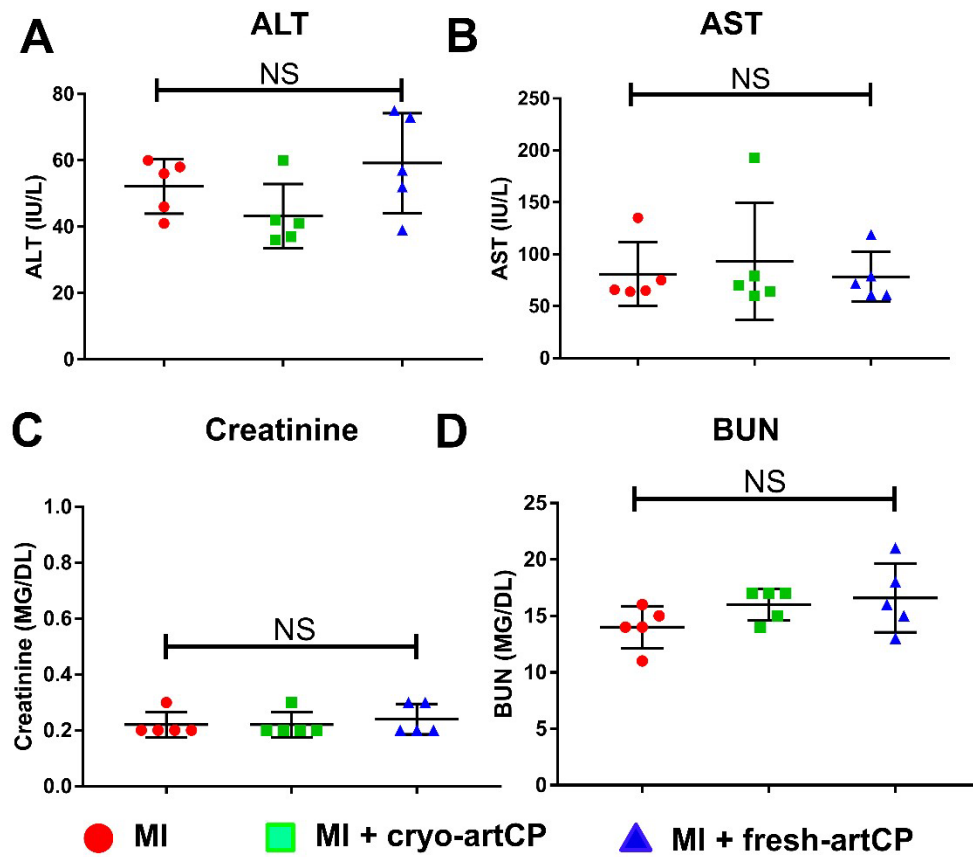
Fig. S9. Liver functions and kidney functions after ArtCP transplantation. (A) The alanine aminotransferase (ALT) and (B) aspartate aminotransferase (AST) expressions were evaluated by blood tests (NC State Veterinary Medicine diagnostic laboratories). (C-D) The blood creatinine (C) and blood urea nitrogen (D) measurements were examined to evaluate kidney toxicity of artCP transplantation (NC State Veterinary Medicine diagnostic laboratories). n=5 in each group. All data were means ± s.d. Comparisons among groups were performed using one-way ANOVA followed by post hoc Bonferroni test. NS indicated P > 0.05.
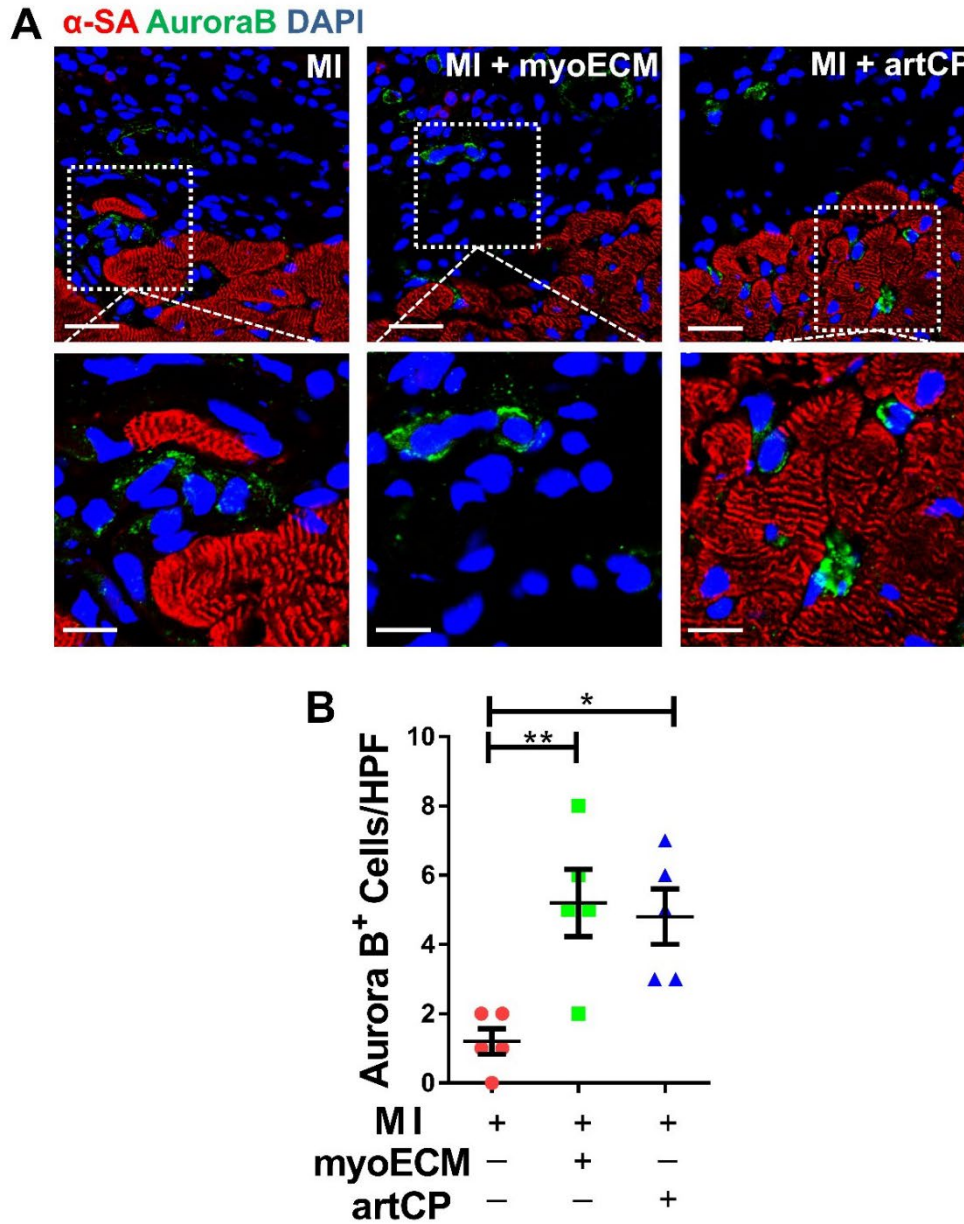
Fig. S10. Proliferation marker Aurora B staining. (A) Aurora B (green) was detected in the infarcted area from the hearts of MI only group, artCP and myoECM transplanted group. Scale bar= 25 μm. Scale bar zoomed snapshot = 10 μm. (B) Aurora B$^+$ cells were quantified. n=5 per group. All data were means ± s.d. Comparisons among groups were performed using one-way ANOVA followed by *post hoc* Bonferroni test. The comparisons between samples were indicated by lines, and the statistical significance was indicated by asterisks above the lines. "*" indicated $P < 0.05$, "**" indicated $P < 0.01$.
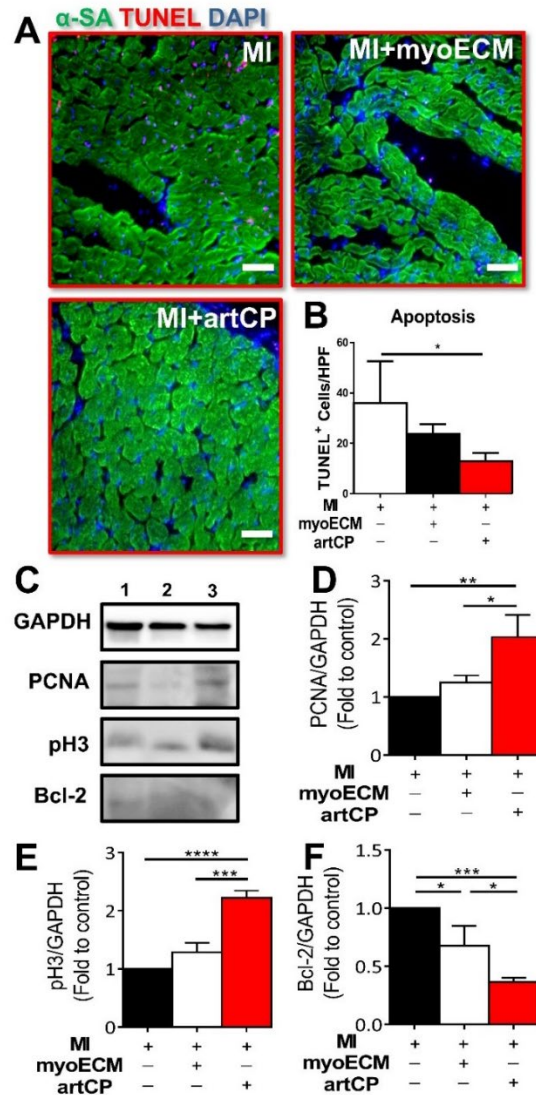
Fig. S11. The cardiac tissue proliferation and apoptosis. (A) The area around MI risk area was analyzed through IHC. All images were taken with an epi-fluorescent microscope (Olympus IX81). Scale bar = 25µm. (B) The TUNEL$^+$ expressed cells were counted and compared from the same images using the NIH Image J software. N=3 in each group. (C) Western blot analyses of protein markers including pCNA, pH3 and Bcl-2 were performed. 1. MI only group; 2. myoECM group; 3. artCP group. Quantification of pCNA (D), pH3 (E) and Bcl-2 (F) levels normalized to MI Control. All data were means ± s.d. Comparisons among groups were performed using one-way ANOVA followed by *post hoc* Bonferroni test. The comparisons between samples were indicated by lines, and the statistical significance was indicated by asterisks above the lines. "*" indicated $P < 0.05$, "**" indicated $P < 0.01$, "***" indicated $P < 0.001$, "****" indicated $P < 0.0001$.
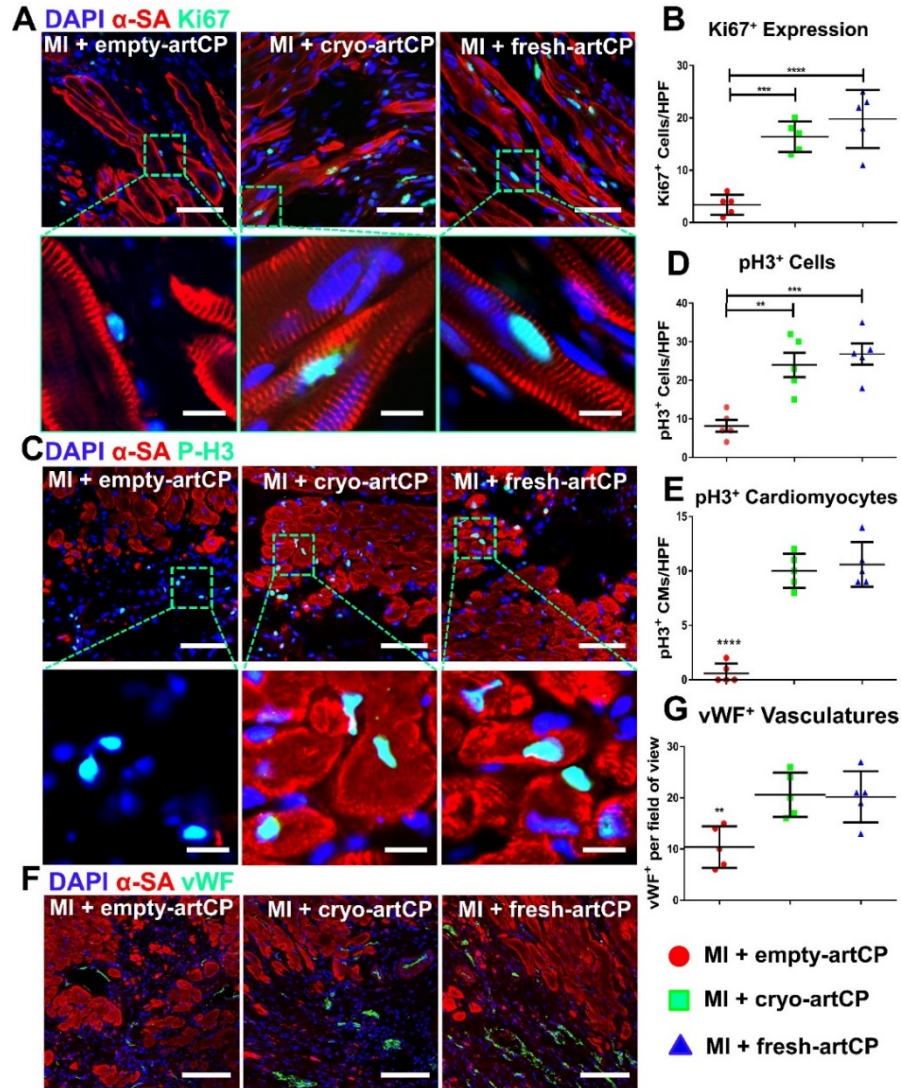
Fig. S12. Mechanistic studies on artCP therapy after empty-, cryo- or fresh-artCP transplantation. (A) Ki67+ cells (green) were detected and quantified on the infarct periphery. Scale bar = 50 µm. Scale bar in zoomed snapshot =10 µm. (B) Ki67$^+$ expressed cells were counted per HPF through Image J software. n=5 in each group. (C) pH3$^+$ (green) were also detected. Scale bar = 50 µm. Scale bar zoomed snapshot =10 µm. (D) pH3$^+$ cells and (E) pH3$^+$ cardiomyocytes were counted per HPF through Image J software. n=5 in each group. (F) vWF$^+$ (green) was detected in the heart infarcted area that interfaced with transplanted empty-artCP, cryo-artCP and fresh artCP group. Scale bar= 100 µm. (G) The pooled data of vWF$^+$ signal counting per high power field (HPF) was assessed by Image J software. n=5 in each group. All data were means ± s.d. Comparisons among groups were performed using one-way ANOVA followed by *post hoc* Bonferroni test. The comparisons between samples were indicated by lines, and the statistical significance was indicated by asterisks above the lines. "**" indicated $P < 0.01$, "***" indicated $P < 0.001$, "****" indicated $P < 0.0001$.
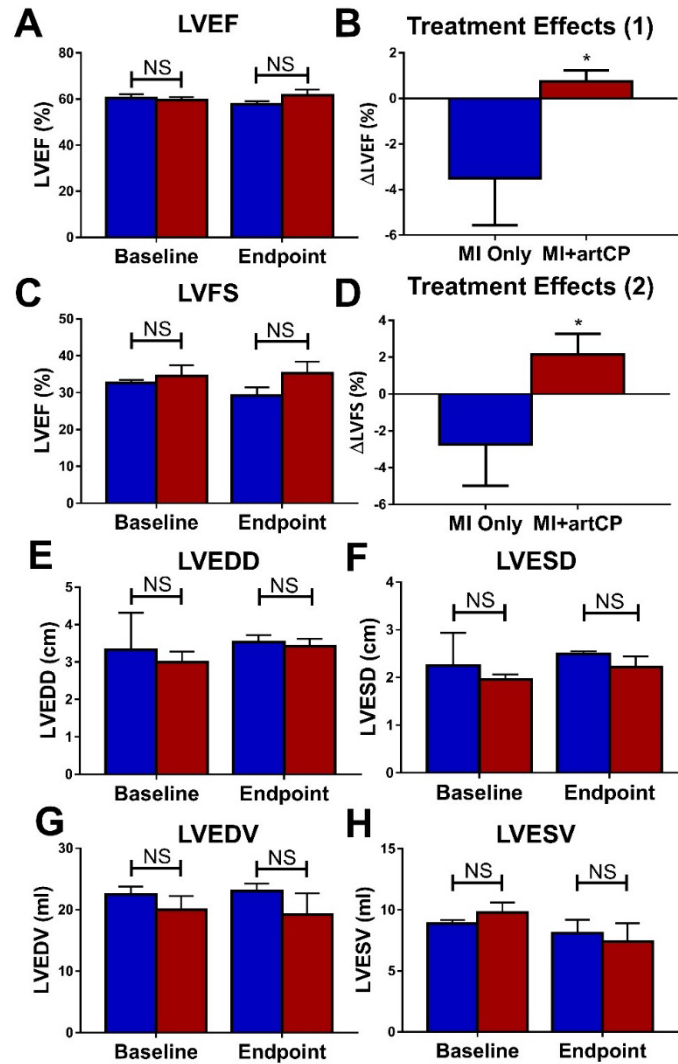
Fig. S13. Cardiac function assessment after artCP therapy in porcine MI models. (A) LVEF was measured at 4hour (baseline) and 7 days (endpoint) post injury. n=3 in each group. (B) cardiac pumping efficiency was measured by LVEF shift after 7 days of artCP transplantation. n=3 in each group. (C) LVFS was measured at 4 hour (baseline) and 7 days (endpoint) post injury. n=3 in each group. (D) Cardiac contractility was measured by LVFS transition. n=3 in each group. From M-mode images at chordae tendineae level, LVEDD at 4 hours (baseline) and 21 days (endpoint) (E) and LVESD at 4 hours (baseline) and 21 days (endpoint) (F) were measured. From B-mode at long axis, LVEDV at 4 hours (baseline) and 21 days (endpoint) (G) were measured. Also, LVESV at 4 hours (baseline) and 21 days (endpoint) (H) were measured. All data were means ± s.d. Comparisons among groups were performed using one-way ANOVA followed by *post hoc* Bonferroni test. The comparisons between samples were indicated by lines, and the statistical significance was indicated by asterisks above the lines. NS indicated $P > 0.05$, "*" indicated $P < 0.05$.
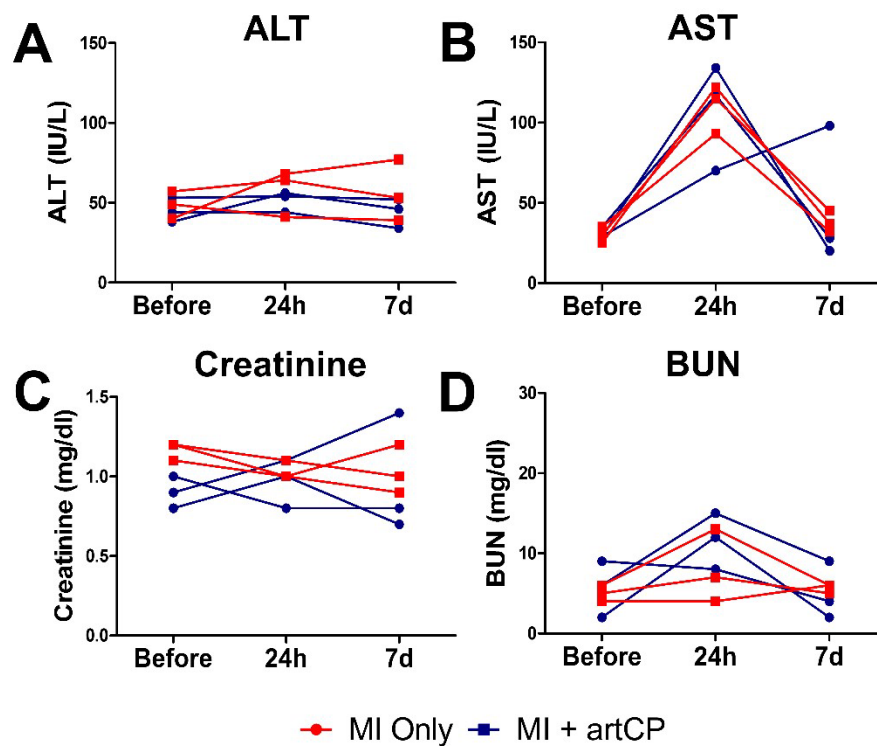
Fig. S14. Liver functions and kidney functions of porcine MI models before and after ArtCP transplantation. (A) The alanine aminotransferase (ALT) and (B) aspartate aminotransferase (AST) expressions were evaluated by blood tests (NC State Veterinary Medicine diagnostic laboratories). (C-D) The blood creatinine (C) and blood urea nitrogen (D) measurements were examined to evaluate kidney toxicity of artCP transplantation (NC State Veterinary Medicine diagnostic laboratories). n=3 in each group. All data were means ± s.d. Comparisons among groups were performed using one-way ANOVA followed by post hoc Bonferroni test.
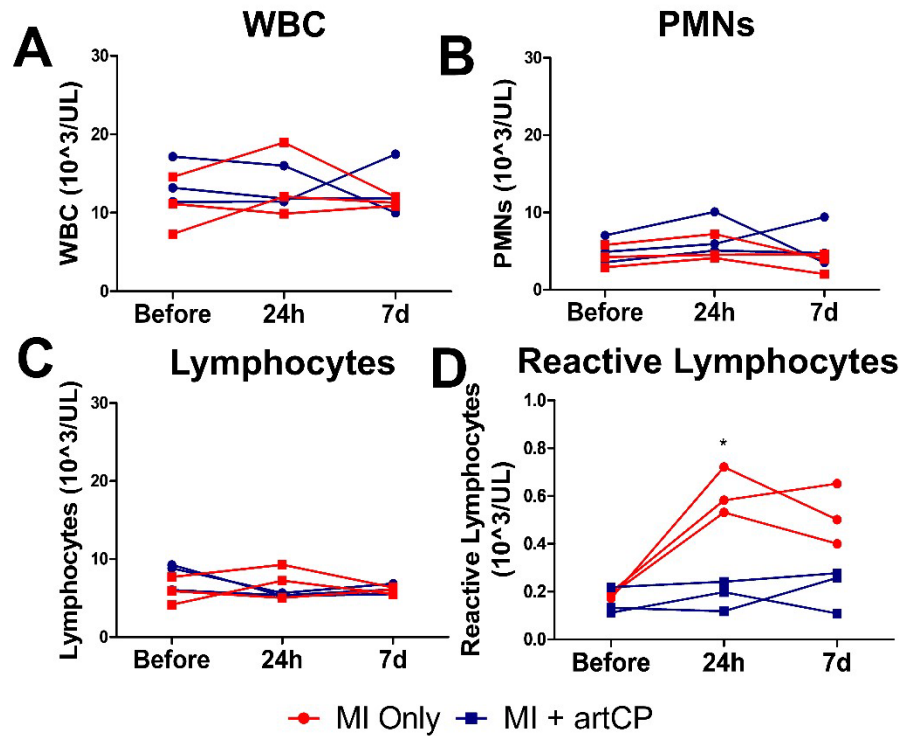
Fig. S15. The immunogenicity detection before and after artCP transplantation in porcine MI Models. (A) WBC, (B) PMNs, (C) lymphocytes, and (D) reactive lymphocytes were measured to address the immune reaction after transplanted artCP. Blood was drawn pre-MI, 24 hours post-MI and 7 days post-MI. n=3 in each group. All data were means ± s.d. Comparisons among groups were performed using one-way ANOVA followed by post hoc Bonferroni test. NS indicated P > 0.05. * indicated P < 0.05.

Supplementary Figures
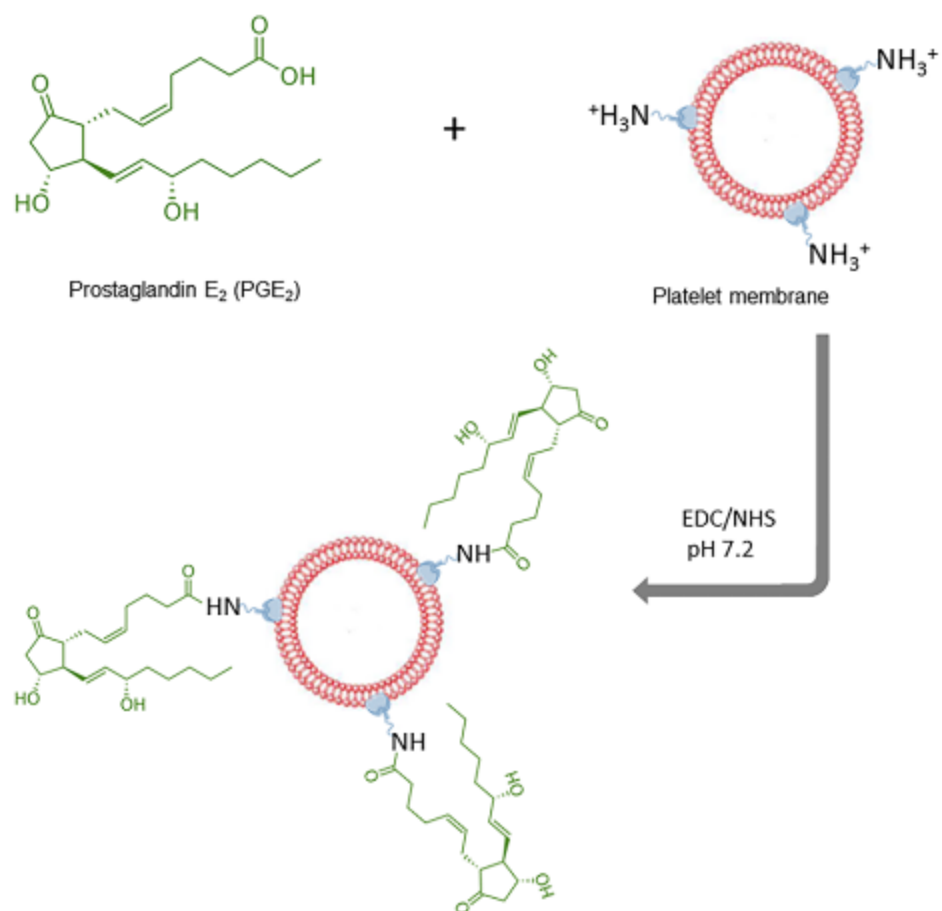
Fig S1. Synthesis of the PGE₂-platelet membrane conjugates.
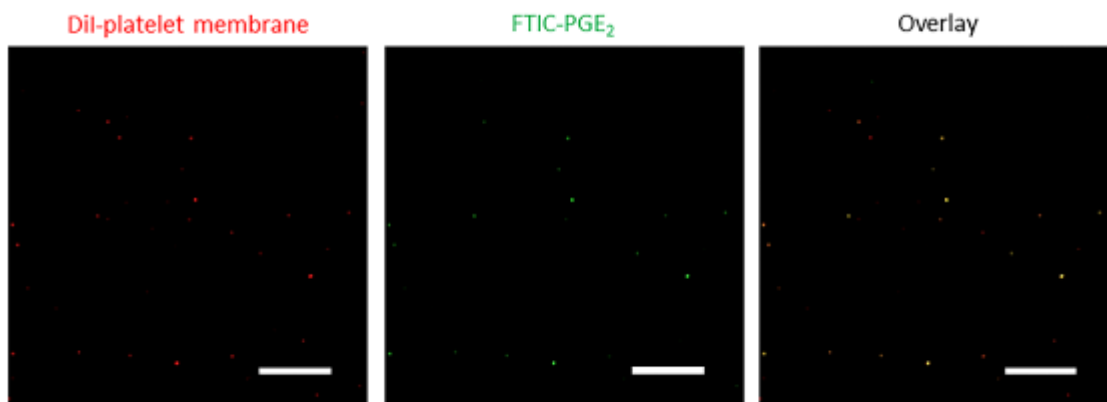
Fig S2. Confocal images of PGE2-platelet membrane conjugate. The platelet membrane was labeled with DiI prior to the synthesis of PGE$_2$-platelet membrane conjugate. Subsequently, the DiI-labeled PGE$_2$-platelet membrane conjugate was incubated with FTIC-labeled PGE$_2$ antibody overnight before imaging. Scale bars, 10 μm.
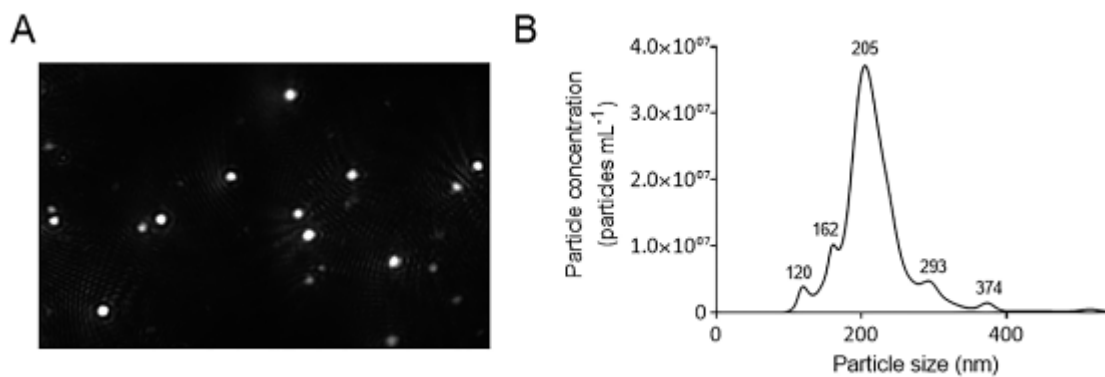
Fig S3. Nanoparticle tracking analysis (NTA) of CS-PGE2-PINCs using NanoSight. (A) Representative particle tracking image of CS-PGE$_2$-PINCs; (B) Size distribution as reported by NTA showing that the average size of CS-PGE$_2$-PINC is about 205 nm, consistent with those determined by DLS and TEM analysis.
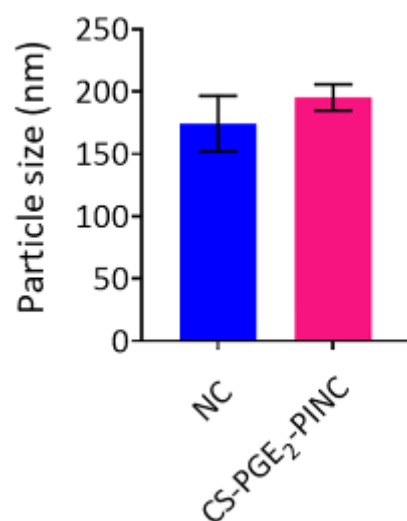
Fig S4. The average particle sizes of the as-prepared NCs and CS-PGE2-PINCs in PBS (1×, pH 7.4). All data are mean ± s.d. ($n = 3$). Comparisons between any two groups were performed using two-tailed unpaired Student's t-test. * indicates $p < 0.05$, ** indicates $p < 0.01$, *** indicates $p < 0.001$.
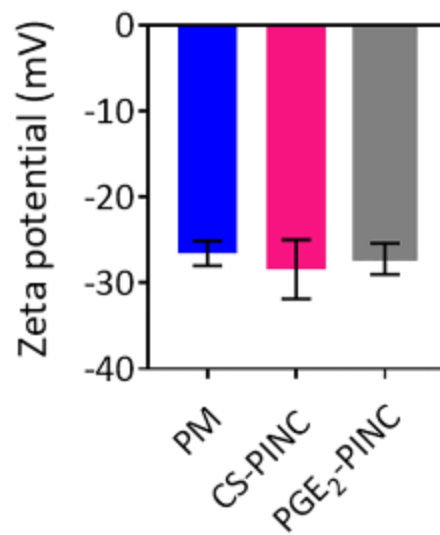
Fig S5. The zeta potentials of platelet membrane (PM), CS-PINCs, and PGE2-PINCs in PBS (1×, pH 7.4). All data are mean ± s.d. ($n = 3$). Comparisons among more than two groups were performed using one-way ANOVA followed by *post hoc* Bonferroni test. * indicates $p < 0.05$, ** indicates $p < 0.01$, *** indicates $p < 0.001$.
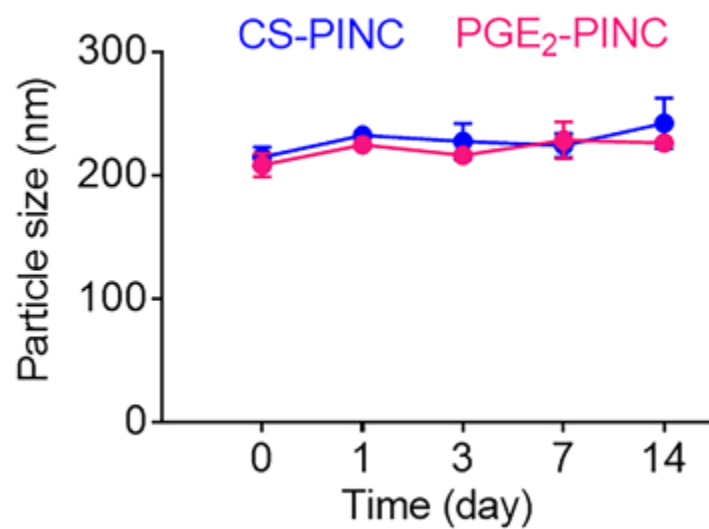
Fig S6. The average particle sizes of CS-PINC and PGE2-PINC over 2 weeks in PBS (1×, pH 7.4). All data are mean ± s.d. (n = 3).
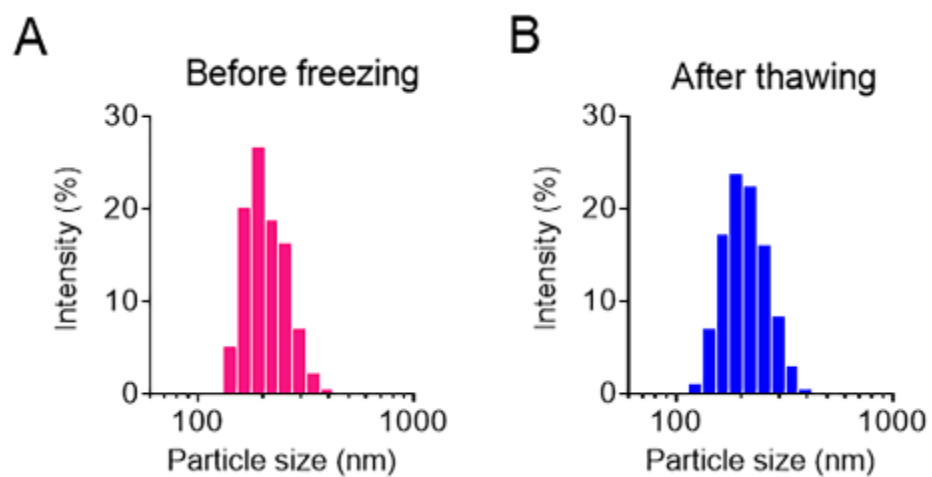
Fig S7. The particle size distribution of CS-PGE$_2$-PINC before freezing at -80 °C and after thawing at room temperature 3 months later.
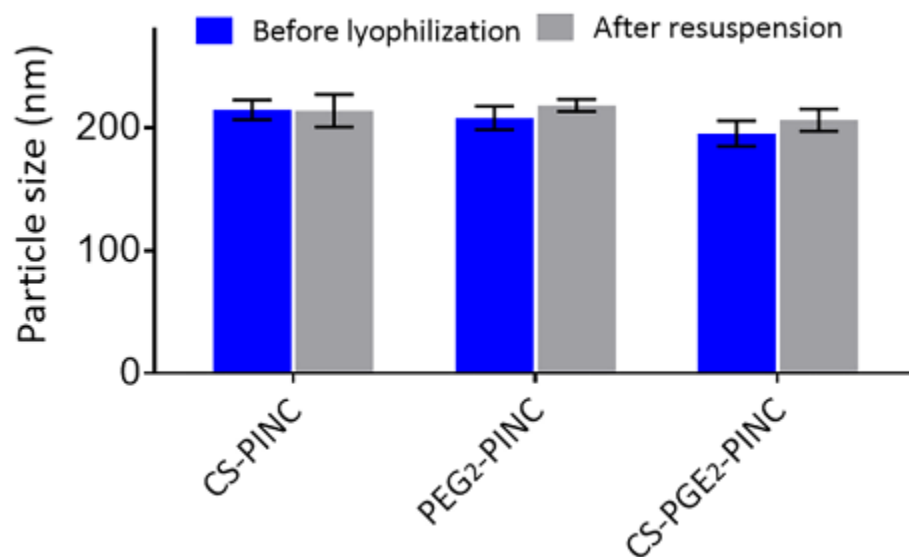
Fig S8. The particle sizes of CS-PINC, PGE2-PINC, CS-PGE2-PINC before lyophilization in 10 wt% sucrose and after resuspension in PBS (1×, pH 7.4). All data are mean ± s.d. ($n = 3$). Comparisons between any two groups were performed using two-tailed unpaired Student's t-test. * indicates $p < 0.05$, ** indicates $p < 0.01$, *** indicates $p < 0.001$.
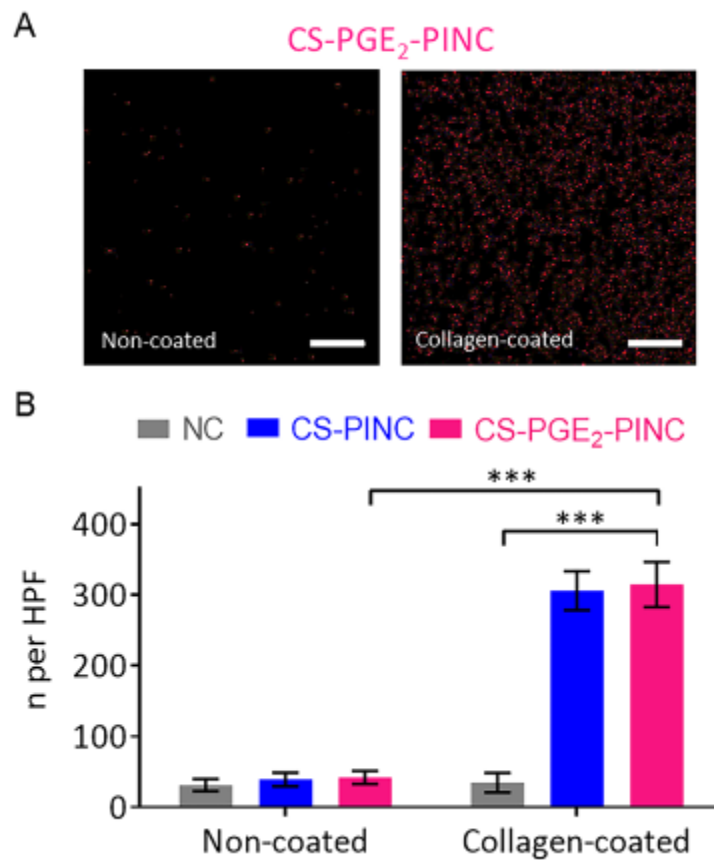
Fig S9. Binding ability of CS-PEG2-PINCs to the collagen-coated and non-coated surface of culture chamber slide. (A) Representative images showing the binding of CS-PEG$_2$-PINCs to the collagen-coated 4-well culture chamber slide surface relative to the non-coated surface. (B) Quantification of the numbers of different nanoparticles binding to the collagen-coated and non-coated surfaces, respectively. All data are mean ± s.d. ($n = 3$). Comparisons between any two groups were performed using two-tailed unpaired Student's *t*-test. Comparisons among more than two groups were performed using one-way ANOVA followed by *post hoc* Bonferroni test. * indicates $p < 0.05$, ** indicates $p < 0.01$, *** indicates $p < 0.001$.
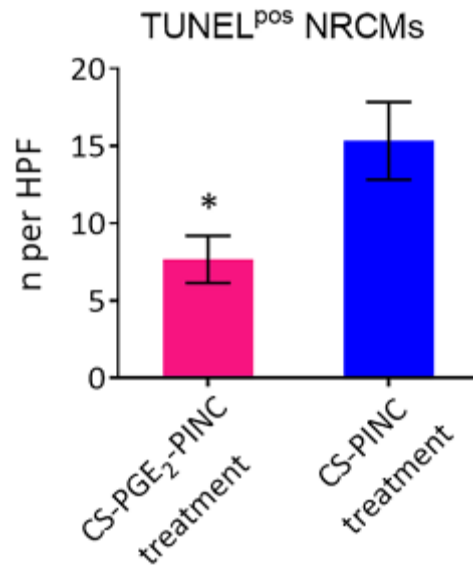
Fig S10. The apoptosis of CS-PGE2-PINC-treated and CS-PINC-treated NRCMs after being exposed to serum-free IMDM medium supplemented with hydrogen peroxide (250 µM) for 3 h, as determined by TUNEL staining. All data are mean ± s.d. ($n = 3$). Comparisons between any two groups were performed using two-tailed unpaired Student's t-test. * indicates $p < 0.05$, ** indicates $p < 0.01$, *** indicates $p < 0.001$.
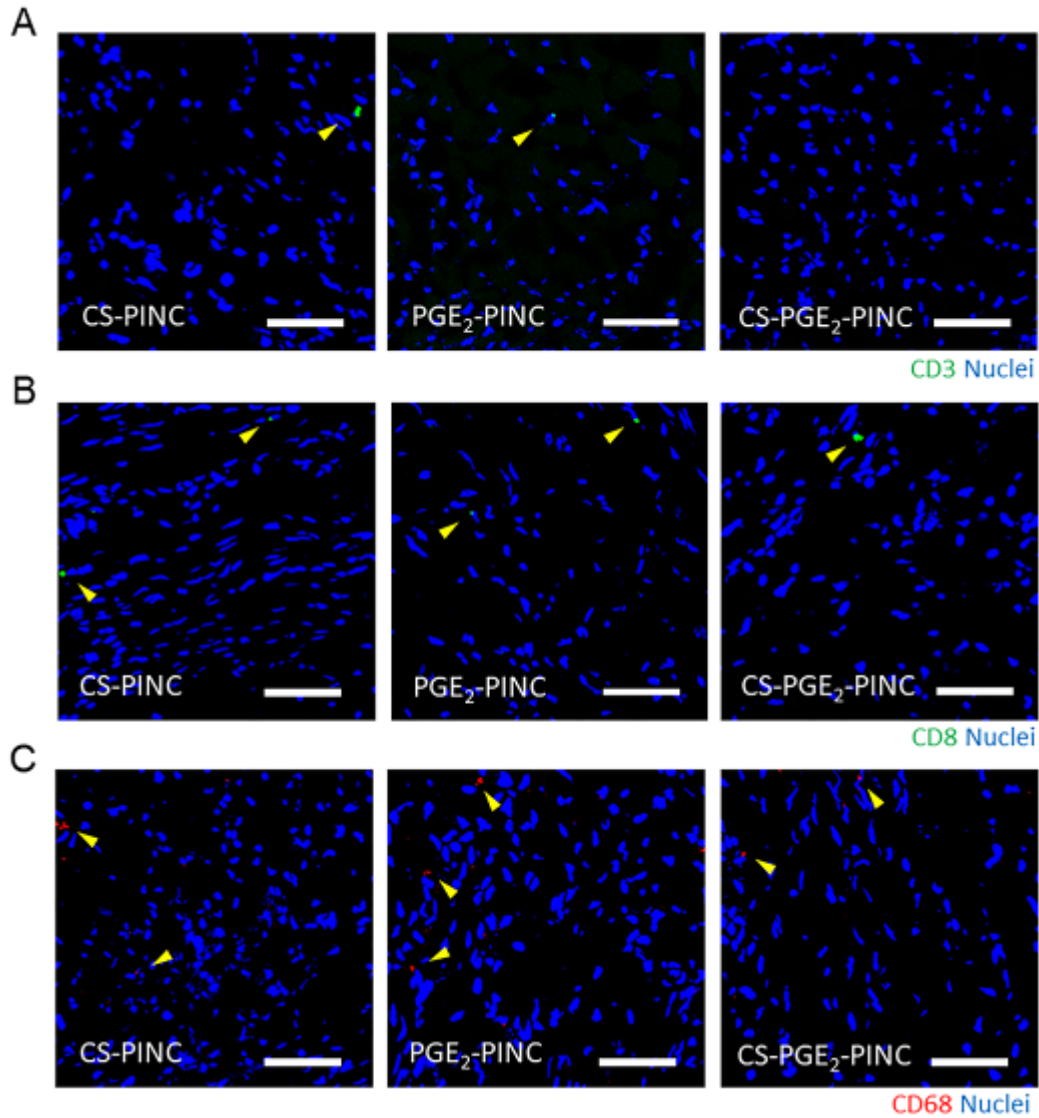
Fig S11. PINC injection does not stimulate local T-lymphocyte and macrophage immune response. The infiltration of T-lymphocytes with CD3 (green, A) and CD8 (green, B) expression was neglectable. Macrophages that labeled with CD68 (red, C) were also barely detected. Nuclei were counterstained with DAPI (blue). Scale bars, 50 μm.
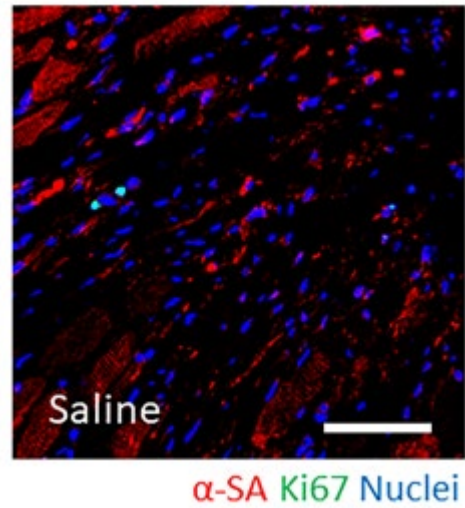
Fig S12. Representative images showing that cycling cardiomyocytes as indicated by α-SA and Ki67 double-positive staining were barely detected in the peri-infarct region of the hearts treated with saline at week 4. Scale bar, 50 μm.

Appendix C: Chapter 4 Supplemental Data

Supplementary Materials and methods

Cardiac function assessment

In order to measure rat cardiac dimensions and function, echocardiography was performed at 4h and 21 days after MI surgical operation following induction of anaesthesia with a 1.5% isofluorane-oxygen mixture. Echocardiography was accomplished by a Philips Cx-30 Ultrasound System with an L15-7io high-frequency probe. Two-dimensional guided M-mode images at chordae tendineae level and B-mode at long axis were evaluated. From M-mode, left ventricle end-diastolic and end-systolic dimensions (LVEdD and LVEsD, respectively) were measured by using the leading-edge method of the American Society of Echocardiography. The B-mode images were obtained for measurements of left ventricle end-diastolic and end-systolic volume (LVEdV and LVEsV, respectively). LVEF was determined from B-mode echocardiography (LVEdV-LVEsV/LVEdV) × 100%, and LVFS was calculated from M-mode echocardiography (LVEdD-LVEsD/LVEdD) × 100%.

Heart morphometry studies

After all animals were euthanized, hearts from mice were collected and frozen in optimum cutting temperature (OCT) compound (Tissue-Tek, Torrance, CA) after equilibrated with increasing sucrose solutions up to 30% overnight. Then, the hearts in OCT were cryo-sectioned with a thickness of 10 μm from the apex to the ligation level with 100 μm intervals for Masson's Trichrome staining as previously performed. Masson's Trichrome stained tissue slides were scanned with a PathScan Enabler IV slide scanner (Advanced Imaging Concepts, Princeton, NJ). Morphometric parameters were measured with ImageJ software.

Immunohistochemistry (IHC)

The IHC analysis of heart cryo-sections was performed as previously described. Briefly, all samples were fixed (4% paraformaldehyde solution), blocked and permeabilized (Dako, Glostrup, Denmark with 0.01% saponin, Sigma-Aldrich, St. Louis, MO) for incubating with primary antibodies overnight at 4°C: mouse anti-alpha sarcomeric actin (1:200, a7811, Sigma), rabbit anti-Ki67 (1:200, ab15580, Abcam), rabbit anti-von Willebrand factor (1:200, ab11713, Abcam), rabbit anti- Histone H3 (1:100, ab5176, Abcam), rabbit anti- AuroraB (1:100, ab2254, Abcam), rat anti- CD34 (1:200, Monoclonal antibody MEC14.7, Invitrogen). FITC- or Texas-Red secondary antibodies (1:400, Abcam) were applied for antibody conjunction (1.5 hours, room temperature). Samples were then mounted in Prolong Gold Antifade Mountant with DAPI (Thermofisher, P36935). Images were taken with an epi-fluorescent microscope (Olympus IX81) and confocal fluorescent microscope (ZEISS LSM 880). Tissue morphology was characterized by images using the NIH Image J software and ZEN lite software.

Statistical analysis

All results are expressed as mean ± s.d. Comparison between two groups was performed with two-tailed Student's t-test. Comparisons among more than two groups were performed using one-way ANOVA followed by post hoc Bonferroni test. Differences were considered statistically significant when the P value < 0.05.
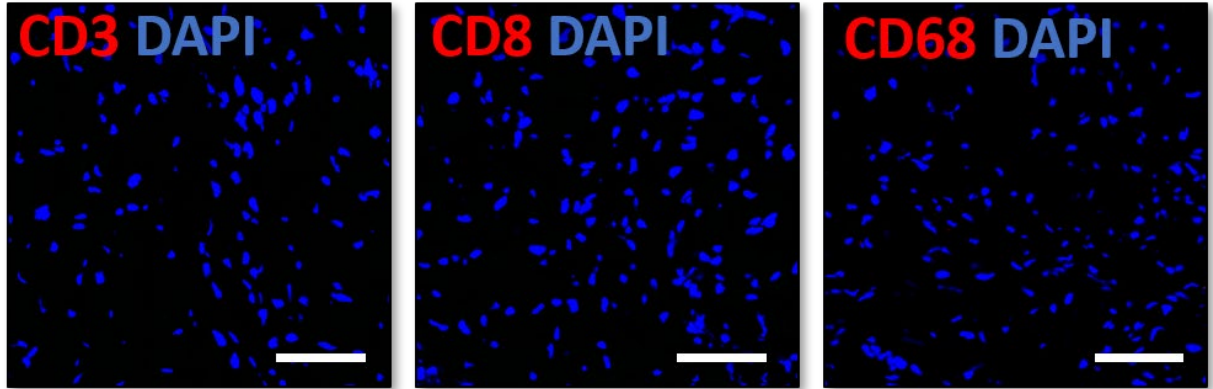
Supplemental Figures

Fig S1. The immunogenicity of SCRD BsAbs. The infiltration of T-lymphocytes with CD8 (green) and CD3 (green) were barely detected. Macrophages that labelled with CD68 (green) were also neglectable. Nuclei were counterstained with DAPI (blue). Scale Bar, 50 μm.
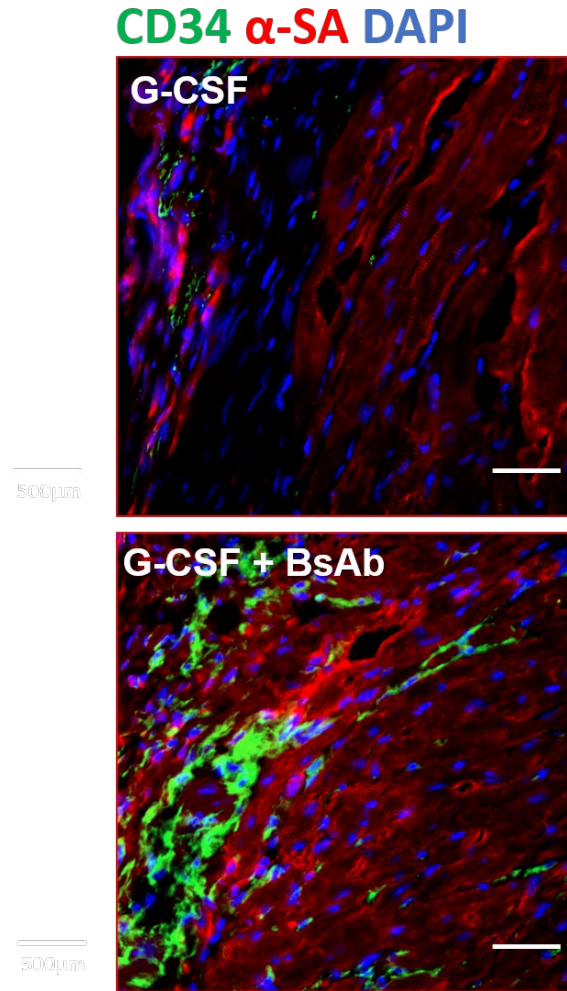
CD34 α-SA DAPI

Figure S2. SCRD BsAbs treatment promotes stem cell recruitment. CD34$^+$ cells in the infarcted area were detected *via* CD34 antibodies (green). Myocardium was counterstained with α-SA (red). Nuclei were counterstained with DAPI (blue). Scale Bar, 50 μm.
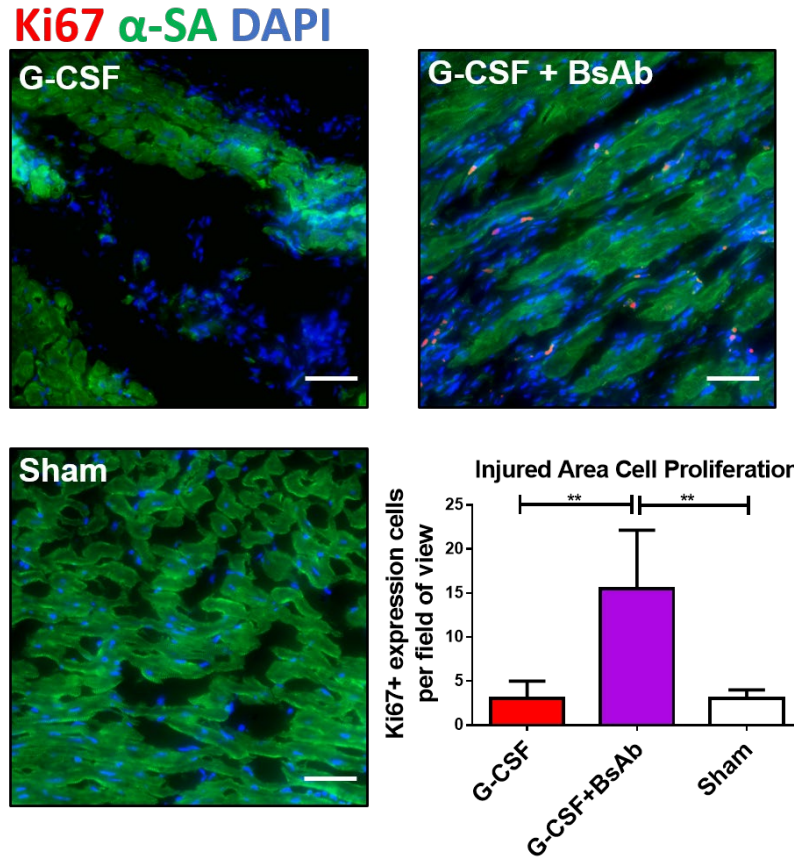
Fig. S3. The effects of SCRD BsAbs treatment on cell-cycling in the infarcted area. The area around MI risk area was analyzed through IHC. Ki67^{+} cells (red) were counted per field of view through Image J software. n=4 in Sham group, n=6 in G-CSF group, n=5 in G-CSF + BsAb group. All data were means ± s.d. Comparisons among groups were performed using one-way ANOVA followed by *post hoc* Bonferroni test. The comparisons between samples were indicated by lines, and the statistical significance was indicated by asterisks above the lines. "**" indicated P <0.01.